Synthesis, Structural, Electronic, And Magnetic Properties Studies of Two-Dimensional Magnetic Materials

Thesis submitted for the degree of
Doctor of Philosophy (Science)
in
Physics (Experimental)

by
Shubham Purwar

Department of Physics
University of Calcutta
2025

Dedicated to

To my beloved papa and maa, whose dreams and sacrifices have shaped my journey. This work stands as a testament to your unwavering love, guidance, and belief in me

Declaration

I hereby declare that the work presented in this dissertation is my own. I have properly cited all the original sources and references used throughout the document. I further declare that I have adhered to the highest standards of academic integrity and honesty. I have not misrepresented, fabricated, or manipulated any data, facts, ideas, or sources in the preparation of this thesis.

Shubham Purwar
Kolkata, India

Acknowledgement

Pursuing my Ph.D. at the S. N. Bose National Centre for Basic Sciences, Kolkata, has been an immensely rewarding experience, enriched by the exceptional research environment and the remarkable individuals who have supported me along the way. From the beginning of my academic journey, I have been fortunate to meet mentors and peers who have instilled in me a deep respect for learning and a passion for research. I am truly grateful to all who have contributed to this journey.

First and foremost, I extend my deepest gratitude to my advisor, Dr. Thirupathaiah Setti, for his exceptional guidance, steadfast support, and visionary insights throughout my Ph.D. journey. Under his mentorship, I had the privilege of working on three impactful projects that have significantly shaped my understanding and expertise in the field. His unwavering dedication, profound knowledge, and constant encouragement have been a source of inspiration, enabling me to grow not only as a researcher but also as an individual. Dr. Setti's mentorship has been the cornerstone of my academic achievements, and I am truly fortunate to have had his guidance during this transformative phase of my life.

I am deeply thankful to the S. N. Bose National Centre for Basic Sciences for providing a nurturing research environment, complete with state-of-the-art facilities, serene surroundings, and comfortable accommodations. The advanced instrumental facilities under the DST Technical Research Centre (TRC) project have been pivotal to my research, and I extend my gratitude to the Department of Science and Technology (DST), India, for the Ph.D. fellowship that sustained my work. A special mention goes to the cricket and badminton grounds at the Centre, and to the friends with whom I shared countless joyful moments, which greatly contributed to my overall well-being.

I sincerely thank the members of the Quantum Materials group, whose camaraderie and support have made this journey memorable. My heartfelt thanks go to Dr. Indrani Kar, Dr. Susmita Changdar, Achintya Low, Sayan Routh, Susanta Ghosh, Soumya Ghorai, Anupam Barik, Ankita Das, and Sutirtha Banerjee for their collaboration and friendship. I am equally grateful to the postdoctoral researchers—Dr. Reena Goyal, Dr. Pankaj Maheshwari, Dr. Tushar Kanti Bhowmik, and Dr. Ayana Mukhopadhyay—for their guidance and support.

I extend my gratitude to my Integrated Ph.D. (iPhD) batchmates from 2017-19, including Nivedita Pan, Samir Rom, Parthapratim, Harmit, Riju, and Manjuri, for their friendship and encouragement. I am particularly thankful to my M.Sc. supervisor, Dr. Thirupathaiah Setti, and my M.Sc. teachers, including Prof. Sakuntala Chatterjee, Prof. Priya Mahadevan, Prof. Amitabha Lahiri, Prof. Anjan Barman, Prof. Sunandan Gangopadhyay, Prof. Rajib Kr. Mitra, Prof. Prosenjit Singha Deo, and Dr. Manoranjan Kumar, whose teaching laid the foundation for my academic growth.

I also express my sincere thanks to my Ph.D. coursework instructors, Dr. Atindra Nath Pal, Prof. Rajib Kr. Mitra, Dr. Suman Chakrabarty, Prof. Tanusri Saha-Dasgupta, and Dr. Thirupathaiah Setti, for strengthening my academic foundation. My gratitude extends to the esteemed members of my examination committee for their time and expertise in evaluating my thesis.

A special acknowledgment goes to Dr. Awadhesh Narayan and Anumita Bose from IISc Bangalore, Shinjhini Paul and Prof. Priya Mahadevan from SNBNCBS, and Tijare Mandar Rajesh and Dr. Bheema Lingam Chittari from IISER Kolkata, for their theoretical insights and significant contributions to DFT calculations. I also thank Dr. Venkatesh and his team at RRCAT, Indore, for providing access to essential measurement setups. My gratitude also extends to Anupam Gorai for his technical assistance.

I am deeply thankful to the administrative staff at SNBNCBS, particularly Ms. Nibedita Konar, Ms. Chandrakana Chatterjee, Mr. Rupam Porel, Mr. Jaydeep Kar, and Mr. Swarup Dutta, for their support. I also acknowledge the technical staff, including Mr. Rishikesh Nandi, Mr. Shakti Nath Das, Mrs. Urmi Chakrabarty, Mr. Joy Bandopadhyay, Mr. Sourabh Sinha, and Mr. Debarghya Ghosh, for their assistance during measurements. My gratitude extends to the SNB mess and canteen team, whose dedication ensured comfort, especially during the COVID-19 pandemic.

I am grateful for the friendships I have formed along this journey. My heartfelt thanks go to Dr. Daloo Ram, Akriti Sinha, Kamini Bharti, Shreesh Mishra, Souvnik da, Sarowar da, Supriya da, Dipanjan da, Shivam Mishra, Vishal Agarwal, Atul Rathor, Tanmoy Chakraborty, Premashish Kumar, Biswajit Panda, Shashank Gupta, Surya Narayan Panda and iPhD batchmates (2018-20). A special note of appreciation goes to Ishita Jana for her unwavering support during challenging times.

I extend my heartfelt thanks to my school teachers—Usman Sir, Jitendra Panday Sir, Umesh Sir, and Mahesh Sir—for nurturing my curiosity for science. I am also grateful to my childhood friends, including Satyam Gupta, Diksha Singh, and Vishal Purwar, for their encouragement.

Above all, I am profoundly grateful to my family for their unwavering support, boundless love, and constant encouragement, which have been the cornerstone of my strength throughout this journey. I cherish the memory of my late father, Ajay Kumar Purwar, whose values and aspirations continue to inspire me every day. My heartfelt thanks go to my mother, Mrs. Sudha Purwar, for her unconditional love and sacrifices that have been the foundation of my success. I deeply appreciate the support of my brothers, Ashwini Purwar, Siddhartha Purwar, and Manu Purwar, as well as my uncles, especially Raju Purwar, and other relatives who have always stood by me. My aunts, Manisha Purwar and Kirti Purwar, and my sister, Shweta Purwar, have been pillars of encouragement throughout my journey. I am equally grateful to my sisters-in-law, Nisha Purwar and Arti Purwar, and my nephews, Arnav Purwar and Arrav Purwar, for their warmth and love. Finally, my cousins, Rishabh, Shreya, Sanskar, and Sankalp Purwar, have brought joy and positivity to my life, for which I am truly thankful. My family's unwavering belief in me has been my greatest source of inspiration and resilience.

Abstract

This thesis explores the structural, magnetic, electrical, and magnetotransport properties of Cr_xTe_y-based layered magnetic compounds, aiming to uncover their potential in magnetocaloric, spintronic, and topological quantum applications. We begin with a comprehensive analysis of the ferromagnetic layered compound $Cr_{1.33}Te_2$ (or Cr_2Te_3), employing the numerical techniques such as the modified Arrott plot, Kouvel-Fisher method, and critical isothermal analysis to examine its critical behavior near the Curie temperature ($T_C \approx 170$ K). The derived critical exponents $\beta = 0.353(4)$ and $\gamma = 1.213(5)$ indicate complex magnetic interactions, while renormalization group theory reveals 3D Ising-type exchange interactions decaying as $J(r) = r^{-4.89}$. Notably, $Cr_{1.33}Te_2$ (or Cr_2Te_3) exhibits a substantial uniaxial magnetocrystalline anisotropy energy (MAE) of 2065 kJ/m^3. Subsequently, we investigate the monoclinic layered ferromagnet $Cr_{1.38}Te_2$ (or $Cr_{2.76}Te_4$), characterized by soft ferromagnetic behavior and strong magnetocrystalline anisotropy. Below 50 K, it experiences an antiferromagnetic-like transition, and between 50 and 150 K, fluctuating magnetic moments yield a noncoplanar spin structure. The itinerant nature is supported by a Rhodes-Wohlfarth ratio of $\mu_{eff}/\mu_s = 1.89$. $Cr_{1.38}Te_2$ shows significant anomalous Hall effect (AHE) due to skew scattering and a topological Hall effect (THE) associated with its noncoplanar spin configuration. Critical behavior analysis shows complex magnetic interactions, with long-range exchange interactions decaying as $J(r) = r^{-4.73}$. The easy axis aligns along the b-axis, and a maximum entropy change of $-\Delta S_{max} \approx 2.51$ J/kg·K near the higher Curie temperature ($T_C \approx 316$ K) highlights its magnetocaloric potential. We also examine the hexagonal itinerant ferromagnet $Cr_{1.66}Te_2$ (or Cr_5Te_6), revealing critical exponents $\beta = 0.4739(4)$, $\gamma = 1.2812(3)$, and $\delta = 3.7037(5)$. Magnetotransport studies demonstrate a notable THE due to noncoplanar spin structures and strong magnetocrystalline anisotropy, alongside AHE due to skew scattering. The magnetocaloric effect, with $-\Delta S_{max} \approx 2.77$ J/kg·K near $T_C \approx 338$K, underscores its potential for the room-temperature magnetic refrigeration application. Finally, we report the discovery of superconductivity in Sn-intercalated Cr_3Te_4 (or $Sn_{0.06}Cr_3Te_4$), exhibiting a transition temperature of $T_c \approx 3.5$ K. This compound posses fascinating physical properties such as superconductivity, magnetism, and a topological Hall effect simultaneously. Spin-resolved density functional theory (DFT) calculations suggest separate conduction channels for magnetism and superconductivity.

सारांश

यह शोधप्रबंध Cr_xTey-आधारित लेयर्ड चुंबकीय यौगिकों की संरचनात्मक, चुंबकीय, विद्युत, और मैग्नेटोट्रांसपोर्ट विशेषताओं का अध्ययन करता है, जिसका उद्देश्य इन्हें मैग्नेटोकैलोरिक, स्पिन्ट्रॉनिक और टोपोलॉजिकल क्वांटम अनुप्रयोगों में उपयोग की संभावनाओं को उजागर करना है। हम सबसे पहले फेरोमैग्नेटिक लेयर्ड यौगिक $Cr_{1.33}Te_2$ (या Cr_2Te_3) का व्यापक विश्लेषण प्रस्तुत करते हैं, जिसमें क्यूरी तापमान ($T_C \approx 170$ K) के पास इसके क्रिटिकल व्यवहार की जांच के लिए मॉडिफाइड एरॉट प्लॉट, कौवेल-फिशर विधि, और क्रिटिकल आइसोथर्मल विश्लेषण जैसी तकनीकों का उपयोग किया गया। प्राप्त क्रिटिकल गुणांक ($\beta = 0.353(4)$ और $\gamma = 1.213(5)$) जटिल चुंबकीय परस्पर क्रियाओं को इंगित करते हैं, जबकि रीनॉर्मलाइज़ेशन ग्रुप थ्योरी 3D इसिंग-प्रकार की एक्सचेंज इंटरैक्शन को $J(r) = r^{-4.89}$ के रूप में दर्शाती है। विशेष रूप से, $Cr_{1.33}Te_2$ (या Cr_2Te_3) में 2065 kJ/m^3 का उल्लेखनीय यूनिएक्सियल मैग्नेटोक्रिस्टलाइन एनीसोट्रॉपी एनर्जी (MAE) पाया गया है।

इसके बाद, हम मोनोक्लिनिक लेयर्ड फेरोमैग्नेट $Cr_{1.38}Te_2$ (या $Cr_{2.76}Te_4$) का अध्ययन करते हैं, जो सॉफ्ट फेरोमैग्नेटिक व्यवहार और मजबूत मैग्नेटोक्रिस्टलाइन एनीसोट्रॉपी द्वारा विशेषीकृत है। 50 K से नीचे, यह एक एंटीफेरोमैग्नेटिक-जैसा संक्रमण दर्शाता है, और 50 K से 150 K के बीच, चुंबकीय क्षणों में उतार-चढ़ाव एक नॉनकोप्लानर स्पिन संरचना उत्पन्न करते हैं। इसका इटिनरेंट स्वभाव रोड्स-वोल्फार्थ अनुपात ($\mu_{eff} / \mu_s = 1.89$) द्वारा समर्थित है। यह यौगिक स्क्यू स्कैटरिंग के कारण एक महत्वपूर्ण अनौमोलस हॉल प्रभाव (AHE) और अपनी नॉनकोप्लानर स्पिन संरचना के कारण टोपोलॉजिकल हॉल प्रभाव (THE) प्रदर्शित करता है। क्रिटिकल व्यवहार विश्लेषण में जटिल चुंबकीय परस्पर क्रियाएं पाई गईं, जिसमें लंबी दूरी की एक्सचेंज इंटरैक्शन $J(r) = r^{-4.73}$ के रूप में क्षयित होती है। इसका ईज़ी एक्सिस b-अक्ष के साथ मेल खाता है, और उच्च क्यूरी तापमान ($T_C \approx 316$ K) के पास $-\Delta S_{max} \approx 2.51$ J/kg·K की अधिकतम एंट्रॉपी परिवर्तन इसकी मैग्नेटोकैलोरिक क्षमता को उजागर करती है।

हम हेक्सागोनल इटिनरेंट फेरोमैग्नेट $Cr_{1.66}Te_2$ (या Cr_5Te_6) का भी अध्ययन करते हैं, जो क्रिटिकल गुणांक $\beta = 0.4739(4)$, $\gamma = 1.2812(3)$, और $\delta = 3.7037(5)$ प्रदर्शित करता है। मैग्नेटोट्रांसपोर्ट अध्ययन में नॉनकोप्लानर स्पिन संरचनाओं से उत्पन्न उल्लेखनीय THE और मजबूत मैग्नेटोक्रिस्टलाइन एनीसोट्रॉपी के साथ-साथ AHE (AHE) पाया गया, जो बाह्य स्क्यू स्कैटरिंग से उत्पन्न होता है। मैग्नेटोकैलोरिक प्रभाव, जिसमें T_C के पास $-\Delta S_{max} \approx 2.77$ J/kg·K पाया गया, इसे कमरे के तापमान पर अनुप्रयोगों के लिए संभावित बनाता है।

अंत में, हम Sn-इंटरकलेशन वाले Cr_3Te_4 (या $Sn_{0.06}Cr_3Te_4$) में सुपरकंडक्टिविटी की खोज करते हैं, जो $T_C \approx 3.5$ K (सुपरकंडक्टिंग संक्रमण तापमान) का संक्रमण तापमान प्रदर्शित करता है। यह यौगिक सुपरकंडक्टिविटी, चुंबकत्व, और टोपोलॉजिकल हॉल प्रभाव का एक रोमांचक सह-अस्तित्व प्रकट करता है, जबकि स्पिन-रिजॉल्व्ड DFT गणनाएं चुंबकत्व और सुपरकंडक्टिविटी के लिए अलग-अलग संचालक चैनल का सुझाव देती हैं।

Contents

Chapter 1

Introduction

The exploration of layered materials has grown significantly in recent years, driven by their unique electronic, optical, and mechanical properties, which open up exciting opportunities in nanotechnology. Starting with graphene [2], a single layer of carbon atoms organized in a hexagonal lattice, researchers discovered remarkable features such as high electrical conductivity, mechanical strength, and flexibility. Following graphene, other 2D materials like hexagonal boron nitride (hBN) [3] and transition metal dichalcogenides (TMDCs), such as MoS_2 [4] and WS_2 [5], gained attention for their diverse physical properties. hBN is an insulator with a wide bandgap, making it ideal as a substrate or encapsulation layer for the graphene-based devices. TMDCs, on the other hand, exhibit layer-dependent bandgaps and unique optoelectronic properties, making them highly suitable for applications in transistors, photodetectors, and flexible electronics [6].

In recent years, magnetic materials with reduced dimensionality have garnered significant attention for their capability to exhibit ferromagnetic order even in the two-dimensional (2D) limit. These materials present exciting opportunities for both fundamental studies and technological advancements, particularly in applications such as magnetic refrigeration, spintronics, and quantum computing [7–14]. Van der Waals (vdW) ferromagnets have become a central focus of study due to their unique magnetic properties in the 2D regime [15–18] and pronounced magnetocrystalline anisotropy [19]. In Heisenberg-type ferromagnetic systems, thermal fluctuations dominate in the 2D limit, suppressing intrinsic long-range magnetic ordering at finite temperatures [20]. However, the incorporation of single-ion anisotropy or exchange anisotropy introduces an energy barrier that mitigates the thermal fluctuations, thereby stabilizing the long-range magnetic ordering in 2D ferromagnetic systems [21].

Figure 1.1 shows the time-line of theoretical and experimental advancements in the exploration of 2D magnetism. Theoretical work on 2D magnets began way back with foundational models like the Ising (1940) and Heisenberg (1946) models, providing early insights into the magnetic interactions in 2D systems. The Dzyaloshinskii-Moriya interaction (DMI) (1957) introduced crucial antisymmetric interactions for understanding the

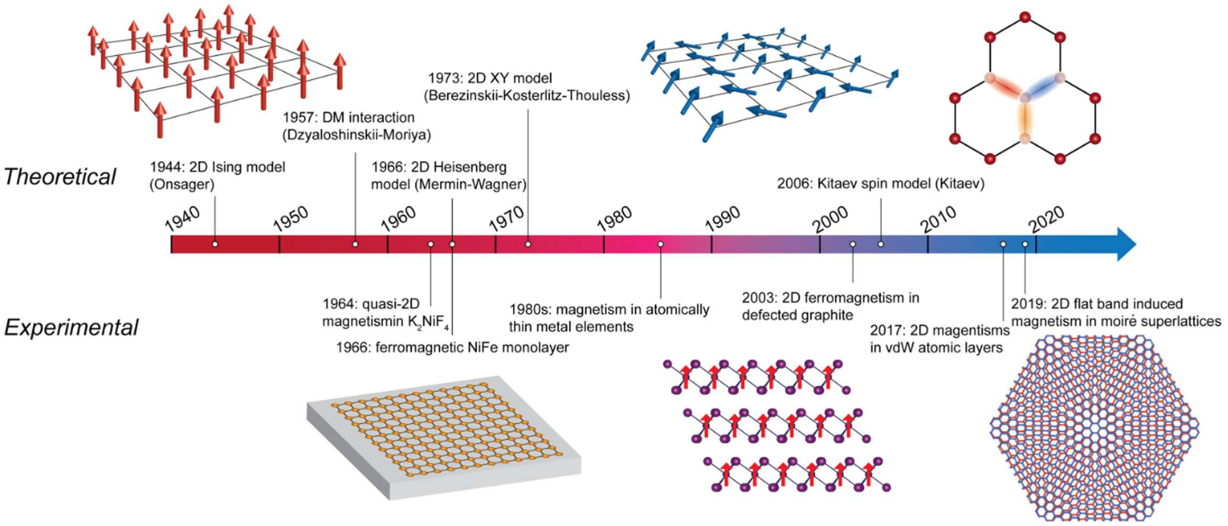

Figure 1.1: Time-line of theoretical and experimental developments in 2D magnetism. Image reprinted from Ref.[1]

non-collinear spin structures, followed by the XY model (1973) which describes the magnetic vortices, and the Kitaev model (2006) which explores the exotic quantum states in 2D lattices. The experimental studies of 2D magnetism can be categorized into four key phases: the exploration of quasi-2D bulk magnetic materials in the 1960s, the examination of magnetic thin films of elemental materials during the 1980s, the study of defect-engineered graphene monolayers in the 2000s, and the recent breakthroughs in intrinsic 2D van der Waals magnetic crystals and moiré superlattices, which began to emerge around 2016.

Experimental evidence of 2D magnetism has been reported in various van der Waals (vdW) materials, including CrI_3 ($T_C \approx 45$ K) [21], $Cr_2Ge_2Te_6$ ($T_C \approx 61$ K) [22], $Cr_2Si_2Te_6$ ($T_C \approx 32$ K) [23, 24], Fe_3GeTe_2 ($T_C \approx 215$ K) [17, 25], $FePS_3$ ($T_N \approx 118$ K) [26], and $FePS_3$ ($T_N \approx 78$ K) [27]. But, most of these materials exhibit Curie or Néel temperatures well below the room temperature, limiting their viability in technological applications. Among these systems, a notable exception is MnP ($T_C \approx 303$ K), which demonstrates room-temperature 2D ferromagnetism in the bulk phase [28]. Therefore, the investigation for new layered materials with room temperature ferromagnetism and possess strong magnetocrystalline anisotropy is essential for potential technological applications.

Theoretical investigations indicate that chromium-based layered tellurides, $Cr_{1+x}Te_2$ ($0 < x < 1$), are potential candidates for realizing the room-temperature 2D ferromagnetism in bulk phase [29]. These compounds generally consist of alternating $CrTe_2$ layers and intercalated Cr layers, where the excess Cr-ion layers are stacked along the z-axis [30]. The concentration of intercalated Cr significantly influences the crystal structure, magnetic order, and transport behavior of these materials [31]. For example, $Cr_{1+x}Te_2$ with $x > 0.8$ adopts a hexagonal NiAs-type structure [32], while $Cr_{1.33}Te_2$ (Cr_2Te_3) and $Cr_{1.5}Te_2$ (Cr_3Te_4) exhibit trigonal or monoclinic symmetries [30]. Similarly, $Cr_{1.25}Te_2$ (Cr_5Te_8)

undergoes a phase transition from trigonal structure at high to monoclinic structure at low temperature [33]. Further, the observation of topological Hall effect (THE) in these systems suggests the existence of nontrivial spin textures, such as skyrmions or bi-skyrmions [34, 35], or complex magnetic configurations like noncoplanar or noncollinear structures [36, 37]. Additionally, the anomalous Hall effect (AHE) in these systems has been attributed to skew-scattering mechanism [38]. The saturation magnetization of $Cr_{1+x}Te_2$ ranges between 1.7 and 2.8 μ_B, which is below the anticipated 3 μ_B for Cr^{3+} ions. This discrepancy likely arises due to the fact of spin canting, the delocalized nature of d-electrons, or presence of mixed valence states [39]. Research on the critical behavior and magnetocaloric properties of $Cr_{1+x}Te_2$ systems has revealed that the type of exchange interactions depend on the Cr concentration. For instance, trigonal $CrTe_2$ ($T_C \approx 320$ K) and $Cr_{1.25}Te_2$ ($T_C \approx 230$ K), along with monoclinic $Cr_{1.5}Te_2$ ($T_C \approx 310$ K) exhibit 3D Ising-type interactions [40, 41]. In contrast, bulk and thin-films of trigonal $Cr_{1.6}Te_2$ ($T_C \approx 338$ K) display 3D Heisenberg-type and mean-field-type behavior, respectively [42]. Furthermore, thin-film hexagonal Cr_2Te_2 ($T_C \approx 201$ K) shows the 2D Heisenberg type interactions [43].

The aim of this PhD thesis is to design and synthesize high quality single crystals of various layered ferromagnets with long-range magnetic interactions near the room temperature for potential next generation spintronics, high-density data storage devices, and magnetic refrigeration technology. In this regard, my PhD work focuses on synthesizing high-quality single crystals of Cr_xTe_y layered systems and study the anomalous and topological Hall effects, magnetocrystalline anisotropy, critical behavior, and magnetocaloric effects.

The first chapter of this thesis provides a comprehensive review of layered magnetic materials, exploring their fundamental magnetic properties. It delves into the basics of magnetism, exchange interactions, spin-orbit coupling, and the role of magnetic anisotropy in these systems. Further, the chapter discusses the key concepts such as the critical behavior analysis and the magnetocaloric effect, particularly in the context of phase transitions. Next, it includes a discussion on various types of Hall effects such as the anomalous and the topological Hall effects, highlighting their relation to the topological properties of materials. The fundamental concepts discussed in this chapter sets the stage for understanding the experimental findings appearing in the subsequent chapters.

The second chapter presents a thorough description of the experimental techniques used for my phD thesis work. It describes techniques used for growing the single crystals, such as the chemical vapor transport (CVT) and the self-flux method. Structural analysis was conducted using X-ray diffraction (XRD), while elemental composition and mapping were examined through energy dispersive X-ray spectroscopy (EDXS). Magnetic measurements were performed using vibrating sample magnetometer (VSM), and electrical as well as magneto-transport properties were investigated using the Quantum Design DynaCool Physical Property Measurement System (PPMS) equiped with 9 Tesla DC magnet.

The third chapter describes the successful growth of high-quality single crystals of $\mathrm{Cr_2Te_3}$ ($\mathrm{Cr_{1.33}Te_2}$) via chemical vapor transport and its critical behavior near the ferromagnetic-paramagnetic (FM-PM) transition at 170 K. Using the Kouvel-Fisher method, critical exponents $\beta = 0.353(4)$ and $\gamma = 1.213(5)$ were derived, indicating complex magnetic interactions between the 3D-Ising and 3D-Heisenberg models. Renormalization group theory suggests 3D-Ising-type interactions, decaying as $J(r) = r^{-4.89}$. Notably, $\mathrm{Cr_2Te_3}$ exhibits the highest uniaxial magnetocrystalline anisotropy (MAE) value among $\mathrm{Cr}_x\mathrm{Te}_y$ systems, with $K_u = 2065$ kJ/m^3.

The fourth chapter presents the electrical transport, Hall effect, and magnetic properties of monoclinic ferromagnet $\mathrm{Cr_{2.76}Te_4}$ ($\mathrm{Cr_{1.38}Te_2}$), identifying it as a soft itinerant ferromagnet with strong magnetocrystalline anisotropy. Below 50 K, an antiferromagnetic-like transition occurs, while between 50 K and 150 K, fluctuating in-plane and out-of-plane magnetic moments form a non-coplanar spin structure. The Rhodes-Wohlfarth ratio $\frac{\mu_{\text{eff}}}{\mu_s} = 1.89$ (> 1) confirms itinerant ferromagnetism. Skew-scattering drives a large anomalous Hall effect, and the non-coplanar spin structure induces a topological Hall effect, further analyzed via first-principles calculations.

The fifth chapter investigates the structural, magnetic, and thermodynamic properties of room-temperature monoclinic ferromagnet $\mathrm{Cr_{1.38}Te_2}$ ($\mathrm{Cr_{2.76}Te_4}$). Critical behavior near the Curie temperature ($T_C = 316$ K) was analyzed using modified Arrott plots, Kouvel-Fisher methods, and Monte Carlo simulations, yielding exponents consistent with 3D-Ising-type long-range exchange interactions $[J(r) \sim r^{-4.73}]$. Temperature-dependent magnetocrystalline anisotropy energy density (K_u) was revealed, with density functional theory (DFT) confirming an easy-axis along the *b*-axis. A maximum entropy change of $-\Delta S_m^{\max} \approx 2.51$ J/kg-K was observed near T_C.

The sixth chapter focuses on $\mathrm{Cr_{0.83}Te}$ ($\mathrm{Cr_5Te_6}$), where substantial topological Hall and anomalous Hall effects are observed, driven by non-coplanar spin structures and skew-scattering, respectively. Critical exponents $\beta = 0.4739(4)$, $\gamma = 1.2812(3)$, and $\delta = 3.7037(5)$ suggest complex magnetic interactions, confirmed by universal rescaling of $-\Delta S_m(T, H)$ curves. The Takahashi's self-consistent renormalization (SCR) theory confirms that $\mathrm{Cr_{0.83}Te}$ exhibits itinerant ferromagnetism.

The seventh chapter describes the successful induction of superconductivity in the layered ferromagnet $\mathrm{Cr_3Te_4}$ through Sn intercalation, achieving an onset transition temperature of $T_c \approx 3.5$ K. $\mathrm{Sn_{0.06}Cr_3Te_4}$ is identified as a type-II superconductor with a lower critical field $H_{c1} = 58 \pm 4$ Oe and an upper critical field $H_{c2} = 209 \pm 10$ Oe. A specific heat jump around T_c with a 33% volume fraction confirms bulk superconductivity. Spin-polarized DFT calculations reveal orbital contributions near the Fermi level, and Sn intercalation tunes the topological Hall effect originating from the skyrmion lattice. This study is the first to demonstrate superconductivity in a skyrmion lattice, introducing a new class of topological quantum materials.

1.1 Magnetism in Materials

The magnetic behavior of materials primarily arises due to two key factors: the spin of electrons and the orbits around the atomic nucleus in which the electrons circulate. The main contributors to the magnetism in solids include (1) the spin angular momentum of electrons, (2) the orbital angular momentum, and (3) the exchange interactions between electron spins which are governed by the Hund's rules.

1.1.1 The Magnetic Moment of Free Atoms

1. Hund's Rules and Electron Configuration

Hund's rules are essential for determining the magnetic ground state of multi-electron atoms. They are:

- **First Rule (Spin-Spin Coupling):** The spins of the electrons remain parallel to each other to the extent possible.
- **Second Rule (Orbital-Orbital Coupling):** The first electron in the shell will go into the maximum value of l_z i.e, maximum of $|l_z|$.
- **Third Rule (Spin-Orbit Coupling):** For atoms with less than half-filled orbitals, the total angular momentum J is determined by $J = |L - S|$. Conversely, for orbitals that are more than half-filled, J is calculated as $J = L + S$.

2. Electron Spin Magnetic Moment

Electrons possess an intrinsic spin momentum, generating a corresponding magnetic moment. The spin magnetic moment is given by:

$$\vec{\mu}_s = -g_s \frac{e}{2m_e} \vec{S} \tag{1.1}$$

Magnetic moment of spin, $\vec{\mu}_s$, is given by expression involving the electron spin g-factor (g_s), which is approximately 2, the electron charge (e), the electron mass (m_e), and spin angular momentum of the electron ($\vec{S}$). The negative sign in expression reflects the fact that the magnetic moment is oriented opposite to the spin direction, due to the electron's negative charge.

3. Orbital Angular Magnetic Moment

Magnetism is also affected by the electrons' orbital motion around the nucleus. The magnetic moment due to orbital angular momentum, $\vec{\mu}_L$, is expressed by:

$$\vec{\mu}_L = -\frac{e}{2m_e}\vec{L} \tag{1.2}$$

where $\vec{L}$ is the orbital angular momentum. In certain atoms, particularly those of transition metal and rare-earth elements, the orbital contribution is significant due to weak quenching effects in solid-state environments.

4. Total Magnetic Moment in an Atom

For multi-electron atoms, the total magnetic moment arises from both spin and orbital contributions. The total angular momentum $\vec{J}$ results from the vector combination of spin ($\vec{S}$) and orbital ($\vec{L}$) angular momenta:

$$\vec{J} = |\vec{L} \pm \vec{S}| \tag{1.3}$$

The corresponding total magnetic moment $\vec{\mu}_J$ of an atom is given by:

$$\vec{\mu}_J = -g_J\frac{e}{2m_e}\vec{J} \tag{1.4}$$

The Landé g-factor, g_J, is determined by the following formula:

$$g_J = 1 + \frac{J(J+1) + S(S+1) - L(L+1)}{2J(J+1)} \tag{1.5}$$

5. Exchange Interactions

In solids, magnetism also depends on the interaction between atomic magnetic moments, primarily through the exchange interactions. The Heisenberg model describes the interaction between two neighboring spins $\vec{S}_i$ and $\vec{S}_j$ as:

$$H = -\sum_{\langle i,j \rangle} J_{ij}\vec{S}_i \cdot \vec{S}_j \tag{1.6}$$

Here J_{ij} presents the exchange integral between spins $\vec{S}_i$ and $\vec{S}_j$. If $J_{ij} > 0$, the interaction is ferromagnetic, favoring parallel alignment of spins; if $J_{ij} < 0$, the interaction is antiferromagnetic, favoring antiparallel alignment.

In the study of magnetism, exchange interactions play a critical role in determining how atomic spins align, leading to various magnetic orders such as ferromagnetism, antiferromagnetism, and more complex magnetic phases. These interactions arise from quantum mechanical effects, particularly follow the Pauli exclusion principle and Heisenberg exchange in governing the spin coupling in materials.Various mechanisms such as direct, super, double, supersuper, extended super, multi-intermediate double exchange, itinerant electron exchange, and the RKKY interaction influence the magnetic properties of materials based on their electronic structure and crystal symmetries. Identifying the dominant exchange mechanism can be challenging, especially for materials with 3d electrons, which may exhibit both localized and delocalized characteristics.

6. Spin-Orbit Coupling

Spin-orbit coupling (SOC) is essential for the stabilization of magnetism in layered materials. In layered systems, conventional isotropic exchange interactions are often inadequate to sustain the long range magnetic ordering at nonzero temperatures. On the other hand, the SOC creates magnetic anisotropy by locking the electron's spin and orbital angular momenta, which breaks the isotropic Heisenberg exchange. The SOC contribution can be expressed by the Hamiltonian,

$$H_{\mathrm{SOC}} = \lambda \vec{L} \cdot \vec{S}, \tag{1.7}$$

where λ is the spin-orbit coupling constant. This term aligns the magnetic moment along specific crystallographic directions, establishing the magnetic anisotropy necessary for the stabilization of 2D magnetism.

SOC also introduces antisymmetric exchange terms, such as the Dzyaloshinskii-Moriya (DM) interaction, expressed as [44, 45]:

$$\hat{H}_{\mathrm{DM}} = \sum_{i \neq j} \vec{D}_{ij} \cdot (\hat{S}_i \times \hat{S}_j), \tag{1.8}$$

where $\vec{D}_{ij}$, the DM vector which depends on the strength of SOC in non-centrosymmetric systems, favoring orthogonal spin configurations between neighboring sites. DM interaction plays a key role in stabilizing non-collinear spin textures in 2D systems.

Additionally, SOC contributes to single-ion magnetocrystalline anisotropy which is a local anisotropy effect described by:

$$\hat{H}_{\mathrm{an}} = \sum_{i} A_i (\hat{S}_i)^2, \tag{1.9}$$

where A_i is the anisotropy constant for site i. The single-ion anisotropy together with the DM interaction is crucial for maintaining the long range magnetic order in 2D materials, which would otherwise be disrupted by thermal fluctuations. Thus, SOC introduces essential anisotropy and exchange interactions that enable long-range magnetic ordering in two-dimensional systems.

In 2D magnets, SOC-induced anisotropic interactions modify the isotropic Heisenberg model to produce the anisotropies such as the uniaxial (Ising-like) and easy-plane (XY-like), that align spins along preferred orientations.

1.1.2 Magnetic Anisotropy

Magnetic anisotropy is a critical feature in 2D magnetic materials to determine the stability and directionality of magnetic ordering. In low-dimensional systems, magnetic anisotropy refers to the energy difference associated with aligning magnetic moments in specific directions relative to the crystal structure. This property is vital in counteracting thermal fluctuations that could otherwise disrupt magnetic order, as discussed in the Mermin-Wagner Theorem [20]. The theorem further asserts that in 2D systems, spontaneous long-range magnetic ordering is typically suppressed at finite temperatures unless anisotropic interactions are present to stabilize it. The subsequent sections outline the various types of magnetic anisotropy, each influencing the behavior and potential applications of 2D magnetic materials.

1. Magnetocrystalline Anisotropy (MCA)

MCA occurs due to the interaction between the crystal lattice and spins. This interaction favors specific crystallographic directions for the alignment of magnetic moments, governed by spin-orbit coupling (SOC). The magnetocrystalline Anisotropy energy can be described by [46, 47]:

$$E_{\mathrm{MCA}} = K_U \sin^2 \theta \tag{1.10}$$

where K_U is the magnetic anisotropy and θ denotes the angle between the magnetic moment and the preferred axis of alignment. Materials such as $\mathrm{CrI_3}$ and $\mathrm{Fe_3GeTe_2}$ demonstrate high magnetocrystalline anisotropy, stabilizing their magnetic ordering even in monolayer form. The strength of magnetic anisotropy often depends on the crystal symmetry and the SOC strength in the material. For instance, the out-of-plane magnetization (perpendicular anisotropy) is typically observed when $K > 0$, while in-plane magnetization is favored when $K < 0$.

2. Shape Anisotropy

Shape anisotropy originates from the material's geometry, especially it is significant in nanoscale systems. The shape anisotropy energy can be described by [48, 49]:

$$E_{\text{shape}} = \frac{1}{2} N M_s^2 \tag{1.11}$$

where M_s denotes saturation magnetization, and N represents the shape-dependent demagnetization factor. In 2D layers, shape anisotropy typically promotes in-plane alignment of magnetic moments to minimize the magnetostatic energy. However, in materials with pronounced magnetocrystalline anisotropy, shape anisotropy can result in perpendicular magnetic anisotropy (PMA), which is crucial for data storage and spintronic devices because it affects coercivity and remanent magnetization.

3. Surface Anisotropy

Surface anisotropy is vital in 2D materials because of their large surface-to-volume ratio. This type of anisotropy arises from broken symmetry at the material's surface or interface, introducing an additional energy term that influences the directionality of magnetization [48]. The surface anisotropy energy can be expressed as:

$$E_{\text{surface}} = -K_s \cos^2 \theta \tag{1.12}$$

where K_s is the surface anisotropy constant. This effect is particularly pronounced in layered 2D structures and heterostructures, where interface engineering can modify or enhance the overall magnetic anisotropy. In systems such as Cr-based multilayer heterostructures, tailored interfacial effects enable tunable magnetic responses that are invaluable for creating stable, high-performance 2D magnetic devices.

4. Exchange Anisotropy (Exchange Bias)

Exchange anisotropy or exchange bias occurs when a ferromagnetic material is coupled to an antiferromagnetic layer by inducing a unidirectional anisotropy [50, 51]. The exchange anisotropy energy can be expressed by

$$E_{\text{ex}} = -J_{\text{ex}} \vec{S}_F \cdot \vec{S}_A \tag{1.13}$$

The exchange coupling constant, J_{ex}, governs the interaction between the spin orientations of the ferromagnetic ($\vec{S}_F$) and antiferromagnetic ($\vec{S}_A$) layers, potentially resulting in a shift in the hysteresis loop of the ferromagnet after field-cooling. Exchange anisotropy is particularly useful for magnetic storage applications as it allows for controlled magnetic domain stabilization in 2D systems, thereby supporting higher-density data storage.

1.2 Theoretical Models on Magnetic Moment Interactions

Theoretical models of interacting magnetic moments are rooted in statistical mechanics, providing fundamental insights into the phase transitions, spin ordering, and critical phenomena in the magnetic systems. The most prominent models include Ising Model, XY Model, and Heisenberg Model, each differing in the degrees of freedom of spin orientations.

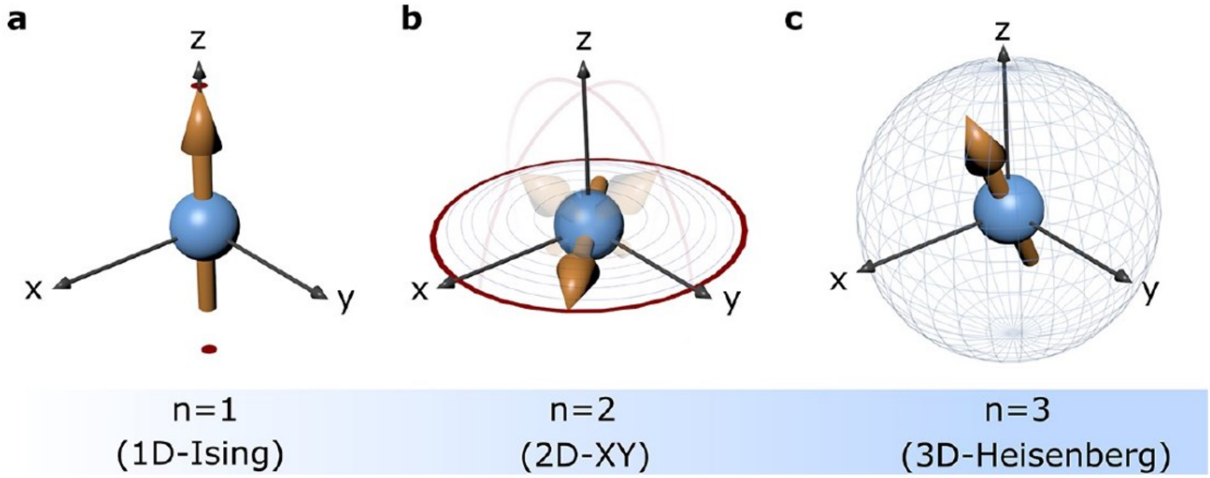

Figure 1.2: Schematic representation of spin alignment for 1D, 2D, and 3D spin dimensionality. Image is adapted from [53].

1.2.1 Ising Model

Ising model describes magnetic systems with spins confined to "up" or "down" states along the z-axis, as demonstrated in Fig. 1.2 (a). It accounts the nearest-neighbor spin interactions through an exchange integral J, effectively characterizing ferromagnetism and phase transitions in one-, two-, and three-dimensional lattices [52].

Hamiltonian of the Ising Model:

$$\mathcal{H}_{\text{Ising}} = -J \sum_{\langle i,j \rangle} S_i S_j - h \sum_i S_i \tag{1.14}$$

In this model, S_i denotes the spin at site i, which can take values of ± 1, representing "up" or "down" spin orientations. The exchange coupling constant J defines the interaction strength. $J > 0$ promotes the ferromagnetic ordering, while $J < 0$ favors the antiferromagnetism. h is the normalised field applied along the z-axis. The notation $\langle i, j \rangle$ indicates summation over the nearest-neighbor pairs, representing the interactions between spins at adjacent lattice sites.

1.2.2 XY Model

XY Model extends the Ising Model by allowing spins to rotate freely in a plane (usually the xy-plane), while still being constrained to two dimensions, as shown in Fig. 1.2 (b). This model is particularly relevant for studying systems with planar anisotropy, such as thin magnetic films. The XY Model is known for exhibiting a Kosterlitz-Thouless (KT) transition in two dimensions, where the system goes from a quasi-ordered phase at low temperatures to a disordered phase at higher temperatures [54, 55].

Hamiltonian of the XY Model:

$$\mathcal{H}_{\mathrm{XY}} = -J \sum_{\langle i,j \rangle} \cos(\theta_i - \theta_j) - h \sum_i \cos(\theta_i) \tag{1.15}$$

Here, θ_i represents the angle of the spin at site i within the xy-plane, indicating its orientation. The constant J denotes the exchange interaction strength between adjacent spins. Additionally, h represents an external magnetic field applied within the plane, influencing the spin alignments.

1.2.3 Heisenberg Model

Heisenberg model is the most general of these three models, allowing the spins to point in any direction in three-dimensional space, as presented in Fig. 1.2 (c). This model is applicable to the systems where no preferred direction of spins is required such as isotropic ferromagnets and antiferromagnets. The Heisenberg model can describe both ferromagnetic and antiferromagnetic interactions and is crucial for understanding the magnetic materials that are exhibiting three-dimensional spin degree of freedom [1, 53].

Hamiltonian of the Heisenberg Model:

$$\mathcal{H}_{\mathrm{Heisenberg}} = -J \sum_{\langle i,j \rangle} \mathbf{S}_i \cdot \mathbf{S}_j - \sum_i \mathbf{h} \cdot \mathbf{S}_i \tag{1.16}$$

Here, $\mathbf{S}_i$ denotes the spin vector at site i, with components (S_i^x, S_i^y, S_i^z), describing the spin's orientation in three-dimensional space. The parameter J is the isotropic exchange coupling constant, where $J > 0$ corresponds to ferromagnetic interactions, favouring parallel alignment and $J < 0$ corresponds to antiferromagnetic interactions, favoring anti parallel alignment. Additionally, $\mathbf{h}$ denotes an external magnetic field vector which influences the orientation of the spins.

1.3 Magnetic Phase Transitions

Magnetic phase transitions are classified based on the nature of changes in the order parameter. Each type of transition exhibits distinct characteristics in terms of magnetization, latent heat, susceptibility, and critical behavior.

1.3.1 First Order Magnetic Transition

In a first-order magnetic transition, the magnetization M changes discontinuously at the transition temperature T_C, involving an abrupt shift from one magnetic state to another, such as ferromagnetic (FM) to paramagnetic (PM) order. This discontinuity in the order parameter is associated with a latent heat L, reflecting an energy change during the transition [56, 57]:

$$M(T \to T_C^+) \neq M(T \to T_C^-). \tag{1.17}$$

This kind of transition does not follow power-law behavior, and critical exponents are not applicable. First-order transitions often exhibit coexistence between two phases (e.g., FM and PM) near T_C and are less sensitive to fluctuations.

1.3.2 Second Order Magnetic Transition

In contrast, second-order transitions, or continuous transitions, involve a gradual change in magnetization as the temperature approaches T_C, leading to a continuous vanishing of the order parameter [56, 57]:

$$M(T) \propto (T_C - T)^{\beta} \quad \text{for } T < T_C. \tag{1.18}$$

These transitions are characterized by critical behavior, where susceptibility χ and correlation length ξ diverge as $T \to T_C$:

$$\chi(T) \propto |T - T_C|^{-\gamma}, \quad \xi(T) \propto |T - T_C|^{-\nu}. \tag{1.19}$$

The divergence of ξ implies long-range correlations in the system, which is the basis for the universality of critical exponents.

1.4 Critical Behavior Analysis

Magnetic phase transitions and critical behavior analysis are vital for understanding the various magnetic interactions in the systems, providing insights into magnetic ordering, fluctuations, and interactions near phase boundaries. These transitions, triggered by variations in temperature, external magnetic fields, or other perturbations, are typically classified as first-order or second-order (continuous) transitions. In second-order transitions, the correlation length diverges as the system approaches the critical temperature (T_c), as illustrated in Fig.1.3, resulting in significant changes in physical properties such as magnetization, specific heat, and susceptibility. These phenomena are extensively studied using the scaling laws and critical exponents [56, 58].

1.4.1 Theoretical Formalism of Critical Behaviour Analysis

1. Order Parameter and Phase Transition

The magnetization (M), acts as the order parameter, reflecting the extent of magnetic alignment in the system. As the temperature approaches the Curie temperature T_C from

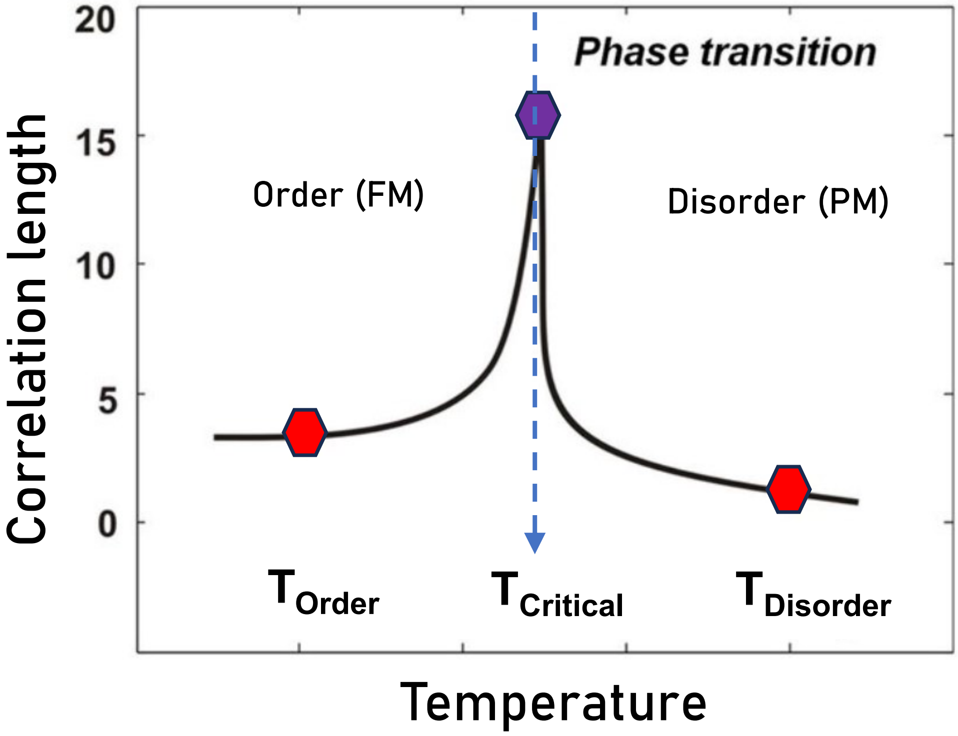

Figure 1.3: Schematic of correlation length (ξ) vs. temperature near a phase transition. At the critical temperature (T_{Critical}), ξ diverges, separating the ordered ferromagnetic ($T < T_{\text{Critical}}$) and disordered paramagnetic ($T > T_{\text{Critical}}$) phases. T_{Order} and T_{Disorder} indicate approximate phase boundaries.

below, the magnetization diminishes, ultimately reaching zero at $T = T_C$, where the system transitions into the paramagnetic phase. In the critical region near T_C, the order parameter exhibits a power-law behavior:

$$M(T) \propto (T_C - T)^{\beta}, \quad T < T_C \tag{1.20}$$

Here, β is the critical exponent for the magnetization.

2. Magnetic Susceptibility

The magnetic susceptibility (χ) quantifies the system's response to an external applied magnetic field H. Near the Curie temperature T_C, χ tends to diverge, following a critical behavior that can be expressed as:

$$\chi(T) \propto |T - T_C|^{-\gamma} \tag{1.21}$$

where γ is the critical exponent for susceptibility, reflecting the alignment of spins below and above T_C in response to H.

3. Specific Heat

The specific heat (C) near the transition provides insight into energy fluctuations within the system. For a second-order phase transition, the specific heat peaks at T_C and follows:

$$C(T) \propto |T - T_C|^{-\alpha} \tag{1.22}$$

where α is the critical exponent for specific heat.

4. Correlation Length

The correlation length ξ, indicating the spatial extent of correlated spins, diverges as $T \to T_C$:

$$\xi(T) \propto |T - T_C|^{-\nu} \tag{1.23}$$

here ν denotes the critical exponent associated with the correlation length. This divergence at T_C underscores the universality of critical behavior.

5. Scaling Laws and Hypothesis

The scaling hypothesis posits that near T_C the free energy F can be represented as:

$$F(t, H) = |t|^{2-\alpha} f_{\pm} \left(\frac{H}{|t|^{\beta+\gamma}} \right) \tag{1.24}$$

where $t = (T - T_C)/T_C$ is the reduced temperature, and $f_{\pm}$ is a scaling function for $T > T_C$ and $T < T_C$. The scaling relations derived in this method as,

$$\gamma = \beta(\delta - 1), \quad \alpha + 2\beta + \gamma = 2, \quad \nu d = 2 - \alpha \tag{1.25}$$

These relations aid in categorizing the phase transitions within the universality classes.

6. Widom Scaling Law and Hyperscaling Relation

According to the Widom scaling law, the critical exponents satisfy:

$$\delta = 1 + \frac{\gamma}{\beta} \tag{1.26}$$

The hyperscaling relation connects the dimensionality d of the system with the critical exponents by

$$d\nu = 2 - \alpha \tag{1.27}$$

This relation highlights the universal nature of phase transitions.

1.4.2 Experimental Analysis of Critical Behavior

This section describes the methods used to analyze the experimental data near T_C for the critical exponents.

1. Modified Arrott Plot (MAP) Analysis

In the modified Arrott plot (MAP) method, magnetization (M) and magnetic field (H) data around the Curie temperature (T_C) are plotted to determine the critical exponents β and γ.

The Modified Arrott plot is constructed by plotting $M^{1/\beta}$ versus $(H/M)^{1/\gamma}$ at various temperatures near T_C, as expressed in the equation [59, 60],

$$M^{1/\beta} = a\left(\frac{H}{M}\right)^{1/\gamma} + b \tag{1.28}$$

where a and b are temperature-dependent constants. If the values of β and γ are accurate, the resulting plots should yield straight lines intersecting at T_C.

2. Kouvel-Fisher Method

The Kouvel-Fisher (KF) method provides a more precise way to extract the critical exponents by examining the temperature dependent magnetization (M) and susceptibility (χ).

For magnetization (M), the relation is given by [61],

$$\frac{d\ln M}{dT} \propto (T - T_C)^{-1/\beta} \tag{1.29}$$

For susceptibility (χ), the relation is given by,

$$\frac{d\ln \chi}{dT} \propto (T - T_C)^{-1/\gamma} \tag{1.30}$$

These equations can be linearized by plotting $M^{1/\beta}$ versus T and $\chi^{1/\gamma}$ versus T, where the slopes of these lines yield the values of β and γ, respectively.

3. Iterative Refinement Process

To refine the critical exponents, an iterative method is applied starting with some initial guess. Through repeated cycles of correction and plotting in the Modified Arrott and KF methods, we verify the following:

1. **Modified Arrott Plot Consistency**: Ensuring straight lines with the selected β and γ.

2. **Kouvel-Fisher Linear Fit**: Verifying that the slopes from KF plots yield stable values for β and γ.
3. **Scaling Laws Verification**: Checking that the critical exponents satisfy Widom's scaling relation and hyperscaling.

This iterative method refines the exponents until they consistently match both the Modified Arrott plot and KF analysis, as well as the scaling laws, confirming their accuracy and alignment with the appropriate universality class.

Table 1.1: Critical exponents for various theoretical models

Model	**Dimension (D)**	α	β	γ	δ	ν
3D Ising Model	3	0.110	0.326	1.237	4.789	0.630
2D Ising Model	2	0	0.125	1.75	15	1.0
3D Heisenberg Model	3	-0.115	0.365	1.386	4.8	0.705
2D Heisenberg Model	2	0	0.231	1.40	6.0	0.670
3D XY Model	3	-0.007	0.345	1.316	4.81	0.671
2D XY Model	2	0	0.230	1.44	6.26	0.670
Mean-field Theory	Any $D \geq 4$	0	0.5	1.0	3.0	0.5

1.5 Magnetocaloric Effect

The magnetocaloric effect (MCE) refers to temperature or entropy changes in a magnetic material under varying magnetic fields. MCE plays a key role in magnetic refrigeration technology. The MCE is explained through the *isothermal* and *adiabatic* processes [62, 63], as shown in Figure 1.4.

1.5.1 Isothermal Process

In the isothermal process, the application or removal of a magnetic field H occurs while maintaining a constant temperature T. Under the magnetic field, the magnetic moments of the system try to align in the field direction, reducing the material's magnetic entropy S. This decrease in entropy can be expressed as:

$$\Delta S \neq 0 \quad \text{where } S_2 > S_1 \tag{1.31}$$

Here, S_2 is the entropy in the disordered state (in the absence of magnetic field), and S_1 is the entropy in the ordered state (under the magnetic field). This isothermal process causes the magnetic entropy $\Delta S_m(T, H)$, given by [64, 62]:

$$\Delta S_m(T, H) = \int_0^H \left(\frac{\partial M}{\partial T}\right)_H dH \tag{1.32}$$

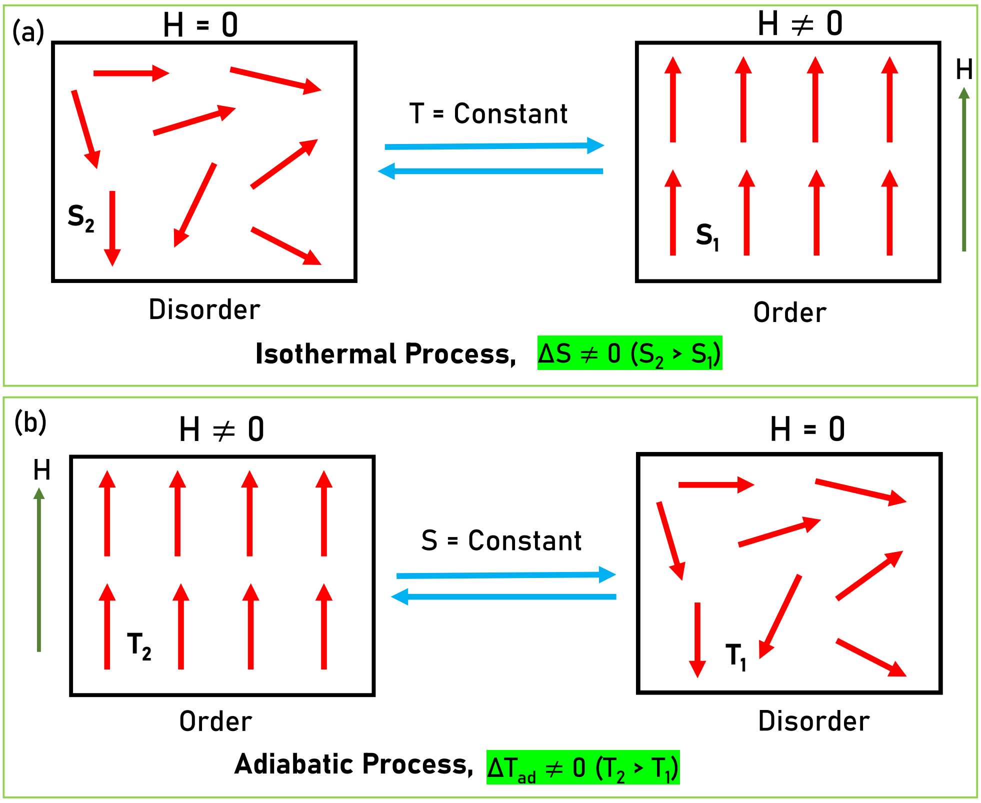

Figure 1.4: Schematic representation of the magnetocaloric effect. (a) In isothermal process, a magnetic field induces a change in entropy $\Delta S \neq 0$ at a constant temperature, resulting in a shift in the material's magnetic order. (b) In adiabatic process, the temperature change $\Delta T_{\text{ad}} \neq 0$ occurs while maintaining constant entropy as the field is applied or removed.

This equation is derived from the Maxwell relation, $\left(\frac{\partial S}{\partial H}\right)_T = \left(\frac{\partial M}{\partial T}\right)_H$, which connects magnetic entropy and magnetization changes.

For practical measurements at small intervals of magnetic field and temperature, the change in magnetic entropy can be approximated as:

$$\Delta S_m(T,H) \approx \int_{H_i}^{H_f} \left(M(T,H)\Big|_{T_i} - M(T,H)\Big|_{T_{i+1}} \right) dH, \tag{1.33}$$

Here, H_i and H_f are the initial and final magnetic fields, and T_i refers to the temperature at the corresponding field.

1.5.2 Adiabatic Process

In the adiabatic process, the magnetic field is either introduced or removed without heat exchange with the surroundings, ensuring no change in total entropy ($\Delta S = 0$). As the magnetic field is introduced, the alignment of magnetic moments leads to a decrease in the system's entropy, which results in an increase in temperature T to maintain the overall entropy balance. The change in temperature during this process (ΔT_{ad}), is described by,

$$\Delta T_{\mathrm{ad}} \neq 0 \quad \text{where } T_1 > T_2 \tag{1.34}$$

Here, T_1 is the temperature in the ordered state (aligned moments), and T_2 is the temperature in the disordered state (after the field has been removed). This temperature variation can be expressed as:

$$\Delta T_{\mathrm{ad}} = -\frac{T}{C(T,H)} \Delta S_m(T,H) \tag{1.35}$$

where $C(T,H)$ is the specific heat capacity of the material under the magnetic field H. The adiabatic MCE process is essential in magneto-refrigeration, as it leads to cooling upon removal of the field.

Figure 1.4 illustrates the two key processes driving the magnetocaloric effect (MCE). In Fig. 1.4 (a), the isothermal process illustrates how an external magnetic field H aligns the magnetic moments, transitioning the system from a high-entropy state S_2 to a low-entropy state S_1, resulting in heating or cooling of the system, depending on whether the field is increased or decreased.

Fig. 1.4 (b), the adiabatic process shows the alignment of magnetic moments under H without heat exchange and preserving the entropy constant. This alignment causes the system's temperature to rise from T_2 to T_1 and the temperature difference $\Delta T_{\mathrm{ad}} = T_1 - T_2$ is a critical parameter for the magneto-refrigeration applications.

1.6 Hall Effect

The Hall effect phenomenon occurs when a current passes through a conductor or semiconductor in a perpendicular magnetic field, causing charge carriers to accumulate on one side due to the Lorentz force [65]. This results in a transverse electric field, producing a Hall voltage (V_H) across the material, as shown in Fig. 1.5(a).

The Hall effect arises when a longitudinal current J_y flows through a material under a magnetic field, creating a transverse electric field E_x. This relationship can be expressed in terms of the Hall resistivity ρ_{xy} in tensor form as:

$$E_x = \rho_{xy} J_y \tag{1.36}$$

Here ρ_{xy} represents the off-diagonal component of the resistivity tensor ρ_{ij} and σ_{xy} is Hall conductivity. These quantities are related through the following expressions [66, 65],

$$\sigma_{xy} = \frac{-\rho_{xy}}{\rho_{xx}^2 + \rho_{xy}^2} \tag{1.37}$$

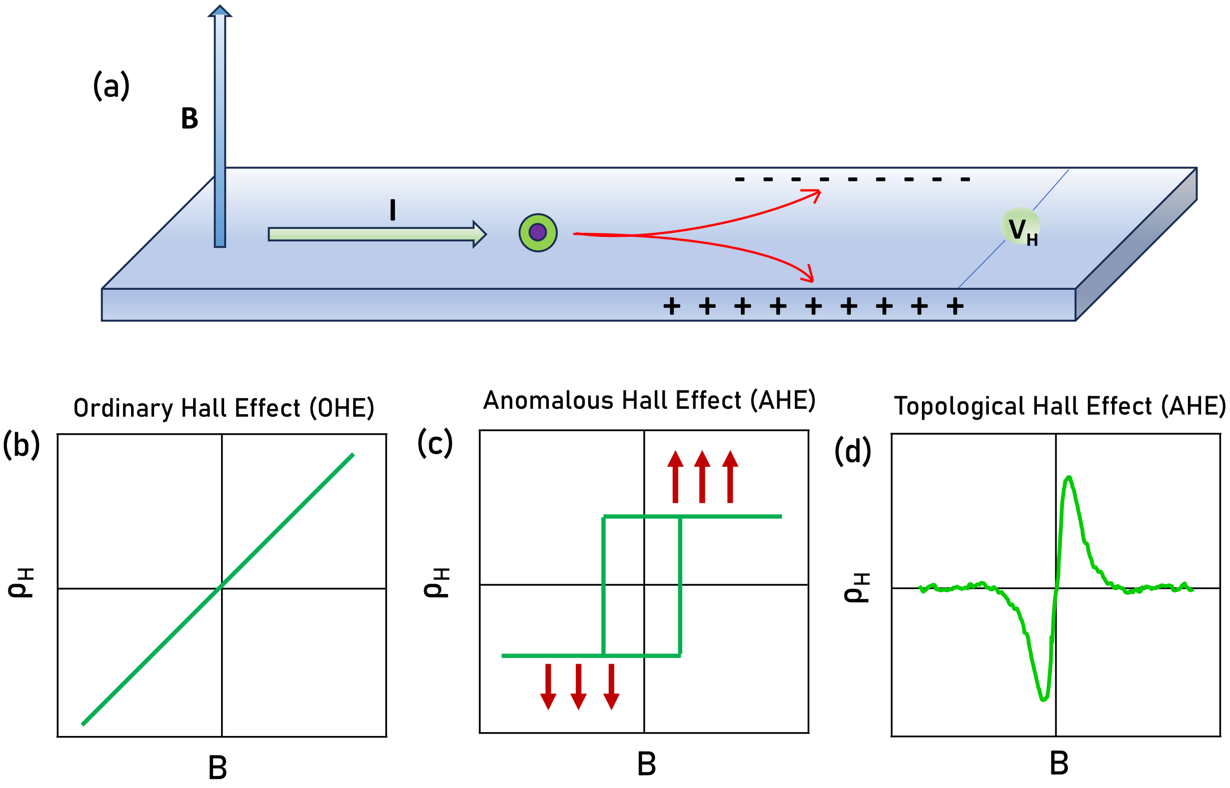

Figure 1.5: (a) Measurement setup for Hall effect. In (a), V_H is the Hall voltage, I is the current, and B is the magnetic field (b) Ordinary Hall Effect (OHE): Hall resistivity (ρ_H) varies linearly with (B) in non-magnetic materials. (c) Anomalous Hall Effect (AHE): Hall resistivity (ρ_H) depends on both (B) and magnetization (M). (d) Topological Hall Effect (THE): Hall resistivity (ρ_H) reflects contributions from topological spin textures, producing a distinctive cusp in the Hall resistivity.

$$\rho_{xy} = \frac{-\sigma_{xy}}{\sigma_{xx}^2 + \sigma_{xy}^2} \tag{1.38}$$

For the case where $\sigma_{xy} \ll \sigma_{xx}$, this can be approximated as:

$$\rho_{xy} \approx \frac{-\sigma_{xy}}{\sigma_{xx}^2} \tag{1.39}$$

Contributions to the Hall Effect

The Hall effect can have contributions from the ordinary (ρ_{xy}^{OHE}), anomalous (ρ_{xy}^{AHE}), and topological Hall effects (ρ_{xy}^{THE}). For systems with small Hall angles, the total Hall resistivity is the sum of the individual contributions [67].

$$\rho_{xy}^{\text{Total}} = \rho_{xy}^{\text{OHE}} + \rho_{xy}^{\text{AHE}} + \rho_{xy}^{\text{THE}} \tag{1.40}$$

1.6.1 Ordinary Hall Effect (OHE)

A thin conductor of thickness d, carrying an electric current I along the x-axis, develops a transverse potential difference across the y-axis when exposed to a magnetic field B directed along the z-axis. The Lorentz force causes charge carriers to accumulate asymmetrically, producing the potential difference. The Hall resistivity as a function of the magnetic field is shown in Fig. 1.5(b).

To derive the Hall voltage V_H, the forces acting on a charge carrier with charge q and drift velocity v_d are considered. The electric force $\vec{F}_E = q\vec{E}_H$, where $\vec{E}_H$ is the Hall electric field generated by the separation of charges, acts in opposition to the magnetic force $\vec{F}_B = q(\vec{v}_d \times \vec{B})$, which arises from the interaction of the charge carrier's motion with the magnetic field. At equilibrium, these forces balance ($\vec{F}_E + \vec{F}_B = 0$) [65], allowing the Hall electric field and, consequently, the Hall voltage to be determined.

$$V_H = E_H w = v_d B w \tag{1.41}$$

The drift velocity v_d relates to the current I and charge carrier density n through the following relation,

$$v_d = \frac{I}{nqA} \tag{1.42}$$

where $A = d \times w$ represents the cross-sectional area, and substituting v_d into the equation for V_H:

$$V_H = \left(\frac{I}{nqA}\right) Bw \tag{1.43}$$

Simplifying further, we get the Hall voltage across the conductor,

$$V_H = \frac{IB}{nqd} \tag{1.44}$$

The Hall coefficient R_H relates the electric field E_H, current density J and magnetic field B by

$$R_H = \frac{E_H}{JB} = \frac{V_H d}{IB} \tag{1.45}$$

By substituting V$_H$ in Eqn.1.45, we get the Hall coefficient,

$$R_H = \frac{1}{nq} \tag{1.46}$$

The Hall coefficient R_H provides insight into the dominant charge carriers responsible for electrical transport in a system. $R_H > 0$ indicates hole-carriers, while negative $R_H < 0$ signifies electrons.

The ordinary Hall effect is widely used in material characterization and devices. It enables direct measurement of carrier density (n) through the Hall coefficient (R_H), serves as the basis for Hall sensors to measure magnetic fields, and identifies charge carrier types (electrons or holes) via the sign of V_H or R_H.

1.6.2 Anomalous Hall Effect (AHE)

The AHE in materials stems from spin-orbit interaction and time-reversal symmetry breaking, while the OHE arises from the Lorentz force in an external magnetic field. The AHE is intrinsic to ferromagnets and can occur without an external field, contributing to the total Hall resistivity alongside the OHE.

The Hall resistivity ρ_{xy} in a ferromagnet can be expressed as [68, 69]:

$$\rho_{xy} = \rho_{xy}^{\mathrm{OHE}} + \rho_{xy}^{\mathrm{AHE}} \tag{1.47}$$

$$\rho_{xy} = R_0 H + R_s M \tag{1.48}$$

ρ_{xy}^{OHE} varies linearly with the applied magnetic field H, while ρ_{xy}^{AHE} depends on the material's magnetization M.

The anomalous Hall conductivity $\sigma_{xy}^{\mathrm{AHE}}$ may arise from different mechanisms, including skew-scattering, side-jump, or intrinsic effects:

$$\sigma_{xy}^{\mathrm{AHE}} = \sigma_{xy}^{\mathrm{skew}} + \sigma_{xy}^{\mathrm{side}} + \sigma_{xy}^{\mathrm{int}}, \tag{1.49}$$

1. Skew-Scattering Mechanism

Skew scattering is an extrinsic mechanism in which the spin-orbit interaction induces asymmetric scattering of charge carriers by impurities, leading to an imbalance in scattering probabilities along opposite polarities. This asymmetry produces a net transverse displacement of charge carriers, giving rise to a Hall voltage, as illustrated in Fig. 1.6 (a). Skew scattering contributes to the anomalous Hall conductivity (AHC) $\sigma_{xy}^{\mathrm{skew}}$, directly proportional to the longitudinal conductivity [68].

$$\sigma_{xy}^{\mathrm{skew}} \propto \sigma_{xx} \tag{1.50}$$

2. Side-Jump Mechanism

The side-jump mechanism is another extrinsic effect and arises due to the shift in the electron's trajectory perpendicular to both the electric field and its velocity during scattering events, as shown in Fig. 1.6 (b). Unlike skew-scattering, the side-jump scattering does not

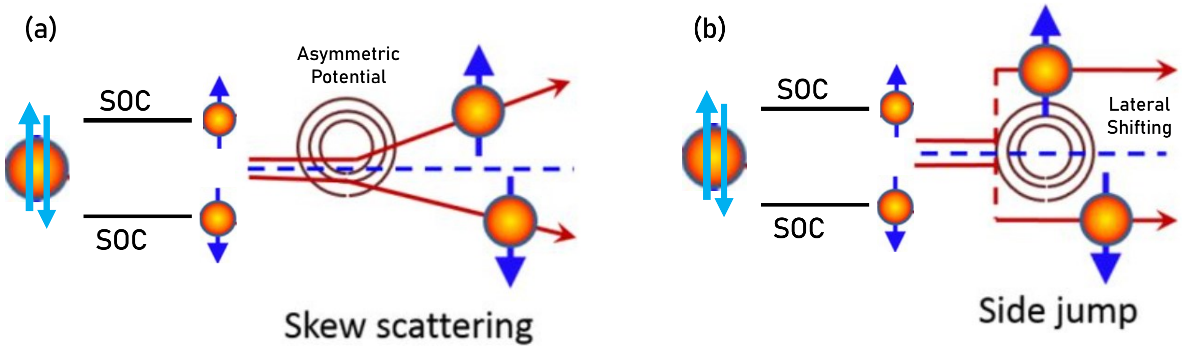

Figure 1.6: Mechanisms of anomalous Hall effect (AHE). (a) Skew scattering: Due to spin-orbit interaction, electrons scatter asymmetrically, leading to the development of a transverse Hall voltage. (b) Side jump: Upon scattering with impurities or lattice vibrations, electrons experience a lateral shift, generating a Hall current without the application of any net force. Image is adapted from Ref.[70].

depend on the electron's longitudinal velocity and thus contributes a Hall current without affecting the net longitudinal conductivity.

The side-jump mechanism contributing to the anomalous Hall conductivity $\sigma_{xy}^{\mathrm{sj}}$ is not influenced by σ_{xx} and exhibits a distinct scaling behavior [68, 71, 72]:

$$\sigma_{xy}^{\mathrm{sj}} \propto \sigma_{xx}^{2} \tag{1.51}$$

This mechanism occurs due to the electron displacement during scattering, which is a consequence of spin-orbit interaction with impurities. Side-jump effects can play a major role in materials with pronounced spin-orbit coupling.

3. Intrinsic Contribution

The intrinsic contribution to the AHE stems from the electronic band structure. In materials with strong spin-orbit coupling, the non-zero Berry curvature in momentum space acts like a fictitious magnetic field, deflecting charge carriers transversely to generate the anomalous Hall current.

The intrinsic AHC ($\sigma_{xy}^{\mathrm{int}}$) is related to the Berry curvature [$\Omega(\mathbf{k})$] summed over all the occupied states in momentum space [68, 73]:

$$\sigma_{xy}^{\mathrm{int}} = -e^{2} \int_{\mathrm{BZ}} \frac{d\mathbf{k}}{(2\pi)^{3}} f(\mathbf{k}) \Omega(\mathbf{k}) \tag{1.52}$$

Here, e represents the electron charge, $f(\mathbf{k})$ is the Fermi-Dirac distribution function. The intrinsic contribution, often temperature-independent, dominates in materials with substantial Berry curvature linked to topologically non-trivial band structures.

1.6.3 Topological Hall Effect (THE)

The Topological Hall Effect (THE) is a unique phenomenon observed in magnetic systems with chiral spin textures, such as skyrmions. These chiral spin configurations induce a Berry phase in conduction electrons, which acts as a fictitious magnetic field in real space, leading to a transverse Hall voltage. Unlike the ordinary Hall effect (OHE), which arises from the Lorentz force, and the anomalous Hall effect (AHE), which is driven by spin-orbit coupling, THE originates from the real-space Berry curvature created by non-trivial spin arrangements.

Mechanism of Topological Hall Effect

In the presence of a chiral spin structure, the conduction electrons interact with the non-collinear spin arrangement, acquiring a real-space Berry curvature. This Berry curvature is directly associated with the scalar spin chirality (χ_{ijk}), defined as:

$$\chi_{ijk} = \mathbf{S}_i \cdot (\mathbf{S}_j \times \mathbf{S}_k), \tag{1.53}$$

where $\mathbf{S}_i$, $\mathbf{S}_j$, and $\mathbf{S}_k$ are spin vectors on neighboring lattice sites. The scalar spin chirality acts as a source of an emergent magnetic field that generates the topological Hall signal.

Quantifying Topological Hall Resistivity

The topological Hall resistivity (ρ_{xy}^{THE}) is a measurable quantity obtained by subtracting the contributions of OHE and AHE from the total Hall resistivity (ρ_{xy}). Mathematically, it is expressed as:

$$\rho_{xy}^{\mathrm{THE}} = \rho_{xy} - \left[\rho_{xy}^{\mathrm{OHE}} + \rho_{xy}^{\mathrm{AHE}}\right], \tag{1.54}$$

where ρ_{xy}^{OHE} and ρ_{xy}^{AHE} are the ordinary and anomalous Hall resistivities, respectively [67].

Emergent Magnetic Field

The origin of THE lies in the emergent magnetic field (B_{em}) produced by the spatially varying magnetic texture, such as a skyrmion lattice. This field arises from the Berry phase induced by the non-coplanarity of spins and can be described as:

$$B_{\mathrm{em}} = \frac{\hbar}{e}\mathbf{n} \cdot \left(\frac{\partial \mathbf{n}}{\partial x} \times \frac{\partial \mathbf{n}}{\partial y}\right), \tag{1.55}$$

where $\hbar$ is the reduced Planck constant, e is the electron charge, and $\mathbf{n}$ represents the unit vector along the local magnetization direction. The term $\frac{\partial \mathbf{n}}{\partial x} \times \frac{\partial \mathbf{n}}{\partial y}$ quantifies the non-coplanarity of the spin texture. The topological Hall resistivity is directly proportional to this emergent magnetic field:

$$\rho_{xy}^{\text{THE}} = R_0 B_{\text{em}}, \tag{1.56}$$

where R_0 is the ordinary Hall coefficient [74].

Non-Trivial Spin Textures Leading to THE

1. Bloch-Type Skyrmions

Bloch-type skyrmions are observed in non-centrosymmetric materials with strong spin-orbit coupling and broken inversion symmetry. These structures are stabilized by the bulk Dzyaloshinskii-Moriya interaction (DMI), as shown in Fig. 1.7 (a). The spin texture of Bloch skyrmions exhibits a swirling pattern around a central core, forming a topologically protected state. Variations such as antiskyrmions, characterized by elongated spin textures, are also prevalent in these systems [75, 76].

2. Néel-Type Skyrmions

Néel-type skyrmions are commonly found in thin films and layered materials with broken structural inversion symmetry, where interfacial DMI dominates. The spin configuration radiates inward or outward from the skyrmion core, forming a distinct radial pattern, as shown in Fig. 1.7 (b). These skyrmions are particularly attractive for spintronic applications due to their efficient manipulation via spin-orbit torques [77].

3. Geometrically Frustrated Systems

Fig. 1.7(c) illustrates the geometric frustration observed in triangular and kagome lattices, where competing exchange interactions result in non-coplanar spin textures. These textures induce scalar spin chirality, expressed as $\chi_{ijk} = \mathbf{S}_i \cdot (\mathbf{S}_j \times \mathbf{S}_k)$, where $\mathbf{S}_i$, $\mathbf{S}_j$, and $\mathbf{S}_k$ are spin vectors at adjacent lattice sites. This scalar spin chirality introduces a Berry phase for conduction electrons, functioning as an emergent magnetic field that contributes to the topological Hall effect (THE). Materials such as MnGe and $\mathrm{Gd_2PdSi_3}$ exemplify this phenomenon, showcasing the intricate interplay between geometric frustration and topological transport properties [78, 79].

4. Magnetic Bubbles and Biskyrmions

Magnetic bubbles and biskyrmions are non-trivial spin textures stabilized by the interplay of exchange interactions [Fig. 1.7(d)], magnetocrystalline anisotropy, and dipole-dipole interactions. Biskyrmions, consisting of two coupled skyrmionic cores, represent a unique topological state. These textures have been observed in materials like MnNiGa and FeGe,

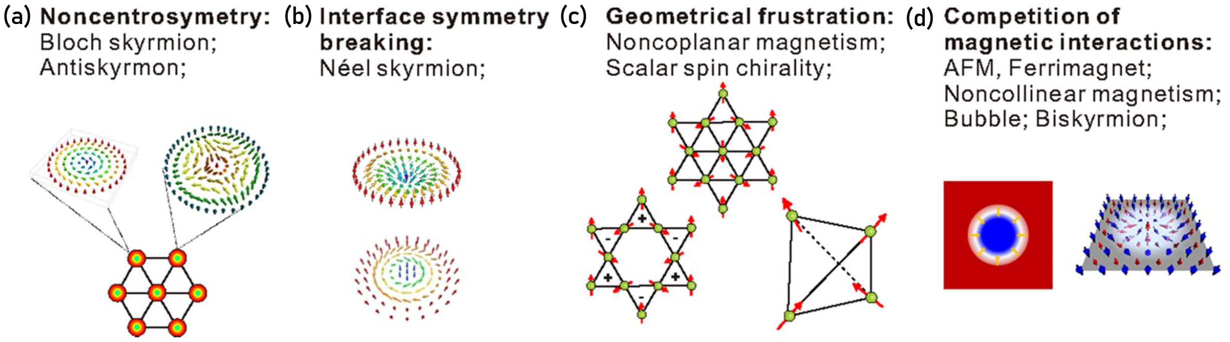

Figure 1.7: Various non-trivial spin textures contributing to THE in magnetic systems. (a) Noncentrosymmetric systems support Bloch-type and antiskyrmions via bulk Dzyaloshinskii-Moriya interaction (DMI). (b) Interface symmetry breaking favors Néel-type skyrmions through interfacial DMI. (c) Geometrical frustration induces noncoplanar magnetism with scalar spin chirality. (d) Competing magnetic interactions produce bubbles and biskyrmions, stabilized by magnetocrystalline anisotropy or/and dipole interactions. Image taken from [82]

showcasing their potential to generate topological Hall signals and expand the understanding of complex magnetic systems [80, 81, 38].

References

[1] Y. Ahn, X. Guo, S. Son, Z. Sun, L. Zhao, Progress and prospects in two-dimensional magnetism of van der waals materials, Progress in Quantum Electronics (2024) 100498.

[2] A. K. Geim, K. S. Novoselov, The rise of graphene, Nature materials 6 (2007) 183–191.

[3] K. Zhang, Y. Feng, F. Wang, Z. Yang, J. Wang, Two dimensional hexagonal boron nitride (2d-hbn): synthesis, properties and applications, Journal of Materials Chemistry C 5 (2017) 11992–12022.

[4] B. Radisavljevic, A. Radenovic, J. Brivio, V. Giacometti, A. Kis, Single-layer MoS_2 transistors, Nature nanotechnology 6 (2011) 147–150.

[5] A. Berkdemir, H. R. Gutiérrez, A. R. Botello-Méndez, N. Perea-López, A. L. Elías, C.-I. Chia, B. Wang, V. H. Crespi, F. López-Urías, J.-C. Charlier, et al., Identification of individual and few layers of WS_2 using raman spectroscopy, Scientific reports 3 (2013) 1755.

[6] M. Long, P. Wang, H. Fang, W. Hu, Progress, challenges, and opportunities for 2d material based photodetectors, Advanced Functional Materials 29 (2019) 1803807.

[7] H. Liu, Y. Zhang, O. E. Glukhova, G. Zhang, L. Wang, J. Zhao, J. Gao, Interlayer Hopping Kinetics of Vacancies in CrI_3 Layers Leading to Monolayer/Bilayer Heterostructures, Adv. Mater. Interfaces 9 (2022) 2200626.

[8] A. Soumyanarayanan, N. Reyren, A. Fert, C. Panagopoulos, Emergent phenomena induced by spin–orbit coupling at surfaces and interfaces, Nature 539 (2016) 509–517.

[9] Y. Deng, Y. Yu, Y. Song, J. Zhang, N. Z. Wang, Z. Sun, Y. Yi, Y. Z. Wu, S. Wu, J. Zhu, et al., Gate-tunable room-temperature ferromagnetism in two-dimensional Fe_3GeTe_2, Nature 563 (2018) 94–99.

[10] B. Wang, Y. Zhang, L. Ma, Q. Wu, Y. Guo, X. Zhang, J. Wang, MnX (X= P, As) monolayers: a new type of two-dimensional intrinsic room temperature ferromagnetic half-metallic material with large magnetic anisotropy, Nanoscale 11 (2019) 4204–4209.

[11] A. K. Geim, I. V. Grigorieva, Van der Waals heterostructures, Nature 499 (2013) 419–425.

[12] J. T. Heron, M. Trassin, K. Ashraf, M. Gajek, Q. He, S. Y. Yang, D. E. Nikonov, Y.-H. Chu, S. Salahuddin, R. Ramesh, Electric-Field-Induced Magnetization Reversal in a Ferromagnet-Multiferroic Heterostructure, Phys. Rev. Lett. 107 (2011) 217202.

[13] Y. Khan, S. M. Obaidulla, M. R. Habib, A. Gayen, T. Liang, X. Wang, M. Xu, Recent breakthroughs in two-dimensional van der Waals magnetic materials and emerging applications, Nano Today 34 (2020) 100902.

[14] M. Hossain, B. Qin, B. Li, X. Duan, Synthesis, characterization, properties and applications of two-dimensional magnetic materials, Nano Today 42 (2022) 101338.

[15] C. Gong, L. Li, Z. Li, H. Ji, A. Stern, Y. Xia, T. Cao, W. Bao, C. Wang, Y. Wang, et al., Discovery of intrinsic ferromagnetism in two-dimensional van der Waals crystals, Nature 546 (2017) 265–269.

[16] K. L. Seyler, D. Zhong, D. R. Klein, S. Gao, X. Zhang, B. Huang, E. Navarro-Moratalla, L. Yang, D. H. Cobden, M. A. McGuire, et al., Ligand-field helical luminescence in a 2D ferromagnetic insulator, Nat. Phys. 14 (2018) 277–281.

[17] Z. Fei, B. Huang, P. Malinowski, W. Wang, T. Song, J. Sanchez, W. Yao, D. Xiao, X. Zhu, A. F. May, et al., Two-dimensional itinerant ferromagnetism in atomically thin Fe_3GeTe_2, Nat. Mater. 17 (2018) 778–782.

[18] M. Gibertini, M. Koperski, A. F. Morpurgo, K. S. Novoselov, Magnetic 2D materials and heterostructures, Nat. Nanotechnol. 14 (2019) 408–419.

[19] H. L. Zhuang, P. R. C. Kent, R. G. Hennig, Strong anisotropy and magnetostriction in the two-dimensional Stoner ferromagnet Fe_3GeTe_2, Phys. Rev. B 93 (2016) 134407.

[20] Mermin, N. D. and Wagner, H., Absence of Ferromagnetism or Antiferromagnetism in One- or Two-Dimensional Isotropic Heisenberg Models, Phys. Rev. Lett. 17 (1966) 1133–1136.

[21] B. Huang, G. Clark, E. Navarro-Moratalla, D. R. Klein, R. Cheng, K. L. Seyler, D. Zhong, E. Schmidgall, M. A. McGuire, D. H. Cobden, W. Yao, D. Xiao, P. Jarillo-Herrero, X. Xu, Layer-dependent ferromagnetism in a van der Waals crystal down to the monolayer limit, Nature 546 (2017) 270–273.

[22] Y. Liu, C. Petrovic, Critical behavior of quasi-two-dimensional semiconducting ferromagnet $Cr_2Ge_2Te_6$, Phys. Rev. B 96 (2017) 054406.

[23] T. J. Williams, A. A. Aczel, M. D. Lumsden, S. E. Nagler, M. B. Stone, J.-Q. Yan, D. Mandrus, Magnetic correlations in the quasi-two-dimensional semiconducting ferromagnet $CrSiTe_3$, Phys. Rev. B 92 (2015) 144404.

[24] Q. Xie, Y. Liu, M. Wu, H. Lu, W. Wang, L. He, X. Wu, Two stage magnetization in van der Waals layered $CrXTe_3$ (X = Si, Ge) single crystals, Mater. Lett. 246 (2019) 60–62.

[25] X. Feng, J. Li, J. Wu, Anisotropy of magnetocaloric effect in Fe_3GeTe_2, Phys. B Condens. Matter 625 (2022) 413478.

[26] J.-U. Lee, S. Lee, J. H. Ryoo, S. Kang, T. Y. Kim, P. Kim, C.-H. Park, J.-G. Park, H. Cheong, Ising-type magnetic ordering in atomically thin $FePS_3$, Nano letters 16 (2016) 7433–7438.

[27] G. Long, H. Henck, M. Gibertini, D. Dumcenco, Z. Wang, T. Taniguchi, K. Watanabe, E. Giannini, A. F. Morpurgo, Persistence of magnetism in atomically thin $MnPS_3$ crystals, Nano letters 20 (2020) 2452–2459.

[28] X. Sun, S. Zhao, A. Bachmatiuk, M. H. Rümmeli, S. Gorantla, M. Zeng, L. Fu, 2D Intrinsic Ferromagnetic MnP Single Crystals, Small 16 (2020) 2001484.

[29] Y. Zhu, X. Kong, T. D. Rhone, H. Guo, Systematic search for two-dimensional ferromagnetic materials, Phys. Rev. Materials 2 (2018) 081001.

[30] J. Dijkstra, H. Weitering, C. Van Bruggen, C. Haas, R. De Groot, Band-structure calculations, and magnetic and transport properties of ferromagnetic chromium tellurides (CrTe, Cr_3Te_4, Cr_2Te_3), J. Phys.: Condens. Matter 1 (1989) 9141.

[31] Z.-L. Huang, W. Bensch, D. Benea, H. Ebert, Anion substitution effects on structure and magnetism in the chromium chalcogenide Cr5Te8—Part I: Cluster glass behavior in trigonal Cr(1+x)Q2 with basic cell (Q=Te, Se; Te:Se=7:1), J. Solid State Chem. 177 (2004) 3245–3253.

[32] H. Ipser, K. L. Komarek, K. O. Klepp, Transition metal-chalcogen systems viii: The CrTe phase diagram, Journal of the Less Common Metals 92 (1983) 265–282.

[33] G. Chattopadhyay, The Cr-Te (chromium-tellurium) system, J. Phase Equilib. 15 (1994) 431–440.

[34] C. Zhang, C. Liu, J. Zhang, Y. Yuan, Y. Wen, Y. Li, D. Zheng, Q. Zhang, Z. Hou, G. Yin, et al., Room-Temperature Magnetic Skyrmions and Large Topological Hall Effect in Chromium Telluride Engineered by Self-Intercalation, Adv. Mater. 35 (2023) 2205967.

[35] B. Li, X. Deng, W. Shu, X. Cheng, Q. Qian, Z. Wan, B. Zhao, X. Shen, R. Wu, S. Shi, et al., Air-stable ultrathin Cr_3Te_4 nanosheets with thickness-dependent magnetic biskyrmions, Mater. Today 57 (2022) 66–74.

[36] Y. Chen, Y. Zhu, R. Lin, W. Niu, R. Liu, W. Zhuang, X. Zhang, J. Liang, W. Sun, Z. Chen, et al., Observation of colossal topological Hall effect in noncoplanar ferromagnet Cr_5Te_6 thin films, Adv. Funct. Mater. (2023) 2302984.

[37] M. Huang, L. Gao, Y. Zhang, X. Lei, G. Hu, J. Xiang, H. Zeng, X. Fu, Z. Zhang, G. Chai, et al., Possible Topological Hall Effect above Room Temperature in Layered $Cr_{1.2}Te_2$ Ferromagnet, Nano Lett. 21 (2021) 4280–4286.

[38] S. Purwar, A. Low, A. Bose, A. Narayan, S. Thirupathaiah, Investigation of the anomalous and topological Hall effects in layered monoclinic ferromagnet $Cr_{2.76}Te_4$, Phys. Rev. Mater. 7 (2023) 094204.

[39] ANDRESEN, ARNE F and Zeppezauer, E and Boive, T and Nordström, B and Brändén, C, Magnetic structure of Cr_2Te_3, Cr_3Te_4, and Cr_5Te_6, Acta Chem. Scand. 24 (1970) 3495–3509.

[40] A. Wang, A. Rahman, Z. Du, J. Zhao, F. Meng, W. Liu, J. Fan, C. Ma, M. Ge, L. Pi, et al., Field-dependent anisotropic room-temperature ferromagnetism in Cr_3Te_4, Phys. Rev. B 108 (2023) 094429.

[41] H. Zheng, C. Huang, F. Lin, J. Fan, H. Liu, L. Zhang, C. Ma, C. Wang, Y. Zhu, H. Yang, Two-dimensional van der Waals ferromagnetic thin film $CrTe_2$ with high Curie temperature and metallic conductivity, Appl. Phys. Lett. 122 (2023) 023103.

[42] L.-Z. Zhang, A.-L. Zhang, X.-D. He, X.-W. Ben, Q.-L. Xiao, W.-L. Lu, F. Chen, Z. Feng, S. Cao, J. Zhang, J.-Y. Ge, Critical behavior and magnetocaloric effect of the quasi-two-dimensional room-temperature ferromagnet Cr_4Te_5, Phys. Rev. B 101 (2020) 214413.

[43] H. Liu, H. Zheng, Y. Wang, C. Huang, C. Ma, Y. Zhu, H. Yang, L. Ling, L. Zhang, J. Fan, Long-Range Magnetic Exchange Coupling in Quasi-2D CrTe Ferromagnetic Thin Films, Phys. Status Solidi RRL 17 (2023) 2300209.

[44] I. Dzyaloshinsky, A thermodynamic theory of “weak” ferromagnetism of antiferromagnetics, Journal of physics and chemistry of solids 4 (1958) 241–255.

[45] T. Moriya, New mechanism of anisotropic superexchange interaction, Phys. Rev. Lett. 4 (1960) 228–230.

[46] C. Zener, Classical theory of the temperature dependence of magnetic anisotropy energy, Phys. Rev. 96 (1954) 1335–1337.

[47] W. H. Meiklejohn, C. P. Bean, New magnetic anisotropy, Phys. Rev. 105 (1957) 904–913.

[48] D. S. Chuang, C. A. Ballentine, R. C. O’Handley, Surface and step magnetic anisotropy, Phys. Rev. B 49 (1994) 15084–15095.

[49] R. Skomski, J. Coey, Magnetic anisotropy—how much is enough for a permanent magnet?, Scripta Materialia 112 (2016) 3–8.

[50] R. Stamps, Mechanisms for exchange bias, Journal of Physics D: Applied Physics 33 (2000) R247.

[51] M. Kiwi, Exchange bias theory, Journal of Magnetism and Magnetic materials 234 (2001) 584–595.

[52] L. Onsager, Crystal statistics. i. a two-dimensional model with an order-disorder transition, Phys. Rev. 65 (1944) 117–149.

[53] Q. H. Wang, A. Bedoya-Pinto, M. Blei, A. H. Dismukes, A. Hamo, S. Jenkins, M. Koperski, Y. Liu, Q.-C. Sun, E. J. Telford, et al., The magnetic genome of two-dimensional van der waals materials, ACS nano 16 (2022) 6960–7079.

[54] V. Berezinskii, Destruction of long-range order in one-dimensional and two-dimensional systems having a continuous symmetry group i. classical systems, Sov. Phys. JETP 32 (1971) 493–500.

[55] J. M. Kosterlitz, The critical properties of the two-dimensional xy model, Journal of Physics C: Solid State Physics 7 (1974) 1046.

[56] H. E. Stanley, Phase transitions and critical phenomena, volume 7, Clarendon Press, Oxford, 1971.

[57] B. Banerjee, On a generalised approach to first and second order magnetic transitions, Physics Letters 12 (1964) 16–17.

[58] M. E. Fisher, The theory of equilibrium critical phenomena, Reports on progress in physics 30 (1967) 615.

[59] A. Arrott, J. E. Noakes, Approximate equation of state for nickel near its critical temperature, Phys. Rev. Lett. 19 (1967) 786–789.

[60] A. K. Pramanik, A. Banerjee, Critical behavior at paramagnetic to ferromagnetic phase transition in $\mathrm{Pr_{0.5}Sr_{0.5}MnO_3}$: A bulk magnetization study, Phys. Rev. B 79 (2009) 214426.

[61] J. S. Kouvel, M. E. Fisher, Detailed Magnetic Behavior of Nickel Near its Curie Point, Phys. Rev. 136 (1964) A1626–A1632.

[62] A. M. Tishin, Y. I. Spichkin, The magnetocaloric effect and its applications, CRC Press, 2016.

[63] M.-H. Phan, S.-C. Yu, Review of the magnetocaloric effect in manganite materials, Journal of Magnetism and Magnetic Materials 308 (2007) 325–340.

[64] V. K. Pecharsky, K. A. Gschneidner Jr, Magnetocaloric effect and magnetic refrigeration, J. Magn. Magn. Mater. 200 (1999) 44–56.

[65] C. Kittel, P. McEuen, Introduction to solid state physics, John Wiley & Sons, 2018.

[66] M. E. Cage, K. Klitzing, A. Chang, F. Duncan, M. Haldane, R. B. Laughlin, A. Pruisken, D. Thouless, The quantum Hall effect, Springer Science & Business Media, 2012.

[67] S. Nakatsuji, N. Kiyohara, T. Higo, Large anomalous Hall effect in a non-collinear antiferromagnet at room temperature, Nature 527 (2015) 212–215.

[68] N. Nagaosa, J. Sinova, S. Onoda, A. H. MacDonald, N. P. Ong, Anomalous hall effect, Rev. Mod. Phys. 82 (2010) 1539–1592.

[69] K. Kuroda, T. Tomita, M.-T. Suzuki, C. Bareille, A. Nugroho, P. Goswami, M. Ochi, M. Ikhlas, M. Nakayama, S. Akebi, R. Noguchi, R. Ishii, N. Inami, K. Ono, H. Kumigashira, A. Varykhalov, T. Muro, T. Koretsune, R. Arita, S. Shin, T. Kondo,

S. Nakatsuji, Evidence for magnetic Weyl fermions in a correlated metal, Nat. Mater. 16 (2017) 1090–1095.

[70] L. Zhu, J. Zhao, Electrical transport of perpendicularly magnetized l 1 0-mnga and mnal films, in: Spin, volume 7, World Scientific, p. 1730001.

[71] J. Smit, The spontaneous hall effect in ferromagnetics II, Physica 24 (1958) 39–51.

[72] L. Berger, Side-jump mechanism for the hall effect of ferromagnets, Phys. Rev. B 2 (1970) 4559–4566.

[73] C. Zeng, Y. Yao, Q. Niu, H. H. Weitering, Linear magnetization dependence of the intrinsic anomalous hall effect, Phys. Rev. Lett. 96 (2006) 037204.

[74] G. Kimbell, C. Kim, W. Wu, M. Cuoco, J. W. Robinson, Challenges in identifying chiral spin textures via the topological hall effect, Communications Materials 3 (2022) 19.

[75] X. Yu, Y. Onose, N. Kanazawa, J. H. Park, J. Han, Y. Matsui, N. Nagaosa, Y. Tokura, Real-space observation of a two-dimensional skyrmion crystal, Nature 465 (2010) 901–904.

[76] O. Meshcheriakova, S. Chadov, A. K. Nayak, U. K. Rößler, J. Kübler, G. André, A. A. Tsirlin, J. Kiss, S. Hausdorf, A. Kalache, W. Schnelle, M. Nicklas, C. Felser, Large Noncollinearity and Spin Reorientation in the Novel Mn_2RhSn Heusler Magnet, Phys. Rev. Lett. 113 (2014) 087203.

[77] W. Jiang, G. Chen, K. Liu, J. Zang, S. G. Te Velthuis, A. Hoffmann, Skyrmions in magnetic multilayers, Physics Reports 704 (2017) 1–49.

[78] T. Kurumaji, T. Nakajima, M. Hirschberger, A. Kikkawa, Y. Yamasaki, H. Sagayama, H. Nakao, Y. Taguchi, T.-h. Arima, Y. Tokura, Skyrmion lattice with a giant topological hall effect in a frustrated triangular-lattice magnet, Science 365 (2019) 914–918.

[79] P. K. Rout, P. V. P. Madduri, S. K. Manna, A. K. Nayak, Field-induced topological hall effect in the noncoplanar triangular antiferromagnetic geometry of Mn_3Sn, Phys. Rev. B 99 (2019) 094430.

[80] B. Ding, Z. Li, G. Xu, H. Li, Z. Hou, E. Liu, X. Xi, F. Xu, Y. Yao, W. Wang, Observation of magnetic skyrmion bubbles in a van der waals ferromagnet Fe_3GeTe_2, Nano Letters 20 (2019) 868–873.

[81] D. A. Gilbert, B. B. Maranville, A. L. Balk, B. J. Kirby, P. Fischer, D. T. Pierce, J. Unguris, J. A. Borchers, K. Liu, Realization of ground-state artificial skyrmion lattices at room temperature, Nature communications 6 (2015) 1–7.

[82] H. Wang, Y. Dai, G.-M. Chow, J. Chen, Topological hall transport: Materials, mechanisms and potential applications, Progress in Materials Science 130 (2022) 100971.

Chapter 2

Experimental Section

2.1 Single Crystal Growth

Single crystals are materials in which the atomic arrangement is highly ordered and extends without interruption throughout the entire volume of the crystal. Unlike polycrystalline materials, where multiple small crystals or grains are randomly oriented, single crystals have a continuous and uniform lattice structure in all three dimensions. This unique character makes the single crystals invaluable for studying intrinsic physical, electronic, and magnetic properties because measurements can be performed along different crystallographic axes, revealing directional dependencies that are often obscured in polycrystalline or amorphous materials.

Single crystal growth can be achieved using a variety of methods, each tailored to the specific characteristics of the material and the desired crystal properties. The most common techniques are the chemical vapor transport (CVT) method, the self-flux method, the Bridgman-Stockbarger process, the Czochralski method, and flux growth, each of which offers unique advantages suited to particular crystal growth challenges. In this research, two prominent techniques—the self-flux method and the chemical vapor transport method were employed to grow the single crystals. Both methods have their distinct benefits and are ideal for different types of materials and growth requirements. The research presented in this thesis focuses on the single crystals: (a) $Cr_{1.33}Te_2$ (or Cr_2Te_3) [1], (b) $Cr_{1.38}Te_2$ (or $Cr_{2.76}Te_4$) [2, 3], (c) $Cr_{1.66}Te_2$ (or Cr_5Te_6) [4], and (d) $Sn_{0.06}Cr_3Te_4$ [5].

2.1.1 Flux Growth Method

The self-flux method is an effective technique for growing high-quality single crystals, particularly of the metallic and intermetallic systems. In this method, the material of interest is dissolved in its molten form in a flux, which acts as a solvent at high temperatures [6, 7]. As the solution cools, crystals of the desired material precipitate out of the flux when the solution becomes supersaturated. This method works well for compounds that

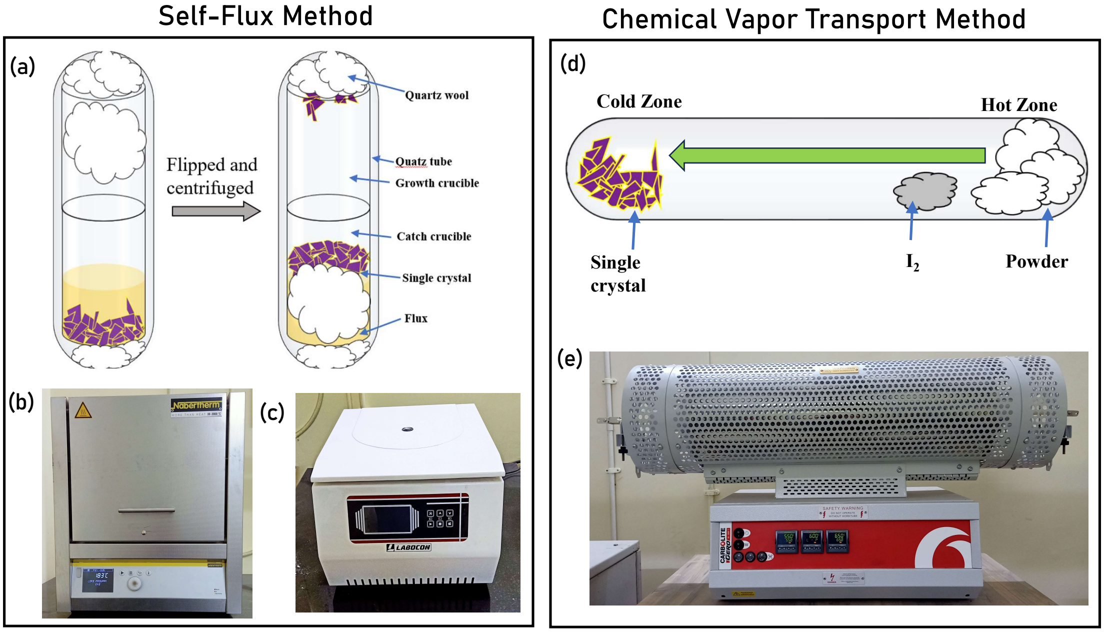

Figure 2.1: Illustration of various single crystal growth techniques such as self-flux method and the chemical vapor transport (CVT) method. (a) Schematic of the self-flux method process, where the growth material is centrifuged to separate the flux from the single crystals. (b) Furnace used for the self-flux process, and (c) centrifuge equipment for separating flux from the single crystals. (d) Schematic of the CVT process, where the crystal growth occurs by transporting material from the hot zone to the cold zone using iodine (I_2) as a transport agent. (e) Tube furnace used for the CVT method.

melt congruently and have good solubility in the molten state.

Detailed procedure involved in this method:

Precursor: The elemental components of the desired material are combined with a flux in a crucible to lower the melting point and aid dissolution. Common crucible materials include alumina (Al_2O_3), boron nitride (BN), graphite, or metals sach as tantalum (Ta) or platinum (Pt) [8, 9]. The crucible along with the mixture is sealed inside a quartz ampoule to avoid the contamination. Then, the whole set-up is placed in a high temperature furnace for heating. The mixture is heated until the components are fully dissolved, followed by controlled cooling to encourage nucleation and crystal growth. Finally, the ampoule is inverted and subjected to centrifugation to separate the formed crystals from the residual flux (see Fig. 2.1 (a)).

Heating: The temperature is progressively raised beyond the melting point of the mixture to allow the components to combine and form a uniform liquid phase. The specific temperature and heating duration are determined according to the material-flux system's phase diagram to ensure all components dissolve completely.

Controlled Cooling: Once the mixture is fully in the solution form, the temperature is gradually reduced at a controlled rate to promote the crystal nucleation and growth. Controlled cooling is crucial in this step, as it allows large, defect-free crystals to form.

The cooling rate is typically optimized to be slow enough for proper crystallization, but fast enough to avoid premature solidification of the entire melt.

Centrifugation and Separation: After the completion of crystal growth process, the ampoule together with crucible is flipped and centrifuged to separate the remaining liquid flux from the solidified single crystals [Fig. 2.1 (c)]. Centrifugation is employed at higher speeds to ensure efficient separation, with the denser single crystals remaining at the bottom of the crucible, while the liquid flux is spun off and collected at the other side of crucible. This step is critical for obtaining pure crystals without residual flux material.

Advantages:

- The self-flux method allows for the growth of high-purity, large single crystals with minimal defects, making it an excellent choice for intermetallic compounds and alloys.
- It enables the precise control of stoichiometry, and by careful selection of the flux material, it is possible to control the crystallization process to achieve high-quality crystals.
- This method also allows for the growth of crystals at relatively low temperatures, reducing the risk of decomposition or volatilization of the sample material.

2.1.2 Chemical Vapor Transport (CVT) Method

The chemical vapor transport (CVT) Method is another highly effective technique for growing single crystals, particularly for compounds that either decompose or have very high melting points [10, 11]. Instead of dissolving the material in a molten flux, the CVT method relies on the transport of material in vapor form through the use of a transport agent, such as iodine (I_2), bromine (Br_2), or chlorine (Cl_2), to achieve crystallization. This method is ideal for growing large crystals of metal, semiconductors, and other materials where the solid-vapor equilibrium is utilized.

During the CVT process, the material reacts with the transport agent at elevated temperatures, forming volatile compounds that migrate to a cooler region within a sealed ampoule. Upon reaching the cooler zone, these compounds decompose, depositing the material as single crystals. Depending on the specific reaction and transport agent, the method can involve either heat absorption (endothermic) or heat release (exothermic). In endothermic reactions, the absorption of heat facilitates the vaporization of the material and its transport, necessitating precise temperature control to maintain efficiency and avoid issues such as excessive cooling. Conversely, exothermic reactions release heat during the deposition process, potentially enhancing crystal growth by creating localized heating in the deposition zone. Careful optimization of these thermal processes is crucial for achieving high-quality crystals with desired size and morphology.

Detailed procedure involved in this method:

Precursor: The starting material, usually in the powdered form, is placed at one end of a sealed quartz ampoule along with a small amount of transport agent (e.g., iodine). The ampoule is sealed under vacuum to prevent contamination and unwanted reactions with atmospheric gases [Fig. 2.1 (d)].

Temperature Gradient: The sealed ampoule is placed inside a two-zone furnace [Fig. 2.1 (e)], which provides a controlled temperature gradient. The starting material is kept in the source-zone, while the desired crystals form in the sink-zone. The temperature difference between these two zones drives the transport of the material in vapor form.

Vapor Transport: The transport agent reacts with the material in the source zone to form volatile compounds (e.g., metal iodides in the case of iodine). These volatile species diffuse along the ampoule towards the sink zone, where the temperature is lower. Upon reaching the cold zone, the volatile compounds decompose, and the transported material is deposited as single crystals.

Crystal Growth: Over the time, single crystals grow in the cold zone as material continues to be transported. The size and quality of the crystals depend on factors such as the temperature gradient, the concentration of the transport agent, and the duration of the process. Typically, the growth period lasts several days to weeks, depending on the system.

Advantages:

- The CVT method is effective for synthesizing high-quality crystals of materials with high melting points or those that decompose before melting. It is widely employed for growing semiconductor compounds and transition metal dichalcogenides..
- The process allows for the precise control of the growth environment, ensuring that large and well-faceted crystals can be grown.
- CVT can also produce crystals of complex stoichiometry, as the transport mechanism can help selectively deposit certain elements at lower temperatures.

2.2 Characterization Techniques

2.2.1 Energy Dispersive X-ray Analysis (EDS)

Energy Dispersive X-ray Spectroscopy (EDS), often paired with Scanning Electron Microscopy (SEM) is a technique used to analyze the elemental composition of materials at a microscopic scale. EDS provides localized compositional information by detecting characteristic X-rays emitted from the sample.

Basic Principle of EDS

EDS functions based on X-ray emission triggered by the interaction of a high-energy electron beam with the sample. The process involves the following steps:

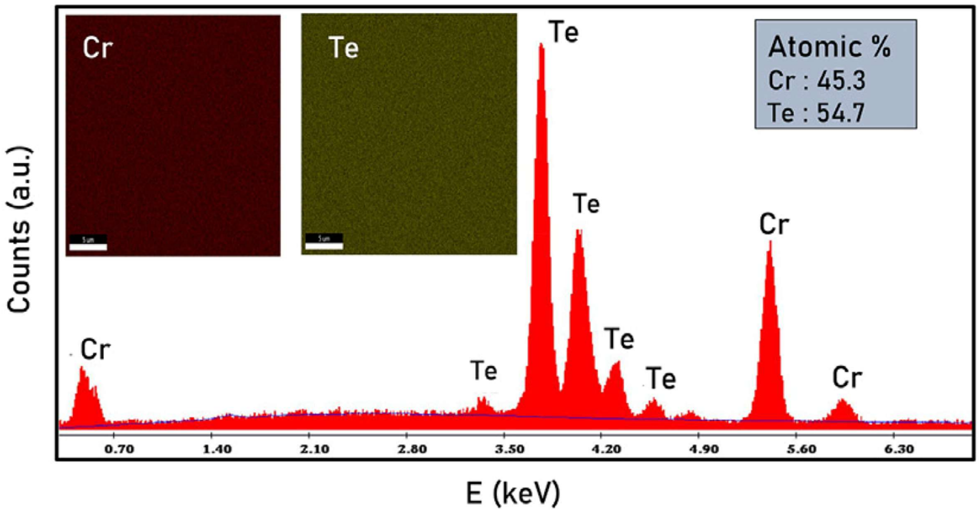

Figure 2.2: Energy Dispersive X-ray Spectroscopy (EDS) results obtained from the Quanta FEG-250 FE-SEM equipped with an EDS detector, showing the elemental mapping of Chromium (Cr) and Tellurium (Te) in the sample, along with their respective atomic percentages.

Excitation: A focused very high energy electron beam strikes the sample, exciting the inner-shell electrons of the atoms, and creats vacancies.

X-ray Emission: Electrons from higher energy levels fill the vacancies at low energy levels by releasing X-rays with energies equal to the energy difference between the two shells.

Detection and Analysis: The emitted X-rays are collected by the EDS detector, which measures the energy and intensity of the x-rays. Each element has a unique set of characteristic X-ray energies, allowing for identification. The resulting data is processed to create an energy spectrum that displays the intensity of X-rays as a function of their energy.

Interpretation and Quantitative Analysis of EDS Spectrum

The EDS spectrum provides a graphical representation of the detected X-rays, where each peak corresponds to a specific element in the sample. The position of the peaks identifies the elements, while their heights or areas indicate their relative abundance. To achieve accurate quantification, background noise in the spectrum is subtracted, and the peak intensities are compared to reference standards with known compositions. This process enables the determination of both the weight and atomic percentages of the elements. As illustrated in Fig. 2.2, the EDS spectrum for a sample highlights the characteristic X-ray peaks corresponding to Chromium (Cr) and Tellurium (Te), providing a clear visualization of the elemental composition and relative proportions of these elements.

Experimental Set up

Fig. 2.3(a) schematically illustrates the FE-SEM set-up. The electron gun at the top generates a focused electron beam via field emission. The beam is accelerated toward the sample, passing through magnetic lenses and scanning coils that focus and direct it

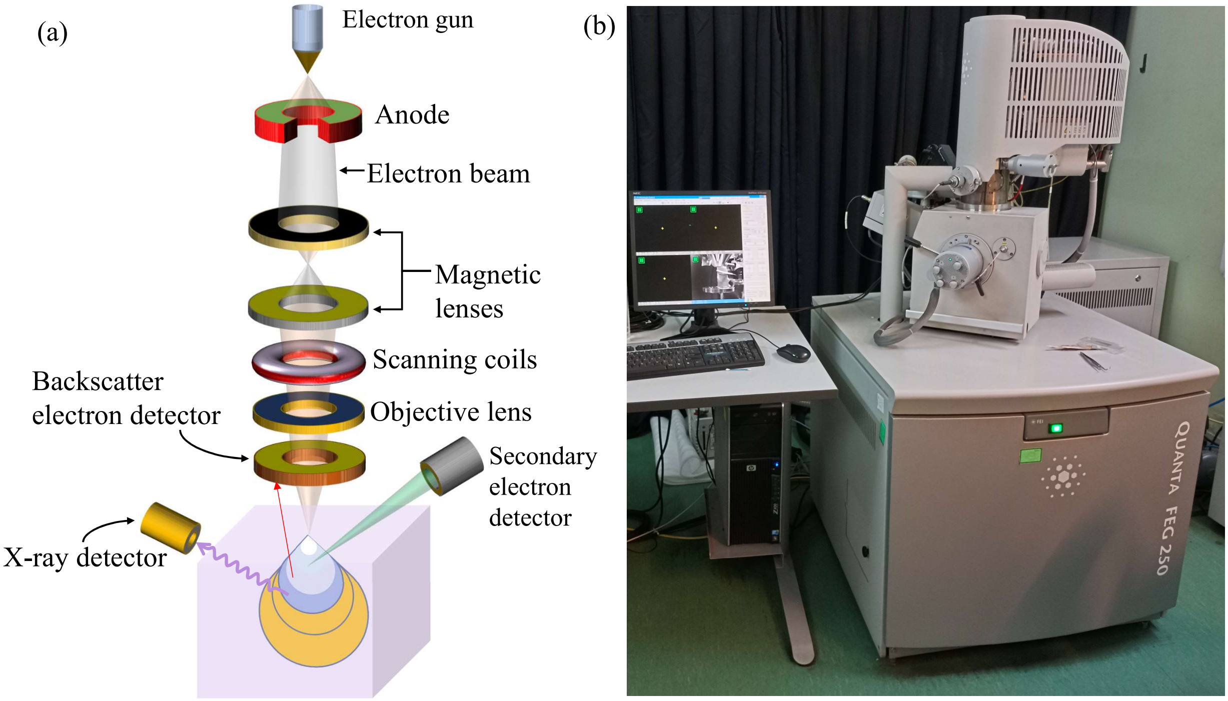

Figure 2.3: (a) Schematic diagram of different parts of a scanning electron microscope (SEM). (b) EDS attached to FE-SEM used for sample characterization at SNBNCBS.

across the sample surface. Electron-sample interactions produce various signals, including secondary electrons, backscattered electrons, and characteristic X-rays, which are detected by corresponding detectors.

Secondary Electron Detector (SED): Provides high-resolution images of the sample surface, capturing fine details of the surface morphology.

Backscatter Electron Detector (BSED): Offers contrast based on atomic number differences, useful for compositional analysis.

X-ray Detector (for EDS): Detects X-rays emitted due to electron transitions between atomic energy levels, allowing for elemental composition analysis.

In this study, we utilized the Quanta FEG-250 FE-SEM, equipped with an Energy Dispersive X-ray Spectroscopy (EDS) attachment [Fig. 2.3(b)], at S. N. Bose National Centre for Basic Sciences (SNBNCBS) to conduct elemental analysis of the synthesized crystals. The system enables precise compositional analysis by detecting characteristic X-rays emitted when the electron beam interacts with the atoms of the sample. This feature allowed us to accurately determine the elemental composition, including weight and atomic percentages, of the samples. The high spatial resolution of the FE-SEM, combined with the elemental mapping capability of the EDS, provided detailed insights into the microstructure and distribution of elements within the crystals. To minimize charging effects that could distort both imaging and EDS measurements, the samples were mounted on conductive carbon tape. The analysis was conducted in high vacuum mode, ensuring optimal resolution and enhanced accuracy in elemental detection.

2.2.2 X-ray Diffraction (XRD)

The crystal structure and symmetry of the synthesized materials were determined using X-ray diffraction (XRD), a technique grounded in Bragg's law, $2d\sin\theta = n\lambda$ [12]. In this equation, d represents the interplanar spacing between Bragg planes, θ is the angle of incidence, and λ is the wavelength of the X-ray source, as illustrated in Fig. 2.4 (a). By applying Bragg's relation, one can precisely calculate the lattice constants and infer the crystal symmetry.

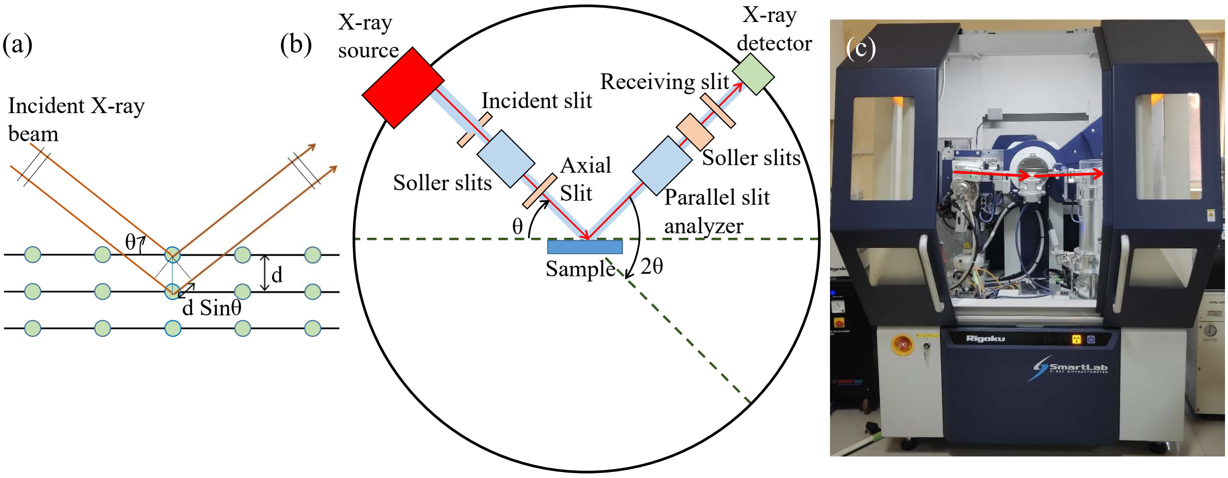

Figure 2.4: (a) Schematic representation of Bragg's law, illustrating the diffraction of X-rays by crystal planes, where 'd' is the interplanar spacing and 'θ' is the angle of incidence. (b) Diagram of the X-ray diffraction (XRD) experimental setup showing key components such as the X-ray source, incident slit, receiving slit, axial slit, and detector system used to measure diffraction patterns. (c) The actual image of the XRD instrument used in this study (Rigaku SmartLab) to perform structural characterization of the crystal samples.

XRD Instrumentation

In Fig. 2.4 (b), the essential components of the X-ray diffraction setup are illustrated. This includes:

X-ray Source: The X-rays are generated using a high-energy source, typically a rotating anode or sealed tube that emits X-rays by bombarding a target material (commonly Cu, producing Cu K_α radiation with a wavelength of 1.54 Å).

Incident Slits: The incident slit system (including Soller slits and parallel slits) controls the beam's width and divergence. This ensures that the X-ray beam hitting the sample has well-defined geometry, minimizing scattered or divergent radiation and improving the resolution of the diffraction pattern [13].

Sample Stage: The sample is positioned at the center of the goniometer. It is aligned such that the X-rays hit the sample at different angles (2θ), allowing for the capture of diffraction peaks from different crystallographic planes. The sample stage can be rotated to vary the incident angle of the X-rays during the measurement.

Soller Slits: These slits reduce the angular divergence of the beam in both the incident and diffracted paths. This enhances the resolution of the diffraction data, providing sharper and more precise diffraction peaks.

Axial and Receiving Slits: These slits ensure that only X-rays diffracted at specific angles reach the detector, further reducing background noise and improving signal-to-noise ratio.

Detector: Intensity of diffracted X-rays is measured as a function of the diffraction angle 2θ by the detector. Advanced XRD systems commonly employ high-sensitivity detectors, such as solid-state or position-sensitive types, to efficiently collect data over a broad angular range.

Goniometer: The goniometer is a crucial component of the XRD setup, designed to precisely control the angular movement of both the sample and the detector. It enables the alignment and rotation of the sample to vary the incident angle of the X-ray beam and ensures that the detector moves synchronously to measure the diffracted intensity at different 2θ angles.

The setup in Fig. 2.4 (b) represents a standard powder XRD configuration, optimized for phase identification, structural analysis, and crystallite size determination.

Rigaku SmartLab XRD System

In this study, weperformed X-ray diffraction (XRD) measurements using a Rigaku SmartLab diffractometer (9 kW), which employed Cu-K_α radiation (λ = 1.54 Å) as depicted in Fig. 2.4 (c). In this setup, electrons emitted from a tungsten cathode are accelerated by applying a voltage between 20 and 45 kV across the cathode and anode, while the electron current is maintained between 10 and 200 mA. The resulting electron beam, with a power of up to 9 kW, bombards the copper anode, producing Cu K_α X-rays. To detect the diffracted X-rays, a hybrid photon counting (HPC) detector is utilized [14]. It is important to note that this diffractometer operates using a θ-θ goniometer, where the sample remains stationary while both the X-ray tube and the detector rotate to collect the diffraction pattern.

2.2.3 Transmission Electron Microscopy (TEM)

Transmission Electron Microscopy (TEM) is a powerful technique used to analyze the structural, crystallographic, and morphological properties of materials at nanometer to atomic resolution. Unlike Energy Dispersive Spectroscopy (EDS), which provides elemental composition, TEM excels in imaging lattice structures, defects, and interfaces with high spatial resolution.

Working Principle of TEM

Transmission Electron Microscopy (TEM) operates by transmitting a high-energy electron beam (typically 100-300 keV) through an ultrathin sample. As the electron beam interacts

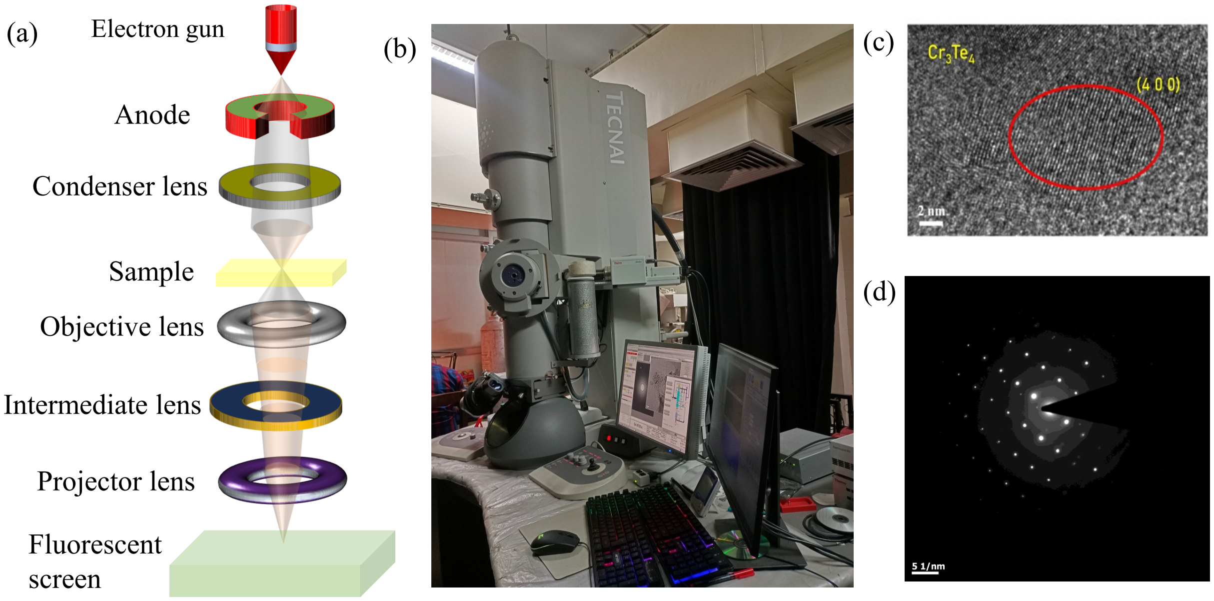

Figure 2.5: (a) Schematic diagram illustrating the working principle and components of a transmission electron microscope (TEM). (b) TECNAI TEM instrument used in the current study. (c) High-resolution TEM (HRTEM) image of Cr_3Te_4 showing lattice fringes corresponding to the (400) plane with an interplanar spacing of 2 nm. (d) Selected Area Electron Diffraction (SAED) pattern of Cr_3Te_4, confirming the crystalline nature of the material.

with the atoms in the sample, various signals, such as transmitted electrons, scattered electrons, and diffraction patterns, are produced. These signals are magnified using a series of electromagnetic lenses to generate high-resolution images and diffraction patterns that reveal the structural, crystallographic, and compositional details of the material. The transmitted electrons create an image of the sample's structure, while the scattered electrons are used for diffraction analysis. Adjustments in the electron optics allow the operator to switch between imaging and diffraction modes seamlessly.

Components of TEM

The main components of a TEM, as shown in Fig. 2.5(a), are as follows:

1. **Electron Gun:** Generates a focused beam of electrons, typically through thermionic or field emission mechanisms.

2. **Anode:** Accelerates the electron beam to high energies required for penetrating the sample.

3. **Condenser Lenses:** Focus the electron beam onto a specific region of the sample while controlling its intensity and convergence.

4. **Sample Stage:** Holds the ultrathin sample, enabling precise positioning, tilting, and rotation to study different orientations.

5. **Objective Lens:** Produces the initial magnified image or diffraction pattern of the sample by focusing the transmitted and scattered electrons.

6. **Intermediate Lens:** Provides additional magnification and allows switching between imaging and diffraction modes.

7. **Projector Lens:** Projects the magnified image or diffraction pattern onto the viewing screen or camera.

8. **Fluorescent Screen/Detector:** Captures the final image or diffraction pattern. Modern systems often use CCD or CMOS cameras for digital imaging.

The TECNAI TEM instrument (Fig. 2.5(b)) was utilized for structural characterization of Cr_3Te_4. The high-resolution TEM (HRTEM) image (Fig. 2.5(c)) reveals distinct lattice fringes corresponding to the (400) plane with an interplanar spacing of 2 nm, confirming the high crystallinity of the sample.

The Selected Area Electron Diffraction (SAED) pattern (Fig. 2.5(d)) displays sharp diffraction spots, validating the crystalline nature of Cr_3Te_4. These results provide critical insights into the structural properties of Cr_3Te_4, which are essential for understanding its physical and magnetic behavior.

2.3 Vibrating Sample Magnetometer (VSM)

Vibrating Sample Magnetometer (VSM) is a widely used scientific instrument that employs Faraday's law of induction [15] to measure the magnetic properties of material. According to the Faraday's law, an electromotive force (emf) is generated in a conducting coil when exposed to a time-varying magnetic field. The induced emf (ϵ) is related to the rate of change of magnetic flux (Φ_B) passing through the coil:

$$\epsilon = -\frac{d\Phi_B}{dt} \tag{2.1}$$

where $\frac{d\Phi_B}{dt}$ represents the rate of change of magnetic flux with time. The negative sign indicates the direction of the induced current, which, according to Lenz's law, opposes the change in magnetic flux.

In the VSM setup, the sample is attached to a non-magnetic rod connected to a vibration unit. It is positioned between two electromagnets that apply a uniform external magnetic field to align the sample's magnetic dipoles. The vibration unit oscillates the sample sinusoidally at a high frequency, causing the magnetic flux from the sample's dipole moment to vary over time. This time-varying flux induces a voltage in the search coils placed near the sample, as shown in Fig. 2.6 (a). The voltage V_{coil} generated in the pickup

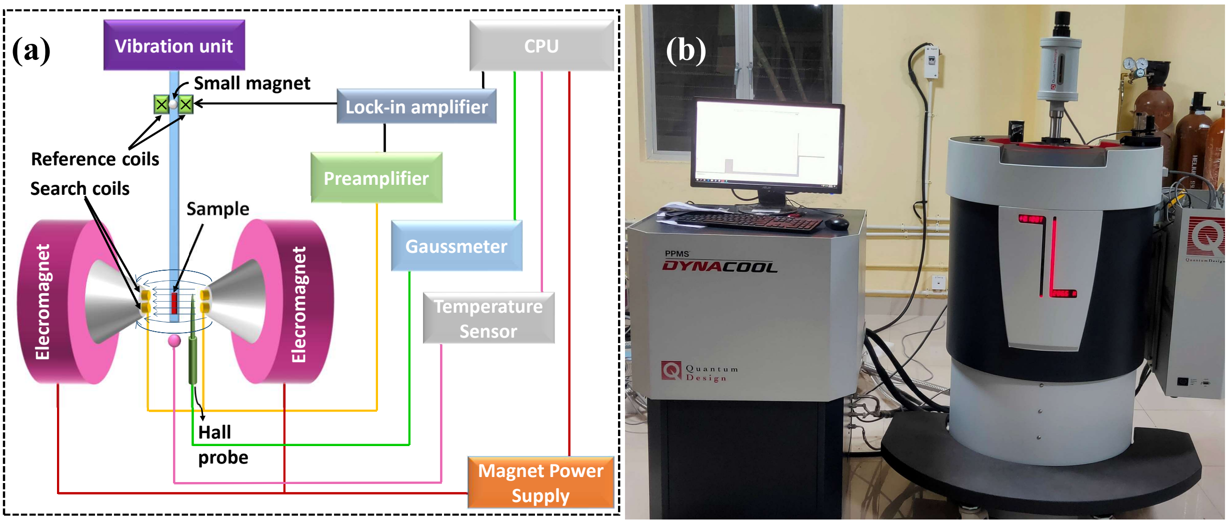

Figure 2.6: (a) Schematic diagram of a VSM setup showing key components such as the vibration unit, electromagnets, search coils, preamplifier, lock-in amplifier, and temperature sensor. The sample is vibrated between the electromagnets, generating an oscillating magnetic field, which induces a voltage in the pickup coils via Faraday's law of induction. (b) VSM option available with the Quantum Design physical property measurement system (PPMS), capable of measuring magnetic moments with high precision under varying temperature and magnetic field conditions.

coils corresponds to the time derivative of the magnetic flux, indicating its proportionality to the flux variation rate:

$$V_{coil} = \frac{d\Phi_B}{dt} \tag{2.2}$$

This can be rewritten in terms of the sample's vertical displacement z:

$$V_{\text{coil}} = \frac{d\Phi_B}{dz} \cdot \frac{dz}{dt} \tag{2.3}$$

For a sample oscillating sinusoidally with frequency f and amplitude A, the induced voltage becomes:

$$V_{coil} = 2\pi f C m A Sin(2\pi f t) \tag{2.4}$$

Here, C represents the coupling constant, m denotes the sample's magnetic moment, and A is the oscillation amplitude. By analyzing the induced voltage, the magnetic moment of the sample under the applied magnetic field can be determined.

For our study, magnetization measurements were performed using the VSM module of the Quantum Design PPMS, with magnetic fields up to 9 T and a temperature range from 2 K to 300 K, as depicted in Fig. 2.6 (b). During the measurements, the sample was oscillated at a frequency of $f = 40$ Hz with an amplitude of 1-3 mm. This setup allows for the detection of very low magnetic moments, down to the order of 10^{-6} emu. Additionally,

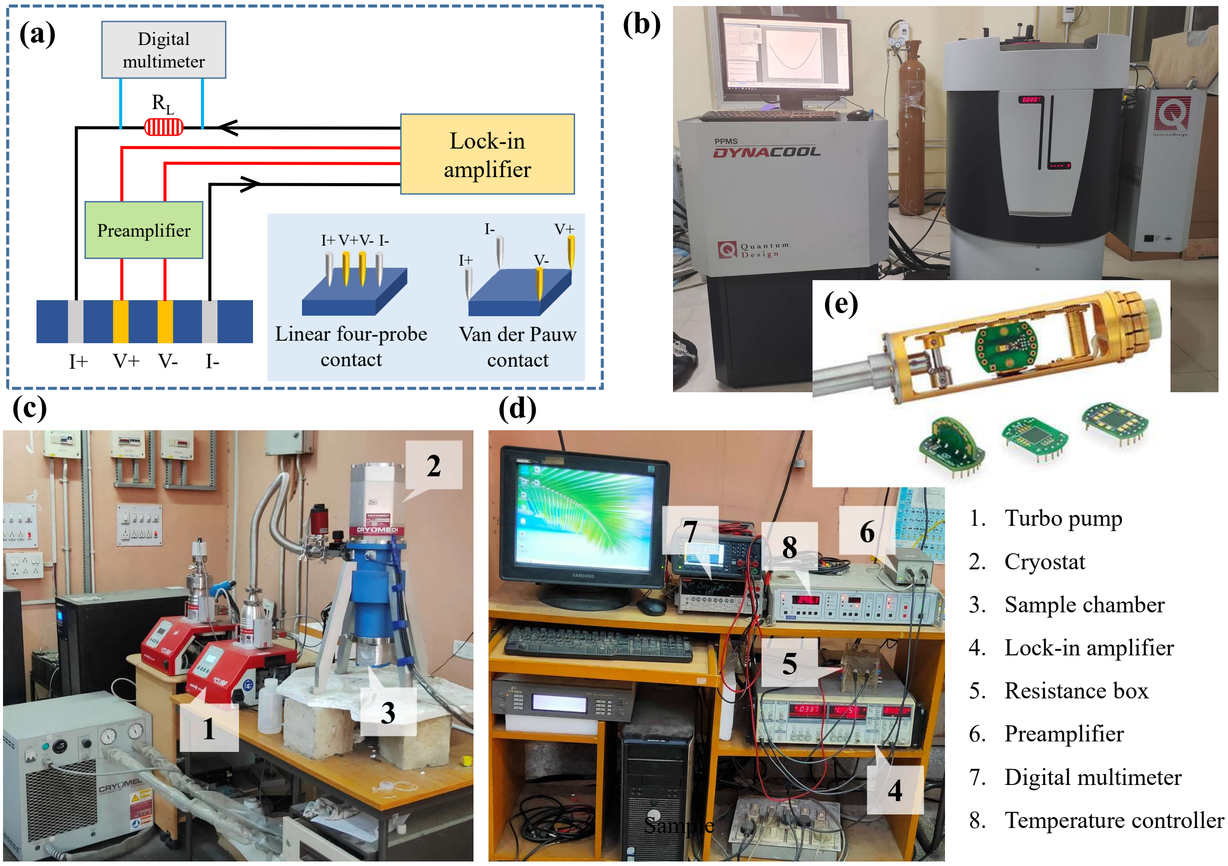

Figure 2.7: (a) Schematic of a four-probe resistivity measurement geometry. The inset shows linear and Van der Pauw configurations for four-probe measurements. (b) Photo of the PPMS at SNBNCBS, used for resistivity measurements of single crystals under varying temperatures and magnetic fields. (c)-(d) Oxford resistivity setup. The components numbered in the white bubbles are listed on the right.

using the VSM oven option, measurements at elevated temperatures (400-1000 K) can be performed.

2.4 Electrical Resistivity

To understand the electrical transport properties of the as-grown single crystals, we performed the resistivity measurements. By observing the temperature-dependent resistivity data, we can identify the nature of the samples, such as metallic, insulating, superconducting, or semiconducting. In this thesis, all of the discussed topological materials are found to be good conductors with resistance in the order of $m\Omega$. Fig. 2.7 illustrates the experimental setups used for the electrical resistivity and magneto-transport measurements.

Four-Probe Measurement Geometry: The schematic in panel 2.7 (a) illustrates the four-probe method, which is widely used for resistivity measurements due to its precision in eliminating contact resistance. In this technique, a known current (I) is applied through the outer probes, while the voltage (V) is measured across the inner probes. The inset shows two common configurations:

- The **Linear Four-Probe Method** is a technique used to measure the resistivity of materials by eliminating the contact resistance between the probes and the sample. In this method, four probes are placed symmetrically along the surface of the sample, with the outer probes injecting a known current and the inner probes measuring the voltage drop. The resistivity (ρ) is determined from the current (I) and the measured voltage (V) using the equation

  $$\rho = \frac{\pi t}{\ln(2)} \cdot \frac{V}{I}$$

  where t is the sample thickness. This approach ensures high accuracy by spatially separating the current injection and voltage measurement, effectively minimizing the influence of contact resistance.

- The **Van der Pauw Method** is a widely used technique for measuring the resistivity of arbitrarily shaped, thin, or homogeneous samples. In this method [16], four electrical contacts are placed at arbitrary points on the sample's perimeter, and the resistivity is determined by applying a current between two contacts and measuring the voltage between the other two contacts. The resistivity (ρ) is calculated by solving the Van der Pauw equation

  $$e^{-\pi R_{12,34}/\rho} + e^{-\pi R_{14,23}/\rho} = 1$$

  where $R_{12,34}$ and $R_{14,23}$ are the measured resistances. This method is effective for samples with complex geometries and does not require the sample to be of a specific shape, making it ideal for thin films or irregularly shaped materials.

Silver paint is used to make the four-probe connections. This method is particularly effective for studying temperature and field-dependent resistivity.

Experimental Set-up

(a) Quantum Design Physical Property Measurement System (PPMS): The PPMS, shown in Fig. 2.7(b), is a sophisticated, commercial measurement system available at SNBNCBS. This system enables the measurement of resistivity and magneto-transport properties, including the Hall effect and magnetoresistance, over a broad range of temperatures (2 K to 300 K) under magnetic fields up to 9 T. The system is fully automated, allowing for temperature and magnetic field sweeps to study transport phenomena such as the anomalous Hall effect (AHE), topological Hall effect (THE), and magnetoresistance (MR) under various experimental conditions.

(b) Oxford Resistivity Setup: The oxford system is a custom equipment designed as a to measure temperature-dependent resistivity and magneto-transport properties, providing flexibility for custom experiments. The key components include:

- Turbo Pump: Ensures a high-vacuum environment within the sample chamber, reducing oxidation or contamination and improving the accuracy of measurements.
- Cryostat: Provides low-temperature conditions, essential for exploring resistivity and magneto-transport properties across a wide temperature range.
- Sample Chamber: Where the sample is placed for measurement. Both the current and voltage signals are controlled and monitored in this isolated environment.
- Lock-In Amplifier: Enhances the signal-to-noise ratio, ensuring precise voltage detection even in low-signal environments, a key feature when measuring minute changes in magneto-transport properties.
- Resistance Box (R_S): Regulates the current flowing through the sample.
- Preamplifier: Amplifies weak signals from the sample before sending them for measurement.
- Digital Multimeter: Measures current, voltage, and resistance with high precision, displaying the results on the monitor.
- Temperature Controller: Allows for the accurate regulation of temperature, ensuring that resistivity and transport data can be recorded across a wide range of temperatures.

Temperature-dependent resistivity measurements between 4 and 300 K were conducted using the oxford resistivity setup [Fig. 2.7(c)-(d)]. For field- and temperature-dependent resistivity, the Quantum Design PPMS [Fig. 2.7(b)] with the ETO option was utilized, providing a magnetic field range of up to 9 T and temperatures from 2 to 300 K.

2.5 Specific Heat Measurements

Specific heat measurement is crucial for investigating the bulk nature of phase transitions in materials. It typically exhibits anomalies at phase transition temperatures, making it an invaluable tool for characterizing such transitions. The total specific heat (C) in solids can be expressed as:

$$C = C_{\mathrm{el}} + C_{\mathrm{ph}} + C_{\mathrm{mag}}, \tag{2.5}$$

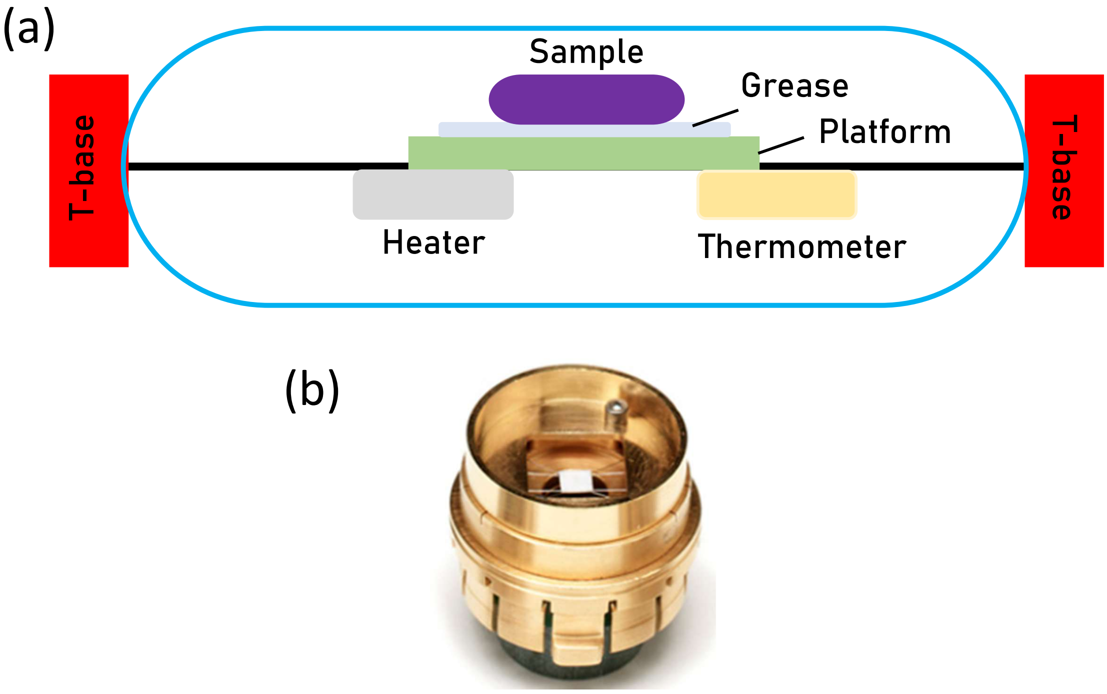

Figure 2.8: (a) Schematic representation of the specific heat measurement setup in a Quantum Design PPMS. (b) The specific heat puck used in the PPMS, designed for precise thermal relaxation measurements.

where C_{el}, C_{ph}, and C_{mag} represent the electronic, phononic, and magnetic contributions, respectively. The temperature-dependent behavior of specific heat is often described using the Debye and Einstein models of lattice vibrations.

In the Quantum Design PPMS, specific heat is measured by mounting the sample onto a specialized platform and analyzing its thermal response using a thermal relaxation method. The measurement process is outlined below, as show in Fig.2.8.

Sample Mounting and Thermal Contact

The sample is mounted on the measurement platform using a thin layer of Apiezon-N grease. This grease ensures effective thermal contact between the sample and the platform, allowing for efficient heat transfer during the measurement process.

Platform Components

The measurement platform is equipped with several key components:

- **Heater:** Provides a controlled, known amount of heat to the platform and sample.
- **Thermometer:** Monitors the temperature changes of the sample during both the heating and cooling phases.

The platform is suspended by thin wires that serve dual purposes:

- **Thermal Isolation:** These wires minimize heat loss to the surrounding environment, ensuring accurate measurement of heat changes within the system.
- **Electrical Connectivity:** They provide electrical connections between the heater, thermometer, and the PPMS control system.

Vacuum Environment

The specific heat measurement is conducted under vacuum conditions to minimize heat transfer through convection and reduce thermal losses. This setup improves the accuracy and sensitivity of the measurements.

Thermal Relaxation Method

The thermal relaxation method consists of two distinct phases:

- **Heating Phase:** A constant, precisely known amount of heat is supplied to both the platform and the sample, causing their temperatures to rise.
- **Relaxation Phase:** After the heat input stops, the sample and platform undergo cooling. The cooling process follows an exponential decay curve, characterized by a thermal relaxation time constant.

Using the thermal relaxation time constant and the known heat input, the specific heat (C_p) of the sample can be determined. To enhance measurement accuracy, the heat capacity of the platform and Apiezon-N grease (referred to as "addenda") is measured separately and subtracted from the total heat capacity of the system.

References

[1] Shubham Purwar, T. K. Bhowmik, S. Ghorai, T. Setti, $3d$ ising type magnetic interactions stabilized by the extremely large uniaxial magnetocrystalline anisotropy in layered ferromagnetic Cr_2Te_3, Materials Today Physics 46 (2024) 101522.

[2] Shubham Purwar, A. Low, A. Bose, A. Narayan, T. Setti, Investigation of the anomalous and topological hall effects in layered monoclinic ferromagnet $Cr_{2.76}Te_4$, Physical Review Materials 7 (2023) 094204.

[3] Shubham Purwar, T. K. Bhowmik, R. T. Mandar, A. Gorai, B. L. Chittari, T. Setti, Experimental and computational insights into the magnetic anisotropy and magnetic behaviour of layered room-temperature ferromagnet $Cr_{1.38}Te_2$, Physica Scripta 99 (2024) 085949.

[4] Shubham Purwar, S. Changdar, S. Ghosh, T. K. Bhowmik, T. Setti, Intricate magnetic interactions and topological hall effect observed in itinerant room-temperature layered ferromagnet $Cr_{0.83}Te$, Acta Materialia 271 (2024) 119898.

[5] Shubham Purwar, A. Bose, A. Low, S. Singh, R. Venkatesh, A. Narayan, T. Setti, $Sn_{0.06}Cr_3Te_4$: A skyrmion superconductor, Applied Materials Today 39 (2024) 102328.

[6] P. C. Canfield, Z. Fisk, Growth of single crystals from metallic fluxes, Philosophical magazine B 65 (1992) 1117–1123.

[7] C. A. Juillerat, V. V. Klepov, G. Morrison, K. A. Pace, H.-C. Zur Loye, Flux crystal growth: a versatile technique to reveal the crystal chemistry of complex uranium oxides, Dalton Transactions 48 (2019) 3162–3181.

[8] J.-Q. Yan, S. Nandi, B. Saparov, P. Čermák, Y. Xiao, Y. Su, W. T. Jin, A. Schneidewind, T. Brückel, R. W. McCallum, T. A. Lograsso, B. C. Sales, D. G. Mandrus, Magnetic and structural transitions in $La_{0.4}Na_{0.6}Fe_2As_2$ single crystals, Phys. Rev. B 91 (2015) 024501.

[9] J. Kim, H. Kim, H.-W. J. Kim, S. Park, J.-K. Kim, J. Kwon, J. Kim, H. W. Seo, J. S. Kim, B. J. Kim, Single crystal growth of iridates without platinum impurities, Phys. Rev. Mater. 6 (2022) 103401.

[10] P. Schmidt, M. Binnewies, R. Glaum, M. Schmidt, Chemical vapor transport reactions–methods, materials, modeling, Advanced Topics on Crystal Growth (2013) 227–305.

[11] A. Ubaldini, J. Jacimovic, N. Ubrig, E. Giannini, Chloride-driven chemical vapor transport method for crystal growth of transition metal dichalcogenides, Crystal Growth & Design 13 (2013) 4453–4459.

[12] W. H. Bragg, W. L. Bragg, The reflection of x-rays by crystals, Proceedings of the Royal Society of London. Series A, Containing Papers of a Mathematical and Physical Character 88 (1913) 428–438.

[13] I. Madsen, R. Hill, Effect of divergence and receiving slit dimensions on peak profile parameters in rietveld analysis of x-ray diffractometer data, Journal of applied crystallography 21 (1988) 398–405.

[14] A. Förster, S. Brandstetter, C. Schulze-Briese, Transforming x-ray detection with hybrid photon counting detectors, Philosophical Transactions of the Royal Society A 377 (2019) 20180241.

[15] B. I. Bleaney, B. I. Bleaney, B. Bleaney, Electricity and Magnetism, Volume 2, volume 2, Oxford University Press (UK), 2013.

[16] L. J. van der PAUW, A method of measuring specific resistivity and Hall effect of discs of arbitrary shape, pp. 174–182.

Chapter 3

3D-Ising-type Magnetic Interactions Stabilized by the Extremely Large Uniaxial Magnetocrystalline Anisotropy in Layered Ferromagnetic Cr_2Te_3

3.1 Introduction

The discovery of intrinsic long-range ferromagnetism in two-dimensional (2D) layered materials has ignited considerable research interest due to their potential technological applications in low-power spintronic devices [1–6]. On the other hand, the Mermin-Wagner theorem proposes certain limitations to have long-range ferromagnetic interactions in the 2D magnets due to thermal fluctuations at finite temperatures [7]. In this regard, the magnetocrystalline anisotropy energy (MAE) becomes crucial to overcome the thermal fluctuations and for the realization of 2D long-range ferromagnetism in layered materials. Recent investigations have focused on enhancing the long-range magnetic ordering in several 2D layered magnets such as CrI_3 [8], $Cr_2Ge_2Te_6$ [9], and $Cr_2Si_2Te_6$ [10]. Nevertheless, the peculiar magnetic behavior observed in chromium-based tellurides (Cr_xTe_y) have drawn significant research attention [11–13].

Under different synthesis conditions and chromium concentrations, Cr_xTe_y exhibits diverse crystal structures owing to the Cr vacancies. For instance, CrTe, Cr_5Te_6, and Cr_7Te_8 exhibit hexagonal crystal structure [14–16], Cr_3Te_4 and Cr_5Te_8 show monoclinic phase [17–19], and Cr_2Te_3 and $CrTe_2$ show trigonal crystal structure [20, 21]. Thus, the

---

This chapter is based on the publication: **Shubham Purwar et al., Materials Today Physics, 46, 101522 (2024)** crystal structure of $\mathrm{Cr}_x\mathrm{Te}_y$ is highly sensitive to the Cr concentration present in the system, *viz.* $\mathrm{Cr_5Te_8}$ shows monoclinic phase for 38.5 - 40.4 % of Cr, while it shows trigonal structure for 38 - 37.5 % of Cr [22]. Moreover, the Cr concentration significantly affects the magnetic properties as well. Though most of the $\mathrm{Cr}_x\mathrm{Te}_y$ systems show ferromagnetic (FM) ordering, $\mathrm{CrTe_3}$ ($\mathrm{Cr_{0.67}Te_2}$) exhibits an antiferromagnetic ordering [23], their Curie temperatures are highly sensitive to the Cr concentration. For instance, $\mathrm{Cr_5Te_8}$ ($\mathrm{Cr_{1.25}Te_2}$) shows FM order below $T_C \approx 230$ K [13, 24], $\mathrm{Cr_3Te_4}$ ($\mathrm{Cr_{1.5}Te_2}$) shows FM order below $T_C \approx 316$ K [17], $\mathrm{Cr_7Te_8}$ ($\mathrm{Cr_{1.75}Te_2}$) shows FM order below $T_C \approx 361$ K [14], $\mathrm{CrTe_2}$ shows FM order below $T_C \approx 310$ K [20], and $\mathrm{Cr_2Te_3}$ ($\mathrm{Cr_{1.33}Te_2}$) shows FM order below $T_C \approx 180$ K [21]. Not only the Curie temperature, the magnetic exchange interactions below the Curie temperature are also sensitive to the Cr concentrations. For instance, below T_C, $\mathrm{Cr_5Te_8}$ shows 3D-Ising type magnetic interactions, $\mathrm{Cr_4Te_5}$ shows 3D-Heisenberg type magnetic interactions [11], and CrTe shows quasi-2D-Heisenberg type magnetic interactions [16].

Although the ground state magnetism of $\mathrm{Cr_2Te_3}$ single crystals has been discussed earlier [25], no study is available on $\mathrm{Cr_2Te_3}$ discussing the magnetic exchange interactions across the Curie temperature. Furthermore, $\mathrm{Cr_2Te_3}$ thin films have exhibited an anomalous Hall effect [26, 27], while the topological Hall effect has been observed in hetero-junction devices [28]. Thus, a better understanding of the magnetic interactions in $\mathrm{Cr_2Te_3}$ is crucial to unravel the potential technological applications of these systems.

In this contribution, we discuss the magnetocrystalline anisotropy, critical behavior, and magnetocaloric effect in $\mathrm{Cr_2Te_3}$. The critical behavior around the Curie temperature (T_C) has been studied using various techniques such as the modified Arrott plot (MAP), the Kouvel-Fisher method (KF), and critical isothermal analysis (CI). Interestingly, the derived critical exponents $\beta = 0.353(4)$ and $\gamma = 1.213(5)$ suggest complex magnetic interactions falling in between the 3D Ising and 3D Heisenberg models across the T_C. On the other hand, the renormalization group theory suggests 3D-Ising type magnetic interactions stabilized by the extremely large magnetocrystalline anisotropy. We performed first-principles calculations to establish the origin of extremely large out-of-plane magnetic anisotropy. Our calculations predict a noncollinear ferromagnetic phase with a canted spin structure that results from the magnetic frustration [29], in the ground state with dominant ferromagnetic ordering along the *c*-axis, while an antiferromagnetic ordering is found in the *ab*-plane, leading to extremely large magnetocrystalline anisotropy. Further, a maximum entropy change of $-\Delta S_M^{max} \approx 2.08\ J/kg-K$ is estimated around T_C for the fields applied parallel to the *c*-axis.

3.2 Experimental and First-principles Calculation Details

High-quality single crystals of Cr_2Te_3 were grown using the chemical vapor transport (CVT) technique by taking 3 : 4 molar ratio of Chromium (Cr, 99.99%, Alfa Aesar) and Tellurium (Te, 99.999%, Alfa Aesar) powders and employing iodine as the transport agent. The growth process involved a three-week thermal heat treatment in a two-zone horizontal tube furnace, with the source-zone maintained at 1000 °C and the growth-zone kept at 820 °C [30]. The as-grown single crystals, sized 3×2 mm^2, were looking shiny and flat [see the inset of Fig. 3.1(c)]. Surface morphology and elemental compositions were studied by using the scanning electron microscope (SEM) and energy dispersive x-ray spectroscopy (EDXS). We find that the as-prepared single crystals have a Cr to Te ratio of 0.663(6):1, leading to the exact chemical formula of $Cr_{1.99}Te_3$. Powder x-ray diffraction (XRD) analysis was conducted using a Rigaku X-ray diffractometer (SmartLab, 9kW) with Cu K_α radiation (wavelength = 1.5406 Å). Magnetic properties studies, $M(T)$ and $M(H)$, were performed using the physical property measurement system (PPMS, 9 Tesla DynaCool, Quantum Design). The magnetization isotherms $M(H)$ were systematically measured with 2 K interval around the Curie temperature to facilitate the critical behavior analysis.

Density functional theory (DFT) calculations on Cr_2Te_3 were performed using the generalized gradient approximation (GGA) of Perdew, Burke and Ernzerhof (PBE) exchange and correlation functionals [31] as implemented in the Quantum Espresso (QE) simulation package [32]. Brillouin zone sampling was done over a $12\times12\times6$ Monkhorst-Pack k-grid. The electronic wave function is expanded using the plane waves up to a cutoff energy of 40 Ry. To accurately determine the spin moment distribution, our approach involved incorporating scalar-relativistic and relativistic pseudopotentials to account the within the self-consistent field (SCF) calculations. We explored both collinear and non-collinear spin structures, the latter involving optimization of the spin angle with respect to the energy.

3.3 Results and Discussion

3.3.1 Structural analysis

The unit cell of Cr_2Te_3 is schematically shown in the top-panel of Fig. 3.1(a), in which distinct chromium atoms are labeled by Cr(1), Cr(2), and Cr(3). The intercalated Cr(1) atoms reside within the van der Waals gap created by two $CrTe_2$ layers, exhibiting ordered vacancies. Cr(2) and Cr(3) are within the $CrTe_2$ layers, but only Cr(3) has the nearest neighboring Cr(1) atoms along the c-axis. On the other hand, Cr(1) has two Cr(3) nearest

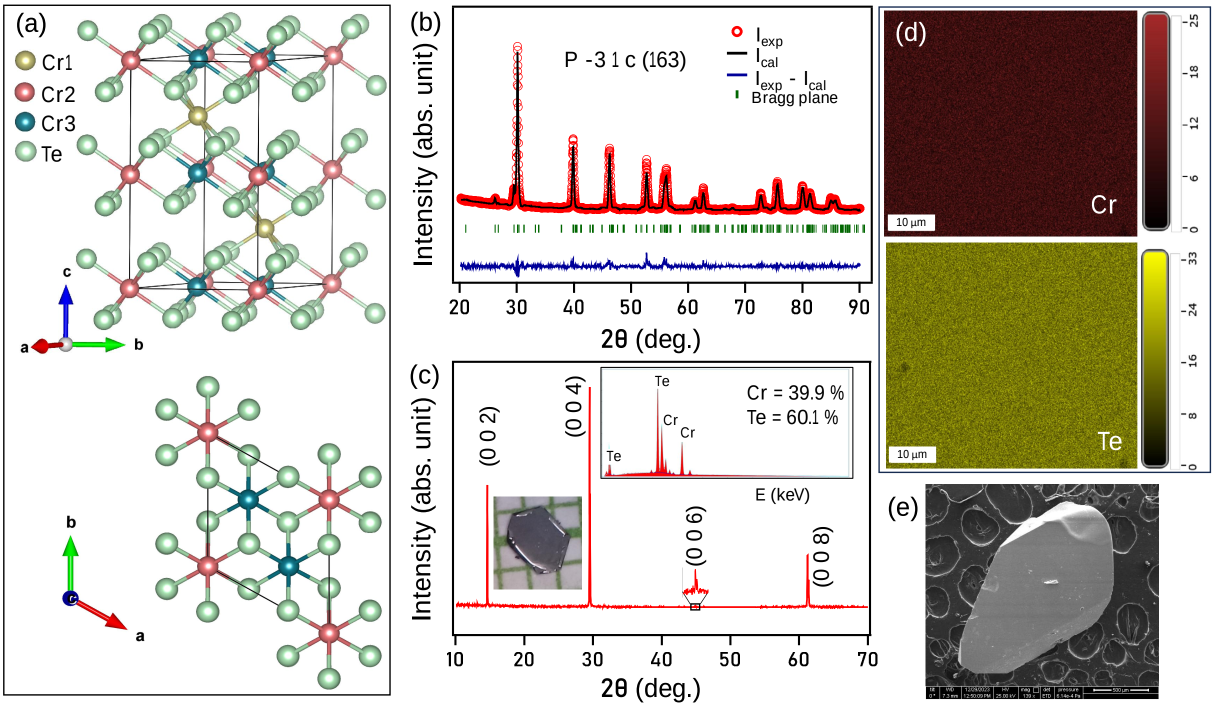

Figure 3.1: (a) Schematic representations of the Cr_2Te_3 crystal structure, obtained from the Rietveld refinement. (b) XRD pattern of Cr_2Te_3 crushed crystals measured at 300 K overlapped with the Rietveld refinement. (c) XRD pattern of Cr_2Te_3 single crystal. Insets in (c) show EDXS data demonstrating the actual chemical composition of as-prepared crystals and the photographic image of a typical Cr_2Te_3 single crystal. (d) Elemental mapping of Cr_2Te_3 for Cr and Te using EDXS. (e) Scanning electron microscopic (SEM) image of Cr_2Te_3 single crystal.

neighbours along the c-axis but has no nearest neighbors in the ab-plane. The bottom-panel of Fig. 3.1(a) depicts projected crystal structure of Cr_2Te_3 onto the ab-plane, showing the intertwined honeycomb lattice with Cr(2), Cr(3), and Te atoms. Fig. 3.1(b) displays the X-ray diffraction (XRD) pattern of the crushed single crystals measured at room temperature. The XRD data confirms the trigonal crystal structure of Cr_2Te_3 having the space group of $P\bar{3}1c$ (163). The derived lattice parameters using the Rietveld refinement, $a = b = 6.7989(7)$ Å, $c = 12.1074(7)$ Å, and the angles $\alpha = \beta = 90°$, $\gamma = 120°$, are close to the previous reports [33, 22, 18]. Fig. 3.1(c) displays the XRD pattern taken on the Cr_2Te_3 single crystal, indicating that the crystal growth is parallel to the $(00l)$ Bragg's plane. Using the Rietveld refinement, bond lengths of Cr_1-Cr_3, Cr_2-Cr_3, Cr_2-Cr_2, and Cr_3-Cr_3 are determined as 3.0269 Å, 3.9254 Å, 6.7990 Å, and 3.9254 Å, respectively. Additionally, the bond angles of Cr_2-Te_1-Cr_3, Cr_1-Te_1-Cr_2, and Cr_1-Te_1-Cr_3 are found as 91.213°, 129.596°, and 67.542°, respectively. Fig. 3.1(d) exhibits the elemental mapping of Cr and Te, confirming the uniform chemical composition of the studied crystal within the measured surface range of $50{\times}45\ (\mu m)^2$. Fig. 3.1(e) shows scanning electron microscopy (SEM) image of Cr_2Te_3, displaying a very flat surface morphology. Thus, the EDXS and SEM data confirm the homogeneity and high-quality of the studied single crystals.

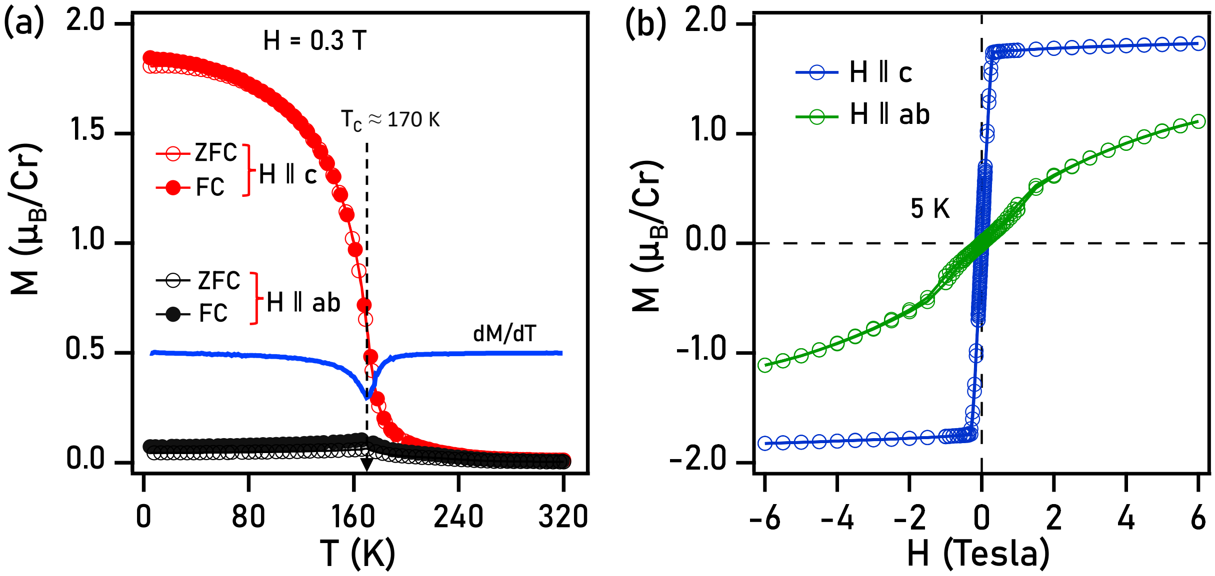

Figure 3.2: (a) Temperature-dependent magnetization $M(T)$ measured for $H \parallel c$ and $H \parallel ab$ in the ZFC and FC modes under an applied of H =0.3 T. In (a), the blue-curve displays first derivative of magnetization with respect to temperature, $\frac{dM}{dT}$, showing a dip at the $T_C \approx 170$ K. (b) Magnetization isotherms $[M(H)]$ measured at 5 K for $H \parallel c$ and $H \parallel ab$ orientations.

3.3.2 Magnetic Properties

Temperature-dependent magnetization $[M(T)]$ of Cr_2Te_3 measured at $H = 0.3$ T for both the $H \parallel c$ and $H \parallel ab$ orientations are shown in Fig. 3.2(a) taken in field-cooled (FC) and zero-field-cooled (ZFC) modes. From Fig. 3.2(a), we observe a ferromagnetic-like magnetic transition at around $T_C \approx 170$ K. The same is confirmed from the overlapped dM/dT data in which a dip is noticed at around 170 K. Most interestingly, we observe an out-of-plane ($H \parallel c$) saturation magnetization (1.8 μ_B/Cr) that is almost 20 times higher than the in-plane ($H \parallel ab$) saturation magnetization (0.08 μ_B/Cr), indicating an extremely large magnetic anisotropy in this system with an easy-axis of magnetization parallel to the c-axis. To further confirm the magnetic anisotropy, we measured magnetization as a function of the field $[M(H)]$ for both orientations as shown in Fig. 3.2(b) at 5 K of the sample temperature. From Fig. 3.2(b), we clearly notice a spontaneous magnetization of 1.8 μ_B/Cr for $H \parallel c$ around the zero applied field with negligible coercivity, suggesting Cr_2Te_3 to be an out-of-plane soft-ferromagnet. On the other hand, for $H \parallel ab$, the lower magnetic fields sustain a canted FM state between neighboring Cr(2) and Cr(3) atoms.

We performed density functional theory (DFT) calculations to reveal the ground state magnetic structure of Cr_2Te_3. Initially we focused on examining the magnetic coupling among various types of Cr atoms, including the collinear ferromagnetic (FM) and non-collinear FM configurations as shown in Figs. 3.3(a) and 3.3(b), respectively. The DFT calculations are done by including the spin-orbit coupling (SOC) effect. Our cal-

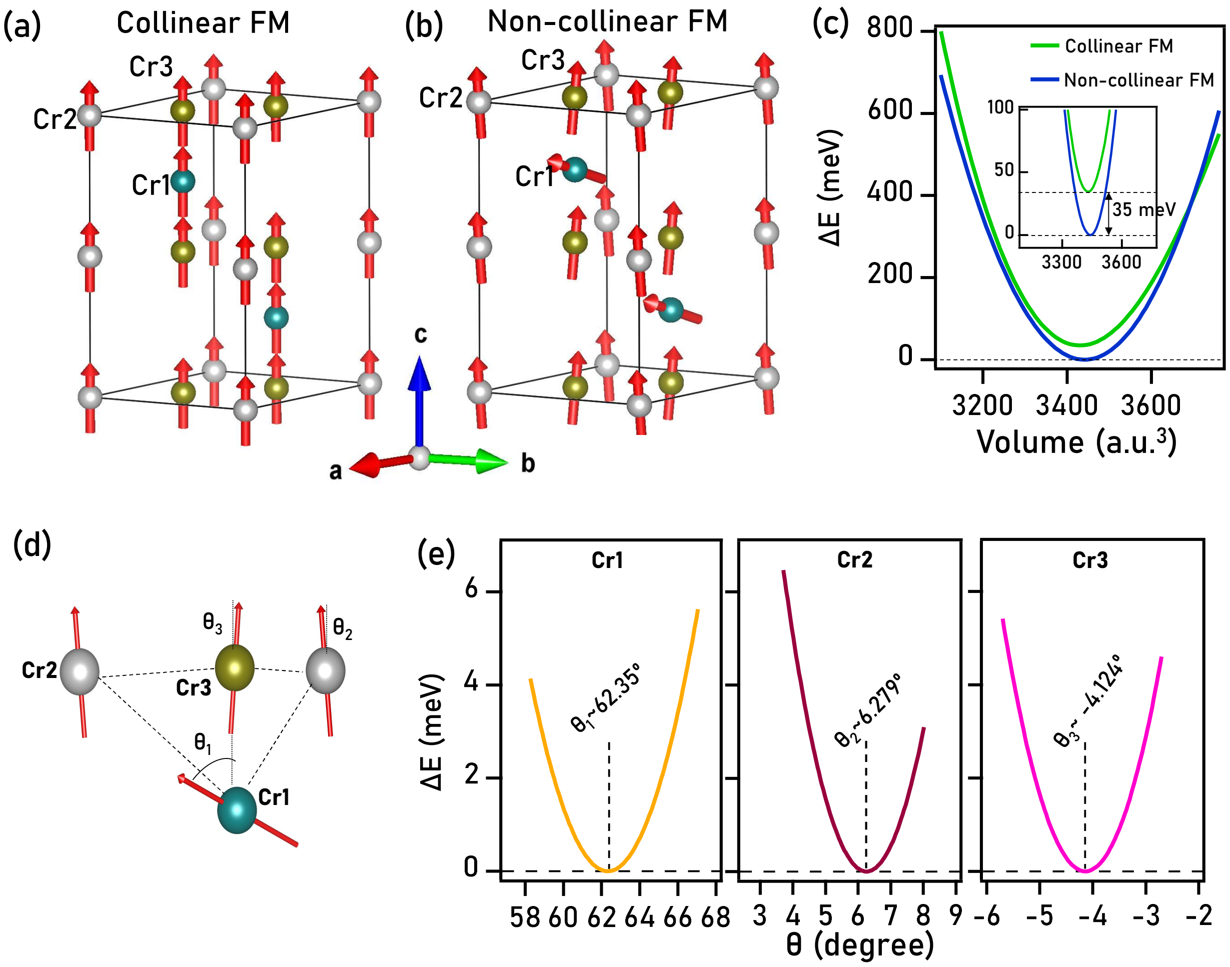

Figure 3.3: Schematic representations of the collinear ferromagnetic (FM) (a) and non-collinear ferromagnetic (b) configurations. (c) Relative total energy (ΔE), with respect to the ground state energy, plotted as a function of unit cell volume for both magnetic configurations, obtained using the DFT calculations. (d) Schematic diagram of the canting spin angles of Cr(1), Cr(2), and Cr(3) atoms with respect to the *c*-axis. (e) Relative total energy (ΔE), with respect to the ground state energy, plotted as a function of spin angles for Cr(1), Cr(2) and Cr(3) atoms.

culations suggest that the noncollinear ferromagnetic configuration [see Fig. 3.3(c)] has a lower ground state energy by about 35 meV compared to the collinear FM configuration, thus the former is a more stable magnetic ground state than the latter in Cr_2Te_3. Distinct spin canting angles were observed for Cr(1), Cr(2), and Cr(3) deviating from the *c*-axis as schematically shown in Fig. 3.3(d). This investigation suggests substantial difference in the canted spin angles, between the intercalated Cr(1) atoms and Cr(2) or Cr(3) of $CrTe_2$ layer [21]. Further, Cr(1) and Cr(2) display spin canting in the second quadrant, while Cr(3) exhibits spin canting in the first quadrant, as depicted in Fig. 3.3(d). Fig. 3.3(e) depicts the plots of relative total energy (ΔE) *vs.* spin canting angle, suggesting 62.35°, 6.279°, and -4.124° are the canted-spin angles of Cr(1), Cr(2), and Cr(3) atoms, respectively in the magnetic ground state. Therefore, the predicted canted angles indicate a dominant ferromagnetic ordering for the spins of Cr(2) & Cr(3) of $CrTe_2$ layer and a dominant antiferromagnetic ordering for the intercalated Cr(1) atoms. As a result, the noncollinear FM ground state in Cr_2Te_3 is stabilized by the magnetic frustration due to a competition between the in-plane AFM and the out-of-plane FM orders. These observations are consistent with predictions on similar systems [34, 21].

Next, with the help of magnetization isotherms [$M(H)$] measured at 5 K for both $H \parallel c$ and $H \parallel ab$ [see Fig. 3.4(a)], we qualitatively estimated the magnetocrystalline anisotropy energy (MAE) K_u in our studied Cr_2Te_3 sample by measuring the area (Yellow-shaded region) between $H \parallel c$ and $H \parallel ab$ curves, using the relation [19],

$$K_u = \mu_0 \int_0^{M_s} [H_c(M) - H_{ab}(M)] \, dM \tag{3.1}$$

Here, μ_0 is the vacuum permeability, M_s represents saturation magnetization. H_c and H_{ab} represent magnetic field applied along the out-of-plane and in-plane directions, respectively.

The derived value of $K_u = 2065$ kJ/m^3 in this method is found to be the highest ever known MAE from any Cr_xTe_y type systems. Moreover, this value is much larger than the K_u values reported on many other 2D magnetic systems such as $Cr_2Si_2Te_6$ / $Cr_2Ge_2Te_6$) ($\approx$ 65 kJ/m^3 / $\approx$20 kJ/m^3) [35], Fe_4GeTe_2 (250 kJ/m^3) [36], $CrBr_3$ / CrI_3 ($\approx$ 86 kJ/m^3 /$\approx$ 300 kJ/m^3) [37], and Fe_3GeTe_2 (1460 kJ/m^3) [38]. Thus, for the first-time we report an extremely large MAE from our studied Cr_2Te_3. Note here that we estimated the MAE value by linearly extrapolating the high-field region of the $M(H)$ data for $H \parallel ab$ [see Fig. 3.4(a)] to find the overlapping filed position (12.8 T) with $H \parallel c$. Therefore, the MAE value $K_u = 2065$ kJ/m^3 is the minimum value that we could estimate in this method. The actual K_u value would be higher than what we estimated, if one is able to perform $M(H)$ measurements at very high applied magnetic fields and find the overlapping field position directly from the measurements. Nevertheless, we could also estimate the magnetocrystalline anisotropy energy using the DFT calculations. In agreement with the experimental value, we find an extremely large MAE for the noncollinear FM state of 8230 kJ/m^3. Whereas for the collinear FM state we find realatively very low MAE of 32 kJ/m^3.

3.3.3 Itinerant Ferromagnetism

To identify the nature of ferromagnetism in Cr_2Te_3 we employed Takahashi's self-consistent renormalization (SCR) theory which takes into account the conservation of zero-point spin fluctuations and thermal spin fluctuations [39]. According to SCR theory, the magnetization M and the magnetic field H at T_C should obey the below relation,

$$M^4 = \frac{1}{4.671} \left[\frac{T_C^2}{T_A^3}\right] \left(\frac{H}{M}\right) \tag{3.2}$$

Here, T_A is the dispersion of the spin fluctuation spectrum in wave-vector space. T_A,

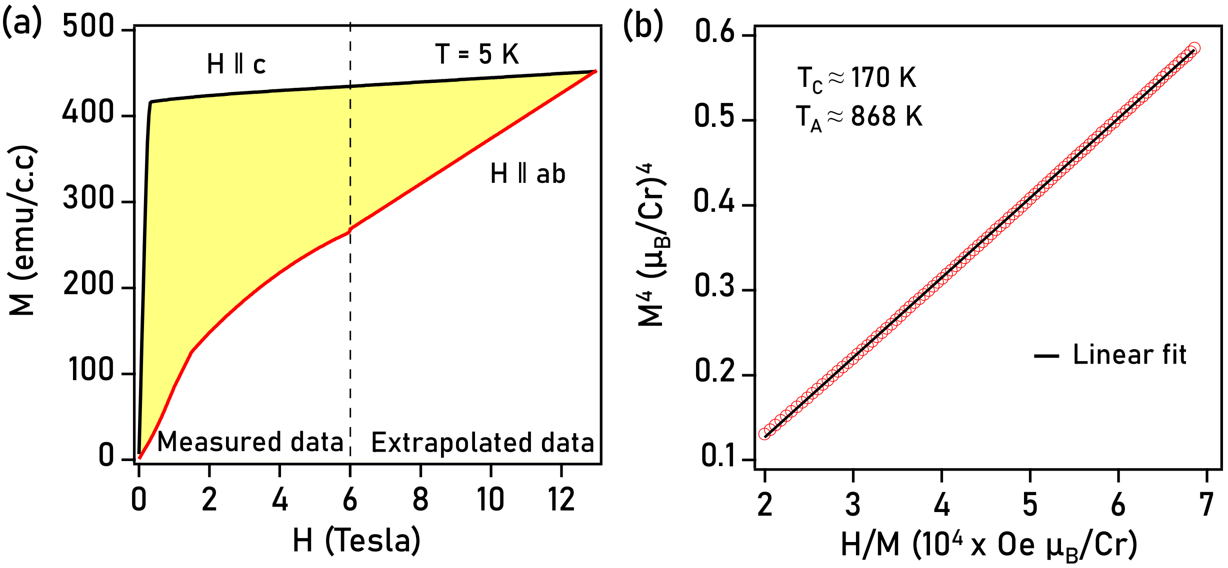

Figure 3.4: (a) Magnetization isotherms $[M(H)]$ measured at 5 K for $H \parallel c$ and $H \parallel ab$. The yellow shaded area represents the magnetocrystalline anisotropy energy (MAE). (b) Plot of M^4 *vs.* H/M

M, and H are in K, μ_B/Cr, and Oe units, respectively. Fig. 3.4(b) shows the plot of M^4 *vs.* H/M, fitted by Eq. 3.2. Such a linear behavior is observed in many itinerant ferromagnets such as MnSi [40], $LaCo_2P_2$ [41], SmCoAsO [42]. From the fitting of Eq. 3.2, we obtained a slope of 9.4778×10^{-6} $(\mu_B/\mathrm{Cr})^5$/Oe. Using the slope and $T_C \approx 170$ K, we derived $T_A \approx 868$ K for $H \parallel c$.

Further, following the SCR theory, T_C can be expressed by,

$$T_C = (60c)^{-3/4} P_S^{3/2} T_A^{3/4} T_0^{1/4} \tag{3.3}$$

Here, $c = 0.3353$, P_S is the spontaneous magnetization in μ_B/Cr, T_0 is the energy width of the dynamical spin fluctuation spectrum in K. Using the value of T_C, P_S, and T_A, we obtain the characteristic temperature $T_0 = 4502$ K for our Cr_2Te_3 single crystal. According to the SCR theory of spin fluctuation, the ratio T_C/T_0 is an important parameter as it characterizes the degree of localization or itineracy of the spin moment. The magnetic materials are found to exhibit itinerant character for $T_C/T_0 \ll 1$, while they show localized magnetism for $T_C/T_0 \approx 1$. In our case of Cr_2Te_3 single crystal, the ratio T_C/T_0 is estimated to be 0.04 which is much smaller than 1, indicating the itinerant nature of the ferromagnetism in Cr_2Te_3.

3.3.4 Critical Behaviour Analysis

Investigating the magnetic interactions across the paramagnetic to ferromagnetic transition involves the critical exponents analysis of magnetization isotherms $[M(H)]$ around T_C. The $M(H)$ data measured for $H \parallel c$ between 150 and 190 K with an interval of 2 K are depicted

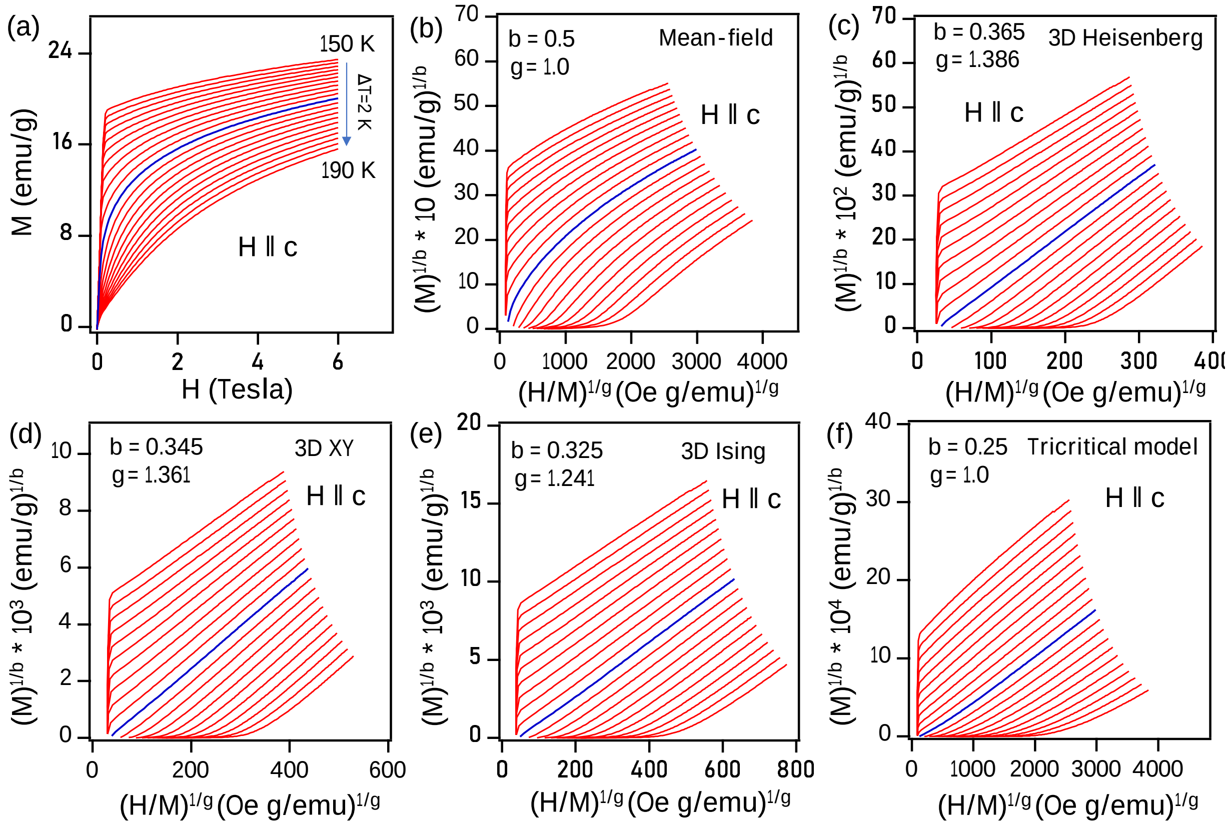

Figure 3.5: (a) Isothermal magnetization $M(H)$ measured between 150 and 190 K with an interval of 2 K for $H \parallel c$. (b) Arrott plots of M^2 *vs.* (H/M) for the Landau mean-field model. Modified Arrott plots of $\mathrm{M}^{1/\beta}$ *vs.* $(\mathrm{H/M})^{1/\gamma}$ for (c) 3D-Heisenberg model, (d) 3D-XY model, (e) 3D-Ising model, and (f) Tricritical mean-field model. In the figures, the blue-colored data is taken at the $T_C \approx 170$ K.

in Fig. 3.5(a). Fig. 3.5(b) shows Arrott plots of M^2 *vs.* (H/M) for the Landau mean-field model. Arrott plots typically display a positive slope of parallel lines in the high-field region, indicative of a second-order magnetic transition [43]. However, our findings show deviation from the linear behavior, particularly below T_C. This deviation suggests that the Landau mean-field theory $(\beta = 0.5, \gamma = 1)$ is not applicable to $\mathrm{Cr_2Te_3}$. Consequently, a modified Arrott plot (MAP) is necessary to determine the critical exponents by following the below equation,

$$(H/M)^{1/\gamma} = a * (T - T_c)/T_c + b * M^{1/\beta} \tag{3.4}$$

where (H/M) is the inverse susceptibility, M is the magnetization, T_C is Curie temperature, β and γ are the critical exponents, and a and b are constants.

Scaling hypothesis of the critical phenomena theory [44] suggests that the second-order phase transitions near T_C are governed by the critical exponents and magnetic equations of the state. The divergence of the correlation length around T_C, $\zeta = \zeta_0[(T - T_C)/T_C]^{-\nu}$, gives rise to universal scaling laws. This results in specific critical exponents β for spontaneous magnetization M_{sp} below T_C, γ for the inverse susceptibility χ_0^{-1} above

T_C, and δ for magnetization isotherms $M(H)$ at T_C which are mathematically represented in the magnetic equations involving these critical exponents,

$$M_{sp}(T) = M_0(-\epsilon)^{\beta} \text{ for } \epsilon < 0, T < T_C, \tag{3.5}$$

$$\chi_0^{-1}(T) = (h_0/m_0)\epsilon^{\gamma}, \text{ for } \epsilon > 0, T > T_C \tag{3.6}$$

$$M = DH^{1/\delta}, \text{ for } \epsilon = 0, T = T_C, \tag{3.7}$$

Table 3.1: Comparison of critical exponents of Cr_2Te_3 with similar 2D magnetic materials and different theoretical models.

Composition	Technique	T_c	β	γ	δ	Reference
Cr_2Te_3	MAP	170.21(1)	0.360(2)	1.221(3)	4.392(6)	This work
Cr_2Te_3	KF method	170.07(6)	0.353(4)	1.213(5)	4.436(2)	This work
Cr_2Te_3	Critical isotherm	170			4.275	This work
Theory	3D Ising		0.325	1.241	4.82	[45]
Theory	3D XY		0.345	1.316	4.81	[45]
Theory	3D Heisenberg		0.365	1.386	4.80	[45]
Theory	Landau mean-field		0.5	1	3	[43]
Theory	Tricritical		0.25	1	5	[46]
Cr_5Te_8	KF method	230.6(3)	0.315(7)	1.81(2)	6.35	[47]
Cr_3Te_4	KF method	320.335(5)	0.365(5)	1.212(9)	4.580(4)	[48]
Cr_4Te_5	KF method	319.06(9)	0.387(9)	1.2885(2)	4.32	[11]
Cr_5Te_6	KF method	338.17(1)	0.405(1)	1.200(1)	3.962(9)	[15]

where $\epsilon = (T - T_C)/T_C$ is the reduced temperature, M_0, h_0/m_0, and D are the critical amplitudes [49]. Attempts were made to derive the critical exponents and T_C through MAP technique by plotting $M^{1/\beta}$ *vs.* $(H/M)^{1/\gamma}$ based on various theoretical models around T_C such as the 3D-Heisenberg model, 3D-XY model, 3D-Ising model, and tricritical mean-field model [50, 45, 46] as shown in Figs. 3.5(c), 3.5(d), 3.5(e), and 3.5(f), respectively. However, none of these models produced the anticipated parallel lines. To further confirm that none of these models can adequately describe the magnetic interactions of this system, in Fig. 3.6 we plotted the normalized slopes (NS), $NS = S(T)/S(T_C)$, as a function of temperature at higher magnetic fields derived from the data shown in Figs. 3.5(b)-3.5(f) for various models. Here, $S(T)$ is the slope defined by $d(M^{1/\beta})/d((H/M)^{1/\gamma})$ at a given temperature T. For any adequate model, the normalized slopes should be equal to one [47, 48]. However, from Fig. 3.6 it is evident that none of the models show NS=1

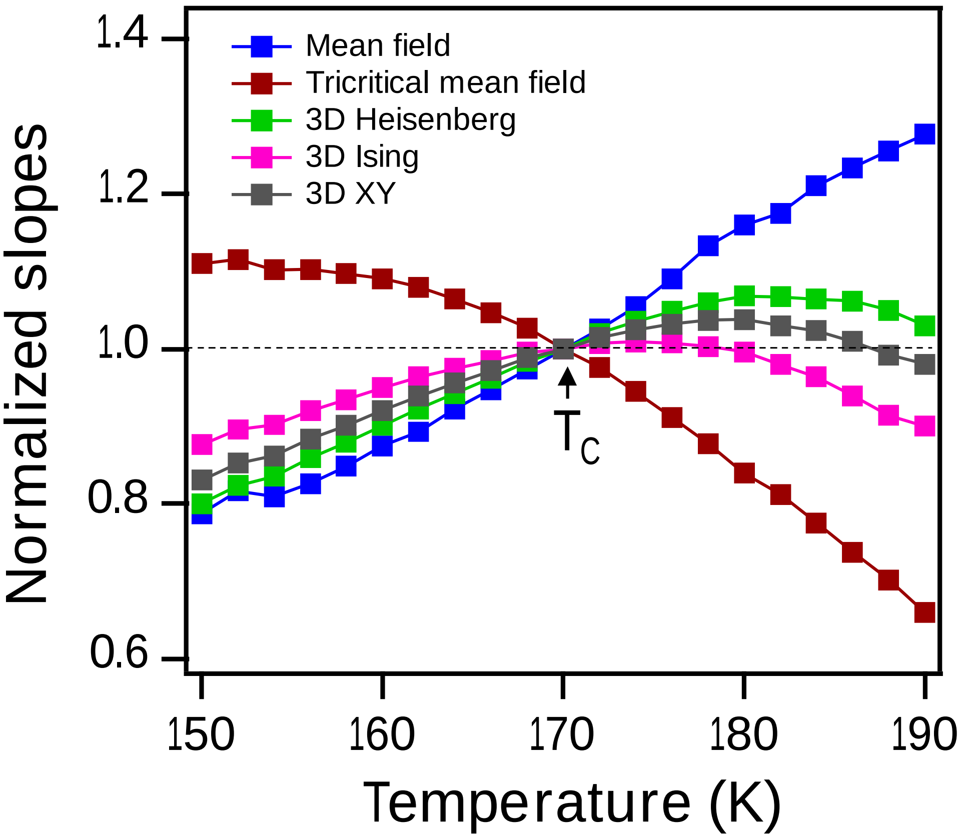

Figure 3.6: Temperature dependent normalized slopes [NS=S(T)/S(T_C)] plotted as a function of temperature, for various models, derived from the data shown in Figs. 3.5(b) - 3.5(f). See the text for more details.

at temperatures other than T_C. Therefore, none of the standard models, Landau mean-field, 3D-Heisenberg, 3D-XY, 3D-Ising, and tricritical mean-field model, can describe the magnetic interactions in Cr_2Te_3 precisely.

Thus, to accurately determine the critical exponents near T_C, an iterative modified Arrott plot (MAP) technique was employed on the data shown in Fig. 3.5(a) [51, 52]. In this method, we start with trial values of β and γ substituted into Eq. 3.4 to derive the MAP data as shown in Fig. 3.7(a). The linear extrapolation of the MAP data from the high field region provides $(M_{sp})^{1/\beta}$ and $(\chi_0^{-1})^{1/\gamma}$ as intercepts on the y and x-axis of the $(M)^{1/\beta}$ vs. $(H/M)^{1/\gamma}$ plot [see Fig. 3.7(a)]. As obtained M_{sp} and χ_0^{-1} are plotted as a function of temperature as shown in Fig. 3.7(c). Next, $M_{sp}(T)$ and $\chi_0^{-1}(T)$ are fitted using Eqs. 3.5 and 3.6 to determine new β and γ values. Using these updated β and γ exponents, a new MAP is created by plotting $(M)^{1/\beta}$ vs. $(H/M)^{1/\gamma}$. This procedure is iteratively repeated, involving fitting the modified Arrott plots, updating the polynomials (Eqs. 3.5 and 3.6), and recalculating the exponents, until the values of β and γ converge ($\beta_{n+1} \to \beta_n$ and $\gamma_{n+1} \to \gamma_n$, here n is the iteration number). After this iterative exercise, Fig. 3.7(a) shows parallel straight lines with $\beta = 0.367$ and $\gamma = 1.263$ in which the straight line corresponding to the T_C passes through the origin. Further, from the converged MAP,

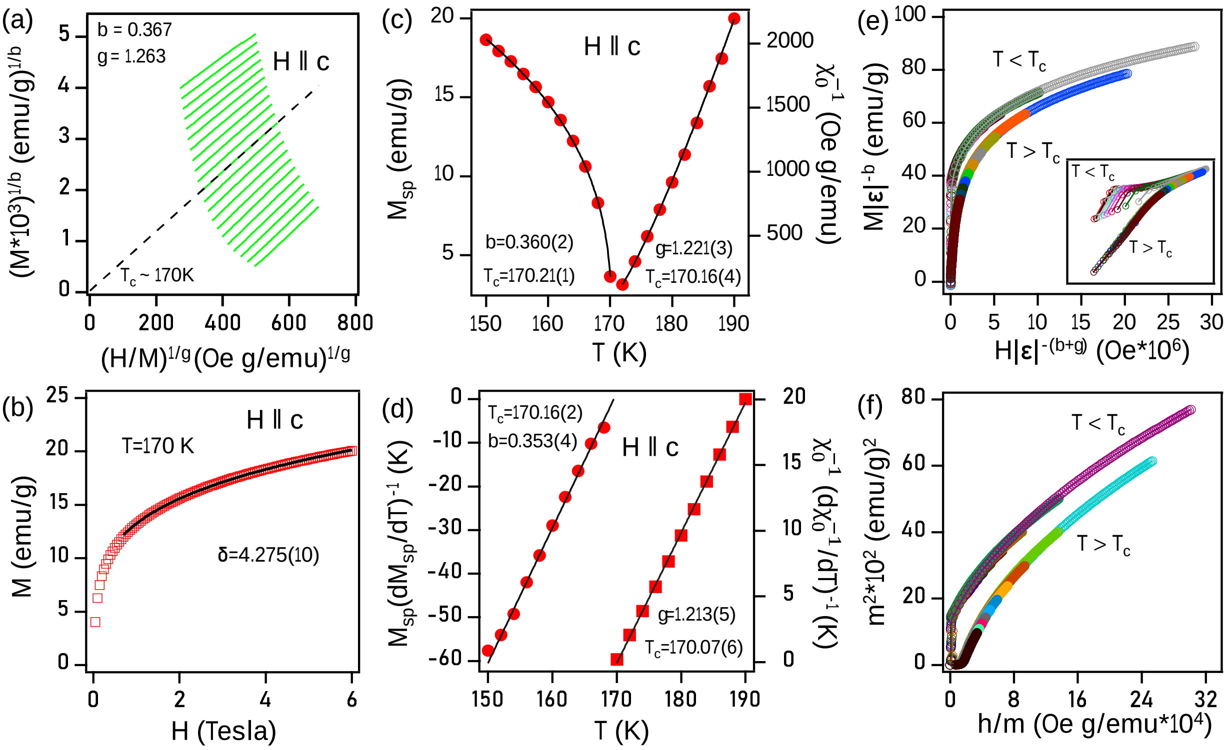

Figure 3.7: (a) Modified Arrott plot (MAP) of $M^{1/\beta}$ *vs.* $(H/M)^{1/\gamma}$ at high-field regions with critical exponents, $\beta = 0.367$ and $\gamma = 1.263$. (b) Isothermal magnetization $M(H)$ data taken at $T_C = 170$ K (c) Temperature dependent spontaneous magnetization $M_{sp}(T)$ (left axis) and inverse initial susceptibility $\chi_0^{-1}(T)$ (right axis). (d) Kouvel-Fisher plot: temperature dependence of $M_{sp}(T)[dM_{sp}(T)/dT]^{-1}$ (left axis) and $\chi_0^{-1}(T)[d\chi_0^{-1}(T)/dT]^{-1}$ (right axis). (e) Scaling plot of normalized magnetization vs. normalized field. (f) Renormalized magnetization (m) and field (h) are plotted in the form of m^2 *vs.* h/m below and above T_C. Inset in (e) shows the same plot of (e) in log-log scale.

the $M_{sp}(T)$ and $\chi_0^{-1}(T)$ are plotted in Fig. 3.7(c) from which the fittings with Eqs. 3.5 and 3.6 derive the critical exponents $\beta = 0.360(2)$ with $T_C = 170.21(1)$ K and $\gamma = 1.221(3)$ with $T_C = 170.16(4)$ K. These T_C values closely match the T_C of 170 K estimated from $M(T)$ data [see Fig. 3.2(a)].

To verify the accuracy and reliability of the critical exponents determined by the modified Arrott plot method, we employed the Kouvel-Fisher (KF) method [53], using the equations,

$$M_{sp}(T)[dM_{sp}(T)/dT]^{-1} = (T - T_C)/\beta, \tag{3.8}$$

$$\chi_0^{-1}(T)[d\chi_0^{-1}(T)/dT]^{-1} = (T - T_C)/\gamma, \tag{3.9}$$

Thus, Fig. 3.7(d) exhibits KF plots fitted using the Eqs. 3.8 and 3.9 both below and above T_C. In this way, we obatined the critical exponents $\beta = 0.353(4)$ with $T_C = 170.16(2)$ K and $\gamma = 1.213(5)$ with $T_C = 170.07(6)$ K, respectively. Notably, these values are very close to the critical exponents obtained from the MAP method, affirming the reliability, self-consistency, and intrinsic nature of the critical exponents. Furthermore, using the Widom scaling relation, $\delta = 1 + (\gamma/\beta)$ [54], we estimate $\delta = 4.392(6)$ and $\delta = 4.436(2)$ from the MAP and KF plots, respectively. Crucially, these δ values, obtained from different methods converge to $\delta = 4.275(10)$ derived through the critical isotherm (CI) method using Eq. 3.7 [see Fig. 3.7(b)]. The experimentally derived critical exponents are summarized in Table 6.1 along with critical exponents of different theoretical models and other $\mathrm{Cr}_x\mathrm{Te}_y$ systems.

Further, in the critical asymptotic region of magnetic materials, the scaling equation of magnetic state is expressed by [44],

$$M(H, \epsilon) = \epsilon^{\beta} f_{\pm}(H/\epsilon^{\beta+\gamma}) \tag{3.10}$$

This equation can also be expressed as,

$$m = f_{\pm}(h) \tag{3.11}$$

where $m = \epsilon^{-\beta} M(H, \epsilon)$ denotes the normalized magnetization and $h = H\epsilon^{-(\beta+\gamma)}$ represents the normalized field. When the values of β and γ obtained from both the MAP and KF methods are accurately chosen, the scaled magnetization m and h are expected to mainly fall into to two distinct branches of universal curves outlined by the Eqs. 3.10 and 3.11. These branches correspond to temperatures below and above T_C as evident in Figs. 3.7(e) and 3.7(f).

The compiled critical exponents in Table 6.1, compared with theoretical predictions across various models, reveal complex magnetic interactions across the Curie temperature in $\mathrm{Cr_2Te_3}$. Specifically, the value of β $(T < T_C)$ obtained from the MAP technique is very close to the 3D-Heisenberg type interactions, while the value of γ $(T > T_C)$ is very close to the 3D-Ising type interactions. However, the value of δ obtained at T_C does not fall into any of the existing standard models of 3D-Heisenberg, 3D-XY, or 3D-Ising (See Table 6.1). The deviation of the magnetic interactions may stem from various factors such as long-range Ruderman-Kittel-Kasuya-Yosida (RKKY) interactions [45], extended interactions beyond nearest neighbors [55], dipole-dipole interaction [56], or strong magnetocrystalline

Table 3.2: Obtained critical parameters from renormalization group theory

{d : n}	γ	β	σ	δ
{3 : 1}	1.213	0.362	1.888	4.395
{3 : 2}	1.213	0.395	1.827	4.116
{3 : 3}	1.213	0.415	1.791	3.964

anisotropy (MAE) [57–59]. Thus, it is necessary to understand the range of magnetic interactions and spin dimensionality of Cr_2Te_3. For a homogeneous magnet, the magnetic phase transition's universality class depends on the exchange interaction $J(r)$ and following the renormalization group (RG) theory the interactions decay with distance as $J(r) = r^{-(d+\sigma)}$. Here, d is the spacial dimensionality and σ is a positive constant. The relation between the critical exponent γ and σ can be expressed by [49, 60],

$$\begin{aligned}\gamma = 1 + \frac{4}{d}\frac{(n+2)}{(n+8)}\Delta\sigma + \frac{8(n-4)(n+2)}{(n+8)^2 d^2} \\ * [\frac{2(7n+20)G(d/2)}{(n+8)(n-4)} + 1]\Delta\sigma^2\end{aligned} \tag{3.12}$$

where $\Delta\sigma = \sigma - d/2$, $G(d/2) = 3 - 0.25 * (d/2)^2$. n and d are the spin and spatial dimensionality of the system [60]. For $\sigma > 2$, the short-range Heisenberg model is valid for describing a 3D-isotropic magnet with magnetic interactions $J(r)$ decaying faster than r^{-5}. Conversely, for $\sigma \leq 3/2$, the system follows the long-range mean-field model with magnetic interactions $J(r)$ decaying slower than $r^{-4.5}$ [61]. For $3/2 \leq \sigma \leq 2$ the system falls into a distinct category characterized by the critical exponents that vary according to the specific value of σ. According to Eq. 3.12, it is found that $\{d : n\} = \{3 : 1\}$ and $\gamma = 1.213$ give the critical exponents $\beta = 0.362$, $\sigma = 1.89$, and $\delta = 4.395$ which are close to our experimental observations. The other exponents (ν, α, γ) can be derived from the following scaling equations, $\nu = \gamma/\sigma$, $\alpha = 2-\nu*d$, $\beta = (2-\alpha-\gamma)/2$, where ν and α are the exponents of correlation length. This is done for various sets of $\{d : n\}$ values, as shown in Table 6.2. Thus, the exchange interactions in Cr_2Te_3 decay as $J(r) = r^{-(d+\sigma)} = r^{-4.89}$. The spin dimensionality $n = 1$ and the spacial dimensionality $d = 3$ as derived from the RG theory suggests 3D-Ising type magnetic interactions, stabilized by the robust uniaxial anisotropy present in the system. This behavior mirrors the observations in other Cr_xTe_y systems [47, 62]. Therefore, in Cr_2Te_3 the magnetism primarily arises from the intralayer coupling [63], as evidenced by the 3.9254 Å bond length between adjacent Cr atoms within the plane, indicative of a relatively weak direct exchange interaction [25]. Moreover, the Cr2-Te1-Cr3 bond angle within the layer, measuring approximately 91.213°, indicates super-exchange interactions that favor ferromagnetism [64, 65]. Further the strong hybridization between Cr $3d$ and Te $5p$ orbitals potentially establishes an indirect exchange between the Cr moments mediated by neighboring Te atoms [66].

Finally, before concluding this section, we would like to mention that during the course of our manuscript preparation a preprint discussing the magnetocrystalline anisotropy and magnetic interactions of $Cr_{1.77}Te_3$ (claimed as Cr_2Te_3) single crystals has appeared [67]. Though, our results of out-of-plane magnetization matches well with the Ref. [67], the in-plane magnetization is slightly different. Moreover, based on the magnetocaloric effect

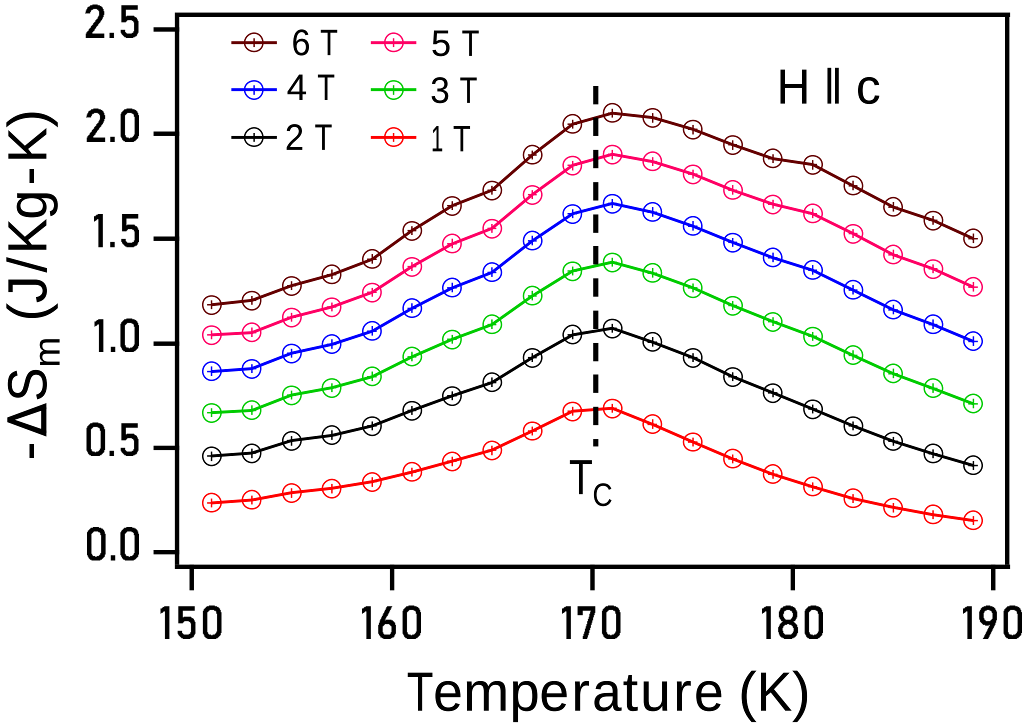

Figure 3.8: Temperature dependent magnetic entropy change -ΔS_m at different applied magnetic fields.

(MCE) analysis, Ref. [67] suggests a 2D-Ising type magnetic interactions in their studied composition of $Cr_{1.77}Te_3$ despite the experimentally obtained $\beta = 0.2435$ and $\gamma = 1.6509$ are quite far from the theoretically predicted values ($\beta = 0.125$ and $\gamma = 1.75$) for a 2D-Ising type magnet. Whereas, our studies demonstrate a complex magnetic interactions falling in between the 3D-Ising and 3D-Heisenberg models. We suggest that the difference in the type of magnetic interactions between our study and Ref. [67] is possibly related to the differing Cr concentrations.

3.3.5 Magnetocaloric Effect

The magnetocaloric effect that is inherent to ferromagnetic system, induces heating or cooling when the system is adiabatically subjected to the external magnetic fields [68]. This phenomenon results in a magnetic entropy change -$\Delta S_m(T, H)$ in the presence of magnetic fields, expressed by the formula,

$$\Delta S_m(T, H) = \int_o^H (\frac{\partial S}{\partial H})_T dH = \int_o^H (\frac{\partial M}{\partial T})_H dH \tag{3.13}$$

According to the Maxwell's relation, $(\frac{\partial S}{\partial H})_T = (\frac{\partial M}{\partial T})_H$. For the magnetization measured within small discrete fields and temperature intervals, $\Delta S_m(T, H)$ can be expressed as

$$\Delta S_m(T, H) = \frac{\int_0^H M(T_{i+1}, H)dH - \int_0^H M(T_i, H)dH}{T_{i+1} - T_i} \tag{3.14}$$

Fig. 3.8 displays the temperature dependence of derived -$\Delta S_m(T,H)$ for $H \parallel c$ at different magnetic field strength. These curves showcase a peak change in entropy around T$_C$, presenting a broad peak pattern. At 6 T of applied field -$\Delta S_m(T,H)$ reaches maximum of approximately 2.08 J kg^{-1} K^{-1} for $H \parallel c$. The observed -$\Delta S_m(T,H)$ values at 6 T are comparable to those obtained from other 2D magnetic materials such as $Cr_2Ge_2Te_6$ (2.64 J kg^{-1} K^{-1}) [35] and Cr_5Te_8 (2.38 J kg^{-1} K^{-1}) [13], larger than $Fe_{3-x}GeTe_2$ (1.14 J kg^{-1} K^{-1}) [69] and CrI_3 (1.56 J kg^{-1} K^{-1}) [70], and smaller than CrB_3 (7.2 J kg^{-1} K^{-1}) [71] and $Cr_2Si_2Te_6$ (5.05 J kg^{-1} K^{-1}) [35].

3.4 Conclusions

We have successfully grown high-quality single crystals of Cr_2Te_3 using the chemical vapor transport method. Our investigation on the critical behavior of Cr_2Te_3 across the ferromagnetic to paramagnetic (FM-PM) transition temperature of 170 K, reveals crucial insights into the magnetic exchange interactions. Specifically, the Kouvel-Fisher (KF) method derives the critical exponents, $\beta = 0.353(4)$ and γ=1.213(5), suggesting complex magnetic interactions falling in between the 3D-Ising and the 3D-Heisenberg models. Further, the renormalization group theory analysis indicates a 3D-Ising-type magnetic interactions decaying with the distance as $J(r) = r^{-4.89}$. Importantly, the uniaxial magnetocrystalline anisotropy (MAE) of $K_u = 2065$ kJ/m^3 is the highest ever known experimental value in Cr_xTe_y type systems. We suggest that the 3D-Ising type magnetic interactions in Cr_2Te_3 are stabilized by the extremely large uniaxial MAE. Further, the DFT calculations predict large MAE of $K_u = 8230$ kJ/m^3, leading to a ground state noncollinear ferromagnetic structure with dominant out-of-plane ferromagnetic and dominant in-plane antiferromagnetic Cr-spin arrangements. The self-consistent renormalization theory (SCR) suggests Cr_2Te_3 to be an out-of-plane itinerant ferromagnet. Investigating the magnetic entropy change, -ΔS_M^{max}, as a function of temperature provided insights on the magnetocalaric effect in this system. These findings collectively lay a robust groundwork for advancing the magnetocaloric and spintronic technologies.

References

[1] J. T. Heron, M. Trassin, K. Ashraf, M. Gajek, Q. He, S. Y. Yang, D. E. Nikonov, Y.-H. Chu, S. Salahuddin, R. Ramesh, Electric-Field-Induced Magnetization Reversal in a Ferromagnet-Multiferroic Heterostructure, Phys. Rev. Lett. 107 (2011) 217202.

[2] A. K. Geim, I. V. Grigorieva, Van der Waals heterostructures, Nature 499 (2013) 419–425.

[3] C. Gong, L. Li, Z. Li, H. Ji, A. Stern, Y. Xia, T. Cao, W. Bao, C. Wang, Y. Wang, et al., Discovery of intrinsic ferromagnetism in two-dimensional van der Waals crystals, Nature 546 (2017) 265–269.

[4] Z. Fei, B. Huang, P. Malinowski, W. Wang, T. Song, J. Sanchez, W. Yao, D. Xiao, X. Zhu, A. F. May, et al., Two-dimensional itinerant ferromagnetism in atomically thin Fe_3GeTe_2, Nat. Mater. 17 (2018) 778–782.

[5] B. Wang, Y. Zhang, L. Ma, Q. Wu, Y. Guo, X. Zhang, J. Wang, MnX (X= P, As) monolayers: a new type of two-dimensional intrinsic room temperature ferromagnetic half-metallic material with large magnetic anisotropy, Nanoscale 11 (2019) 4204–4209.

[6] M. Gibertini, M. Koperski, A. F. Morpurgo, K. S. Novoselov, Magnetic 2D materials and heterostructures, Nat. Nanotechnol. 14 (2019) 408–419.

[7] N. D. Mermin, H. Wagner, Absence of Ferromagnetism or Antiferromagnetism in One- or Two-Dimensional Isotropic Heisenberg Models, Phys. Rev. Lett. 17 (1966) 1133–1136.

[8] B. Huang, G. Clark, E. Navarro-Moratalla, D. R. Klein, R. Cheng, K. L. Seyler, D. Zhong, E. Schmidgall, M. A. McGuire, D. H. Cobden, W. Yao, D. Xiao, P. Jarillo-Herrero, X. Xu, Layer-dependent ferromagnetism in a van der Waals crystal down to the monolayer limit, Nature 546 (2017) 270–273.

[9] Y. Liu, C. Petrovic, Critical behavior of quasi-two-dimensional semiconducting ferromagnet $Cr_2Ge_2Te_6$, Phys. Rev. B 96 (2017) 054406.

[10] T. J. Williams, A. A. Aczel, M. D. Lumsden, S. E. Nagler, M. B. Stone, J.-Q. Yan, D. Mandrus, Magnetic correlations in the quasi-two-dimensional semiconducting ferromagnet $CrSiTe_3$, Phys. Rev. B 92 (2015) 144404.

[11] L.-Z. Zhang, A.-L. Zhang, X.-D. He, X.-W. Ben, Q.-L. Xiao, W.-L. Lu, F. Chen, Z. Feng, S. Cao, J. Zhang, J.-Y. Ge, Critical behavior and magnetocaloric effect of the quasi-two-dimensional room-temperature ferromagnet Cr_4Te_5, Phys. Rev. B 101 (2020) 214413.

[12] Y. Wang, S. Kajihara, H. Matsuoka, B. K. Saika, K. Yamagami, Y. Takeda, H. Wadati, K. Ishizaka, Y. Iwasa, M. Nakano, Layer-Number-Independent Two-Dimensional Ferromagnetism in Cr_3Te_4, Nano Lett. 22 (2022) 9964.

[13] Y. Liu, M. Abeykoon, E. Stavitski, K. Attenkofer, C. Petrovic, Magnetic anisotropy and entropy change in trigonal Cr_5Te_8, Phys. Rev. B 100 (2019) 245114.

[14] T. Hashimoto, M. Yamaguchi, Magnetic Properties of Cr_7Te_8, J. Phys. Soc. Jpn. 27 (1969) 1121–1126.

[15] L.-Z. Zhang, Q.-L. Xiao, F. Chen, Z. Feng, S. Cao, J. Zhang, J.-Y. Ge, Multiple magnetic phase transitions and critical behavior in single crystal Cr_5Te_6, J. Magn. Magn. Mater. 546 (2022) 168770.

[16] H. Liu, H. Zheng, Y. Wang, C. Huang, C. Ma, Y. Zhu, H. Yang, L. Ling, L. Zhang, J. Fan, Long-range magnetic exchange coupling in quasi-two-dimensional CrTe ferromagnetic thin films, Physica Status Rolidi (RRL)–Rapid Research Letters 17 (2023) 202300209.

[17] M. Yamaguchi, T. Hashimoto, Magnetic properties of Cr_3Te_4 in ferromagnetic region, J. Phys. Soc. Jpn. 32 (1972) 635–638.

[18] G. Chattopadhyay, The Cr-Te (chromium-tellurium) system, J. Phase Equilib. 15 (1994) 431–440.

[19] S. Purwar, A. Low, A. Bose, A. Narayan, S. Thirupathaiah, Investigation of the anomalous and topological Hall effects in layered monoclinic ferromagnet $Cr_{2.76}Te_4$, Phys. Rev. Materials 7 (2023) 094204.

[20] D. C. Freitas, R. Weht, A. Sulpice, G. Remenyi, P. Strobel, F. Gay, J. Marcus, M. Núñez-Regueiro, Ferromagnetism in layered metastable 1T-$CrTe_2$, J. Phys.: Condens. Matter 27 (2015) 176002.

[21] M. Bian, A. N. Kamenskii, M. Han, W. Li, S. Wei, X. Tian, D. B. Eason, F. Sun, K. He, H. Hui, et al., Covalent 2D Cr_2Te_3 ferromagnet, Mater. Res. Lett. 9 (2021) 205–212.

[22] H. Ipser, K. L. Komarek, K. O. Klepp, Transition metal-chalcogen systems viii: The CrTe phase diagram, Journal of the Less Common Metals 92 (1983) 265–282.

[23] M. A. McGuire, V. O. Garlea, S. KC, V. R. Cooper, J. Yan, H. Cao, B. C. Sales, Antiferromagnetism in the van der Waals layered spin-lozenge semiconductor $CrTe_3$, Phys. Rev. B 95 (2017) 144421.

[24] R. Mondal, R. Kulkarni, A. Thamizhavel, Anisotropic magnetic properties and critical behaviour studies of trigonal Cr_5Te_8 single crystal, J. Magn. Magn. Mater. 483 (2019) 27–33.

[25] Z. Jiang, X. Liang, X. Luo, J. Gao, W. Wang, T. Wang, X. Yang, X. Wang, L. Zhang, Y. Sun, et al., Evolution of ground state in Cr_2Te_3 single crystal under applied magnetic field, Phys. Rev. B 106 (2022) 094407.

[26] Y. Wen, Z. Liu, Y. Zhang, C. Xia, B. Zhai, X. Zhang, G. Zhai, C. Shen, P. He, R. Cheng, et al., Tunable room-temperature ferromagnetism in two-dimensional Cr_2Te_3, Nano Lett. 20 (2020) 3130–3139.

[27] F.-S. Luo, J.-S. Ying, T.-W. Chen, F. Tang, D.-W. Zhang, W.-Q. Dong, Y. Zhang, S.-S. Li, Y. Fang, R.-K. Zheng, Anomalous Hall effect and anisotropic magnetoresistance of molecular beam epitaxy grown Cr_2Te_3 thin films, J. Cryst. Growth 582 (2022) 126541.

[28] J. H. Jeon, H. R. Na, H. Kim, S. Lee, S. Song, J. Kim, S. Park, J. Kim, H. Noh, G. Kim, et al., Emergent topological Hall effect from exchange coupling in ferromagnetic Cr_2Te_3/Noncoplanar antiferromagnetic Cr_2Te_3 bilayers, ACS nano 16 (2022) 8974–8982.

[29] N. Abuawwad, M. dos Santos Dias, H. Abusara, S. Lounis, Noncollinear magnetism in two-dimensional $CrTe_2$, Journal of Physics: Condensed Matter 34 (2022) 454001.

[30] T. Hashimoto, K. Hoya, M. Yamaguchi, I. Ichitsubo, Magnetic properties of single crystals $Cr_{2-\delta}Te_3$, J. Phys. Soc. Jpn. 31 (1971) 679–682.

[31] J. P. Perdew, K. Burke, M. Ernzerhof, Generalized Gradient Approximation Made Simple, Phys. Rev. Lett. 77 (1996) 3865–3868.

[32] P. Giannozzi, S. Baroni, N. Bonini, M. Calandra, R. Car, C. Cavazzoni, D. Ceresoli, G. L. Chiarotti, M. Cococcioni, I. Dabo, et al., QUANTUM ESPRESSO: a modular and open-source software project for quantum simulations of materials, J. Phys.: Condens. Matter 21 (2009) 395502.

[33] T. Hamasaki, T. Hashimoto, Y. Yamaguchi, H. Watanabe, Neutron diffraction study of Cr_2Te_3 single crystal, Solid State Commun. 16 (1975) 895–897.

[34] A. F. ANDRESEN, E. Zeppezauer, T. Boive, B. Nordström, C. Brändén, Magnetic structure of Cr_2Te_3, Cr_3Te_4, and Cr_5Te_6, Acta Chem. Scand. 24 (1970) 3495–3509.

[35] Y. Liu, C. Petrovic, Anisotropic magnetic entropy change in $Cr_2X_2Te_6$ (X = Si and Ge), Phys. Rev. Materials 3 (2019) 014001.

[36] S. Mondal, N. Khan, S. M. Mishra, B. Satpati, P. Mandal, Critical behavior in the van der Waals itinerant ferromagnet Fe_4GeTe_2, Phys. Rev. B 104 (2021) 094405.

[37] N. Richter, D. Weber, F. Martin, N. Singh, U. Schwingenschlögl, B. V. Lotsch, M. Kläui, Temperature-dependent magnetic anisotropy in the layered magnetic semiconductors CrI_3 and $CrBr_3$, Phys. Rev. Materials 2 (2018) 024004.

[38] N. León-Brito, E. D. Bauer, F. Ronning, J. D. Thompson, R. Movshovich, Magnetic microstructure and magnetic properties of uniaxial itinerant ferromagnet Fe_3GeTe_2, J. Appl. Phys. 120 (2016) 083903.

[39] Y. Takahashi, Spin fluctuation theory of itinerant electron magnetism, volume 9, Springer, 2013.

[40] M. Chattopadhyay, P. Arora, S. Roy, Magnetic properties of the field-induced ferromagnetic state in MnSi, J. Phys.: Condens. Matter 21 (2009) 296003.

[41] M. Imai, C. Michioka, H. Ueda, K. Yoshimura, Static and dynamical magnetic properties of the itinerant ferromagnet $LaCo_2P_2$, Phys. Rev. B 91 (2015) 184414.

[42] H. Ohta, C. Michioka, A. Matsuo, K. Kindo, K. Yoshimura, Magnetic study of SmCoAsO showing a ferromagnetic-antiferromagnetic transition, Phys. Rev. B 82 (2010) 054421.

[43] A. Arrott, Criterion for Ferromagnetism from Observations of Magnetic Isotherms, Phys. Rev. 108 (1957) 1394–1396.

[44] H. E. Stanley, Phase transitions and critical phenomena, volume 7, Clarendon Press, Oxford, 1971.

[45] S. Kaul, Static critical phenomena in ferromagnets with quenched disorder, J. Magn. Magn. Mater. 53 (1985) 5–53.

[46] D. Kim, B. Revaz, B. L. Zink, F. Hellman, J. J. Rhyne, J. F. Mitchell, Tricritical Point and the Doping Dependence of the Order of the Ferromagnetic Phase Transition of $La_{1-x}Ca_xMnO_3$, Phys. Rev. Lett. 89 (2002) 227202.

[47] Y. Liu, C. Petrovic, Critical behavior of the quasi-two-dimensional weak itinerant ferromagnet trigonal chromium telluride $Cr_{0.62}Te$, Phys. Rev. B 96 (2017) 134410.

[48] A. Wang, A. Rahman, Z. Du, J. Zhao, F. Meng, W. Liu, J. Fan, C. Ma, M. Ge, L. Pi, et al., Field-dependent anisotropic room-temperature ferromagnetism in Cr_3Te_4, Phys. Rev. B 108 (2023) 094429.

[49] M. E. Fisher, The theory of equilibrium critical phenomena, Reports on progress in physics 30 (1967) 615.

[50] J. C. Le Guillou, J. Zinn-Justin, Critical exponents from field theory, Phys. Rev. B 21 (1980) 3976–3998.

[51] A. Arrott, J. E. Noakes, Approximate equation of state for nickel near its critical temperature, Phys. Rev. Lett. 19 (1967) 786–789.

[52] A. K. Pramanik, A. Banerjee, Critical behavior at paramagnetic to ferromagnetic phase transition in $Pr_{0.5}Sr_{0.5}MnO_3$: A bulk magnetization study, Phys. Rev. B 79 (2009) 214426.

[53] J. S. Kouvel, M. E. Fisher, Detailed Magnetic Behavior of Nickel Near its Curie Point, Phys. Rev. 136 (1964) A1626–A1632.

[54] B. Widom, Degree of the critical isotherm, J. Chem. Phys. 41 (1964) 1633–1634.

[55] S. N. Kaul, Detailed magnetization study of an amorphous ferromagnet, Phys. Rev. B 24 (1981) 6550–6565.

[56] N. Tateiwa, Y. Haga, T. D. Matsuda, E. Yamamoto, Z. Fisk, Unconventional critical scaling of magnetization in ferromagnetic uranium superconductors UGe_2 and URhGe, Phys. Rev. B 89 (2014) 064420.

[57] X. Yang, J. Pan, S. Liu, M. Yang, L. Cao, D. Chu, K. Sun, Critical behavior and anisotropic magnetocaloric effect of the quasi-one-dimensional hexagonal ferromagnet $PrCrGe_3$, Phys. Rev. B 103 (2021) 104405.

[58] Y. Liu, Z. Hu, E. Stavitski, K. Attenkofer, C. Petrovic, Magnetic critical behavior and anomalous Hall effect in $2H-Co_{0.22}TaS_2$ single crystals, Phys. Rev. Res. 3 (2021) 023181.

[59] X. Yang, J. Pan, W. Gai, Y. Tao, H. Jia, L. Cao, Y. Cao, Three-dimensional critical behavior and anisotropic magnetic entropy change in quasi-two-dimensional $LaCrSb_3$, Phys. Rev. B 105 (2022) 024419.

[60] S. F. Fischer, S. N. Kaul, H. Kronmüller, Critical magnetic properties of disordered polycrystalline $Cr_{75}Fe_{25}$ and $Cr_{70}Fe_{30}$ alloys, Phys. Rev. B 65 (2002) 064443.

[61] M. E. Fisher, S.-k. Ma, B. G. Nickel, Critical Exponents for Long-Range Interactions, Phys. Rev. Lett. 29 (1972) 917–920.

[62] X. Zhang, T. Yu, Q. Xue, M. Lei, R. Jiao, Critical behavior and magnetocaloric effect in monoclinic Cr_5Te_8, J. Alloys Compd. 750 (2018) 798–803.

[63] S. Youn, S. Kwon, B. Min, Correlation effect and magnetic moments in Cr_2Te_3, J. Appl. Phys. 101 (2007) 09G522.

[64] J. B. Goodenough, Theory of the role of covalence in the perovskite-type manganites $[La, M(II)]\mathrm{MnO}-3$, Phys. Rev. 100 (1955) 564.

[65] J. Kanamori, Superexchange interaction and symmetry properties of electron orbitals, J. Phys. Chem. Solids 10 (1959) 87–98.

[66] J. Dijkstra, H. H. Weitering, C. F. van Bruggen, C. Haas, R. A. de Groot, Band-structure calculations, and magnetic and transport properties of ferromagnetic chromium tellurides $(CrTe, Cr_3Te_4, Cr_2Te_3)$, J. Phys.: Condens. Matter 1 (1989) 9141–9161.

[67] A. Goswami, N. Ng, A. M. Abeykoon, E. Yakubu, S. Guchhait, High magnetic anisotropy and magnetocaloric effects in single crystal Cr_2Te_3, 2023.

[68] V. K. Pecharsky, K. A. Gschneidner Jr, Magnetocaloric effect and magnetic refrigeration, J. Magn. Magn. Mater. 200 (1999) 44–56.

[69] Y. Liu, J. Li, J. Tao, Y. Zhu, C. Petrovic, Anisotropic magnetocaloric effect in $Fe_{3-x}GeTe_3$, Sci. Rep. 9 (2019) 13233.

[70] Y. Liu, C. Petrovic, Anisotropic magnetocaloric effect in single crystals of CrI_3, Phys. Rev. B 97 (2018) 174418.

[71] X. Yu, X. Zhang, Q. Shi, S. Tian, H. Lei, K. Xu, H. Hosono, Large magnetocaloric effect in van der Waals crystal $CrBr_3$, Front. Phys-beijing. 14 (2019) 43501.

Chapter 4

Investigation of the Anomalous and Topological Hall Effects in Layered Monoclinic Ferromagnet $Cr_{2.76}Te_4$

4.1 Introduction

Two-dimensional (2D) magnetic materials with topological properties [1–3] have sparked significant research attention recently due to their potential applications in spintronics and magnetic storage devices [4–6]. Importantly, these are the van der Waals (vdW) magnets possessing peculiar magnetic properties with strong magnetocrystalline anisotropy (MCA) [7–9]. In general, the Heisenberg-type ferromagnet does not exist with long-range magnetic ordering at a finite temperature in the 2D limit due to dominant thermal fluctuations [10]. However, the strong magnetic anisotropy that usually present in the low-dimensional materials can stabilize the long-range magnetic ordering to become a 2D Ising-type ferromagnet [11]. Till date many 2D ferromagnets have been discovered experimentally [12, 13], but only a few of them can show the topological signatures such as the topological Hall effect (THE) or skyrmion lattice. For instance, the recent microscopic studies on $Cr_2Ge_2Te_6$ [14], Fe_3GeTe_2 [15], and Fe_5GeTe_2 [16, 17] demonstrated topological magnetic structure in the form of skymion bubbles in their low-dimensional form.

On the other hand, soon after predicting the layered Cr_xTe_y-type systems as potential candidates to realize the 2D ferromagnetism in their bulk form [18, 19], a variety of Cr_xTe_y compounds were grown including CrTe [20], Cr_2Te_3 [21], Cr_3Te_4 [22], and Cr_5Te_8 [23]. Interestingly, all these systems are formed by the alternative stacking of Cr-full ($CrTe_2$-layer) and Cr-vacant (intercalated Cr-layer) layers along either *a*-axis or *c*-axis [24]. Thus, the Cr concentration plays a critical role in forming the crystal structure, magnetic, and transport properties. The compounds like Cr_5Te_8, Cr_2Te_3, and Cr_3Te_4 are reported to

---

This chapter is based on the publication: **Shubham Purwar et al., Physical Review Materials, 07, 094204 (2023)** crystallize in monoclinic or trigonal structures, whereas $Cr_{1-x}Te$ ($x < 0.1$) crystallizes in the hexagonal NiAs-type structures [25]. The electronic band structure calculations performed on CrTe, Cr_2Te_3, and Cr_3Te_4 suggest a strong out-of-plane Cr $3d$ e_g orbital, $d_{z^2} - d_{z^2}$, overlapping along the c-axis to have relatively smaller nearest neighbor $Cr - Cr$ distance [24]. In addition, Cr_5Te_8 [23], $Cr_{1.2}Te_2$ [26], $Cr_{0.87}Te$ [27] are known to show topological properties in the hexagonal phase.

In this work, we systematically investigate the electrical transport, Hall effect, and magnetic properties of monoclinic $Cr_{2.76}Te_4$ which is very close to the stoichiometric composition of Cr_3Te_4. We observe that the easy-axis of magnetization is parallel to the bc-plane, leading to strong magnetocrystalline anisotropy. Below 50 K, the system shows antiferromagnetic-like transition. In addition, we find fluctuating Cr magnetic moments between in-plane and out-of-plane directions within the temperature range of 50 and 150 K. Electrical resistivity data suggest $Cr_{2.76}Te_4$ to metallic throughout the measured temperature range with a *kink* at around 50 K due to AFM ordering. Our studies clearly point $Cr_{2.76}Te_4$ to an itinerant ferromagnet. Magnetotransport measurements demonstrate large anomalous Hall effect (AHE) and topological Hall effect (THE) in this system. First-principles calculations point to an intrinsic AHE due to non-zero Berry curvature near the Fermi level, while experimentally it is found to be an extrinsic AHE due to the skew-scattering [28].

4.2 Experimental details

High quality single crystals of $Cr_{2.76}Te_4$ were grown by the chemical vapor transport (CVT) technique with iodine as a transport agent as per the procedure described earlier [29]. Excess Iodine present on the crystals was removed by washing with ethanol several times and dried under vacuum. The as-grown single crystals were large in size (3×2 mm^2), were looking shiny, and easily cleavable in the bc-plane. Photographic image of typical single crystals is shown in the inset of Fig. 4.1(a). Crystal structural and phase purity of the single crystals were identified by the X-ray diffraction (XRD) technique using Rigaku X-ray diffractometer (SmartLab, 9kW) with Cu K_α radiation of wavelength 1.54059 Å. Compositional analysis of the single crystals was done using the energy dispersive X-ray spectroscopy (EDS of EDAX). Magnetic and transport studies were carried out on the physical property measurement system (9 Tesla-PPMS, DynaCool, Quantum Design). Electrical resistivity and Hall measurements were performed in the standard four-probe method. To eliminate the longitudinal magnetoresistance contribution due to voltage probe misalignment, the Hall resistance was calculated as ρ_{yz}(H)=$[\rho_{yz}(+H) - \rho_{yz}(-H)]/2$.

4.3 Density Functional Theory Calculations

We have performed density functional theory (DFT) calculations using the Quantum Espresso package [30, 31]. We used fully relativistic pseudopotentials in order to include the spin-orbit interaction. Generalized gradient approximation was considered based on Perdew-Burke-Ernzerhof implementation [32] within the projector augmented wave (PAW) basis [33]. For wave function and charge density expansions, cutoff values of 50 Ry and 300 Ry were chosen, respectively. For the self-consistent calculation, a 7×7×7 Monkhorst-Pack grid was used [34]. In order to consider the van der Waals forces, Semi-empirical Grimme's DFT-D2 correction [35] was included. We further constructed tight-binding model based on the maximally localized Wannier functions using the wannier90 code [36], with Cr 3*d*, Cr 3*s*, Te 5*p*, and Te 5*s* orbitals as the basis. Then utilizing the as obtained tight-binding model, we calculated Berry curvature along the high symmetry directions using Kubo formula [37] encoded in wannier90 code [36]. We have calculated intrinsic anomalous Hall conductivity (AHC) by integrating the x-component of Berry curvature over the entire BZ using WannierTools code [38].

4.4 Results and Discussion

4.4.1 Structural Analysis

Fig. 4.1(a) shows the XRD pattern of $Cr_{2.76}Te_4$ single crystal with intensity peaks of (l 0 0) Bragg plane, indicating that the crystal growth plane is along the a-axis. Inset in Fig. 4.1(a) shows the photographic image of $Cr_{2.76}Te_4$ single crystal. Fig. 4.1(b) shows XRD pattern of crushed $Cr_{2.76}Te_4$ single crystals measured at room temperature. All peaks in the XRD pattern can be attributed to the monoclinic crystal structure of $C12/m1$ space group (No.12) without any impurity phases, consistent with the crystal phase of Cr_3Te_4 [39]. Rietveld refinement confirms the monoclinic structure with lattice parameters a=13.9655(2) Å, b=3.9354(4)Å, c=6.8651(7) Å, $\alpha=\beta=90°$, and γ=118.326(7)°. These values are in good agreement with previous reports on similar systems [40, 41]. Fig. 4.1(c) shows schematic crystal structure of $Cr_{2.76}Te_4$ projected onto the ac-plane (top panel) and ab-plane (bottom panel). Cr1 atoms are located in the Cr-vacant layer with an occupancy of 0.189/$u.c$, whereas Cr2 atoms are located in the Cr-full layer with an occupancy of 0.5/$u.c.$ The intercalated Cr atoms (Cr1) are sandwiched within the van der Waals gap created by the two $CrTe_2$ layers, as shown in Fig. 4.1(c). The EDS measurements suggest an actual chemical composition of $Cr_{2.76}Te_4$. The studied sample of $Cr_{2.76}Te_4$ is close to the nominal composition of Cr_3Te_4. Moreover, both $Cr_{2.76}Te_4$ and Cr_3Te_4 show the same monoclinic crystal structure with a space group of $C12/m1$. We made two attempts to grow these crystals. We examined the chemical composition of nearly ten samples across

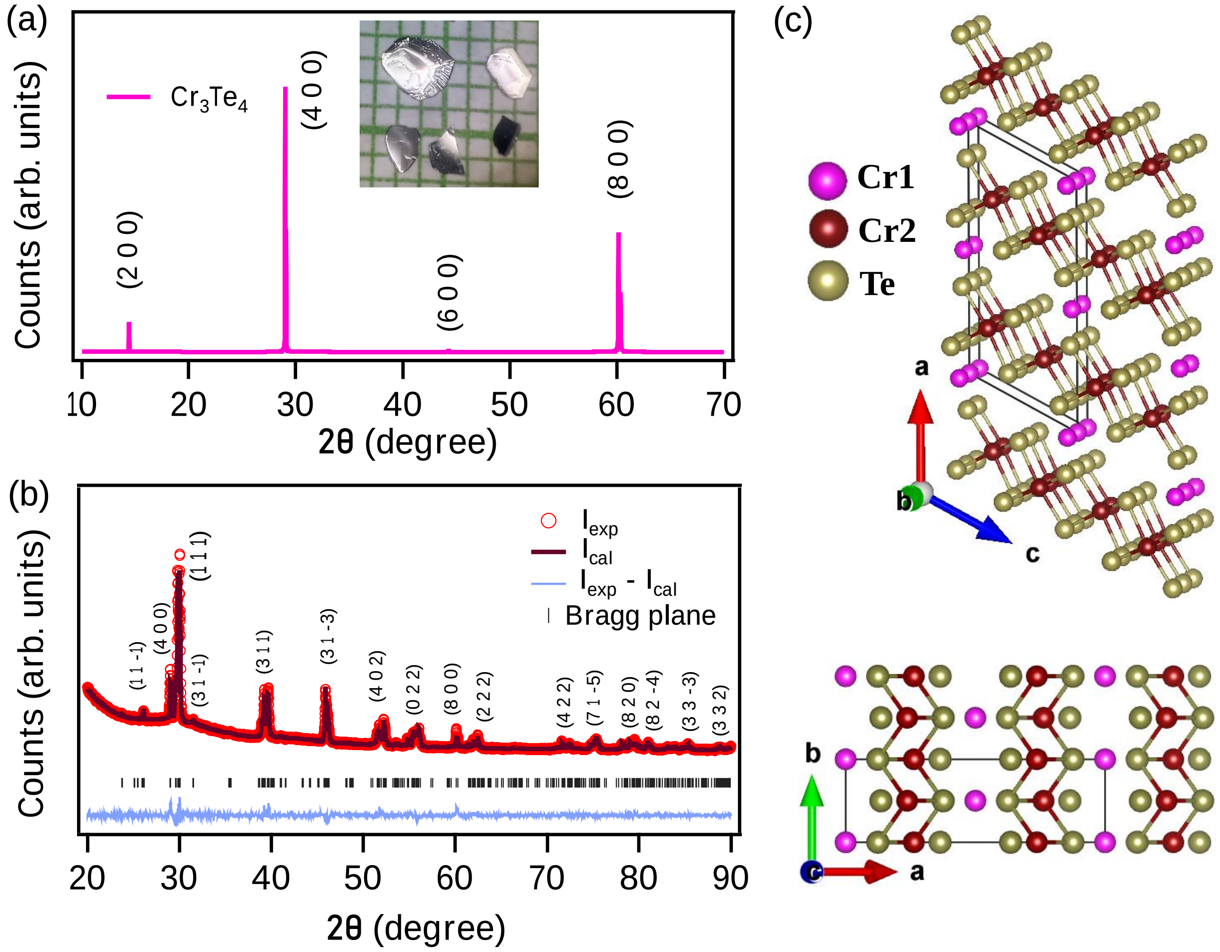

Figure 4.1: (a) XRD pattern from $Cr_{2.76}Te_4$ single crystals. Inset in (a) shows the photographic image of the single crystals. (b) X-ray diffraction pattern from the crushed $Cr_{2.76}Te_4$ single crystals, overlapped with Rietveld refinement. (c) Schematic crystal structure of $Cr_{2.76}Te_4$ obtained from the Rietveld refinement.

the two batches. The chemical composition is varied between $Cr_{2.75}Te_4$ to $Cr_{2.77}Te_4$ over ten samples. The crystal that we chose for further measurements was $Cr_{2.76}Te_4$, as it is in between them. We think, the slight difference in the chemical composition of our grown single crystals from the nominal composition is mainly influenced by the growth conditions like the quantity of transport agent (Iodine), temperature gradience inside the furnace, quartz-ample dimensions, etc.

4.4.2 Magnetic Measurements and Analysis

To explore the magnetic properties of $Cr_{2.76}Te_4$, magnetization as a function of temperature $[M(T)]$ was measured as shown in Fig. 4.2(a) at a field of 1000 Oe applied parallel to the *bc*-plane ($H \parallel bc$) and *a*-axis ($H \parallel a$) for both zero-field-cooled (ZFC) and field-cooled (FC) modes. We observe that $Cr_{2.76}Te_4$ exhibits paramagnetic (PM) to ferromagnetic (FM) transition at a Curie temperature (T_C) of 310 K, which is close to the Curie temperature of Cr_3Te_4 (T_C=316 K). Decrease in the sample temperature results into a decrease in the

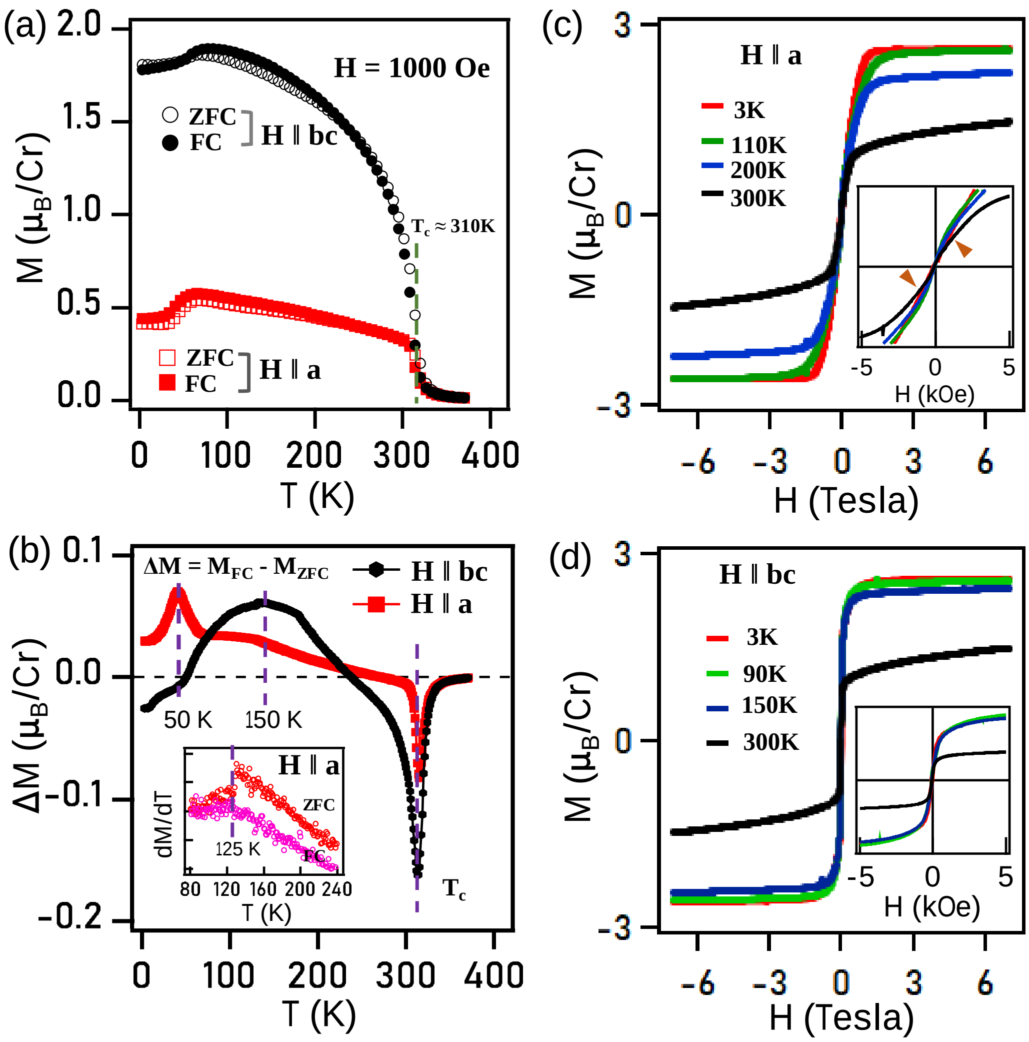

Figure 4.2: (a) Temperature dependent magnetization $M(T)$ measured under ZFC and FC modes with a magnetic field H=1000 Oe for $H \parallel a$ and $H \parallel bc$. (b) Variation of magnetization ΔM=(M$_{FC}$-M$_{FC}$) plotted as a function of temperature. Inset in (b) shows first derivative of magnetization with respect to the temperature (dM/dT) of the data shown in (a) for $H \parallel a$. (c) and (d) Field dependent magnetization $M(H)$ measured at different temperatures for $H \parallel a$ and $H \parallel bc$, respectively.

magnetization for both $H \parallel bc$ and $H \parallel a$ at around 50 K, possibly due to spin-canting emerged from the coupling between in-plane (bc-plane) AFM order and out-of-plane (a-axis) FM orders [42, 43]. Also, the in-plane saturated magnetic moment of 1.78 μ_B/Cr is almost 4 times higher than the out-of-plane saturated magnetic moment of 0.43 μ_B/Cr at 2 K with an applied field of 1000 Oe, clearly demonstrating strong magnetocrystalline anisotropy in $Cr_{2.76}Te_4$. From the magnetization difference between ZFC and FC, $\Delta M = M_{FC} - M_{ZFC}$, shown in Fig. 4.2(b), we notice significant magnetization fluctuations as the maximum of ΔM varies between in-plane and out-of-plane directions in going from 50 K to 150 K [44].

The magnetic state of $Cr_{2.76}Te_4$ is further explored by measuring the magnetization isotherms $[M(H)]$ for $H \parallel a$ and $H \parallel bc$ at various sample temperatures as shown in

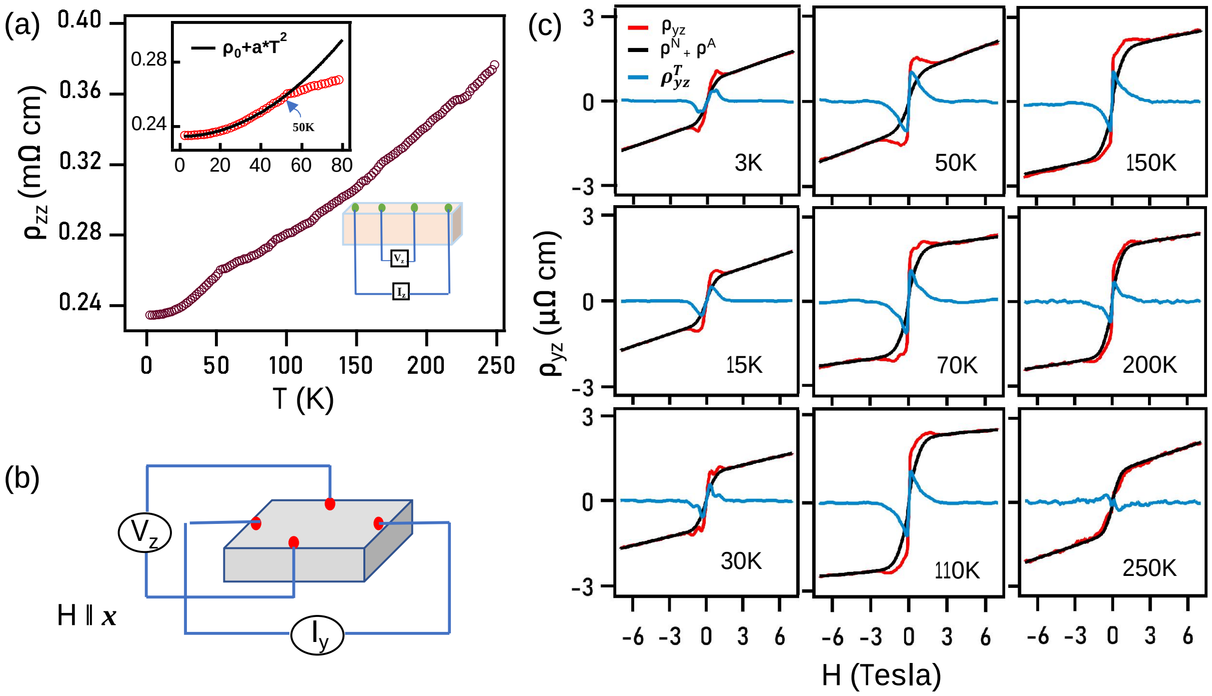

Figure 4.3: (a) Temperature dependent longitudinal resistivity ρ_{zz}(T). Top-inset in (a) shows low temperature resistivity fitted by ρ(T) = ρ_0 + bT^2 and bottom-inset in (a) shows schematic diagram of linear-four-probe contacts. (b) Hall measuring geometry is shown schematically. (c) Hall resistivity (ρ_{yz}) plotted as a function of magnetic field measured at various temperatures. In (c), Red curves represent the experimental data of total Hall resistivity (ρ_{yz}), black curves represent the contributions from the normal and anomalous Hall resistivities ($\rho^N + \rho^A$), and Blue curves represent the topological Hall resistivity (ρ^T_{yz}). See the text for more details.

Figs. 4.2(c) and 4.2(d), respectively. Consistent with $M(T)$ data, the magnetization saturation occurs at an applied field of 0.7 T and 1.4 T for $H \parallel bc$ and $H \parallel a$, respectively, suggesting bc-plane to be the easy-magnetization plane. Also, $Cr_{2.76}Te_4$ is a soft ferromagnet as it has a negligible coercivity [see Fig. 4.4(a)]. The observed saturation magnetisation (M_s) 2.586 μ_B/Cr and 2.55 μ_B/Cr for $H \parallel a$ and $H \parallel bc$, respectively, are smaller than the stand alone Cr atom (3 μ_B), indicating correlated magnetic states in $Cr_{2.76}Te_4$. These observations are in good agreement with report on $Cr_{2.76}Te_4$ [45].

4.4.3 Magneto-transport Analysis

Next, coming to the main results of this contribution, Fig. 4.3(a) exhibits temperature dependent longitudinal electrical resistivity (ρ_{zz}) of $Cr_{2.76}Te_4$. $\rho_{zz}(T)$ suggests metallic nature throughout the measured temperature range [46]. However, a *kink* at around 50 K is noticed in the resistivity, related to the AFM ordering [see Fig. 4.2(a)]. Bottom inset of Fig. 4.3(a) depicts schematic diagram of linear-four-probe measuring geometry and the top inset elucidates the quadratic nature of low temperature resistivity up to 50 K as it can be explained well by the Fermi liquid (FL) theory, $\rho(T) = \rho_0 + aT^2$

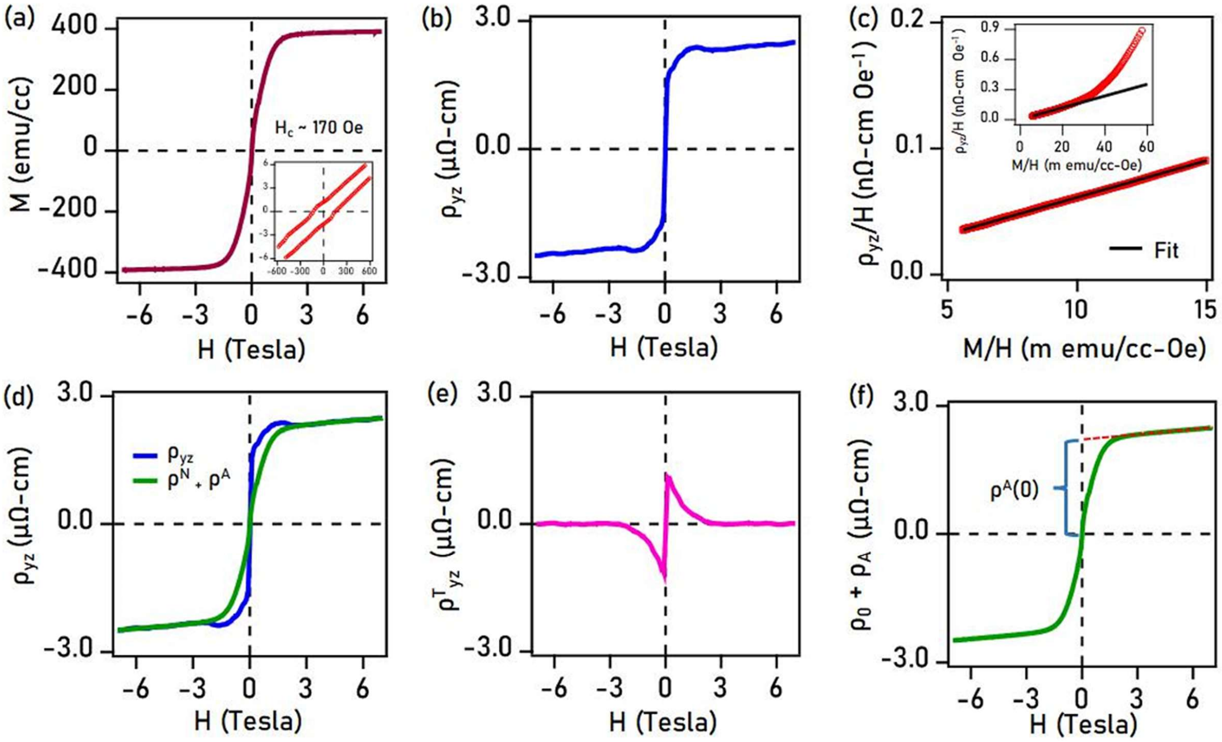

Figure 4.4: Data taken on $\mathrm{Cr_{2.76}Te_4}$ at $T = 110\,\mathrm{K}$: (a) Magnetization isotherms $M(H)$. The inset shows a zoomed-in view of $M(H)$, highlighting the coercivity $H_c \sim 170\,\mathrm{Oe}$. (b) Field-dependent total Hall resistivity ρ_{yz}. (c) ρ_{yz}/H vs. M/H, where the red curve represents the data and the black line indicates the linear fit in the higher-field region. The inset shows the data for the entire field range. (d) Fitting of normal and anomalous Hall resistivities overlaid on the total Hall resistivity. (e) Extracted topological Hall resistivity from the total Hall resistivity. (f) Extracted normal and anomalous Hall resistivities, along with a linear fit (red line), used to determine the anomalous Hall resistivity at zero fields $[\rho_A(0)]$.

where ρ_0 is the temperature independent residual resistivity. Schematic diagram of Hall measuring geometry is shown in Fig. 4.3(b). The Hall resistivity, ρ_{yz}, is measured with current along the y-axis and magnetic field applied along the x-axis to get the Hall voltage along the z-axis. Thus, Fig. 4.3(c) shows field dependent Hall resistivity ρ_{yz} (black curve) measured at various sample temperatures. The total Hall resistivity, as shown in Fig. 4.4(b), (ρ_{yz}) may have contributions from the normal Hall effect (ρ^N) and the anomalous Hall effect (ρ^A). Thus, the total Hall resistivity can be expressed by the empirical formula, $\rho_{yz}(H) = \rho^N(H) + \rho^A(H) = \mu_0 R_0 H + \mu_0 R_S M$, where R_0 and R_S are the normal and anomalous Hall coefficients, respectively. These coefficients can be obtained by performing a linear fit using the relation $\frac{\rho_{yz}}{\mu_0 H} = R_0 + R_S \frac{M}{H}$, as illustrated in Fig.4.4(c). Having obtained the normal and anomalous Hall coefficients, we can now fit the total Hall resistivity using the equation, $\rho_{yz}(H) = \mu_0 R_0 H + \mu_0 R_s M$. The fitting should be nearly perfect if there is no additional Hall contribution. However, as evident from Fig. 4.4(d), the fit (green curve) deviates from the experimental data (blue curve), indicating the presence of an additional contribution. To account for this, the total Hall resistivity is further expressed

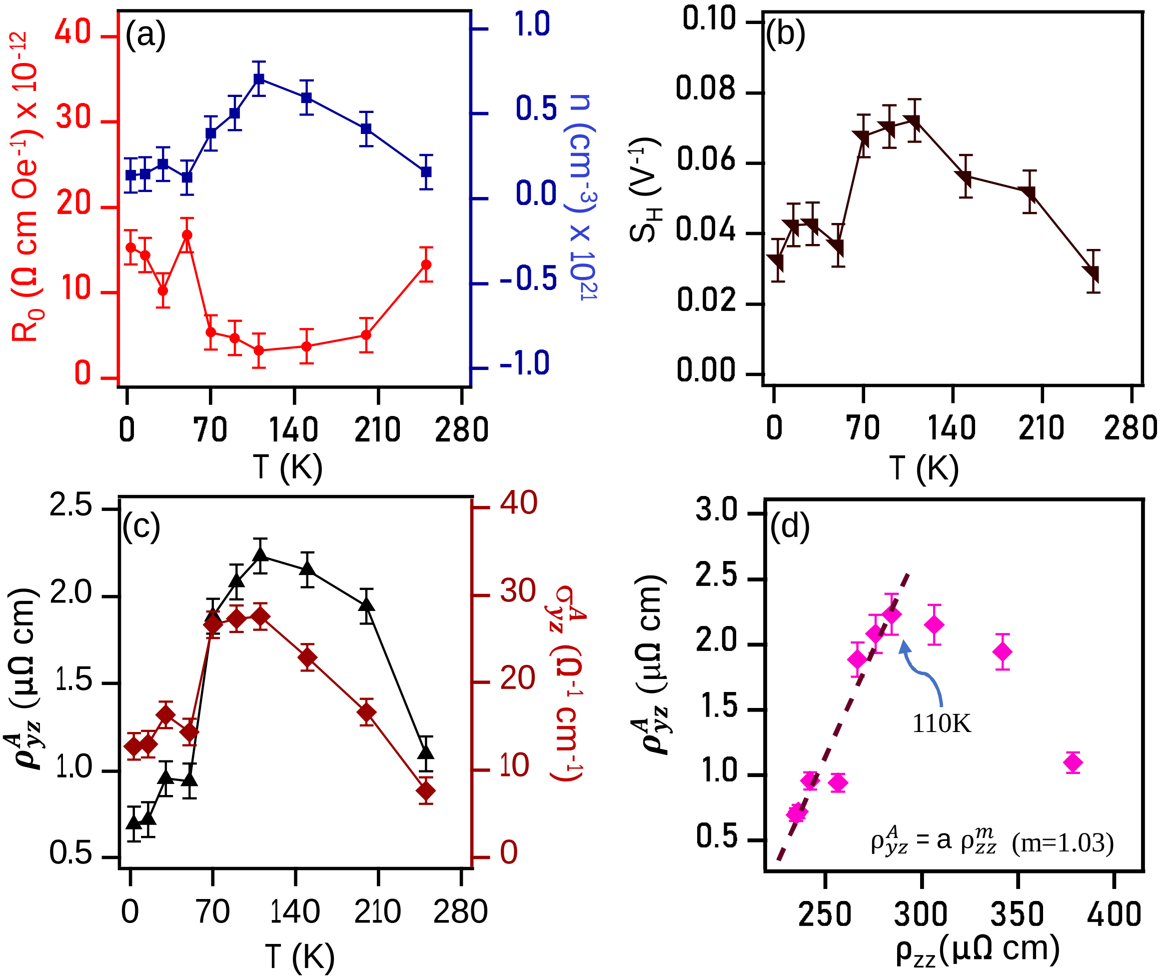

Figure 4.5: Temperature dependence of (a) Normal Hall coefficient R_0 (left axis) and charge carrier density n (right axis). (b) Anomalous Hall scaling coefficient S_H plotted as a function of temperature. (c) Anomalous Hall resistivity (ρ^A_{yz}) and Hall conductivity (σ^A_{yz}). (d) Plot of ρ^A_{yz} *vs.* ρ_{zz}. Dashed line in (d) is linear fitting with equation shown on the figure.

as: $\rho_{yz}(H) = \rho^N(H) + \rho^A(H) + \rho^T(H)$, where $\rho^T(H)$ denotes the topological Hall resistivity. This contribution is extracted using the relation: $\rho^T(H) = \rho_{yz}(H) - [\rho^N(H) + \rho^A(H)]$, as shown in Fig.4.4(e) and discussed in previous studies[47–49].

Fig. 4.5(a) depicts the normal Hall coefficient (R_0) and the charge carrier density (n) derived using the formula, ($R_0 = 1/n|e|$), plotted as a function of temperature. We clearly notice from Fig. 4.5(a) that as the temperature decreases the carrier density increases up to 110 K. However, below 110 K, the carrier density decreases with temperature and gets saturated below 50 K. Fig. 4.5(b) (left axis) presents the anomalous Hall resistivity (ρ^A_{yz}) at zero field obtained by linearly intersecting the field axis [see Fig. 4.3(c)]. Maximum anomalous Hall resistivity is noticed at around 110 K. Anomalous Hall conductivity, σ^A_{yz}, derived using the formula $\sigma^A_{yz} = \frac{\rho_{yz}}{\rho^2_{yz}+\rho^2_{zz}}$ is shown in the right axis of Fig. 4.5(c), again to find the maximum Hall conductivity of σ^A_{yz}=27 $\Omega^{-1}cm^{-1}$ at around 110 K. Fig. 4.5(b) shows anomalous scaling coefficient $S_H = \frac{\rho^A_{yz}}{M\rho^2_{zz}}$, plotted as a function of temperature. The

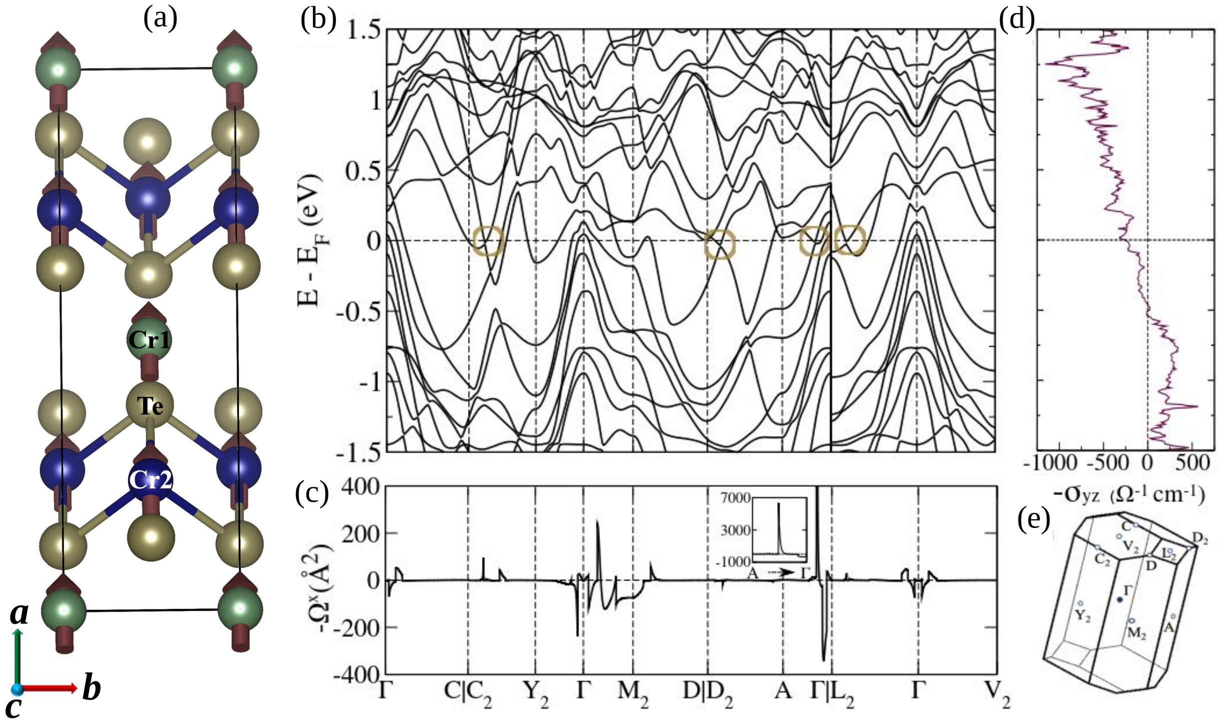

Figure 4.6: (a) Schematic monoclinic unit cell of $Cr_{2.76}Te_4$. (b) Electronic band structure of $Cr_{2.76}Te_4$ calculated with inclusion of spin-orbit coupling (SOC). In (b) the Weyl points near the Fermi level are encircled. (c) x-component of the Berry curvature, Ω^x, calculated at the Fermi level. Inset in (c) shows zoomed-in view of Ω^x for the $A - \Gamma$ segment. (d) Anomalous Hall conductivity, σ_{yz}, plotted as a function of energy. (e) High symmetry points defined on the Brillouin zone of monoclinic primitive unit cell.

values of S_H are inline with the itinerant ferromagnetic systems of S_H=0.01-0.2 V^{-1} [50]. In general, anomalous Hall effect can occur in solids either intrinsically originated from the nonzero-Berry curvature in the momentum space [51, 52] or extrinsically due to side-jump/scew-scattering mechanisms [28, 51, 53]. Therefore, to elucidate the mechanism of AHE in $Cr_{2.76}Te_4$, we plotted ρ^A_{yz} $vs.$ ρ_{zz} as shown in Fig. 4.5(d). From Fig. 4.5(d) it is evident that ρ^A_{yz} linearly changes with ρ_{zz} [$\rho_{yz} = \alpha\rho^m_{zz}$ for $m = 1.03 \pm 0.02$] up to 110 K and then deviates on further increasing the sample temperature [54]. In the case of itinerant ferromagnetic system, the Hall resistivity can be expressed by the relation $\rho_{yz} = \alpha\rho_{zz} + \beta\rho^2_{zz}$ where α and β are the screw-scattering and side-jump terms, respectively [55, 46, 56]. That means, in the case of skew-scattering ρ^A_{yz} linearly depends on ρ_{zz}, while ρ^A_{yz} quadratically depends on ρ_{zz} in the case of side-jump. Since the Hall resistivity (ρ_{yz}) linearly depends on ρ_{zz}, the skew-scattering could be the most suitable mechanism of AHE observed in this system [57, 58]. Note that the intrinsic Berry curvature contribution to the AHR also quadratically dependents on ρ_{zz} [54]. To make a point, it looks that 110 K is the critical temperature of the properties discussed in Figs. 4.5(a)-(d). However, as per the dM/dT data shown in the inset of Fig. 4.2(b), we think that the critical temperature could be ≈ 125 K instead of 110 K as we can see significant change in magnetization across ≈ 125 K.

Our experimental findings on the AHE have been examined using the density functional theory calculations as presented in Fig. 4.6. For the calculations, we considered primitive unit cell of Cr_3Te_4, consisting of three Cr (one Cr1 and two Cr2 type) and four Te atoms. The magnetic spins of Cr atoms were considered along the x-direction. Our calculations suggest a ferromagnetic ground state with average magnetic moments of $3.23\mu_B$ and $3.15\mu_B$ per Cr1 and Cr2 atoms, respectively, slightly higher than the experimental average value of 2.568 μ_B/Cr. In Fig. 4.6(b), we present bulk electronic band structure of Cr_3Te_4. The system is found to be metallic with several bands crossing the Fermi level (E_F). Several band crossing points are found near E_F along $C_2 - Y_2$, $D_2 - A$, $A - \Gamma$ and $L_2 - \Gamma$ k-paths, but slightly away from the high symmetry points. Next, we explore the Berry curvature (Ω) calculated using the formula $\Omega(k) = \nabla(k) \times A(k)$ (where $A(k)$ is the Berry connection). Variation of the x-component of Berry curvature (Ω^x) at E_F along the high symmetry k-path is shown in Fig. 4.6(c). We can notice from Fig. 4.6(c) that Ω^x is strongly enhanced along the $A - \Gamma$ (k_z)direction. Further, Fig. 4.6(d) shows the anomalous Hall conductivity (AHC), σ_{yz}, of Cr_3Te_4 calculated as a function of energy using the Eqn. 4.1.

$$\sigma_{yz} = \frac{e^2}{\hbar} \int f(\epsilon_n(\mathbf{k}))\Omega_n^x(\mathbf{k})\frac{d\mathbf{k}}{(2\pi)^3} \tag{4.1}$$

Where, $f(\epsilon_n(\mathbf{k}))$ is the Fermi-Dirac distribution function.

Our calculations suggest an intrinsic AHC of σ_{yz}≈260 Ω^{-1} cm^{-1} near E_F, much larger than the experimental value of σ^A_{yz}=27 Ω^{-1} cm^{-1}. Such a small AHC suggests dominant impurity scattering contribution to the total anomalous Hall effect of Cr_3Te_4 [59], i.e., the skew-scattering contribution in the dirty limit [60]. However, despite the system is in the dirty limit, the total AHC should be at least comparable to the value of intrinsic AHC (≈260 Ω^{-1} cm^{-1}) as it has contributions from both intrinsic Berry-curvature and extrinsic skew-scattering. In contrast, experimentally, we find a much smaller AHC compared to theoretical calculations. Note here that the calculations performed on the stoichiometric Cr_3Te_4 predict a large intrinsic AHC near E_F due to the presence of several band crossing points (Weyl points). But the intrinsic AHC rapidly decreases as we move away from E_F. This is particularly true when E_F is shifted to lower binding energies [see Fig. 4.6(d)]. Therefore, a genuine reason behind the discrepancy of AHC between experiment and theory could be that the experiments are performed on a slightly off-stoichiometric composition of $Cr_{2.76}Te_4$ with 8% Cr deficiency per formula unit, shifting the Fermi level towards the lower binding energy. Maximum topological Hall resistivity (ρ^T_{max}) is plotted as a function of temperature in Fig. 4.7(a) by the black-colored data points. Also, green-colored data points in Fig. 4.7(a) represent the magnetocrystalline anisotropy constant K_u calculated using the Eqn. 4.2.

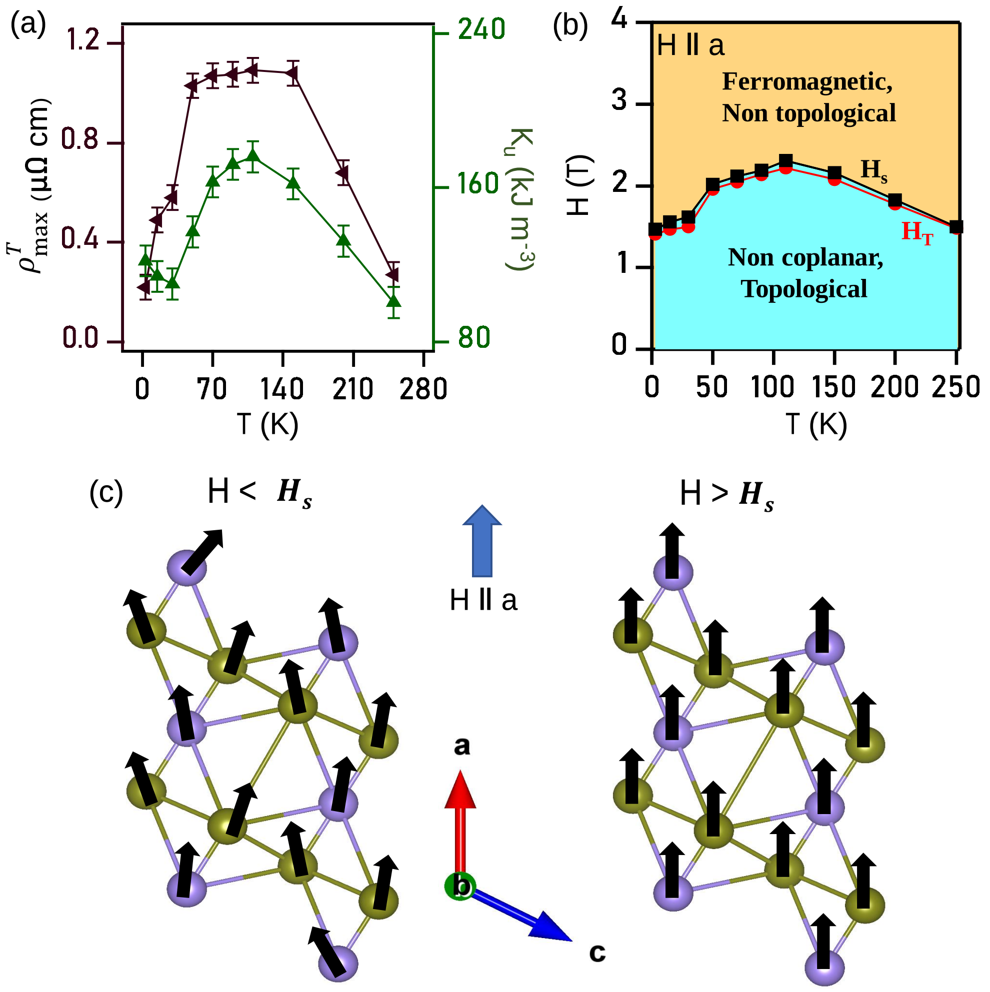

Figure 4.7: (a) Maximum value of ρ^T_{max} and magnetocrystalline anisotropy (K_u) plotted as a function of temperature. (b) Saturation magnetic field (H_s) and magnetic field (H_T) above which the topological Hall effect disappears for $H \parallel a$. (c) Schematic representation of Cr spin configuration for $H < H_s$ (left) and $H > H_s$. See the text for more details.

$$K_u = \mu_0 \int_0^{M_s} [H_{bc}(M) - H_a(M)] \, dM \tag{4.2}$$

Here, M$_s$ represents saturation magnetization. H$_{bc}$ and H$_a$ represent $H \parallel bc$ and $H \parallel a$, respectively.

From Fig. 4.7(a), we can notice that the topological Hall resistivity is highest within the temperature range of 50 and 150 K. Also, most importantly, the temperature dependance of K_u resembles ρ^T_{max}. In Fig. 4.7(b), the black-colored data points illustrate temperature dependent saturation field (H_s) beyond which the system becomes ferromagnetic [extracted from Fig. 4.2(c)] and the red-colored data points illustrate temperature dependent field (H_T) beyond which ρ^T_{yz} becomes zero [extracted from Fig. 4.3(c)]. Interestingly, both fields H_T and H_s perfectly overlap at all measured temperatures. This can be understood using the schematics shown in Fig. 4.7(c). Means, at a given temperature up to the saturation field ($H < H_s$), the system possess non-coplanar spin structure and hence shows the topological Hall effect [61]. However, for the applied field beyond magnetic saturation ($H > H_s$), the system becomes ferromagnetic and thus THE disappears.

Further, the maximum topological Hall resistivity $\rho^T_{max} \approx 1.1$ $\mu\Omega$-cm over a broad temperature range of ($50K < T < 150K$) observed in this vdW ferromagnetic $Cr_{2.76}Te_4$ is in the same order of magnitude found in the chiral semimetals such as Mn_2PtSn [62], Gd_3PdSi_3 [63], $LaMn_2Ge_2$ [64], and in other Cr_xTe_y based systems [23, 26]. Interestingly, so far THE is observed in Cr_xTe_y systems in their hexagonal (trigonal) crystal structure [65, 23, 26] but not in the monoclinic structure that we found in the present study. As discussed above, the easy-axis of magnetization in $Cr_{2.76}Te_4$ is found to be in the bc-plane and thus for small applied fields the Cr spins are canted out of the bc-plane towards the a-axis for $H \parallel a$. In this way, the non-coplanar spin-structure has been generated for sufficiently smaller fields [65, 66, 64, 67, 23, 26].

Several mechanisms are proposed to understand the topological Hall effect. Such as the antisymmetric exchange or Dzyaloshinskii–Moriya (DM) interaction in the non-centrosymmetric systems [68–70] and the uniaxial magnetocrystalline anisotropy in the centrosymmetric systems [71–74]. In the case of monoclinic Cr_3Te_4 ($C21/m1$) which is a centrosymmetric crystal, the chiral-spin structure could be stabilized by the strong MCA. This analogy is completely supported by our experimentally estimated MCA values at various temperatures as shown in Fig. 4.7(a). Most importantly, highest ρ^T_{max} value has been obtained at the highest magnetocrystalline anisotropy of K_u=165 kJ/m^3. This is because, in presence of the chiral-spin structure, the itinerant electrons acquire real-space Berry curvature associated with finite scalar-spin chirality $\chi_{ijk} = S_i.(S_j \times S_k)$ which serves as fictitious magnetic field to generate the topological Hall signal [75–77].

4.5 Conclusions

To summarize, we have grown high quality single crystal of layered ferromagnetic $Cr_{2.76}Te_4$ in the monoclinic phase to study the electrical transport, Hall effect, and magnetic properties. Our studies suggest $Cr_{2.76}Te_4$ to be a soft ferromagnet with a negligible coercivity. The easy-axis of magnetization is found to be parallel to the bc-plane, leading to strong magnetocrystalline anisotropy. Below 50 K, an antiferromagnetic-like transition is noticed. Interestingly, in going from 50 K to 150 K the strength of magnetic moments switches between out-of-plane to in-plane, suggests fluctuating Cr spins. From the electrical resistivity measurements the system is found to be metallic throughout the measured temperature range. Also, a *kink* at around 50 K due to AFM ordering is noticed. Magnetotransport measurements demonstrate large anomalous Hall effect (AHE) and topological Hall effect (THE) in this systems. First-principles calculations point to an intrinsic AHE due to non-zero Berry curvature near the Fermi level, while experimentally it is found to be an extrinsic AHE due to skew-scattering. Topological Hall effect has been observed due to the non-coplanar spin-structure in the presence of strong magnetocrystalline anisotropy.

References

[1] M. Augustin, S. Jenkins, R. F. Evans, K. S. Novoselov, E. J. Santos, Properties and dynamics of meron topological spin textures in the two-dimensional magnet $CrCl_3$, Nature Communications 12 (2021) 185.

[2] L. Chen, J.-H. Chung, M. B. Stone, A. I. Kolesnikov, B. Winn, V. O. Garlea, D. L. Abernathy, B. Gao, M. Augustin, E. J. G. Santos, P. Dai, Magnetic field effect on topological spin excitations in CrI_3, Phys. Rev. X 11 (2021) 031047.

[3] K. Choudhary, K. F. Garrity, J. Jiang, R. Pachter, F. Tavazza, Computational search for magnetic and non-magnetic 2d topological materials using unified spin–orbit spillage screening, npj Computational Materials 6 (2020) 49.

[4] N. Nagaosa, Y. Tokura, Topological properties and dynamics of magnetic skyrmions, Nature nanotechnology 8 (2013) 899–911.

[5] J. R. Schaibley, H. Yu, G. Clark, P. Rivera, J. S. Ross, K. L. Seyler, W. Yao, X. Xu, Valleytronics in 2d materials, Nature Reviews Materials 1 (2016) 1–15.

[6] A. Fert, N. Reyren, V. Cros, Magnetic skyrmions: advances in physics and potential applications, Nature Reviews Materials 2 (2017) 1–15.

[7] C. Gong, L. Li, Z. Li, H. Ji, A. Stern, Y. Xia, T. Cao, W. Bao, C. Wang, Y. Wang, et al., Discovery of intrinsic ferromagnetism in two-dimensional van der waals crystals, Nature 546 (2017) 265–269.

[8] K. L. Seyler, D. Zhong, D. R. Klein, S. Gao, X. Zhang, B. Huang, E. Navarro-Moratalla, L. Yang, D. H. Cobden, M. A. McGuire, et al., Ligand-field helical luminescence in a 2D ferromagnetic insulator, Nature Physics 14 (2018) 277–281.

[9] Z. Fei, B. Huang, P. Malinowski, W. Wang, T. Song, J. Sanchez, W. Yao, D. Xiao, X. Zhu, A. F. May, et al., Two-dimensional itinerant ferromagnetism in atomically thin Fe_3GeTe_2, Nature materials 17 (2018) 778–782.

[10] N. D. Mermin, H. Wagner, Absence of ferromagnetism or antiferromagnetism in one- or two-dimensional isotropic heisenberg models, Phys. Rev. Lett. 17 (1966) 1133–1136.

[11] B. Huang, G. Clark, E. Navarro-Moratalla, D. R. Klein, R. Cheng, K. L. Seyler, D. Zhong, E. Schmidgall, M. A. McGuire, D. H. Cobden, W. Yao, D. Xiao, P. Jarillo-Herrero, X. Xu, Layer-dependent ferromagnetism in a van der Waals crystal down to the monolayer limit, Nature 546 (2017) 270–273.

[12] K. S. Burch, D. Mandrus, J.-G. Park, Magnetism in two-dimensional van der Waals materials, Nature 563 (2018) 47–52.

[13] C. Gong, X. Zhang, Two-dimensional magnetic crystals and emergent heterostructure devices, Science 363 (2019) eaav4450.

[14] M.-G. Han, J. A. Garlow, Y. Liu, H. Zhang, J. Li, D. DiMarzio, M. W. Knight, C. Petrovic, D. Jariwala, Y. Zhu, Topological magnetic-spin textures in two-dimensional van der waals $Cr_2Ge_2Te_6$, Nano Letters 19 (2019) 7859–7865.

[15] Y. You, Y. Gong, H. Li, Z. Li, M. Zhu, J. Tang, E. Liu, Y. Yao, G. Xu, F. Xu, W. Wang, Angular dependence of the topological hall effect in the uniaxial van der waals ferromagnet Fe_3GeTe_2, Phys. Rev. B 100 (2019) 134441.

[16] Y. Gao, S. Yan, Q. Yin, H. Huang, Z. Li, Z. Zhu, J. Cai, B. Shen, H. Lei, Y. Zhang, S. Wang, Manipulation of topological spin configuration via tailoring thickness in van der waals ferromagnetic $Fe_{5-x}GeTe_2$, Phys. Rev. B 105 (2022) 014426.

[17] M. Schmitt, T. Denneulin, A. Kovács, T. G. Saunderson, P. Rüßmann, A. Shahee, T. Scholz, A. H. Tavabi, M. Gradhand, P. Mavropoulos, et al., Skyrmionic spin structures in layered Fe_5GeTe_2 up to room temperature, Communications Physics 5 (2022) 254.

[18] Y. Zhu, X. Kong, T. D. Rhone, H. Guo, Systematic search for two-dimensional ferromagnetic materials, Phys. Rev. Materials 2 (2018) 081001.

[19] Y. Liu, C. Petrovic, Critical behavior of the quasi-two-dimensional weak itinerant ferromagnet trigonal chromium telluride $Cr_{0.62}Te$, Phys. Rev. B 96 (2017) 134410.

[20] T. Eto, M. Ishizuka, S. Endo, T. Kanomata, T. Kikegawa, Pressure-induced structural phase transition in a ferromagnet CrTe, Journal of Alloys and Compounds 315 (2001) 16–21.

[21] F. Wang, J. Du, F. Sun, R. F. Sabirianov, N. Al-Aqtash, D. Sengupta, H. Zeng, X. Xu, Ferromagnetic Cr_2Te_3 nanorods with ultrahigh coercivity, Nanoscale 10 (2018) 11028–11033.

[22] B. Hessen, T. Siegrist, T. Palstra, S. Tanzler, M. Steigerwald, Hexakis (triethylphosphine) octatelluridohexachromium and a molecule-based synthesis of chromium telluride, Cr_3Te_4, Inorganic chemistry 32 (1993) 5165–5169.

[23] Y. Wang, J. Yan, J. Li, S. Wang, M. Song, J. Song, Z. Li, K. Chen, Y. Qin, L. Ling, H. Du, L. Cao, X. Luo, Y. Xiong, Y. Sun, Magnetic anisotropy and topological hall effect in the trigonal chromium tellurides Cr_5Te_8, Phys. Rev. B 100 (2019) 024434.

[24] J. Dijkstra, H. H. Weitering, C. F. van Bruggen, C. Haas, R. A. de Groot, Band-structure calculations, and magnetic and transport properties of ferromagnetic chromium tellurides $(\mathrm{CrTe}, \mathrm{Cr_3Te_4}, \mathrm{Cr_2Te_3})$, Journal of Physics: Condensed Matter 1 (1989) 9141–9161.

[25] H. Ipser, K. L. Komarek, K. O. Klepp, Transition metal-chalcogen systems viii: The CrTe phase diagram, Journal of the Less Common Metals 92 (1983) 265–282.

[26] M. Huang, L. Gao, Y. Zhang, X. Lei, G. Hu, J. Xiang, H. Zeng, X. Fu, Z. Zhang, G. Chai, et al., Possible topological hall effect above room temperature in layered $\mathrm{Cr_{1.2}Te_2}$ ferromagnet, Nano Letters 21 (2021) 4280–4286.

[27] J. Liu, B. Ding, J. Liang, X. Li, Y. Yao, W. Wang, Magnetic skyrmionic bubbles at room temperature and sign reversal of the topological hall effect in a layered ferromagnet $\mathrm{Cr_{0.87}Te}$, ACS nano 16 (2022) 13911–13918.

[28] J. Smit, The spontaneous hall effect in ferromagnetics II, Physica 24 (1958) 39–51.

[29] T. Hashimoto, K. Hoya, M. Yamaguchi, I. Ichitsubo, Magnetic properties of single crystals $\mathrm{Cr_{2-\delta}Te_3}$, Journal of the Physical Society of Japan 31 (1971) 679–682.

[30] P. Giannozzi, S. Baroni, N. Bonini, M. Calandra, R. Car, C. Cavazzoni, D. Ceresoli, G. L. Chiarotti, M. Cococcioni, I. Dabo, et al., QUANTUM ESPRESSO: a modular and open-source software project for quantum simulations of materials, J. Phys. Condens. Matter 21 (2009) 395502.

[31] P. Giannozzi, O. Andreussi, T. Brumme, O. Bunau, M. B. Nardelli, M. Calandra, R. Car, C. Cavazzoni, D. Ceresoli, M. Cococcioni, et al., Advanced capabilities for materials modelling with Quantum ESPRESSO, J. Phys. Condens. Matter 29 (2017) 465901.

[32] J. P. Perdew, K. Burke, M. Ernzerhof, Generalized Gradient Approximation Made Simple, Phys. Rev. Lett. 77 (1996) 3865–3868.

[33] P. E. Blöchl, Projector augmented-wave method, Phys. Rev. B 50 (1994) 17953–17979.

[34] H. J. Monkhorst, J. D. Pack, Special points for Brillouin-zone integrations, Phys. Rev. B 13 (1976) 5188–5192.

[35] S. Grimme, Semiempirical GGA-type density functional constructed with a long-range dispersion correction, J. Comput. Chem. 27 (2006) 1787.

[36] A. A. Mostofi, J. R. Yates, Y.-S. Lee, I. Souza, D. Vanderbilt, N. Marzari, wannier90: A tool for obtaining maximally-localised Wannier functions, Comput. Phys. Commun. 178 (2008) 685–699.

[37] D. J. Thouless, M. Kohmoto, M. P. Nightingale, M. den Nijs, Quantized Hall Conductance in a Two-Dimensional Periodic Potential, Phys. Rev. Lett. 49 (1982) 405–408.

[38] Q. Wu, S. Zhang, H.-F. Song, M. Troyer, A. A. Soluyanov, WannierTools: An open-source software package for novel topological materials, Comput. Phys. Commun. 224 (2018) 405–416.

[39] M. Yamaguchi, T. Hashimoto, Magnetic Properties of Cr_3Te_4 in Ferromagnetic Region, Journal of the Physical Society of Japan 32 (1972) 635–638.

[40] S. Ohta, Magnetic Properties of $(Cr_{1-u}V_u)_3Te_4$, J. Phys. Soc. Jpn. 54 (1985) 1076–1086.

[41] D. Babot, M. Wintenberger, B. Lambert-Andron, M. Chevreton, Propriétés magnétiques et conductibilité electrique des composés ternaires $Cr_3Se_{4-x}Te_x$, Journal of Solid State Chemistry 8 (1973) 175–181.

[42] C. Li, K. Liu, D. Jiang, C. Jin, T. Pei, T. Wen, B. Yue, Y. Wang, Diverse Thermal Expansion Behaviors in Ferromagnetic $Cr_{1-\delta}Te$ with NiAs-Type, Defective Structures, Inorganic Chemistry 61 (2022) 14641–14647.

[43] L.-Z. Zhang, A.-L. Zhang, X.-D. He, X.-W. Ben, Q.-L. Xiao, W.-L. Lu, F. Chen, Z. Feng, S. Cao, J. Zhang, J.-Y. Ge, Critical behavior and magnetocaloric effect of the quasi-two-dimensional room-temperature ferromagnet Cr_4Te_5, Phys. Rev. B 101 (2020) 214413.

[44] P. Chen, C. Zhang, Y. Wang, B. Lv, P. Liu, Y. Tian, J. Ran, C. Gao, Q. Liu, D. Xue, Topological Hall effect in frustrated B2-ordered $Mn_{0.74}Co_{0.57}Al_{0.69}$ films, Phys. Rev. B 104 (2021) 064409.

[45] K. Shimada, T. Saitoh, H. Namatame, A. Fujimori, S. Ishida, S. Asano, M. Matoba, S. Anzai, Photoemission study of itinerant ferromagnet $Cr_{1-\delta}Te$, Phys. Rev. B 53 (1996) 7673–7683.

[46] Y. Liu, C. Petrovic, Anomalous hall effect in the trigonal Cr_5Te_8 single crystal, Phys. Rev. B 98 (2018) 195122.

[47] S. Nakatsuji, N. Kiyohara, T. Higo, Large anomalous Hall effect in a non-collinear antiferromagnet at room temperature, Nature 527 (2015) 212–215.

[48] K. Kuroda, T. Tomita, M.-T. Suzuki, C. Bareille, A. Nugroho, P. Goswami, M. Ochi, M. Ikhlas, M. Nakayama, S. Akebi, R. Noguchi, R. Ishii, N. Inami, K. Ono, H. Kumigashira, A. Varykhalov, T. Muro, T. Koretsune, R. Arita, S. Shin, T. Kondo, S. Nakatsuji, Evidence for magnetic Weyl fermions in a correlated metal, Nat. Mater. 16 (2017) 1090–1095.

[49] N. Kanazawa, Y. Onose, T. Arima, D. Okuyama, K. Ohoyama, S. Wakimoto, K. Kakurai, S. Ishiwata, Y. Tokura, Large Topological Hall Effect in a Short-Period Helimagnet MnGe, Phys. Rev. Lett. 106 (2011) 156603.

[50] S. N. Kaul, Anomalous Hall effect in nickel and nickel-rich nickel-copper alloys, Phys. Rev. B 20 (1979) 5122–5130.

[51] N. Nagaosa, J. Sinova, S. Onoda, A. H. MacDonald, N. P. Ong, Anomalous hall effect, Rev. Mod. Phys. 82 (2010) 1539–1592.

[52] C. Zeng, Y. Yao, Q. Niu, H. H. Weitering, Linear magnetization dependence of the intrinsic anomalous hall effect, Phys. Rev. Lett. 96 (2006) 037204.

[53] L. Berger, Side-jump mechanism for the hall effect of ferromagnets, Phys. Rev. B 2 (1970) 4559–4566.

[54] J. Shen, S. Zhang, T. Liang, J. Wang, Q. Zeng, Y. Wang, H. Wei, E. Liu, X. Xu, Intrinsically enhanced anomalous Hall conductivity and Hall angle in Sb-doped magnetic Weyl semimetal $Co_3Sn_2S_2$, APL Mater. 10 (2022) 090705.

[55] Y. Tian, L. Ye, X. Jin, Proper scaling of the anomalous hall effect, Phys. Rev. Lett. 103 (2009) 087206.

[56] Y. Wang, C. Xian, J. Wang, B. Liu, L. Ling, L. Zhang, L. Cao, Z. Qu, Y. Xiong, Anisotropic anomalous hall effect in triangular itinerant ferromagnet $\mathrm{Fe_3GeTe_2}$, Phys. Rev. B 96 (2017) 134428.

[57] Y. Liu, C. Petrovic, Anomalous Hall effect in the trigonal $\mathrm{Cr_5Te_8}$ single crystal, Phys. Rev. B 98 (2018) 195122.

[58] Z. Z. Jiang, X. Luo, J. Yan, J. J. Gao, W. Wang, G. C. Zhao, Y. Sun, J. G. Si, W. J. Lu, P. Tong, X. B. Zhu, W. H. Song, Y. P. Sun, Magnetic anisotropy and anomalous Hall effect in monoclinic single crystal $\mathrm{Cr_5Te_8}$, Phys. Rev. B 102 (2020) 144433.

[59] Y. Liu, H. Tan, Z. Hu, B. Yan, C. Petrovic, Anomalous Hall effect in the weak-itinerant ferrimagnet $\mathrm{FeCr_2Te_4}$, Phys. Rev. B 103 (2021) 045106.

[60] S. Onoda, N. Sugimoto, N. Nagaosa, Intrinsic Versus Extrinsic Anomalous Hall Effect in Ferromagnets, Phys. Rev. Lett. 97 (2006) 126602.

[61] X. Zheng, X. Zhao, J. Qi, X. Luo, S. Ma, C. Chen, H. Zeng, G. Yu, N. Fang, S. U. Rehman, et al., Giant topological hall effect around room temperature in noncollinear ferromagnet $\mathrm{NdMn_2Ge_2}$ single crystal, Applied Physics Letters 118 (2021) 072402.

[62] Z. Liu, A. Burigu, Y. Zhang, H. M. Jafri, X. Ma, E. Liu, W. Wang, G. Wu, Giant topological hall effect in tetragonal heusler alloy Mn_2PtSn, Scripta Materialia 143 (2018) 122–125.

[63] T. Kurumaji, T. Nakajima, M. Hirschberger, A. Kikkawa, Y. Yamasaki, H. Sagayama, H. Nakao, Y. Taguchi, T.-h. Arima, Y. Tokura, Skyrmion lattice with a giant topological hall effect in a frustrated triangular-lattice magnet, Science 365 (2019) 914–918.

[64] G. Gong, L. Xu, Y. Bai, Y. Wang, S. Yuan, Y. Liu, Z. Tian, Large topological hall effect near room temperature in noncollinear ferromagnet $LaMn_2Ge_2$ single crystal, Phys. Rev. Materials 5 (2021) 034405.

[65] Y. He, J. Kroder, J. Gayles, C. Fu, Y. Pan, W. Schnelle, C. Felser, G. H. Fecher, Large topological hall effect in an easy-cone ferromagnet $Cr_{0.9}B_{0.1}Te$, Applied Physics Letters 117 (2020) 052409.

[66] H. Li, B. Ding, J. Chen, Z. Li, E. Liu, X. Xi, G. Wu, W. Wang, Large anisotropic topological hall effect in a hexagonal non-collinear magnet Fe_5Sn_3, Applied Physics Letters 116 (2020) 182405.

[67] Q. Wang, Q. Yin, H. Lei, Giant topological hall effect of ferromagnetic kagome metal Fe_3Sn_2, Chinese Physics B 29 (2020) 017101.

[68] X. Yu, Y. Onose, N. Kanazawa, J. H. Park, J. Han, Y. Matsui, N. Nagaosa, Y. Tokura, Real-space observation of a two-dimensional skyrmion crystal, Nature 465 (2010) 901–904.

[69] W. Jiang, G. Chen, K. Liu, J. Zang, S. G. Te Velthuis, A. Hoffmann, Skyrmions in magnetic multilayers, Physics Reports 704 (2017) 1–49.

[70] O. Meshcheriakova, S. Chadov, A. K. Nayak, U. K. Rößler, J. Kübler, G. André, A. A. Tsirlin, J. Kiss, S. Hausdorf, A. Kalache, W. Schnelle, M. Nicklas, C. Felser, Large Noncollinearity and Spin Reorientation in the Novel Mn_2RhSn Heusler Magnet, Phys. Rev. Lett. 113 (2014) 087203.

[71] P. K. Rout, P. V. P. Madduri, S. K. Manna, A. K. Nayak, Field-induced topological hall effect in the noncoplanar triangular antiferromagnetic geometry of Mn_3Sn, Phys. Rev. B 99 (2019) 094430.

[72] B. Ding, Z. Li, G. Xu, H. Li, Z. Hou, E. Liu, X. Xi, F. Xu, Y. Yao, W. Wang, Observation of magnetic skyrmion bubbles in a van der waals ferromagnet Fe_3GeTe_2, Nano Letters 20 (2019) 868–873.

[73] D. A. Gilbert, B. B. Maranville, A. L. Balk, B. J. Kirby, P. Fischer, D. T. Pierce, J. Unguris, J. A. Borchers, K. Liu, Realization of ground-state artificial skyrmion lattices at room temperature, Nature communications 6 (2015) 1–7.

[74] M. Nakamura, D. Morikawa, X. Yu, F. Kagawa, T.-h. Arima, Y. Tokura, M. Kawasaki, Emergence of topological hall effect in half-metallic manganite thin films by tuning perpendicular magnetic anisotropy, Journal of the Physical Society of Japan 87 (2018) 074704.

[75] Y. Machida, S. Nakatsuji, Y. Maeno, T. Tayama, T. Sakakibara, S. Onoda, Unconventional anomalous hall effect enhanced by a noncoplanar spin texture in the frustrated kondo lattice $Pr_2Ir_2O_7$, Phys. Rev. Lett. 98 (2007) 057203.

[76] Y. Taguchi, Y. Oohara, H. Yoshizawa, N. Nagaosa, Y. Tokura, Spin chirality, berry phase, and anomalous hall effect in a frustrated ferromagnet, Science 291 (2001) 2573–2576.

[77] H. Wang, Y. Dai, G. M. Chow, J. Chen, Topological hall transport: materials, mechanisms and potential applications, Progress in Materials Science (2022) 100971.

Chapter 5

Experimental and Computational Insights Into the Magnetic Anisotropy and Magnetic Behaviour of Layered Room-Temperature Ferromagnet $Cr_{1.38}Te_2$

5.1 Introduction

Two-dimensional (2D) van der Waals (vdW) magnetic materials with intrinsic long-range ferromagnetic (FM) ordering have recently received immense research interests due to their potential technological applications in the low-power spintronic devices [1–6]. However, their technological applications are limited as the ferromagnetic long-range ordering is destabilized by the dominating thermal fluctuations at higher temperatures [7]. In this regard, strong magnetic anisotropy is required to stabilize the long-range magnetic ordering at room temperature to overcome the thermal fluctuations. Recently, several 2D magnetic materials such as CrI_3 ($T_C \approx 45$ K) [8], $Cr_2Ge_2Te_6$ ($T_C \approx 61$ K) [9], and $Cr_2Si_2Te_6$ ($T_C \approx 32$ K) [10] were synthesized with weak inter-layer coupling leading to strong magnetic anisotropy, but the T_C of these systems is far below the room temperature (RT). Therefore, investigating the layered room-temperature 2D ferromagnetic materials with large magnetocrystalline anisotropy is crucial for potential applications in spintronics and data storage devices [11–13].

On the other hand, theoretically, it was proposed that the layered binary chromium-based telluride, $Cr_{1+x}Te_2$ ($0<x<1$), are potential candidates to realize the much-anticipated

---

This chapter is based on the publication: **Shubham Purwar et al., Physica Scripta, 99, 085949 (2024)** room-temperature 2D ferromagnetism in the bulk [14]. Since then, many $Cr_{1+x}Te_2$ based compounds were grown experimentally to study their peculiar 2D magnetism. Generally, $Cr_{1+x}Te_2$ possess alternative stacking of $CrTe_2$ (Cr-full) layers intercalated by the Cr-layers (Cr-vacant) within the van der Waals gap between the two $CrTe_2$ layers stacked along the crystal growth axis [15]. Importantly, the intercalated Cr atoms play a vital role in exhibiting various structural, magnetic, and magnetotransport properties depending on the amount of intercalated Cr present in the system. For instance, $Cr_{1+x}Te_2$ with x > 0.8 forms into the hexagonal NiAs-type structure [16], $Cr_{1.33}Te_2$ (Cr_2Te_3) and $Cr_{1.5}Te_2$ (Cr_3Te_4) crystallize into trigonal or monoclinic symmetries [17, 15], $Cr_{1.25}Te_2$ (Cr_5Te_8) forms into the trigonal phase at higher temperatures and forms into monoclinic phase at low temperatures [16, 18]. Interestingly, several recent reports on $Cr_{1+x}Te_2$ systems reveal exotic physical properties such as the noncollinear spin-textures [19], anomalous and topological Hall effects (AHE) [20–23], and skyrmion lattice [22, 24]. In addition, as the FM vdW materials are best suited for magnetic refrigeration due to their large magnetocaloric effect (MCE), these systems have also attracted a great deal of research interest from this direction as well [25].

In this contribution, magnetic properties, critical behaviour analysis, and magnetocaloric effect have been studied in detail on the high-quality single crystals of monoclinic $Cr_{1.38}Te_2$. We systematically investigated the structural properties of $Cr_{1.38}Te_2$ by performing temperature dependent X-ray diffraction measurements and established a relation between the magnetic transitions and the crystal lattice. The critical exponents were investigated by the modified Arrott plot, the Kouvel-Fisher method, and the critical isotherm analysis. The critical exponents are tested to be self-consistent and obey the rescaling mechanism around the T_C. The Monte-Carlo simulations were conducted to reproduce the experimentally obtained critical exponents. Since the critical exponents do not fall into any particular universality class of the magnetic interactions, we employed the renormalization group (RG) theory. The RG theory suggests 3D-Ising type long-range exchange interactions $[J(r)]$ in $Cr_{1.38}Te_2$, decaying with distance (r) as $J(r) = r^{-(d+\sigma)} = r^{-4.73}$. Further, magnetocrystalline anisotropy energy density (K_u) is found to be temperature dependent, reaching the maximum (180 k-J/m^3) at 110 K. The magnetic easy-axis is identified theoretically by analyzing the magnetocrystalline anisotropy energy (MAE) using the density functional theory calculations. Further, we have explored the isothermal magnetic entropy change $-\Delta S_m$ as a function of the field.

5.2 Experimental and Computational Methods

High-quality single crystals were grown using the chemical vapour transport (CVT) method with iodine as a transport agent [26]. The exact chemical composition of the as-grown single crystals was determined to be $Cr_{1.38(2)}Te_2$ using the energy dispersive X-ray spectroscopy

(EDS), indicates a 38% of excess Cr compared to the nominal composition of $CrTe_2$. The as-grown single crystals were large in size (4×4 mm^2) and were looking shiny. Powder X-ray diffraction (XRD) measurements were performed on the crushed single crystals using Rigaku X-ray diffractometer (SmartLab, 9kW) with Cu K_α radiation of wavelength 1.5406 Å at various sample temperatures. Magnetic measurements [$M(T)$ and $M(H)$] were carried out using the physical property measurement system (9 Tesla-PPMS, DynaCool, Quantum Design).

We performed density functional theory (DFT) calculations to determine the ground state magnetic easy axis in $Cr_{1.38}Te_2$ crystal. For this purpose, we used the crystal structure determined from our experimental data. We employed plane-wave basis set as implemented in QUANTUM-ESPRESSO (QE) simulation package [27], with fully relativistic pseudopotentials of Perdew-Burke-Ernzerhof (PBE) type exchange and correlations [28]. We utilized a k-point mesh of 3×8×6 with electronic relaxation convergence upto 1E-9Ry without any external constraints. Spin-orbit coupling (SOC) was included for all the magnetocrystalline anisotropy energy (MAE) calculations. We followed the force theorem as implemented in QE and a two-step process to describe the MAE [29]. Initially, the self-consistent field (SCF) calculations were performed with scalar-relativistic pseudopotentials to obtain the charge density and the spin moment distribution in real space. After that the spin moment is globally rotated to a desired direction and the spin moment-dependent energy was calculated through non-SCF calculations. The energy difference between two spin moment directions gives the MAE.

Monte-Carlo simulations using the single-flip Metropolis algorithm was conducted to investigate the critical behavior of $Cr_{1.38}Te_2$ [30–32]. To capture the characteristic behaviour, we adapted a discrete 3D Ising-like spin model with the Hamiltonian,

$$H = -\sum_{<i,j>} J_{ij} S_i S_j - h \sum_i S_i \tag{5.1}$$

where, h is the external applied field, J_{ij} is the nearest neighbour (NN) exchange interaction. S_i and S_j are the total spin at the i^{th} and j^{th} site, respectively. The value of J_{ij} is calculated from the density functional theory (DFT) as discussed in the Monte-Carlo simulations section.

5.3 Results and Discussion

5.3.1 Structural Properties

Figure 5.1(a) shows powder XRD patterns of the crushed $Cr_{1.38}Te_2$ single crystals measured at various sample temperatures. The top-right inset in Fig. 5.1(a) shows the Rietveld refinement of the room temperature XRD pattern performed using the Fullprof software [33],

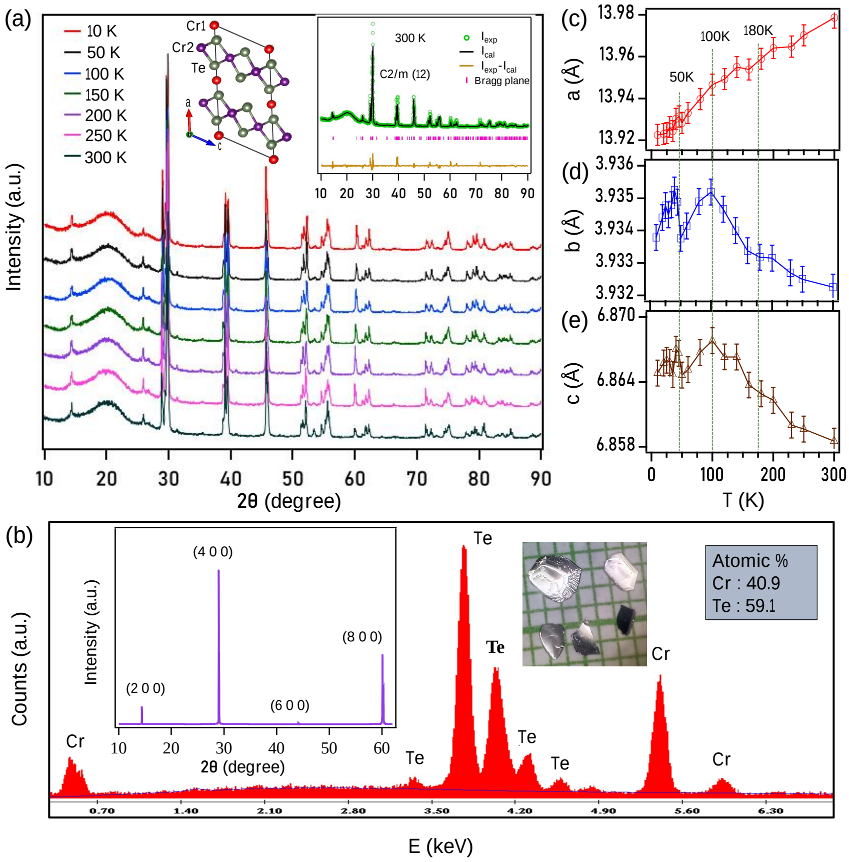

Figure 5.1: Structural analysis of $Cr_{1.38}Te_2$. (a) X-ray diffraction (XRD) measured at different sample temperatures in the range of 10-300 K. Top-right inset in (a) shows XRD pattern measured at T=300 K overlapped with Rietveld refinement. The middle inset in (a) shows a schematic diagram of the crystal structure derived from the Rietveld refinement. (b) Energy dispersive X-ray spectroscopy data showing the actual chemical composition by the atomic percentage. Insets in (b) present X-ray diffraction pattern and photographic image of $Cr_{1.38}Te_2$ single crystal. (c), (d), and (e) show temperature dependent lattice parameters a, b, and c, respectively.

confirming the monoclinic crystal structure with a space group of $C2/m$ (12) without any impurity phases. At room temperature, the lattice parameters were found to be $a = 13.9655(2)$ Å, $b = 3.9354(4)$ Å, $c = 6.8651(7)$ Å, $\alpha = \beta = 90°$, and $\gamma = 118.326(7)°$. The layered crystal structure of $Cr_{1.38}Te_2$ is schematically shown in the middle inset of Fig. 5.1(a). There are two types of Cr [Cr(1) and Cr(2)] atoms present in the unit cell in such a way that the intercalated Cr(1) atoms are sandwiched between two Cr(2)Te_2 layers. Fig. 5.1(b) shows EDS spectra of as-grown single crystals, confirming the actual chemical composition of $Cr_{1.38}Te_2$ (see the table at the top-right inset). The middle inset in Fig. 5.1(b) shows photographic image of several $Cr_{1.38}Te_2$ single crystals. The top-left inset in Fig. 5.1(b) depicts the XRD pattern taken on a $Cr_{1.38}Te_2$ single crystal, showing the intensity of (2 0 0) Bragg's plane, confirming that the crystal growth is along the a-axis. Figs. 5.1(c), 5.1(d), and 5.1(e) depict the temperature dependent lattice parameters of a, b, and c, respectively. Although we do not observe any low-temperature structural phase transition in $Cr_{1.38}Te_2$ as no splitting in the Bragg's peaks is noticed down to 10 K. However, we could observe a monotonic decrease in the lattice constant a with decreasing temperature. On the other hand, we observe unusual behavior of the lattice constants b and c with temperature. Specifically, down to 100 K, both b and c monotonically increase with decreasing temperature. But below 100 K, b and c decrease with decreasing temperature to have a minimum at 50 K and again increase with decreasing temperature to peak out at 35 K. Worth to mention here that at around 180±20 K we find a noticeable change in the lattice constants a, b and c. Such an unusual lattice constants behavior with temperature plausibly due to the magneto-volume effect in these type of systems $Cr_{1+x}Te_2$ [34, 35].

5.3.2 Magnetic Properties

Magnetization of $Cr_{1.38}Te_2$ plotted as a function of temperature [$M(T)$], measured at a magnetic field (H) of 100 Oe, applied perpendicular ($H \parallel bc$) and parallel ($H \parallel a$) to the a-axis is shown in Figs. 5.2(a) and 5.2(b), respectively taken in the field-cooled (FC) and zero-field-cooled (ZFC) modes. Figs. 5.2(c)-(d) and Figs. 5.2(e)-(f) are same as Figs. 5.2(a)-(b) except that the former data are measured at $H = 500$ Oe and the latter data are measured at $H = 5000$ Oe. From Fig. 5.2, we observe a high-temperature paramagnetic (PM) to a low-temperature ferromagnetic (FM) transition at around a Curie temperature of $T_C \approx 315\pm0.5$ K, which is close to the previously reported value of 316 K on a similar system [36]. In the ferromagnetic state, we observe a significant thermal irreversibility between ZFC and FC modes for the low applied fields [see Figs. 5.2(a) and 5.2(b)], indicating the presence of magnetocrystalline anisotropy (MCA) in the system [37, 38]. In addition, we notice another magnetic transition at around 50 K for $H \parallel bc$ and $H \parallel a$. While the magnetic transition for $H \parallel bc$ looks more like a spin-canting effect, the magnetic transition for $H \parallel a$ is an antiferromagnetic type. Such complex low-temperature directional-dependent magnetic transitions can be attributed to the competition between FM and canted-AFM phases [39–41]. Further, with increasing applied magnetic field, the spin-canting type in-plane (bc-plane) magnetic transition gradually dissipates [see Figs. 5.2(b) and 5.2(c)] and becomes a clean AFM-type at higher applied fields. Similarly, the out-of-plane (a-axis) AFM transition gradually dissipates with increasing applied field and completely disappears at $H = 5000$ Oe. In support of the magneto-volume effect in these systems [34, 35], we could clearly find a change in magnetization $M(T)$ (FC data) at around $T_t = 180$ K where we also observe a noticeable change in the lattice constants [see Figs. 5.1(c)-(d)].

Previous neutron diffraction studies on $Cr_{1.5}Te_2$ suggested a mixed spin-state of Cr^{2+} (Cr1) and Cr^{3+} (Cr2), leading to a canted spin structure due to the ferromagnetic components of Cr1 and Cr2 tilted by 30^o and 38^o, respectively, about the a-axis and the antiferromagnetic (AF) components of Cr1 and Cr2 are aligned in the bc-plane [42]. Therefore,

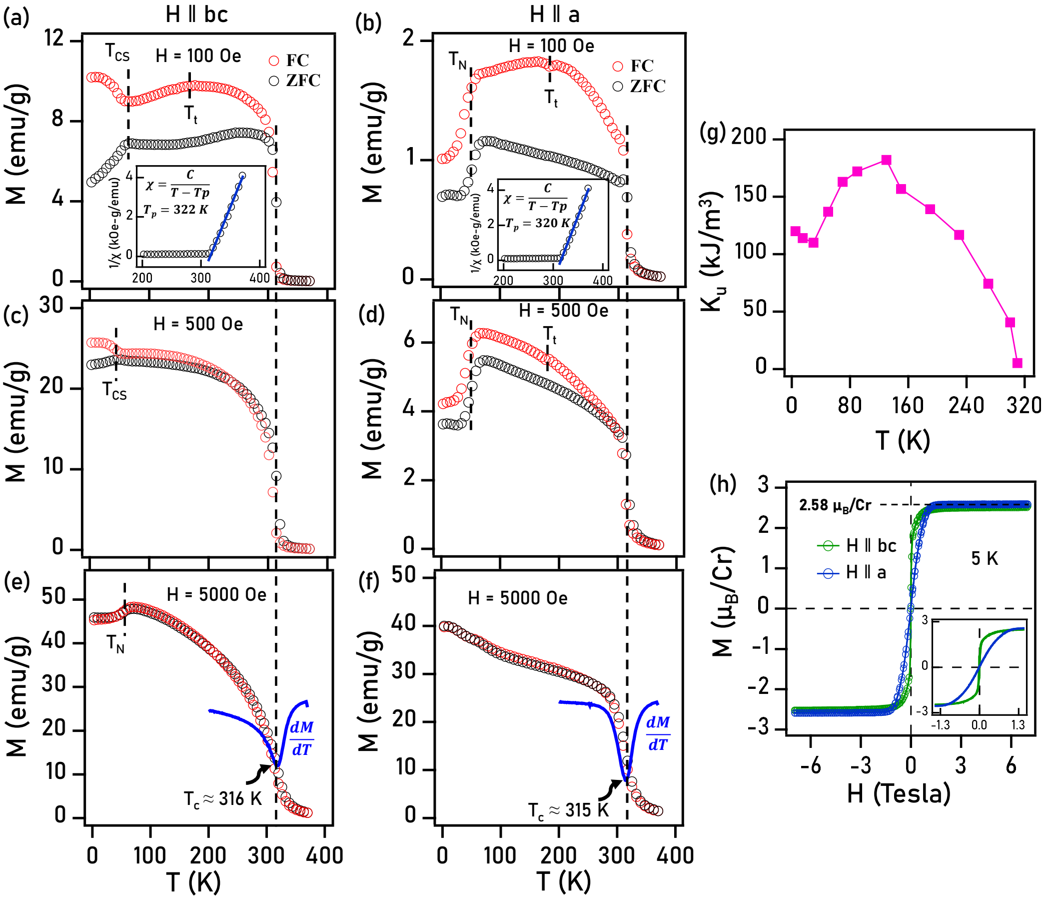

Figure 5.2: Temperature dependent magnetization $M(T)$ measured under zero-field-cooling (ZFC) and field-cooling (FC) modes at different applied magnetic fields (H). (a)-(f) show the $M(T)$ measured at various fields for $H \parallel bc$ and $H \parallel a$. Insets in (a) and (b) show the fittings with Curie-Weiss law. Here T_C is the Curie temperature, T_N is the Néel temperature, T_{CS} is the spin-canting related transition, and T_t is lattice related transition. Blue curves in (e) and (f) represent dM/dT in which the peak-dip corresponds to the Curie temperature (T_C). (g) Magnetocrystalline anisotropy energy density (K_u) is plotted as a function of temperature. (h) Magnetization isotherms $M(H)$ measured at T = 5 K for $H \parallel bc$ and $H \parallel a$. Inset in (h) shows the zoomed-in image demonstrating the magnetic anisotropy between $H \parallel bc$ and $H \parallel a$.

the competition between FM and AFM phases could be playing a vital role in garnering the multiple magnetic transitions, in addition to the canted spin structure, in these systems [43, 44]. The inverse susceptibility ($1/\chi$) plotted as a function of temperature, as shown in the inset of Figs. 5.2(a) and 5.2(b), for both field directions follow the Curie-Weiss law $\chi(T) = C/(T - T_p)$. Here χ is magnetic susceptibility, C is the Curie constant, and T_p is the Curie-Weiss temperature. From the fittings we obtained T$_p$ that are greater than T_C for both directions, indicating a predominant FM exchange interactions in this system. We further calculated the effective magnetic moment in the paramagnetic region using the relation $\mu_{eff} \approx 2.84\sqrt{MC}$ [45], where M is a molar-mass (in gram). The calculated effective moment (μ_{eff}) is 4.531 μ_B for $H \parallel a$ and 4.403 μ_B for $H \parallel bc$. The values of μ_{eff} lies between the theoretical predictions of 3.87 μ_B for Cr^{3+} and 4.90 μ_B for Cr^{2+}, the mixed valence state existing in this system is consistent with previous reports [39, 42, 46].

Further, the magnetocrystalline anisotropy energy density K_u can be obtained using the Eqn. 5.2. Fig. 5.2(g) depicts K_u plotted as a function of temperature. We can observe that K_u monotonically increases with decreasing temperature from 320 K down to 110 K. But below 110 K, due to the additional magnetic transition as noticed in Fig. 5.2, K_u decreases with decreasing temperature. Usually during the disorder to order magnetic transition (PM-FM), the $Cr_{1+x}Te_2$-based systems exhibit a negative volume thermal-expansion leading to strong magnetoelastic coupling [47]. The same could be true in our studied system of $Cr_{1.38}Te_2$ as well, as we observe fluctuating lattice constants below 110 K [see Figs. 5.1(c-e)]. Nevertheless, the obtained K_u = 120 kJ/m^3 at 2 K in $Cr_{1.38}Te_2$ is much higher than the K_u values of some of the other 2D magnetic systems such as $CrBr_3$ ($\approx$ 86 kJ/m^3 at 5 K) [48], $Cr_2Ge_2Te_6$ ($\approx$ 20 kJ/m^3 at 2 K) [49], and $Cr_2Si_2Te_6$ ($\approx$ 65 kJ/m^3 at 2 K) [49]. Further, the large $K_u \approx 180$ kJ/m^3 at 110 K with a Curie temperature of 315 K observed in $Cr_{1.38}Te_2$ poses potential room-temperature technological applications in magnetic storage devices [50], spin valves [51], magnetic tunnel junctions [51], and spin-transfer torque devices [52].

$$K_u = \mu_0 \int_o^{M_s} [H_{bc}(M) - H_a(M)]dM \tag{5.2}$$

Fig. 5.2(h) depicts the magnetization isotherms $M(H)$ measured for $H \parallel bc$ and $H \parallel a$ at T=5 K, respectively, suggesting the *bc*-plane as the easy-plane of magnetization. Further, since we do not observe significant hysteresis in the $M(H)$ curves, $Cr_{1.38}Te_2$ can act as a soft ferromagnet. The in-plane and out-of-plane saturation magnetization (M_S) are found to be 2.55 μ_B and 2.586 μ_B, respectively, which are smaller compared to the free-Cr ion (3.0 μ_B). This discrepancy may be ascribed to the itinerant nature of $Cr_{1.38}Te_2$ [53]. To check the degree of itinerancy in $Cr_{1.38}Te_2$, we employed the itinerant magnetism model by Rhodes and Wohlfarth [54, 55]. In this method, one estimates the Rhodes-Wohlfarth ratio (RWR), M_c/M_S. Here M_S is the saturation magnetization and M_c is the ground state magnetic moment which is calculated using the equation $M_c(M_c + 2) = \mu_{eff}^2$. In this way, we estimated RWR=1.89 for $H \parallel a$ and RWR = 1.82 for $H \parallel bc$. It is known that for the localized magnetic systems $RWR = 1$ and for the itinerant systems $RWR > 1$ [54, 55]. Since estimated RWR values of $Cr_{1.38}Te_2$ are greater than one, it must be an itinerant magnetic system.

To further elucidate the magnetic structure of $Cr_{1.38}Te_2$, we performed DFT calculations as shown in Fig. 5.3. We calculated the magnetocrystalline anisotropy energy (MAE) of $Cr_{1.38}Te_2$ for three different spin structures projected onto the *ac*-, *bc*-, and *ab*-planes as described in the Figs. 5.3(a), 5.3(b), and 5.3(c), respectively. In Fig. 5.3(d), the blue-, red- and black-curves show the MAE plotted for the spin configurations shown in Figs. 5.3(a), 5.3(b), and 5.3(c), respectively. From Fig. 5.3(d), it is clear that the spin

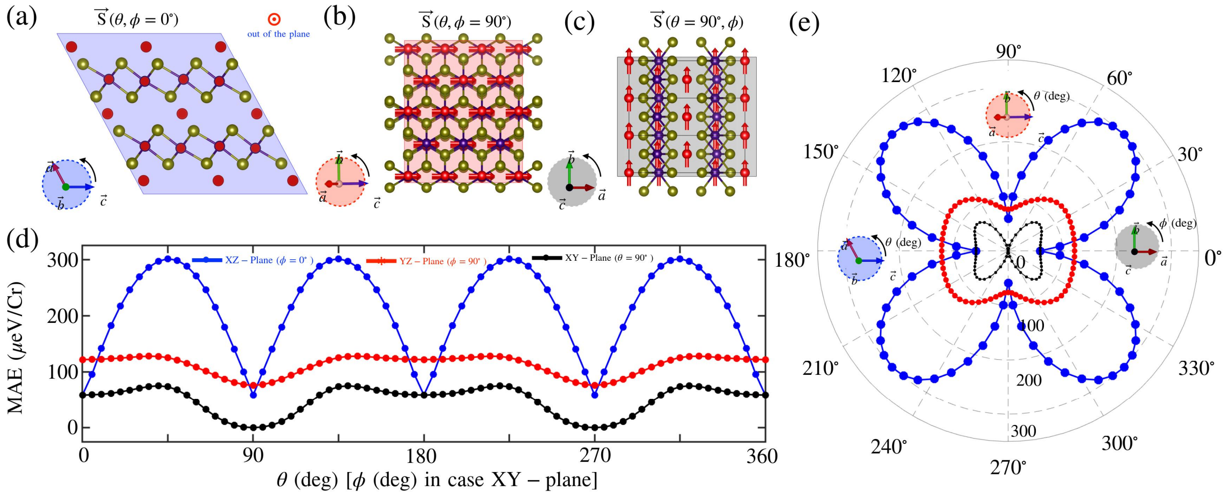

Figure 5.3: The magnetocrystalline anisotropy energy (MAE) of $Cr_{1.38}Te_2$: The spin direction of Cr atoms, denoted as S(θ), is defined as $\theta = 0°$ along the Z-axis. The inclined spin direction ($\theta \neq 0$) projects onto the XY-plane, with the projection measured from the X-axis at an angle (ϕ). $\phi = 0°$ aligns with the X-axis. For $\theta \neq 0$, the spin moment direction with $\phi = 0°$ is confined to the XZ-plane, and for $\theta \neq 0$ and $\phi = 90°$, the spin rotation is restricted to the YZ-plane. XY-plane spin rotation occurs at $\theta = 90°$ with $\phi \neq 0$. The spin rotation (S) of Cr atoms in $Cr_{1.38}Te_2$ is described in three planes (a) XZ (ac)-plane, (b) YZ (bc)-plane, and (c) XY (ab)-plane. (d) MAE per Cr atom for $Cr_{1.38}Te_2$ concerning spin rotation in three different planes. (e) MAE plotted in polar graph for a better visualization.

configuration shown Fig. 5.3(c) has the minimum MAE at $\theta = \phi = 90°$. That means, the ground state magentic easy-axis of $Cr_{1.38}Te_2$ is parallel to the *b*-axis, which is precisely predicted compared to the experimental observation of *bc*-plane. It is further interesting to note that the projected spin configurations onto the *ab*- and *ac*-planes have the same magnetocrystalline anisotropy energy along the *c*- and *a*-axes. Further, maximum energy is found at $\theta = 45°$ for all the spin configurations and the highest MAE is found for the spin configuration shown in Figs. 5.3(c). Fig. 5.3(e) depicts the angle-dependent MAE plotted in the polar graph for a better visualization. From Fig. 5.3(e) we can notice that the magnetocrystalline anisotropy energy of the spin configuration shown in Fig. 5.3(a) has the four-fold symmetry, while the MAE of the spin configurations shown in Figs. 5.3(b) and 5.3(c) have the two-fold symmetry.

5.3.3 Critical Analysis

To understand the nature and dimensionality of the ferromagnetism in $Cr_{1.38}Te_2$, we investigated the critical exponents β, δ, γ which are coupled to the spontaneous magnetization (M_{SP}) below T_C, inverse initial susceptibility $\chi_0^{-1}(T)$ above T_C , and magnetization isotherms $[M(H)]$ at T_C, respectively. In this regard, magnetization isotherms $M(H)$ measured within the temperature of 290 to 338 K with a step size of 2 K for both $H \parallel bc$ and

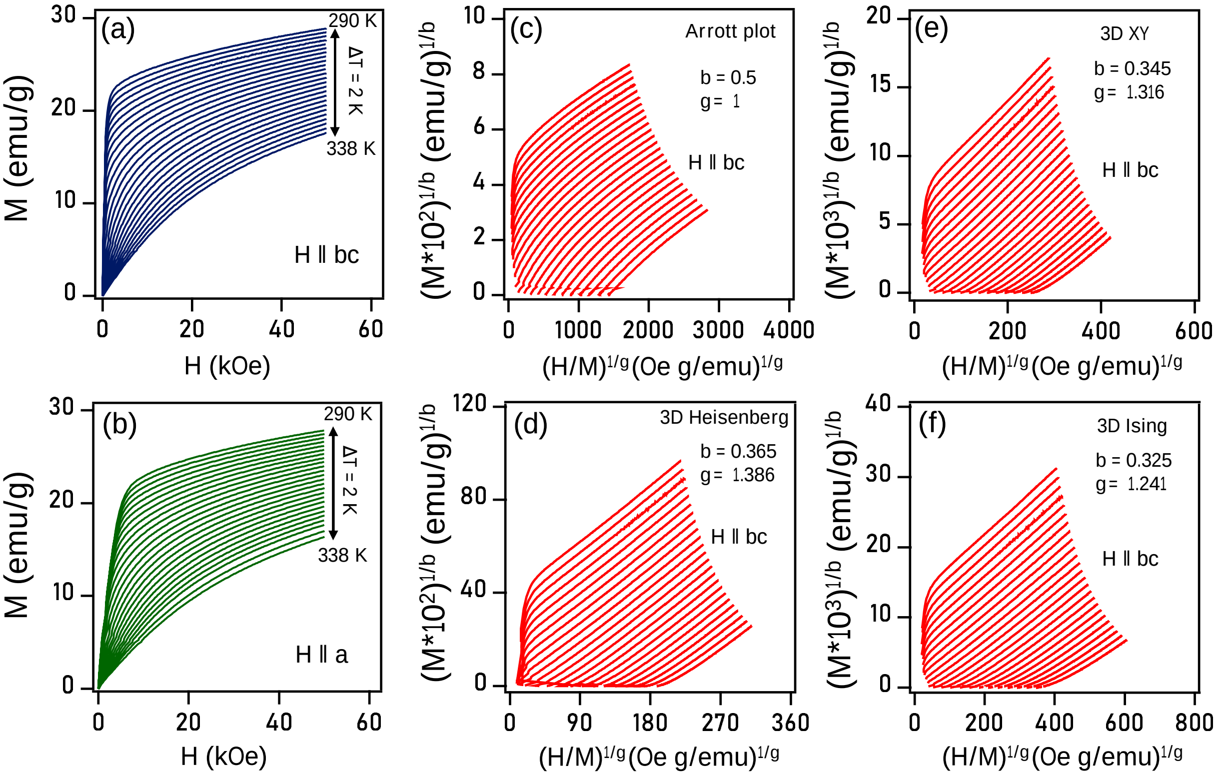

Figure 5.4: Isothermal magnetization $M(H)$ measured between 290 and 338 K at an interval of $\Delta T = 2$ K for (a) $H \parallel bc$ and (b) $H \parallel a$. (c) Arrott plots of M^2 vs H/M. Modified Arrott plot (Arrott-Noaks plot) of $\mathrm{M}^{1/\beta}$ vs $(\mathrm{H/M})^{1/\gamma}$ for (d) 3D Heisenberg model, (e) 3D XY model, and (f) 3D Ising model done for the easy-plane of magnetization (bc-plane).

$H \parallel a$ are shown in Figs. 5.4(a) and 5.4(b), respectively. Fig. 5.4(c) shows Arrott plots (M^2 vs H/M) obtained from the $M(H)$ data. Usually Arrott plots show a set of parallel lines of various temperatures in the high field region [56]. At T_C, positive slope of the Arrott plot suggest second-order magnetic transition, while the negative slope of the Arrott plot suggest first-order magnetic transition [57]. Since the Arrot plot slope at T_C is positive in Fig. 5.4(c), the ferromagnetic transition observed in $\mathrm{Cr}_{1.38}\mathrm{Te}_2$ is a second-order phase transition. On the other hand, the scaling hypothesis suggests that the second-order phase transition around T_C can be described by a set of critical exponents and equations of the magnetic state [58]. Moreover, in the vicinity of second-order phase transition, the divergence of correlation length $\zeta = \zeta_0[(\mathrm{T} - \mathrm{T}_c)/\mathrm{T}_c]^{-\nu}$ leads to the universal scaling laws [58, 59]. The mathematical equations involving the critical exponents are given by,

$$M_{sp}(T) = M_0(-\epsilon)^{\beta}, for \quad \epsilon < 0, T < T_c \tag{5.3}$$

$$\chi_0^{-1}(T) = (h_0/m_0)\epsilon^{\gamma}, for \quad \epsilon > 0, T > T_c \tag{5.4}$$

$$M = DH^{1/\delta}, for \quad \epsilon = 0, T = T_c \tag{5.5}$$

where $\epsilon = (\mathrm{T} - \mathrm{T}_C)/\mathrm{T}_C$ is the reduced temperature, M_0, h_0/m_0, and D are the critical amplitudes [59]. To obtain the critical exponents β, γ, and δ as well as the exact value of T_C, we first tried the modified Arrott plot (MAP) technique and plotted $\mathrm{M}^{1/\beta}$ vs. $(\mathrm{H/M})^{1/\gamma}$ following different models around T_C. Fig. 5.4(d) shows MAP for 3D Heisenberg model ($\beta = 0.365, \gamma = 1.386$) [60], Fig. 5.4(e) shows MAP for 3D XY model ($\beta = 0.345, \gamma = 1.316$) [61], and Fig. 5.4(f) shows MAP for 3D Ising model ($\beta = 0.325, \gamma = 1.241$) [60]. Some other models like 2D-Ising model ($\beta = 0.125, \gamma = 1.75$) [62] and Tricritical mean field model ($\beta = 0.25, \gamma = 1$) [63] were also studied (not shown). It can be seen that none of these models can produce the required parallel lines in the high field region to properly explain the magnetic interactions present in $\mathrm{Cr}_{1.38}\mathrm{Te}_2$.

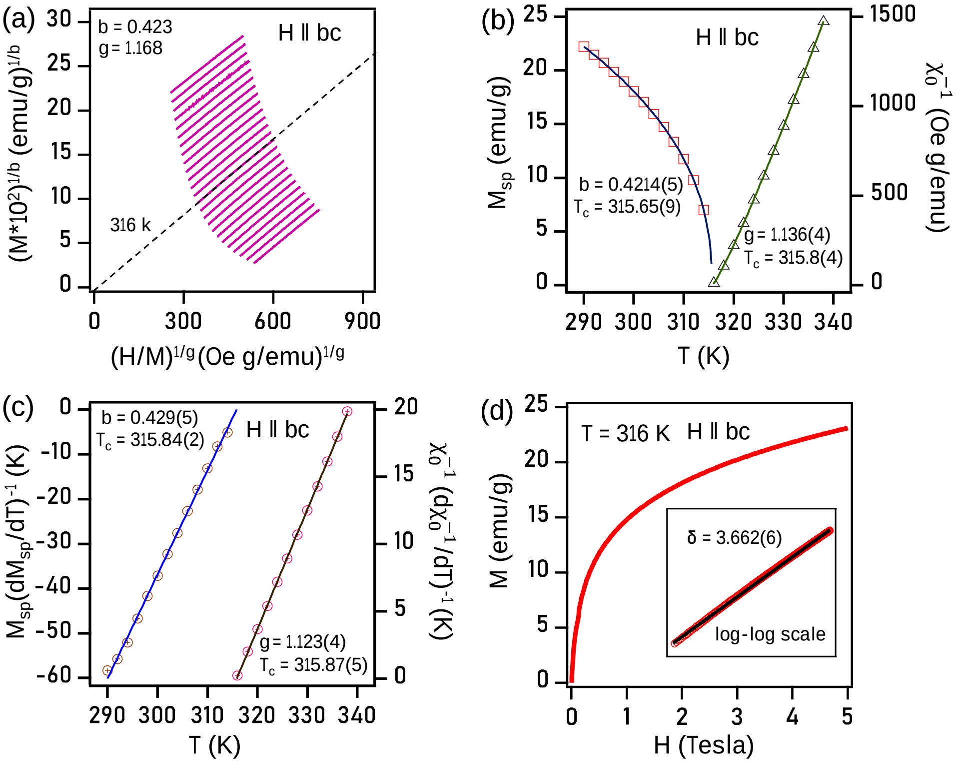

Figure 5.5: (a) Modified Arrott plot of $\mathrm{M}^{1/\beta}$ vs $(\mathrm{H/M})^{1/\gamma}$ done at high field values with critical parameters, $\beta = 0.423$ and $\gamma = 1.168$, (b) Temperature dependent spontaneous magnetization $\mathrm{M}_{sp}(\mathrm{T})$ (left axis) and inverse initial susceptibility $\chi_0^{-1}(T)$ (right axis). Solid curves in (b) are the fits by Eqns. 5.3 and 5.4. (c) Kouvel-Fisher plots as a function of temperature, $M_{sp}(T)[dM_{sp}(T)/dT]^{-1}$ (left axis) and $\chi_0^{-1}(T)[d\chi_0^{-1}(T)/dT]^{-1}$ (right axis). Solid lines in (c) are the fits by Eqns. 5.6 and 5.7, (d) Isothermal magnetization $M(H)$ plot at $T_C = 316$ K. Inset shows the plot in $log - log$ scale, fitted with the Eqn. 5.5.

Therefore, we used modified Arrott plot (MAP) technique iteratively and plotted $\mathrm{M}^{1/\beta}$ vs. $(\mathrm{H/M})^{1/\gamma}$ as shown in Fig. 5.5(a). This method produces the required parallel lines of all the measured temperatures. Thus, $\chi_0^{-1}(T)$ and $\mathrm{M}_{sp}(T)$ are the intercepts on the x-axis and y-axis of these linear plots, respectively [64, 65]. The critical exponents obtained in this method are given by β=0.423 and γ=1.168. Fig. 5.5(b) depicts M$_{sp}$ and χ_0^{-1} plotted as a function of temperature derived from Fig. 5.5(a). From the Eqns. 5.3 and 5.4 we estimate the critical exponents β = 0.421(5) with T_C = 315.65(9) K and γ = 1.136(4) with T_C = 315.8(4) K. The estimated T_C values are very close to the value of 315±0.5 K obtained from the $M(T)$ data [see Fig. 5.2]. Further, the critical exponents can be found more accurately using the Kouvel-Fisher (KF) plots [66], involving the equations,

$$M_{sp}(T)[dM_{sp}(T)/dT]^{-1} = (T - T_c)/\beta, \tag{5.6}$$

$$\chi_0^{-1}(T)[d\chi_0^{-1}(T)/dT]^{-1} = (T - T_c)/\gamma, \tag{5.7}$$

Fig. 5.5(c) depicts the KF plots fitted with the Eqns. 5.6 and 5.7 below and above T_C. The derived critical exponents in the KF method are given by β = 0.429(5) with T_C = 315.84(2) K and γ = 1.123(4) with T_C = 315.87(5) K, respectively. The values of β, γ, and T$_C$ obtained from the KF method are in good agreement with the values obtained from the MAP method, confirming that critical exponents are reliable and intrinsic.

In addition, the exponent δ has been calculated using the Widom scaling relation, δ = 1 + (γ/β) [67]. We estimate δ = 3.700(6) and δ = 3.617(8) from the MAP and the KF plots, respectively. Importantly, the δ values obtained from both MAP and KF methods are close to the value δ = 3.662(6) obtained from the critical isotherm (CI) method following the Eqn. 5.5 as shown in Fig. 5.5(d). Therefore, the critical exponents derived by different approaches are self-consistent and reasonably accurate within the experimental precision. Reliability of the derived critical exponents and the critical temperature has been examined by the scaling theory. For the magnetic materials, in the critical asymptotic region, the scaling equation of state is given by [58],

$$M(H, \epsilon) = \epsilon^{\beta} f_{\pm}(H/\epsilon^{\beta+\gamma}) \tag{5.8}$$

or

$$m = f_{\pm}(h) \tag{5.9}$$

where $m = \epsilon^{-\beta}M(H, \epsilon)$ is normalized magnetization and $h = H\epsilon^{-(\beta+\gamma)}$ is the normalized field. Now, if the β and γ values derived from the MAP and KF methods are appropriately chosen, the scaled magnetization m and field h should fall onto two different branches of the universal curves following the Eqns. 5.8 and 5.9. One branch is for $T < T_C$ and another branch is for $T > T_C$, as shown in Figs. 5.6(a) and 5.6(b). This suggests that the magnetic interactions get properly re-normalized in the vicinity of T_C. In addition, the scaling equation of state can also be expressed by,

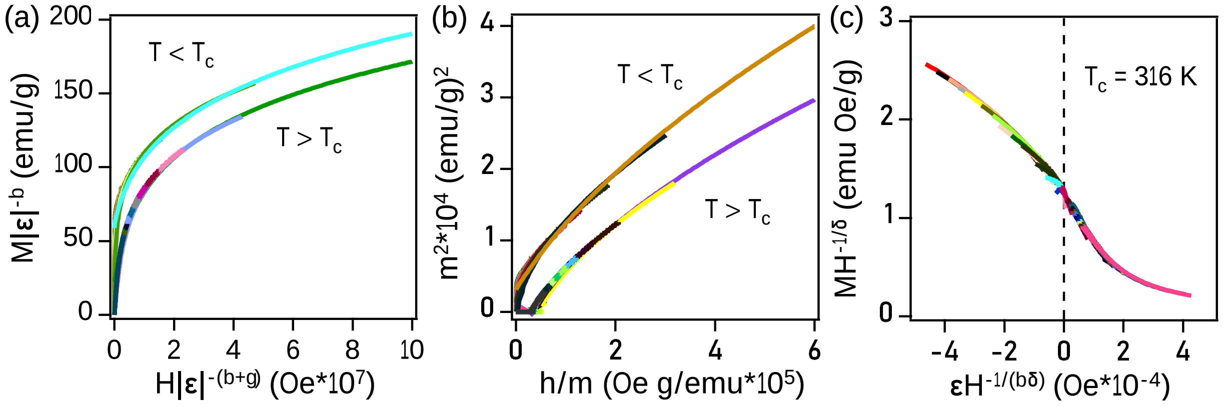

Figure 5.6: (a) and (b) are the plots of normalized magnetization $'m'$ as a function of re-normalized field $'h'$ below and above T_C. (c) Rescaling of $M(H)$ curves by MH$^{-1/\delta}$ vs $\epsilon H^{-1/\beta\delta}$.

$$\frac{H}{M^{\delta}} = k\frac{\epsilon}{H^{1/\beta}} \tag{5.10}$$

where k is the scaling constant. Thus, all the experimental data collapse into a single curve following the Eqn. 5.10 as shown in Fig. 5.6(c). In Fig. 5.6(c), T_C is located at the zero point of the x-axis. Therefore, the scaling hypothesis reaffirms the reliability of the derived critical exponents.

The obtained critical exponent $\beta = 0.429(5)$ is in between the 3D Heisenberg-type ($\beta = 0.365$) and the Landau mean-field-type ($\beta = 0.5$) magnetic interactions, whereas γ=1.123(4) is close to the 3D Ising model (γ=1.241). This indicates that $Cr_{1.38}Te_2$ does not fall into any particular universality class of the ferromagnetism, consistent with the complex magnetic interactions reported in previous studies on the similar systems [68, 69], except for that the reported β values are closer to the 3D Heisenberg-type. On the other hand, the renormalization group (RG) theory suggests that the long-range exchange interactions decay with the distance r as $J(r) = r^{-(d+\sigma)}$ and short-range exchange interactions decay as $J(r) = e^{-r/b}$, respectively [59, 62]. Here, d is the spatial dimensionality, σ is a positive constant, and b is a spatial scaling factor. The relation between the critical exponent γ and σ can be expressed by,

$$\gamma = 1 + \frac{4}{d}\frac{(n+2)}{(n+8)}\Delta\sigma + \frac{8(n-4)(n+2)}{(n+8)^2 d^2} * [\frac{2(7n+20)G(d/2)}{(n+8)(n-4)} + 1]\Delta\sigma^2 \tag{5.11}$$

where $\Delta\sigma = \sigma - d/2$, $G(d/2) = 3 - 0.25 * (d/2)^2$. n and d are the spin and spatial dimensionality of the system. RG theory analysis proposes that the spin interaction is either short or long-range depending on σ >2 or σ <2, respectively. By considering the experimental γ value of 1.123 from the KF method, following the RG theory, we have calculated the range of exchange interaction σ and critical exponent β following the equations, $\nu = \gamma/\sigma$, $\alpha = 2 - \nu * d$, $\beta = (2 - \alpha - \beta)/2$, where ν and α are the exponents of

Table 5.1: Comparison of the critical exponents of $Cr_{1.38}Te_2$ with different theoretical models.

Composition	Technique	Crystal Structure	β	γ	δ	Reference
$Cr_{1.38}Te_2$	MAP	Monoclinic	0.421(5)	1.136(4)		This work
	KF method	Monoclinic	0.429(5)	1.123(4)		This work
	Critical Isotherm	Monoclinic			3.662(6)	This work
	Monte-Carlo Simulation		0.413(1)	1.175(2)		This work
Theory	Landau mean field		0.5	1	3	[56]
Theory	3D Heisenberg		0.365	1.386	4.80	[60]
Theory	3D Ising		0.325	1.241	4.82	[60]

correlation length. This is done for various sets of $d : n$ values. We find that the critical exponents derived using $d : n = 3 : 1$ matches well with the values obtained from the KF method. From this, we suggest that $Cr_{1.38}Te_2$ is close to the 3D-Ising type exchange interactions with long-range order decaying as $J(r) = r^{-(d+\sigma)} = r^{-4.73}$ for $d = 3$ and σ=1.73.

In $Cr_{1+x}Te_2$ systems, the crystal structure features an alternating arrangement of a fully occupied $CrTe_2$-layer and a Cr-vacant layer along its growth direction. Tuning the x value not only influences the crystal symmetry, but also changes the spin configuration of the system [70, 53, 71–75]. Therefore, several studies exist on the critical analysis of $Cr_{1+x}Te_2$ systems and found differing exchange interactions for different Cr concentrations and crystal structures. For instance, the trigonal $CrTe_2$, trigonal $Cr_{1.25}Te_2$, the monoclinic $Cr_{1.5}Te_2$ exhibit 3D Ising-type magnetic interactions [53, 76, 77, 68], bulk and thin-film of trigonal $Cr_{1.6}Te_2$ follow 3D Heisenberg and mean-field type interactions, respectively [73, 78], thin-film hexagonal Cr_2Te_2 displays 2D Heisenberg type interactions [79].

5.3.4 Monte-Carlo Simulations

In order to be sure on the universality class of $Cr_{1.38}Te_2$, derived using the RG theory with the help of experimental critical exponents, we performed Monte-Carlo simulations on $Cr_{1.38}Te_2$ for the 3D-Ising model. In Fig. 5.7(a), we observe the energy-volume optimization for both FM and AFM configurations. The energy curve for FM exhibits the lowest energy compared to the AFM curve, indicating that the system possesses a ferromagnetic ground state, consistent with the experimental findings as shown in the main text. The derived ground-state energies of FM and AFM are -60623.565062 Ry and -60623.564555 Ry, respectively. The magnetic coupling constant (J) is determined by calculating the difference between these two ground-state energies, using the Eqn. 5.12 [80].

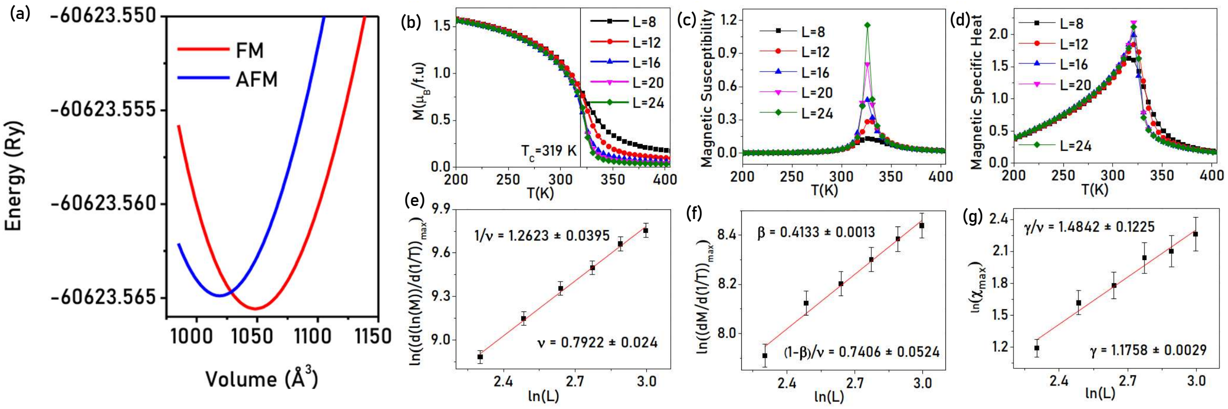

Figure 5.7: (a) The energy-volume curve for ferromagnetic and antiferromagnetic configurations of $Cr_{1.38}Te_2$ at room temperature, (b) Temperature dependent magnetization for different lattice sizes (L), (c) Magnetic susceptibility per spin plotted as a function of temperature, (d) Magnetic specific heat plotted as a function of temperature. $ln - ln$ plot of (e) $[\frac{d(lnM)}{d(1/T)}]_{max}$, (f) $[\frac{dM}{d(1/T)}]_{max}$, (g) χ_{max}. Red-colored line in (e), (f), and (g) are the linear fits.

$$J_{ij} = \frac{E_{\text{AFM}} - E_{\text{FM}}}{S_i \cdot S_j} \tag{5.12}$$

The spin components S_i and S_j refer to the Cr_1 and Cr_2 magnetic moments, as in this system, there are two types of Cr ions present with Cr^{2+} (Cr_1) and Cr^{3+} (Cr_2). Cr^{2+} has a total spin value of 2, while Cr^{3+} has 1.5. Using these spin values, we calculated the magnetic coupling constant (J) to be 2.29 meV. This value obtained from the first-principles calculations is subsequently utilized in the Monte Carlo simulation to solve the Ising-Model Hamiltonian. Figs. 5.7(b), 5.7(c), and 5.7(d) show the simulated temperature-dependent magnetization [$M(T)$], susceptibility [$\chi(T)$], and magnetic specific heat [$C_m(T)$] data following the Eqns. 5.13, 5.14, and 5.15, respectively. Importantly, the $M(T)$ data exhibit an ascending magnetization trend as the system is cooled and shows a paramagnetic to a ferromagnetic transition at a critical temperature of $T_C \approx$319 K. This critical temperature is very close to the experimental value of 316 K. From the magnetic susceptibility and magnetic specific heat data, depicted in Figs. 5.7(c) and 5.7(d), the peaks observed at 319 K again remarkably support the critical temperature obtained from the simulated magnetization. Further with the help of simulated magnetic data, we determined the critical exponents ν = 0.7922±0.024, β = 0.4133± 0.0013, and γ = 1.1758±0.0029, consistent with the experimental values. Critical exponents of $Cr_{1.38}Te_2$ obtained by various techniques such as MAP, KF, critical isotherm analysis, and Monte-Carlo simulations are tabulated in Tab 6.1. The critical exponents from various standard models such as the Landau meanfield, 3D Ising, and 3D Heisenberg are also listed in Tab 6.1.

$$M = < \frac{1}{N} \sum_i S_i > \tag{5.13}$$

$$\chi = \frac{< M^2 > - < M >^2}{k_B T} \tag{5.14}$$

$$C_m = \frac{< E^2 > - < E >^2}{k_B T^2} \tag{5.15}$$

The critical behavior of the observable quantities is determined by [81]:

$$M \sim |t|^{\beta} \tag{5.16}$$

$$\chi \sim |t|^{-\gamma} \tag{5.17}$$

$$C_m \sim |t|^{-\alpha} \tag{5.18}$$

In this context, α, β, and γ represent the critical exponents associated with specific quantities, and t is defined as

$$t = \frac{T - T_C}{T_C} \tag{5.19}$$

While infinite systems exhibit singularities in thermal quantities at the critical temperature, real-world systems are finite in size. As a result, the thermal quantities are determined by finite-size scaling laws, and their values evolve asymptotically for sufficiently large system sizes. Thus, the exponents are calculated using the following equations, guided by finite-size scaling principles [81]:

$$\chi(L) = L^{\gamma/\nu} f_{\chi}(tL^{1/\nu}) \tag{5.20}$$

$$\frac{dM}{d(1/\nu f_M(tL^{1/\nu}))} = L^{1-\beta} \tag{5.21}$$

$$\frac{d(\ln M)}{d(1/k_B T)} = L^{1/\nu} f'_M(tL^{1/\nu}) \tag{5.22}$$

Where f_{χ}, f_{α}, f_M, and f'_M are the finite-size scaling functions.

To eliminate the singularity at the phase transition point, we employed the finite-size scaling method. The determination of critical exponents is crucial for understanding the material's critical behavior, and these exponents were obtained using equations 5.20–5.22. Initially, we constructed ln-ln plots Fig. 5.7 (e, f, g) for these quantities. To generate these curves, we evaluated the corresponding values for various lattice sizes: $L = 10$, 12, 14, 16, 18, and 20. By analyzing the slope of these ln-ln plots, we derived the values of the critical exponents ν, β, and γ. Specifically, we found these exponents to be 0.7922 ± 0.024, 0.4133 ± 0.0013, and 1.1758 ± 0.0029, respectively.

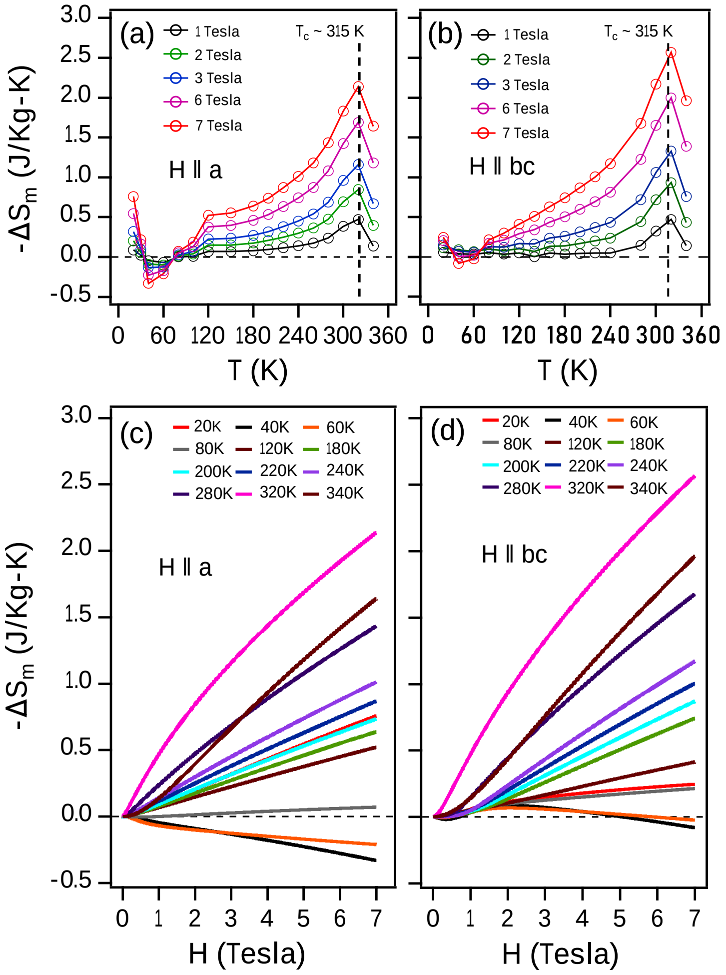

Figure 5.8: Calculated magnetic entropy change -ΔS_m as a function of temperature under different magnetic fields for (a) $H \parallel a$ and (b) $H \parallel bc$. (c) Magnetic entropy change (-ΔS_m) plotted as a function of field at different sample temperatures for (c) $H \parallel a$ and (d) $H \parallel bc$.

5.3.5 Magnetocaloric Effect

With the help of magnetization isotherms $[M(T)]$ shown in Figs. 5.4(a) and 5.4(b), we investigated the magnetocaloric effect (MCE) around the T_C in $\mathrm{Cr}_{1.38}\mathrm{Te}_2$ for $H \parallel bc$ and $H \parallel a$ orientations due to potential applications in the magneto-refrigeration technology. Magnetocaloric effect is an intrinsic property of a ferromagnetic system which causes heating or cooling effect, adiabatically, under the influence of external magnetic fields [82]. Thus, a magnetic entropy change -$\Delta S_m(T, H)$ is induced in the presence of magnetic fields which is represented by,

$$\Delta S_m(T, H) = \int_o^H (\frac{\partial S}{\partial H})_T dH = \int_o^H (\frac{\partial M}{\partial T})_H dH \tag{5.23}$$

here $(\frac{\partial S}{\partial H})_T = (\frac{\partial M}{\partial T})_H$ follows the Maxwell's relation. In case of magnetization measured at small discrete fields and temperature intervals, $\Delta S_m(T,H)$ could be written as

$$\Delta S_m(T,H) = \frac{\int_0^H M(T_{i+1},H)dH - \int_0^H M(T_i,H)dH}{T_{i+1} - T_i} \tag{5.24}$$

Figs. 5.8(a) and 5.8(b) depict -$\Delta S_m(T,H)$, taken in the temperature range of 5-330 K at various magnetic fields varied up to 7 T, respectively for $H \parallel a$ and $H \parallel bc$ orientations. The -$\Delta S_m(T,H)$ curves exhibit a maximum (normal MCE) around the PM-FM magnetic transition ($T_C \approx 315$ K) and a minimum (inverse MCE) around the FM-AFM transition of $T_N \approx 50$ K [83]. Further, the value of -$\Delta S_m(T,H)$ increases monotonically with field for both orientations as shown in Figs. 5.8(c) and 5.8(d), at all the measured temperatures down to 50 K. But below 50 K, -$\Delta S_m(T)$ various non-monotonically with field, which is consistent with -$\Delta S_m(H)$ shown in Figs. 5.8(a) and 5.8(b). As discussed in the *structural properties* section, the non-monotonic changes of lattice distortion induced by the magneto-volume effect might be playing the crucial role in the non-monotonic changes of -$\Delta S_m(T)$. Further, under the field of 7 T around T_C, the maximum value of -$\Delta S_m(T,H)$ is about 2.08 J kg^{-1} K^{-1} for $H \parallel a$ and is about 2.51 J kg^{-1} K^{-1} for $H \parallel bc$. These -$\Delta S_m(T,H)$ values taken at 7 T are comparable to the values obtained from the other 2D magnetic systems such as $Cr_2Ge_2Te_6$ (2.64 J kg^{-1} K^{-1}) [49] and Cr_5Te_8 (2.38 J kg^{-1} K^{-1}) [37] and larger than the values of $Fe_{3-x}GeTe_2$ (1.14 J kg^{-1} K^{-1}) [84] and CrI_3 (1.56J kg^{-1} K^{-1}) [85]. However, significantly smaller than the values of $CrBr_3$ (7.2 J kg^{-1} K^{-1}) [86] and $Cr_2Si_2Te_6$ (5.05 J kg^{-1} K^{-1}) [49].

5.4 Summary

In summary, we studied the magnetocrystalline anisotropy, critical behaviour, and magnetocaloric effect in the layered room-temperature monoclinic ferromagnet $Cr_{1.38}Te_2$. Our systematic investigation on the structural properties of $Cr_{1.38}Te_2$ as a function of temperature establishes a relation between the magnetic transitions and the crystal lattice. The derived critical exponents $\beta = 0.429(5)$ ($T_C \approx 315.84(2)$ K), $\gamma = 1.123(4)$ ($T_C \approx 315.87(5)$ K) using the KF method, and $\delta = 3.662(6)$ using the CI analysis at $T_C = 316$ K are self-consistent and obey the rescaling analysis. The renormalization group (RG) theory suggests that the derived critical exponents of $Cr_{1.38}Te_2$ exhibit a three-dimensional (3D) Ising-like long-range exchange interactions $[J(r)]$, decaying as $J(r) = r^{-(d+\sigma)} = r^{-4.73}$. The RG theory suggests 3D-Ising type magnetic interactions in this system which is further confirmed by the Monte-Carlo simulations. Further, the magnetocrystalline anisotropy energy density (K_u) is found to be temperature dependent and reaches a maximum (180 kJ/m^3) at 110 K. Maximum entropy change -$\Delta S_m^{max} \approx 2.51$ J/ kg-K is found near the T_C for $H \parallel bc$. The density functional theory predicts *b*-axis as the magnetic easy-axis by analyzing the magnetocrystalline anisotropy energy values for different spin configurations.

References

[1] J. T. Heron, M. Trassin, K. Ashraf, M. Gajek, Q. He, S. Y. Yang, D. E. Nikonov, Y.-H. Chu, S. Salahuddin, R. Ramesh, Electric-Field-Induced Magnetization Reversal in a Ferromagnet-Multiferroic Heterostructure, Phys. Rev. Lett. 107 (2011) 217202.

[2] A. K. Geim, I. V. Grigorieva, Van der Waals heterostructures, Nature 499 (2013) 419–425.

[3] C. Gong, L. Li, Z. Li, H. Ji, A. Stern, Y. Xia, T. Cao, W. Bao, C. Wang, Y. Wang, et al., Discovery of intrinsic ferromagnetism in two-dimensional van der Waals crystals, Nature 546 (2017) 265–269.

[4] Z. Fei, B. Huang, P. Malinowski, W. Wang, T. Song, J. Sanchez, W. Yao, D. Xiao, X. Zhu, A. F. May, et al., Two-dimensional itinerant ferromagnetism in atomically thin Fe_3GeTe_2, Nat. Mater. 17 (2018) 778–782.

[5] B. Wang, Y. Zhang, L. Ma, Q. Wu, Y. Guo, X. Zhang, J. Wang, MnX (X= P, As) monolayers: a new type of two-dimensional intrinsic room temperature ferromagnetic half-metallic material with large magnetic anisotropy, Nanoscale 11 (2019) 4204–4209.

[6] M. Gibertini, M. Koperski, A. F. Morpurgo, K. S. Novoselov, Magnetic 2D materials and heterostructures, Nat. Nanotechnol. 14 (2019) 408–419.

[7] N. D. Mermin, H. Wagner, Absence of Ferromagnetism or Antiferromagnetism in One- or Two-Dimensional Isotropic Heisenberg Models, Phys. Rev. Lett. 17 (1966) 1133–1136.

[8] B. Huang, G. Clark, E. Navarro-Moratalla, D. R. Klein, R. Cheng, K. L. Seyler, D. Zhong, E. Schmidgall, M. A. McGuire, D. H. Cobden, W. Yao, D. Xiao, P. Jarillo-Herrero, X. Xu, Layer-dependent ferromagnetism in a van der Waals crystal down to the monolayer limit, Nature 546 (2017) 270–273.

[9] Y. Liu, C. Petrovic, Critical behavior of quasi-two-dimensional semiconducting ferromagnet $Cr_2Ge_2Te_6$, Phys. Rev. B 96 (2017) 054406.

[10] T. J. Williams, A. A. Aczel, M. D. Lumsden, S. E. Nagler, M. B. Stone, J.-Q. Yan, D. Mandrus, Magnetic correlations in the quasi-two-dimensional semiconducting ferromagnet $CrSiTe_3$, Phys. Rev. B 92 (2015) 144404.

[11] H. L. Zhuang, P. R. C. Kent, R. G. Hennig, Strong anisotropy and magnetostriction in the two-dimensional Stoner ferromagnet Fe_3GeTe_2, Phys. Rev. B 93 (2016) 134407.

[12] A. Soumyanarayanan, N. Reyren, A. Fert, C. Panagopoulos, Emergent phenomena induced by spin-orbit coupling at surfaces and interfaces, Nature 539 (2016) 509–517.

[13] H. Liu, Y. Zhang, O. E. Glukhova, G. Zhang, L. Wang, J. Zhao, J. Gao, Interlayer Hopping Kinetics of Vacancies in CrI_3 Layers Leading to Monolayer/Bilayer Heterostructures, Adv. Mater. Interfaces 9 (2022) 2200626.

[14] Y. Zhu, X. Kong, T. D. Rhone, H. Guo, Systematic search for two-dimensional ferromagnetic materials, Phys. Rev. Materials 2 (2018) 081001.

[15] J. Dijkstra, H. H. Weitering, C. F. van Bruggen, C. Haas, R. A. de Groot, Band-structure calculations, and magnetic and transport properties of ferromagnetic chromium tellurides ($CrTe, Cr_3Te_4, Cr_2Te_3$), J. Phys.: Condens. Matter 1 (1989) 9141–9161.

[16] H. Ipser, K. L. Komarek, K. O. Klepp, Transition metal-chalcogen systems viii: The CrTe phase diagram, Journal of the Less Common Metals 92 (1983) 265–282.

[17] T. Hamasaki, T. Hashimoto, Y. Yamaguchi, H. Watanabe, Neutron diffraction study of Cr_2Te_3 single crystal, Solid State Commun. 16 (1975) 895–897.

[18] G. Chattopadhyay, The Cr-Te (chromium-tellurium) system, J. Phase Equilib. 15 (1994) 431–440.

[19] Y. Wang, J. Yan, J. Li, S. Wang, M. Song, J. Song, Z. Li, K. Chen, Y. Qin, L. Ling, H. Du, L. Cao, X. Luo, Y. Xiong, Y. Sun, Magnetic anisotropy and topological Hall effect in the trigonal chromium tellurides Cr_5Te_8, Phys. Rev. B 100 (2019) 024434.

[20] J. Yan, X. Luo, G. Lin, F. Chen, J. Gao, Y. Sun, L. Hu, P. Tong, W. Song, Z. Sheng, W. Lu, X. Zhu, Y. Sun, Anomalous Hall effect of the quasi-two-dimensional weak itinerant ferromagnet $Cr_{4.14}Te_8$, Europhys. Lett. 124 (2019) 67005.

[21] B. Tang, X. Wang, M. Han, X. Xu, Z. Zhang, C. Zhu, X. Cao, Y. Yang, Q. Fu, J. Yang, et al., Phase engineering of Cr_5Te_8 with colossal anomalous Hall effect, Nature Electronics 5 (2022) 224–232.

[22] J. Liu, B. Ding, J. Liang, X. Li, Y. Yao, W. Wang, Magnetic Skyrmionic bubbles at room temperature and sign reversal of the topological Hall effect in a layered ferromagnet $Cr_{0.87}Te$, ACS Nano 16 (2022) 13911–13918.

[23] M. Huang, L. Gao, Y. Zhang, X. Lei, G. Hu, J. Xiang, H. Zeng, X. Fu, Z. Zhang, G. Chai, et al., Possible Topological Hall Effect above Room Temperature in Layered $Cr_{1.21}Te_2$ Ferromagnet, Nano Lett. 21 (2021) 4280–4286.

[24] C. Zhang, C. Liu, J. Zhang, Y. Yuan, Y. Wen, Y. Li, D. Zheng, Q. Zhang, Z. Hou, G. Yin, et al., Room-Temperature Magnetic Skyrmions and Large Topological Hall Effect in Chromium Telluride Engineered by Self-Intercalation, Adv. Mater. (2022) 2205967.

[25] L. M. Moreno-Ramírez, V. Franco, Reversibility of the Magnetocaloric Effect in the Bean-Rodbell Model, Magnetochemistry 7 (2021).

[26] T. Hashimoto, K. Hoya, M. Yamaguchi, I. Ichitsubo, Magnetic properties of single crystals $Cr_{2-\delta}Te_3$, J. Phys. Soc. Jpn. 31 (1971) 679–682.

[27] P. Giannozzi, S. Baroni, N. Bonini, M. Calandra, R. Car, C. Cavazzoni, D. Ceresoli, G. L. Chiarotti, M. Cococcioni, I. Dabo, et al., QUANTUM ESPRESSO: a modular and open-source software project for quantum simulations of materials, J. Phys.: Condens. Matter 21 (2009) 395502.

[28] J. P. Perdew, K. Burke, M. Ernzerhof, Generalized Gradient Approximation Made Simple, Phys. Rev. Lett. 77 (1996) 3865–3868.

[29] D. Li, C. Barreteau, M. R. Castell, F. Silly, A. Smogunov, Out- versus in-plane magnetic anisotropy of free Fe and Co nanocrystals: Tight-binding and first-principles studies, Phys. Rev. B 90 (2014) 205409.

[30] N. Metropolis, A. W. Rosenbluth, M. N. Rosenbluth, A. H. Teller, E. Teller, Equation of state calculations by fast computing machines, Technical Report, 1953.

[31] K. Binder, D. Heermann, L. Roelofs, A. J. Mallinckrodt, S. McKay, Monte Carlo Simulation in Statistical Physics, Comput. Phys. 7 (1993) 156–157.

[32] M. E. J. Newman, G. T. Barkema, Monte Carlo methods in statistical physics, Clarendon Press, Oxford, 1999.

[33] J. Rodríguez-Carvajal, Recent advances in magnetic structure determination by neutron powder diffraction, Phys. B Condens. Matter 192 (1993) 55–69.

[34] Y. Kubota, Y. Okamoto, T. Kanematsu, T. Yajima, D. Hirai, K. Takenaka, Large magnetic-field-induced strains in sintered chromium tellurides, Appl. Phys. Lett. 122 (2023) 042404.

[35] C. Li, K. Liu, D. Jiang, C. Jin, T. Pei, T. Wen, B. Yue, Y. Wang, Diverse Thermal Expansion Behaviors in Ferromagnetic $Cr_{1-\delta}Te$ with NiAs-Type, Defective Structures, Inorg. Chem. 61 (2022) 14641–14647.

[36] M. Yamaguchi, T. Hashimoto, Magnetic properties of Cr_3Te_4 in ferromagnetic region, J. Phys. Soc. Jpn. 32 (1972) 635–638.

[37] Y. Liu, M. Abeykoon, E. Stavitski, K. Attenkofer, C. Petrovic, Magnetic anisotropy and entropy change in trigonal Cr_5Te_8, Phys. Rev. B 100 (2019) 245114.

[38] P. S. A. Kumar, P. A. Joy, S. K. Date, Comparison of the irreversible thermomagnetic behaviour of some ferro- and ferrimagnetic systems, Bull. Mater. Sci. 23 (2000) 97–101.

[39] E. Bertaut, G. Roult, R. Aleonard, R. Pauthenet, M. Chevreton, R. Jansen, Structures magnétiques de Cr_3X_4 $(X = S, Se, Te)$, Journal de Physique 25 (1964) 582–595.

[40] L.-Z. Zhang, X.-D. He, A.-L. Zhang, Q.-L. Xiao, W.-L. Lu, F. Chen, Z. Feng, S. Cao, J. Zhang, J.-Y. Ge, Tunable Curie temperature in layered ferromagnetic $Cr_{5+\delta}Te_8$ single crystals, APL Mater. 8 (2020) 031101.

[41] Z.-L. Huang, W. Kockelmann, M. Telling, W. Bensch, A neutron diffraction study of structural and magnetic properties of monoclinic Cr_5Te_8, Solid State Sci. 10 (2008) 1099–1105.

[42] A. F. ANDRESEN, E. Zeppezauer, T. Boive, B. Nordström, C. Brändén, Magnetic structure of Cr_2Te_3, Cr_3Te_4, and Cr_5Te_6, Acta Chem. Scand. 24 (1970) 3495–3509.

[43] L.-Z. Zhang, Q.-L. Xiao, F. Chen, Z. Feng, S. Cao, J. Zhang, J.-Y. Ge, Multiple magnetic phase transitions and critical behavior in single crystal Cr_5Te_6, J. Magn. Magn. Mater. 546 (2022) 168770.

[44] Y. Chen, Y. Zhu, R. Lin, W. Niu, R. Liu, W. Zhuang, X. Zhang, J. Liang, W. Sun, Z. Chen, et al., Observation of colossal topological Hall effect in noncoplanar ferromagnet Cr_5Te_6 thin films, Adv. Funct. Mater. (2023) 2302984.

[45] G. Makovetskii, G. Shakhlevich, Magnetic properties of the $CrS_{1-x}Se_x$ system, Physica Status Solidi (a) 47 (1978) 219–222.

[46] K. Shimada, T. Saitoh, H. Namatame, A. Fujimori, S. Ishida, S. Asano, M. Matoba, S. Anzai, Photoemission study of itinerant ferromagnet $Cr_{1-\delta}Te$, Phys. Rev. B 53 (1996) 7673–7683.

[47] J. Xu, X. Zheng, S. Yang, L. Xi, S. Wang, L. Zhang, W. Yang, J. Yang, X. Ma, D. Chen, et al., Large Linear Negative Thermal Expansion in NiAs-type Magnetic Intermetallic $Cr-Te-Se$ Compounds, Inorg. Chem. 59 (2020) 8603–8608.

[48] N. Richter, D. Weber, F. Martin, N. Singh, U. Schwingenschlögl, B. V. Lotsch, M. Kläui, Temperature-dependent magnetic anisotropy in the layered magnetic semiconductors CrI_3 and $CrBr_3$, Phys. Rev. Materials 2 (2018) 024004.

[49] Y. Liu, C. Petrovic, Anisotropic magnetic entropy change in $\mathrm{Cr}_2X_2\mathrm{Te}_6$ (X = Si and Ge), Phys. Rev. Materials 3 (2019) 014001.

[50] R. Sbiaa, H. Meng, S. N. Piramanayagam, Materials with perpendicular magnetic anisotropy for magnetic random access memory, Phys. Status Solidi RRL 5 (2011) 413–419.

[51] D. L. Cortie, G. L. Causer, K. C. Rule, H. Fritzsche, W. Kreuzpaintner, F. Klose, Two-Dimensional Magnets: Forgotten History and Recent Progress towards Spintronic Applications, Adv. Funct. Mater. 30 (2020) 1901414.

[52] V. Krizakova, E. Grimaldi, K. Garello, G. Sala, S. Couet, G. S. Kar, P. Gambardella, Interplay of Voltage Control of Magnetic Anisotropy, Spin-Transfer Torque, and Heat in the Spin-Orbit-Torque Switching of Three-Terminal Magnetic Tunnel Junctions, Phys. Rev. Appl. 15 (2021) 054055.

[53] Y. Liu, C. Petrovic, Critical behavior of the quasi-two-dimensional weak itinerant ferromagnet trigonal chromium telluride $\mathrm{Cr}_{0.62}\mathrm{Te}$, Phys. Rev. B 96 (2017) 134410.

[54] E. Wohlfarth, Magnetic properties of crystallineand amorphous alloys: A systematic discussion based on the Rhodes-Wohlfarth plot, J. Magn. Magn. Mater. 7 (1978) 113–120.

[55] T. Moriya, Recent progress in the theory of itinerant electron magnetism, J. Magn. Magn. Mater. 14 (1979) 1–46.

[56] A. Arrott, Criterion for Ferromagnetism from Observations of Magnetic Isotherms, Phys. Rev. 108 (1957) 1394–1396.

[57] B. Banerjee, On a generalised approach to first and second order magnetic transitions, Physics Letters 12 (1964) 16–17.

[58] H. E. Stanley, Phase transitions and critical phenomena, volume 7, Clarendon Press, Oxford, 1971.

[59] M. E. Fisher, The theory of equilibrium critical phenomena, Rep. Prog. Phys. 30 (1967) 615.

[60] S. Kaul, Static critical phenomena in ferromagnets with quenched disorder, J. Magn. Magn. Mater. 53 (1985) 5–53.

[61] J. C. Le Guillou, J. Zinn-Justin, Critical exponents from field theory, Phys. Rev. B 21 (1980) 3976–3998.

[62] M. E. Fisher, S.-k. Ma, B. G. Nickel, Critical Exponents for Long-Range Interactions, Phys. Rev. Lett. 29 (1972) 917–920.

[63] D. Kim, B. Revaz, B. L. Zink, F. Hellman, J. J. Rhyne, J. F. Mitchell, Tricritical Point and the Doping Dependence of the Order of the Ferromagnetic Phase Transition of $La_{1-x}Ca_xMnO_3$, Phys. Rev. Lett. 89 (2002) 227202.

[64] A. Arrott, J. E. Noakes, Approximate Equation of State For Nickel Near its Critical Temperature, Phys. Rev. Lett. 19 (1967) 786–789.

[65] A. K. Pramanik, A. Banerjee, Critical behavior at paramagnetic to ferromagnetic phase transition in $Pr_{0.5}Sr_{0.5}MnO_3$: A bulk magnetization study, Phys. Rev. B 79 (2009) 214426.

[66] J. S. Kouvel, M. E. Fisher, Detailed Magnetic Behavior of Nickel Near its Curie Point, Phys. Rev. 136 (1964) A1626–A1632.

[67] B. Widom, Degree of the critical isotherm, J. Chem. Phys. 41 (1964) 1633–1634.

[68] A. Wang, A. Rahman, Z. Du, J. Zhao, F. Meng, W. Liu, J. Fan, C. Ma, M. Ge, L. Pi, et al., Field-dependent anisotropic room-temperature ferromagnetism in Cr_3Te_4, Phys. Rev. B 108 (2023) 094429.

[69] A. Goswami, N. Ng, E. Yakubu, A. M. Abeykoon, S. Guchhait, Critical behavior in monoclinic Cr_3Te_4, Phys. Rev. B 109 (2024) 054413.

[70] Y. Liu, S. K. Bose, J. Kudrnovský, First-principles theoretical studies of half-metallic ferromagnetism in CrTe, Phys. Rev. B 82 (2010) 094435.

[71] R. Mondal, R. Kulkarni, A. Thamizhavel, Anisotropic magnetic properties and critical behaviour studies of trigonal Cr_5Te_8 single crystal, J. Magn. Magn. Mater. 483 (2019) 27–33.

[72] G. Cao, Q. Zhang, M. Frontzek, W. Xie, D. Gong, G. E. Sterbinsky, R. Jin, Structure, chromium vacancies, and magnetism in a $Cr_{12-x}Te_{16}$ compound, Phys. Rev. Materials 3 (2019) 125001.

[73] L.-Z. Zhang, A.-L. Zhang, X.-D. He, X.-W. Ben, Q.-L. Xiao, W.-L. Lu, F. Chen, Z. Feng, S. Cao, J. Zhang, J.-Y. Ge, Critical behavior and magnetocaloric effect of the quasi-two-dimensional room-temperature ferromagnet Cr_4Te_5, Phys. Rev. B 101 (2020) 214413.

[74] Y. Fujisawa, M. Pardo-Almanza, J. Garland, K. Yamagami, X. Zhu, X. Chen, K. Araki, T. Takeda, M. Kobayashi, Y. Takeda, et al., Tailoring magnetism in self-intercalated $Cr_{1+\delta}Te_2$ epitaxial films, Phys. Rev. Materials 4 (2020) 114001.

[75] Y. Fujisawa, M. Pardo-Almanza, C.-H. Hsu, A. Mohamed, K. Yamagami, A. Krishnadas, G. Chang, F.-C. Chuang, K. H. Khoo, J. Zang, et al., Widely Tunable Berry Curvature in the Magnetic Semimetal $Cr_{1+\delta}Te_2$, Adv. Mater. 35 (2023) 2207121.

[76] X. Zhang, T. Yu, Q. Xue, M. Lei, R. Jiao, Critical behavior and magnetocaloric effect in monoclinic Cr_5Te_8, J. Alloys Compd. 750 (2018) 798–803.

[77] H. Zheng, C. Huang, F. Lin, J. Fan, H. Liu, L. Zhang, C. Ma, C. Wang, Y. Zhu, H. Yang, Two-dimensional van der Waals ferromagnetic thin film $CrTe_2$ with high Curie temperature and metallic conductivity, Appl. Phys. Lett. 122 (2023).

[78] Y. Wang, S. Kajihara, H. Matsuoka, B. K. Saika, K. Yamagami, Y. Takeda, H. Wadati, K. Ishizaka, Y. Iwasa, M. Nakano, Layer-Number-Independent Two-Dimensional Ferromagnetism in Cr_3Te_4, Nano Lett. (2022).

[79] H. Liu, H. Zheng, Y. Wang, C. Huang, C. Ma, Y. Zhu, H. Yang, L. Ling, L. Zhang, J. Fan, Long-range magnetic exchange coupling in quasi-two-dimensional CrTe ferromagnetic thin films, Physica Status Solidi (RRL)–Rapid Research Letters (????).

[80] H. J. Xiang, E. J. Kan, S.-H. Wei, M.-H. Whangbo, X. G. Gong, Predicting the spin-lattice order of frustrated systems from first principles, Phys. Rev. B 84 (2011) 224429.

[81] M. E. Newman, G. T. Barkema, Monte Carlo methods in statistical physics, Clarendon Press, 1999.

[82] V. K. Pecharsky, K. A. Gschneidner Jr, Magnetocaloric effect and magnetic refrigeration, J. Magn. Magn. Mater. 200 (1999) 44–56.

[83] S. Purwar, A. Low, A. Bose, A. Narayan, S. Thirupathaiah, Investigation of the anomalous and topological Hall effects in layered monoclinic ferromagnet $Cr_{2.76}Te_4$, Phys. Rev. Materials 7 (2023) 094204.

[84] Y. Liu, J. Li, J. Tao, Y. Zhu, C. Petrovic, Anisotropic magnetocaloric effect in $Fe_{3-x}GeTe_2$, Sci. Rep. 9 (2019) 13233.

[85] Y. Liu, C. Petrovic, Anisotropic magnetocaloric effect in single crystals of CrI_3, Phys. Rev. B 97 (2018) 174418.

[86] X. Yu, X. Zhang, Q. Shi, S. Tian, H. Lei, K. Xu, H. Hosono, Large magnetocaloric effect in van der Waals crystal $CrBr_3$, Front Phys Beijing 14 (2019).

Chapter 6

Intricate Magnetic Interactions and Topological Hall Effect Observed in Itinerant Room-temperature Layered Ferromagnet $Cr_{0.83}Te$

6.1 Introduction

Investigation of the low dimensional magnetic materials with ferromagnetic ordering at room temperature and strong magnetocrystalline anisotropy has gained a lot of research interests in recent days due to their potential applications in magnetic refrigeration and spintronic devices [1–6]. Hence, the van der Waals (vdW) ferromagnets are of great research interest from the fundamental science and advanced technology point of view due to their peculiar two-dimensional (2D) magnetic properties [7–10] and strong magnetocrystalline anisotropy [11]. Usually, the Heisenberg-type ferromagnet does not exist with intrinsic long-range magnetic ordering at finite temperature in the 2D limit due to dominant thermal fluctuations [12]. Nevertheless, the single domain anisotropy or the exchange anisotropy can overcome the thermal fluctuation and allow the long-range magnetic ordering in 2D ferromagnets [13]. In this way, the 2D ferromagnetism has been found experimentally in many vdW materials such as $Cr_2Ge_2Te_6$ ($T_C \approx 61$ K) [14], $Cr_2Si_2Te_6$ ($T_C \approx 32$ K) [15, 16], Fe_3GeTe_2 ($T_C \approx 215$ K) [9, 17], and CrI_3 ($T_C \approx 45$ K) [13], but the long-range FM ordering temperature is far below the room temperature, limiting their usage in technological applications. Since a very few systems such as MnP ($T_C \approx 303$ K) show room temperature 2D ferromagnetism in the bulk phase [18], searching for new room-temperature layered FM materials coupled with large magnetocrystalline anisotropy is crucial for realizing potential

---

This chapter is based on the publication: **Shubham Purwar et al., Acta Materialia, 271, 119898 (2024)** technological applications.

Furthermore, the FM vdW materials posses another peculiar property such as the magnetocaloric effect (MCE). The magnetocaloric effect (MCE) at room temperature in the FM vdW materials with maximum entropy change -ΔS_m^{max} is of recent research interest due to their technological applications in the environmental friendly magnetic refrigerators [19]. There exists quite a few 2D FM systems showing significant -ΔS_M^{max} such as $Fe_{3-x}GeTe_2$ (1.1 $J/kg-K$ at 5 T) [20], Cr_5Te_8 (1.6 $J/kg-K$ at 5 T) [21], $Cr_2Si_2Te_6$ (5.05 $J/kg-K$ at 5 T), and $Cr_2Ge_2Te_6$ (2.64 $J/kg-K$ at 5 T) [22].

Theoretical studies suggest that the layered Cr_xTe_y systems are the potential candidates to realize the much-anticipated room-temperature 2D ferromagnetism in bulk [23]. Since then, a variety of Cr_xTe_y compounds have been grown experimentally and studied for their peculiar 2D ferromagnetism, including CrTe [24], Cr_2Te_3 [25], Cr_3Te_4 [26], Cr_4Te_5 [27–29], and Cr_5Te_8 [30, 31]. Generally, Cr_xTe_y compounds possess alternating stacks of $CrTe_2$ layers intercalated by the Cr layers (excess) along the z-axis [32]. The intercalated Cr concentration plays an important role in the formation of these compounds' crystal structure, magnetic structure, and transport properties [33–36]. The topological Hall effect observed in Cr_xTe_y systems implies the presence of non-trivial spin texture such as skyrmions and bi-skyrmions [37, 38] or the noncoplanar magnetic structures [39–41].

On the other hand, though there exist a couple of studies on the hexagonal $Cr_{1-x}Te$ type systems, discussing the magnetic, transport, and Hall effect properties [42, 43], no systematic study is available on the magnetocrystalline anisotropy (MCA) and magneto-entropy scaling analysis which offer a better understanding on the topological Hall effect and magnetic exchange interactions, respectively. Importantly, the magnetic exchange interactions are profoundly influenced by the MCA, manifesting the Heisenberg, XY, Ising, or complex magnets [44–46]. In addition, the strong MCA is crucial for engineering the non-coplanar spin-structure that leads to generating the skyrmion lattice [47, 48]. On the other hand, the magneto-entropy scaling analysis deduces the critical exponents, defining the strength and the type of magnetic interactions present in the system [21, 22, 49, 50].

Therefore, this study reports the anisotropic magnetic properties, anomalous and topological Hall effects, and magnetocaloric effect in the hexagonal $Cr_{0.83}Te$ single crystal. $Cr_{0.83}Te$ is an interesting system as it falls in between the van der Waals trigonal (vdW) $CrTe_2$ [51] and non-vdW hexagonal CrTe [52], despite all three being layered systems. As the intercalated Cr atoms play a vital role in shaping the magnetic and magnetotransport properties, $Cr_{0.83}Te$ could be a potential candidate to show the topological Hall effect (THE) originating from the noncoplanar spin structure of the intercalated Cr spins. Moreover, it is one of the few Cr_xTe_y type systems showing room temperature ferromagnetism, idle for room temperature technological applications such as magnetic storage devices [53], spin valves [54], magnetic tunnel junctions [54], and spin-transfer torque devices [55]. Although an earlier study on the similar composition of hexagonal $Cr_{0.833}Te$ (Cr_5Te_6) performed critical analysis but lacked details on the relation between the anisotropic magnetic properties and the topological Hall effect [56]. Another study performed magnetotransport measurements on a different crystal structure of monoclinic thin film $Cr_{0.833}Te$, yet lacks the discussion on the relation between MCA and THE [39]. Therefore, this study aims to unravel the relation between the magnetocrystalline anisotropy, the topological Hall effect, and the magnetic exchange interactions in the hexagonal $Cr_{0.83}Te$. Further, the re-scaled magnetoentropy change, -$\Delta S_m(T, H)$, exhibits a remarkable convergence onto a universal curve, suggesting a second-order magnetic transition in this systems [57, 58]. Extracted critical exponents from the field-dependent magnetoentropy change highlight the interplay between the 3D-Ising and the meanfield-type exchange interactions.

6.2 Experimental details

High-quality single crystals of $Cr_{0.83}Te$ were grown using the chemical vapor transport (CVT) method with iodine as a transport agent. We thoroughly mixed Cr (99.99%, Alfa Aesar) and Te (99.99%, Alfa Aesar) powders in a 5 : 5 ratio, and a small quantity of iodine (3 mg/cc) was added to the powder mixture. The mixture was sealed in a quartz tube under argon gas and placed in a gradient two-zone horizontal tube furnace for about 15 days. One end of the tube was heated at 1000°C (source) and the other end was kept at 820°C (sink), following a previously established procedure [59]. The obtained single crystals were large, measuring up to 5×5 mm^2, and looking shiny. A representative photographic image of a typical single crystal is shown in the inset of Fig. 6.1(b).

The crystal structure of as-grown $Cr_{0.83}Te$ single crystals was examined by the x-ray diffraction (XRD) technique using the Rigaku x-ray diffractometer (SmartLab, 9 kW) with Cu K_α radiation of wavelength of λ =1.5406 Å. We employed scanning electron microscopy (SEM) and energy-dispersive X-ray spectroscopy (EDXS) techniques to explore surface morphology and elemental compositions. Magnetic and transport properties were studied by the physical property measurement system (9 Tesla-PPMS, DynaCool, Quantum Design). Electrical resistivity and Hall measurements were conducted using the conventional four-probe technique. To eliminate the influence of longitudinal magnetoresistance, caused mainly by the voltage probe misalignment, the Hall resistivity was determined as $\rho_{xy}(H) = [\rho_{xy}(+H) - \rho_{xy}(-H)]/2$. In addition, Raman spectra were captured using a micro-Raman spectrometer (LabRam HR Evolution HORIBA France SAS) equipped with a 532 nm laser.

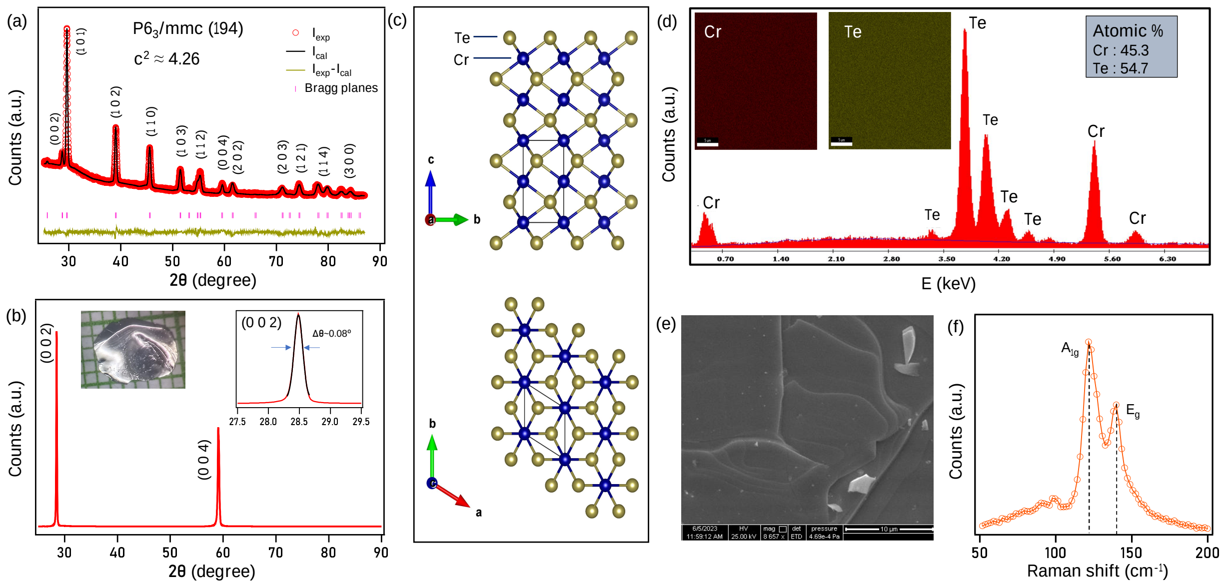

Figure 6.1: (a) Powder x-ray diffraction (XRD) of the crushed $Cr_{0.83}Te$ single crystals overlapped with Rietveld refinement. (b) XRD pattern of $Cr_{0.83}Te$ single crystal. The left inset of (b) shows the photographic image of a typical $Cr_{0.83}Te$ single crystal. The right inset of (b) shows the rocking curve of (0 0 2) Bragg's reflection with FWHM of 0.08°. (c) Schematics of the CrTe hexagonal crystal structure projected onto the *bc*-plane and *ab*-plane. (d) Energy dispersive X-ray spectroscopy (EDXS) spectra of $Cr_{0.83}Te$ single crystal. Top-insets of (d) show the elemental mapping of Cr and Te. (e) Scanning electron microscopy (SEM) image of $Cr_{0.83}Te$ single crystal. (f) Raman spectra of $Cr_{0.83}Te$ single crystal.

6.3 Results and Discussion

6.3.1 Structural Properties

Figure 6.1(a) displays the XRD pattern of crushed $Cr_{0.83}Te$ single crystals taken at room temperature, confirming the hexagonal crystal structure with $P6_3/mmc$ space group. No additional impurity phases were detected. Rietveld refinement, overlapped on the XRD data, yields lattice parameters $a = b = 3.9808(4)$ Å and $c = 6.2122(3)$ Å, which are very close to the previous reports on similar systems [60, 42]. Fig. 6.1(b) depicts the XRD pattern of $Cr_{0.83}Te$ single crystal, showing the intensity of (0 0 l) Bragg plane, suggesting that the crystal growth axis is along the c-axis. The rocking curve of (0 0 2) plane shown in the right-inset of Fig. 6.1(b) displays a single sharp peak with a full width at half maximum (FWHM) of $\Delta\theta = 0.08°$, confirming the high quality of single crystals [61]. The crystal structure of $Cr_{0.83}Te$, as schematically presented in the top-panel of Fig. 6.1(c), reveals stacking of $CrTe_2$ layers along the c-axis arrangement without significant vdWs gap between two $CrTe_2$ layers. This arrangement differs from other Cr_xTe_y-based systems in which a significant vdW gap is present [40, 51]. From the crystal structure projected onto the *ab*-plane, as shown in the bottom-inset of Fig. 6.1(c), we can observe an intertwined honeycomb lattice consisting of Cr and Te atoms. Fig. 6.1(d) depicts the EDXS spectra, revealing the Cr:Te atomic ratio of 0.83:1, consistent with the chemical composition of $Cr_{0.83}Te$ obtained from the powder XRD refinement. The EDXS mappings shown in the insets of Fig. 6.1(d) confirm the uniform distribution of Cr and Te elements in the studied single crystal. The obtained sample composition of $Cr_{0.83}Te$ hints at the 17% of Cr vacancies. These vacancies seem critical in maintaining the NiAs-type hexagonal crystal structure [32, 42, 62]. Fig. 6.1(e) presents the SEM image of $Cr_{0.83}Te$ single crystal with terraces of the different layers, demonstrating the layered nature of the system. The Raman spectra of $Cr_{0.83}Te$ as shown in Fig. 6.1(f) unveil two prominent phonon peaks, positioned at approximately 123.5 cm^{-1} and 139.79 cm^{-1}. These peaks correspond to the distinct vibrational modes, the out-of-plane A_{1g} and the in-plane E_g, of the Cr_xTe_y system [63, 62].

6.3.2 Magnetic Properties

Magnetization Measurements

To explore the magnetic properties of $Cr_{0.83}Te$, we performed magnetization measurements as a function of temperature [$M(T)$] and field [$M(H)$]. The magnetic field was applied parallel to both the xy-plane [$H \parallel xy$] and the z-axis [$H \parallel z$]. Figs. 6.2(a) and 6.2(b) exhibit the in-plane ($H \parallel xy$) and out-of-plane ($H \parallel z$) $M(T)$ curves obtained under magnetic fields of 0.02 T and 0.4 T, respectively. As we can notice, the system undergoes a paramagnetic-to-ferromagnetic (PM-FM) transition at a Curie temperature (T_C) of approximately 338 K, very close to the previously reported value on a similar system [42]. The bifurcation in the $M(T)$ curves at T_C between ZFC and FC, as observed in Fig. 6.2(a), can be ascribed to the magnetic ordering, which is thermally irreversible at lower fields (0.02 T) due to canted magnetic moments [64, 65]. This interpretation is supported by the $M(T)$ data taken at 0.4 T of the applied field [see Fig. 6.2(b)], in which we can see the absence of bifurcation between ZFC and FC data at the T_C due to complete alignment of the canted moments along the field direction. Further, at an applied field of 0.02 T, a sharp downturn in the ZFC $M(T)$ data is noticed at around 15 K, which disappears at 0.4 T, suggesting a possible spin-glass type transition below 15 K [66] at lower fields. Nevertheless, we notice significant magnetization anisotropy between in-plane and out-of-plane orientations at both applied fields.

Figs. 6.2(c) and 6.2(d) depict the magnetization isotherms, $M(H)$, measured at different temperatures for $H \parallel xy$ and $H \parallel z$ orientations, respectively. The $M(H)$ data suggest $Cr_{0.83}Te$ to be a soft-ferromagnet with negligible coercivity. The magnetic anisotropy observed from the $M(T)$ data is further verified by the magnetization isotherms by plotting in-plane and out-of-plane $M(H)$ at 3 K, as shown in the inset of Fig. 6.2(d). The magnetic anisotropy observed in these systems plausibly stems from the non-coplanar magnetic structure resulting from the Cr vacancies [39, 40]. From Figs. 6.2(c) and 6.2(d), it is clear

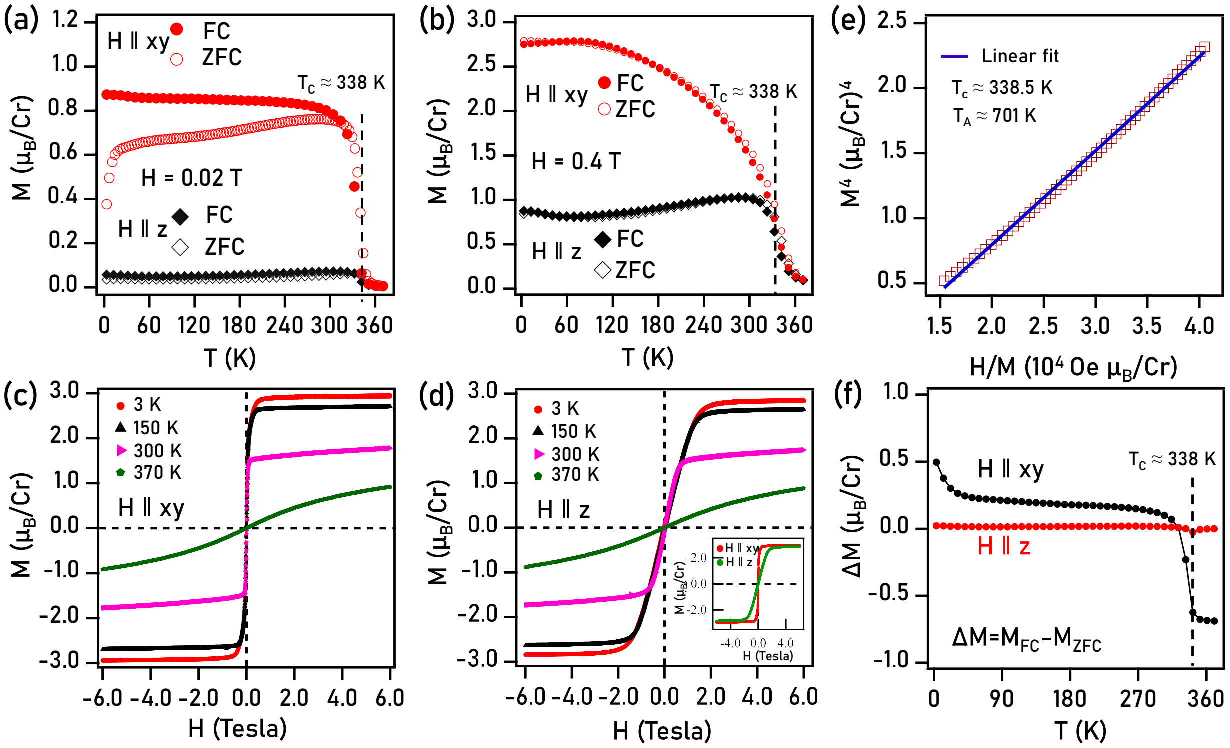

Figure 6.2: Temperature-dependent magnetization $[M(T)]$ of $Cr_{0.83}Te$ taken in zero-field-cooled (ZFC) and field-cooled (FC) modes with magnetic fields H = 0.02 T (a) and 0.4 T (b) for $H \parallel xy$ and $H \parallel z$. Magnetization isotherms $[M(H)]$ measured at various sample temperatures for (c) $H \parallel xy$ and (d) $H \parallel z$. (e) Plot of M^4 *vs* H/M. (f) Temperature-dependent ΔM $(M_{FC} - M_{ZFC})$ derived for $H \parallel xy$ and $H \parallel z$.

that $Cr_{0.83}Te$ has an easy-axis parallel to the xy-plane. This observation is substantiated by the magnetization saturation occurring at an applied field of 0.5 T for $H \parallel xy$. In comparison, 1.9 T is needed for the same with $H \parallel z$ when measured at 3 K. Note here that an easy-axis of magnetization parallel to the z-axis was found from a similar system of $Cr_{0.87}Te$ which has 4.6% of higher Cr compared to our studied $Cr_{0.83}Te$, again confirming that the magnetic structure is highly sensitive to the Cr concentration present in these systems [67, 37]. The saturation magnetization (M_s) for both in-plane and out-of-plane orientations is determined as 2.95 μ_B/Cr and 2.86 μ_B/Cr, respectively. This is notably smaller than the calculated ordered moment of Cr (3.4 μ_B/Cr) from the band structure calculations due to the itinerant nature of the Cr-d electrons [68, 32].

Next, to estimate the degree of itinerant ferromagnetism in $Cr_{0.83}Te$, we employed Takahashi's self-consistent renormalization (SCR) theory around T_C [69]. According to the SCR theory, the magnetization M and the magnetic field H at T_C are related by,

$$M^4 = \frac{1}{4.671} \left[\frac{T_C^2}{T_A^3}\right] \left(\frac{H}{M}\right) \tag{6.1}$$

Here, T_A denotes the dispersion of the spin fluctuation spectrum in the wave-vector space. Fig. 6.2(e) shows the M^4 *vs.* H/M for $H \parallel xy$, fitted nicely by the linear Eq. 6.1. This linear relationship is generally observed in itinerant ferromagnetic systems like $LaCo_2P_2$ ($T_C/T_0 \approx 0.14$) [70], Fe_4GeTe_2 ($T_C/T_0 \approx 0.16$) [71], SmCoAsO ($T_C/T_0 \approx 0.12$) [72], and Cr_4Te_5 ($T_C/T_0 \approx 0.063$) [28]. The fit yields a slope of 7.2168×10^{-5} $[\mu_B/\mathrm{Cr}]^5$/Oe. Using the slope and T_C values, we estimate T_A to be approximately 701 K for $H \parallel xy$. As per the SCR theory, the T_C can be described by,

$$T_C = (60c)^{-3/4} M_{sp}^{3/2} T_A^{3/4} T_0^{1/4} \tag{6.2}$$

Here, c =0.3353, M_{sp} represents the spontaneous magnetization, and T_0 denotes the energy width of the dynamical spin fluctuation spectrum. Using the values of T_C, M_{sp}, and T_A, we deduce the characteristic temperature T_0 = 4963 K for $Cr_{0.83}Te$. Further, the SCR spin fluctuation theory suggests that the ratio T_C/T_0 defines the degree of itineracy in the ferromagnets. Such as, the spin moments are localized for $T_C/T_0 \approx 1$ and delocalized for $T_C/T_0 \ll 1$ [73]. In $Cr_{0.83}Te$ single crystals, we estimate $T_C/T_0 \approx 0.07$ ($\ll 1$), confirming the itinerant ferromagnetic behavior.

Fig. 6.2(f) depicts $\Delta M(M_{FC}$-$M_{ZFC})$ plotted as a function of temperature for both $H \parallel z$ and $H \parallel xy$. From Fig. 6.2(f) it is evident that the out-of-plane magnetization does not change much between ZFC and FC modes, while the ΔM of in-plane magnetization is very sensitive at around T_C. More importantly, ΔM rapidly increases with decreasing temperature below 40 K. This kind of magnetic behavior could stem from multiple factors, including the inherent magnetic anisotropy of these systems [42, 30] or the noncoplanar magnetic structure resulting from the Cr vacancies [39, 40].

Magnetocrystalline Anisotropy

With the help of magnetization isotherms $[M(H)]$ as shown in the Figs. 6.3(a) and 6.3(b), we studied the magnetocrystalline anisotropy (MCA) energy density (K_u) using the expression [38],

$$K_u = \mu_0 \int_0^{M_s} [H_{xy}(M) - H_z(M)] dM \tag{6.3}$$

Here M_s denotes the saturation magnetization. H_{xy} and H_z represent the fields applied along xy and z directions, respectively. Fig. 6.3(c) depicts the temperature-dependent K_u derived from the experimental data. We find K_u = 78.11 kJ/m^3 at T = 310 K, gradually decreasing with increasing temperature and reaching 23.73 kJ/m^3 at T_C (338 K). On the other hand, the estimated $K_u \approx 390$ kJ/m^3 at 40 K [see Fig. 6.6(d)] is much larger than the K_u values reported on many 2D magnetic systems such as $CrBr_3$ [74], $Cr_2Ge_2Te_6$ [22], and $Cr_2Si_2Te_6$ [22] and comparable to the K_u values of CrI_3 [74] and Fe_4GeTe_2 [75, 71]. Though Fe_3GeTe_2 shows a large magnetocrystalline anisotropy of 1460 kJ/m^3 at 2 K [76], its Curie temperature is much below the room temperature (T_C = 220 K) [76]. Thus, $Cr_{0.83}Te$ having a large K_u value of ≈ 390 kJ/m^3 with a Curie temperature of 338 K seems

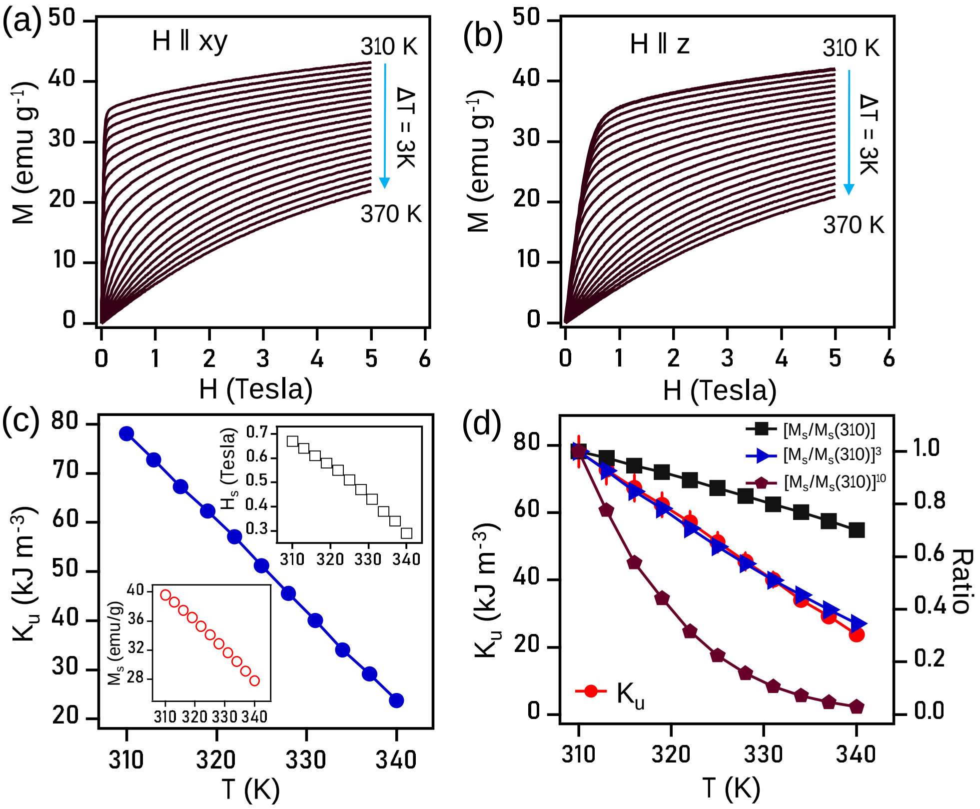

Figure 6.3: Magnetization isotherms measured around T_C for (a) $H \parallel xy$ and (b) $H \parallel z$. (c) Temperature-dependent in-plane magnetocrystalline anisotropy energy density K_u. The bottom inset in (c) presents saturation magnetization (M_s) and the top inset shows saturation magnetic field (H_s) estimated below T_C. (d) Ratios of $[\mathrm{M}_s/\mathrm{M}_s(310\ \mathrm{K})]^{n(n+1)/2}$ (right-axis) overlaid with magnetocrystalline anisotropy (left-axis) for n = 1, 2, and 4.

to be a promising candidate from the technological applications point of view. See Table 6.1 for a list of 2D materials and their respective magnetocrystalline anisotropy energies (K_u).

Since the magnetic anisotropy expectation value $< K^n >$ is directly proportional to $M_s^{n(n+1)/2}$, as per the classical theory of magnetism [77, 78], we plotted $[\frac{M_s(T)}{M_s(310)}]^{n(n+1)/2}$ for n = 1, 2, and 4. Here, n = 1 represents intrinsic anisotropy, n = 2 represents uniaxial anisotropy, and n = 4 represents cubic anisotropy, giving rise to the exponents 1, 3, and 10, respectively. In Fig. 6.3(d), we plotted $[M_s(T)/M_s(310)]$, $[M_s(T)/M_s(310)]^3$, and $[M_s(T)/M_s(310)]^{10}$ ratios as a function of temperature. Most importantly, in Fig. 6.3(d), the overlapped K_u(T) of Fig. 6.3(c) matches very well with $[M_s(T)/M_s(310)]^3$ ratio, confirming the dominant uniaxial anisotropy in this system that is strongly temperature dependent. The temperature-dependent K_u originates from the fluctuating local spin clusters activated from the thermal energy [77, 78].

Magnetocaloric Effect

To investigate the magnetocaloric effect (MCE), we analyzed the field-dependent isotherms $M(H)$ acquired at different temperatures [see Figs. 6.3(a) and 6.3(b)] in the vicinity of

Table 6.1: Magnetocrystalline anisotropy energies (K_u) of different layered materials.

Composition	$\approx K_u$ (in kJ/m^3)	Ref.
$Cr_{0.83}Te$	390	This work
$Cr_{0.87}Te$	270	[42]
$Cr_{0.69}Te$	165	[40]
$Cr_{0.625}Te$	94	[21]
$Cr_{0.6}Te$	174	[41]
$CrBr_3$	86	[74]
CrI_3	300	[74]
$Cr_2Ge_2Te_6$	20	[22]
$Cr_2Si_2Te_6$	65	[22]
Fe_4GeTe_2	250	[75]
Fe_3GeTe_2	1460	[76]

Table 6.2: Critical exponents of $Cr_{0.83}Te$ single crystal compared with several theoretical models (MEC = Magnetic Entropy Change).

Composition	Technique	β	γ	δ	p	q	Ref.
$Cr_{0.83}Te$	MEC	0.4739(4)	1.2812(3)	3.7037(5)	0.70	1.27	This work
Landau mean field	Theory	0.5	1	3	0.667	1.333	[80]
3D Heisenberg	Theory	0.365	1.386	4.80	0.637	1.208	[44]
3D Ising	Theory	0.325	1.241	4.82	0.569	1.207	[44]

T_C for both $H \parallel xy$ and $H \parallel z$ orientations. The magnetocaloric effect is an intrinsic property of a ferromagnetic system, resulting from adiabatic heating or cooling under external magnetic fields [79]. This effect leads to the generation of magnetic entropy change $\Delta S_m(T, H)$, which can be quantified using the formula,

$$\Delta S_m(T, H) = \int_o^H (\frac{\partial S}{\partial H})_T dH = \int_o^H (\frac{\partial M}{\partial T})_H dH \tag{6.4}$$

where $(\frac{\partial S}{\partial H})_T = (\frac{\partial M}{\partial T})_H$ based on Maxwell's relation. For the magnetization data acquired at smaller discrete field and temperature intervals, the magnetic entropy change $\Delta S_m(T, H)$ can be expressed as

$$\Delta S_m(T, H) = \frac{\int_0^H M(T_{i+1}, H)dH - \int_0^H M(T_i, H)dH}{T_{i+1} - T_i} \tag{6.5}$$

Figs. 6.4(a) and 6.4(b) show - $\Delta S_m(T, H)$ plotted as a function temperature under various magnetic fields up to 5 T taken with a step size of 1 T for both $H \parallel xy$ and $H \parallel z$

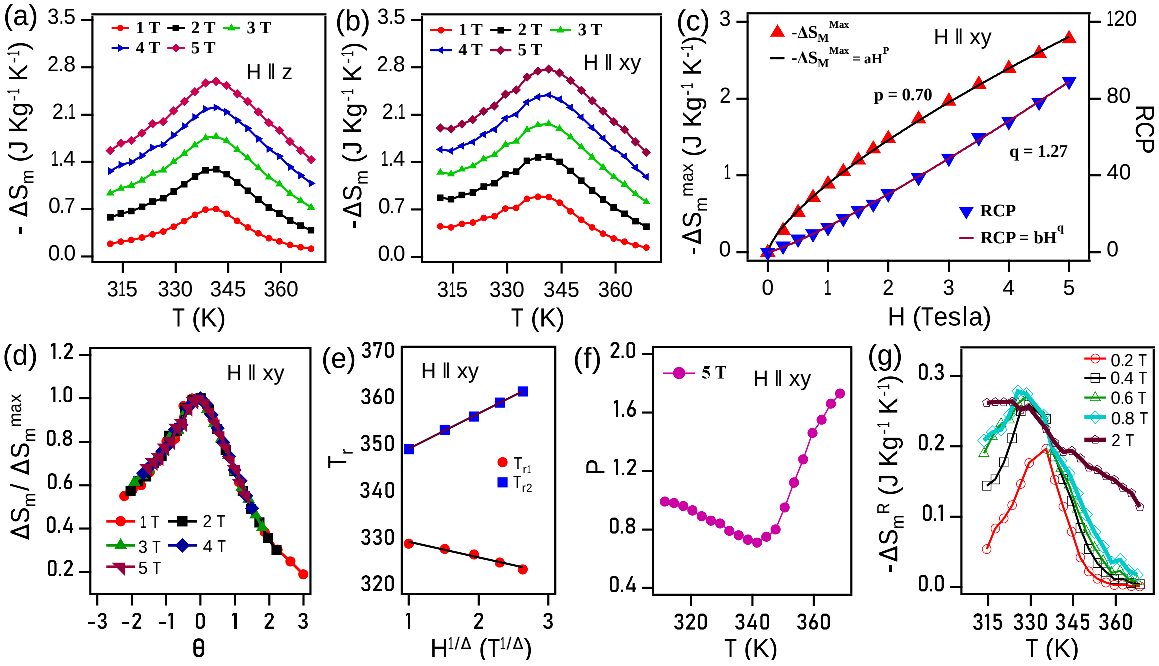

Figure 6.4: Magnetic entropy change -ΔS_m plotted as a function of temperature at different magnetic fields for (a) $H \parallel z$ and (b) $H \parallel xy$. (c) Field-dependent maximum magnetic entropy change (-ΔS_m^{max}) (left axis) and relative cooling power (RCP) (right axis). (d) Normalized magnetic entropy change as a function of rescaled temperature θ for various applied fields. (e) T_r *vs* $H^{1/\Delta}$. (f) Exponent p plotted as a function of temperature. (g) Rotational magnetic entropy change (-ΔS_m^R) plotted as a function of temperature.

orientations, respectively. All - $\Delta S_m(T,H)$ curves show a maximum change in entropy with a broad peak at around T_C as can be seen from Figs. 6.4(a) and 6.4(b). Further, we observe that the value of - $\Delta S_m^{max}(T,H)$ increase monotonically with field for $H \parallel xy$ [see Fig. 6.4(c)]. Under an applied field of 5 T, the maximum of -$\Delta S_m(T,H)$ is about 2.78 J kg^{-1} K^{-1} for $H \parallel xy$ and is about 2.58 J kg^{-1} K^{-1} for $H \parallel z$. These -$\Delta S_m(T,H)$ values taken at 5 T are comparable to the other 2D ferromagnetic systems such as $Cr_2Ge_2Te_6$ (2.64 J kg^{-1} K^{-1}) [22] and Cr_5Te_8 (2.38 J kg^{-1} K^{-1}) [21], larger than the values of $Fe_{3-x}GeTe_2$ (1.14 J kg^{-1} K^{-1}) [81] and CrI_3 (1.56J kg^{-1} K^{-1}) [82], and smaller than the values of CrB_3 (7.2 J kg^{-1} K^{-1}) [83] and $Cr_2Si_2Te_6$ (5.05 J kg^{-1} K^{-1}) [22].

To estimate the relative cooling power (RCP) as shown in Fig. 6.4(c), we employed the relation RCP = -$\Delta S_m^{max} \times \delta T_{FWHM}$, where -$\Delta S_m^{max}$ is the maximum entropy change near T_C and δT_{FWHM} is the full width at half maximum of the peak [84]. The calculated RCP in $Cr_{0.83}Te$ is 88.29 J kg^{-1} at around T_C with an applied field of 5 T parallel to the *xy*-plane. The RCP value of $Cr_{0.83}Te$ obtained in this study is comparable to the RCP value obtained in the other 2D systems such as $Cr_2Ge_2Te_6$ (87 J kg^{-1})[22], but smaller than the values obtained from Cr_5Te_8 (131.2 J kg^{-1}) [21], CrI_3 (122.6 J kg^{-1}) [82], $Cr_2Si_2Te_6$ (114 J kg^{-1}) [22], $Fe_{3-x}GeTe_2$(113 J kg^{-1}) [81], and $CrBr_3$(191.5 J kg^{-1}) [83].

In addition, both -ΔS_m^{max} and RCP are related by the power law of magnetic field as given below [84, 85],

$$-\Delta S_m^{max} = aH^p \tag{6.6}$$

$$RCP = \ bH^q \tag{6.7}$$

where p and q are the exponents. At T = T_C, they can be written as

$$p = 1 + \frac{\beta - 1}{\beta + \gamma} \tag{6.8}$$

$$q = 1 + \frac{1}{\delta} \tag{6.9}$$

Where β, γ, and δ are critical exponents, which can be found using alternative theoretical models such as isothermal analysis, these exponents obtained from the magnetic entropy analysis, however, are more dependable without the use of initial exponents. In addition, the exponent δ has been calculated using the Widom scaling relation, δ = 1 + (γ/β) [86]. The fit of -ΔS_m^{max} by the Eq. 6.6 yields p = 0.70. Similarly, the field dependence of RCP is fitted by Eq. 6.7, yielding q = 1.27. Based on Eq. 6.8 and Eq. 6.9, the derived critical exponents are β = 0.4739(4), γ = 1.2812(3), and δ = 3.7037(5). Note that no single conventional universality class can describe the derived critical exponents. The critical exponents suggest a crossover between the mean-field model (β = 0.5) and the 3D-Ising model (γ = 1.241). Thus, our study indicates complex magnetic interactions in the $Cr_{0.83}Te$ system.

Next, we performed the scaling analysis of MCE following the procedure given by Franco *et. al.* [85, 87]. The scaling analysis of - $\Delta S_m(T, H)$ is constructed by normalizing the - $\Delta S_m(T, H)$ curves with respect to the maximum of -ΔS_m^{max} [$\frac{\Delta S_m(T,H)}{\Delta S_m^{max}}$]. The reduced temperature ($\theta_\mp$) is defined by choosing two reference temperatures ($T_{r1} \leq T_C$ and $T_{r2} > T_C$), satisfying the condition, $\frac{\Delta S_m(T_{r1}<T_c)}{\Delta S_m^{max}} = \frac{\Delta S_m(T_{r2}>T_c)}{\Delta S_m^{max}}$ = h. Here, h is a scaling constant with values within the $0 < h < 1$ range. Then, the rescaled temperature $\theta_\mp$ can be written as

$$\theta_- = (T_C - T)/(T_{r1} - T_C), T \leq T_C \tag{6.10}$$

$$\theta_+ = (T - T_C)/(T_{r2} - T_C), T > T_C \tag{6.11}$$

Following the MCE scaling analysis, all the curves of $\frac{\Delta S_m}{\Delta S_m^{max}}$ plotted as a function of reduced temperature θ at various magnetic fields collapse into a single curve as shown in Fig. 6.4(d), confirming the second-order magnetic phase transition in $Cr_{0.83}Te$ [57, 58, 88]. Moreover, it can be seen that the universal curve of MCE is independent of the applied magnetic field and temperature, as it is generally determined by the intrinsic magnetization of the system [85]. Further, the reference temperatures T_{r1} and T_{r2} linearly depend on $H^{1/\Delta}$

for $\Delta = \beta + \gamma$ as shown in Fig. 6.4(e). Fig. 6.4(f) displays the temperature dependence of p. The $p(T)$ curve follows universal behavior across T_C as it reaches the value 1 for T < T_C [89]. On the other hand, well above T_C, p reaches the value of two due to the Curie-Weiss law [89]. At T = T_C, $p(T)$ has a minimum value of 0.7, in line with the universal law of $p(T)$ [57]. Overall, the temperature dependence of p perfectly follows the universal behavior of a second-order phase transition [85]. The rotational magnetic entropy changes (ΔS_m^R) can be calculated using the formula $\Delta S_m^R(T, H) = \Delta S_m(T, H_{ab})$ - $\Delta S_m(T, H_c)$. Fig. 6.4(g) depicts the temperature dependence of - $\Delta S_m^R(T, H)$. From Fig. 6.4(g), we can find a maximum of -$\Delta S_m^R(T, H)$ at around T$_C$ when derived at a field interval of 0.2 T. The maxima of -$\Delta S_m^R(T, H)$ shifts to lower temperatures with increasing field intervals, and for 2 T of field interval, no maxima is found down to 315 K. This behavior is generally found in systems with strong magnetic anisotropy [21].

6.3.3 Electrical and Magnetotransport Properties

Figure 6.5(a) displays temperature-dependent longitudinal resistivity ρ_{xx} of Cr$_{0.83}$Te single crystal, revealing the metallic nature throughout the measured temperature range [90]. A change in the resistivity curve is noticed at around 245 K, while the exact origin is not very clear to us, but we noticed a small cusp in the dM/dT (not shown) at around 245 K from the FC data measured with 0.02 T [see Fig. 6.2(a)]. The top inset of Fig. 6.5(a) elucidates the quadratic temperature dependence of ρ_{xx}, fitted by $\rho(T) = \rho_0 + aT^2$, indicating dominant electron-electron scattering at low temperatures. This observation is in agreement with the theoretical studies on weak itinerant ferromagnetic metals in which a T^2 dependence of ρ_{xx} was predicted at low temperatures [91]. The bottom inset of Fig. 6.5(a) depicts the linear four-probe geometry used for measuring the longitudinal resistivity. The transverse resistivity ρ_{xy} (Hall resistivity) as a function of the applied field (H) is shown in Fig. 6.5(c) measured at various sample temperatures. The Hall resistivity, ρ_{xy}, was measured with the current applied along the x-axis, the magnetic field applied along the z-axis, and the resulting Hall voltage was detected along the y-axis as demonstrated in Fig. 6.5(b). Thus, the red-colored curves shown in the panels of Fig. 6.5(c) exhibit the raw data of field-dependent Hall resistivity ρ_{xy} recorded at various sample temperatures, and the black-colored curves are the fittings to the total Hall resistivity using the formula [92],

$$\rho_{xy}(H) = \rho^N(H) + \rho^A(H) = \mu_0 R_0 H + \mu_0 R_s M \tag{6.12}$$

Here, ρ^N and ρ^A are the normal Hall and anomalous Hall contributions to the total Hall resistivity, respectively. R_0 is the normal Hall coefficient, R_s is the anomalous Hall coefficient, and M is the isothermal magnetization. The normal and anomalous Hall coefficients can be determined by a linear fit at the high field region following the relation $\frac{\rho_{xy}}{\mu_0 H} = R_0 + \frac{R_s M}{H}$. However, as can be seen from the panels of Fig. 6.5(c), the fitting of ρ_{xy}

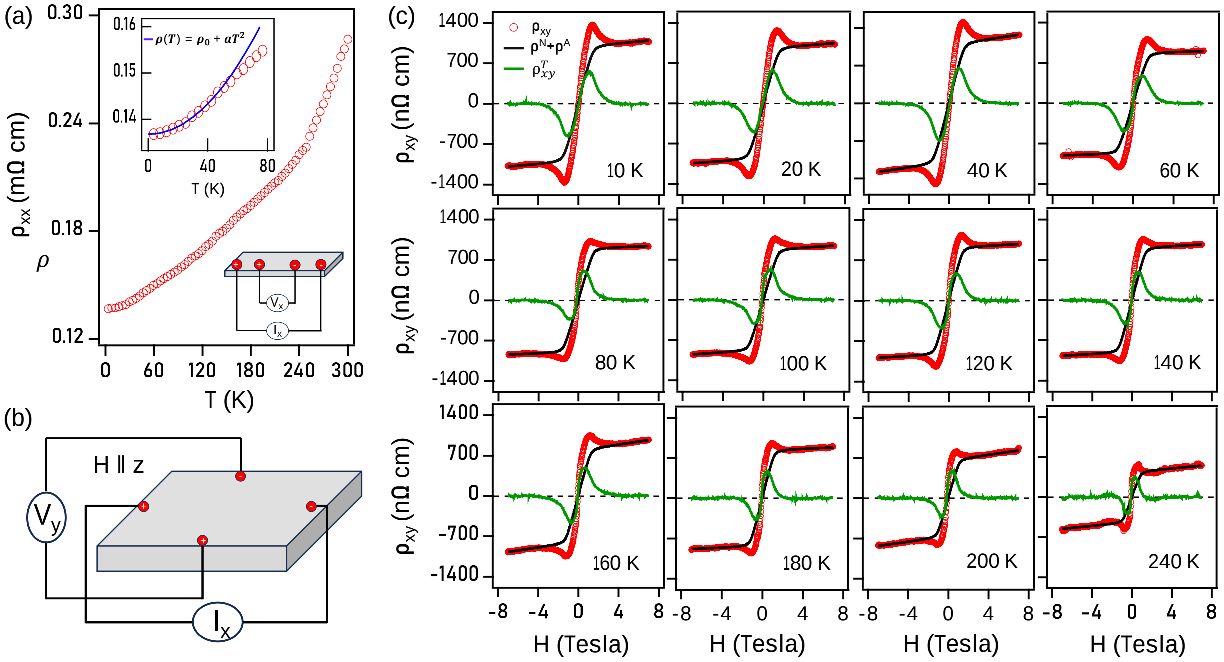

Figure 6.5: (a) Temperature-dependent longitudinal electrical resistivity ρ_{xx}. The top inset of (a) displays low-temperature resistivity fitted by $\rho(T) = \rho_0 + aT^2$ and the bottom inset of (a) shows a schematic of linear four-probe geometry. (b) Schematic diagram of the Hall measurement geometry. (c) Transverse resistivity ρ_{xy} (Hall resistivity), ρ_{xy} plotted as a function of the magnetic field measured at various temperatures. In (c), the red curves represent total Hall resistivity (raw data), the black curves are the fittings using the equation $\rho_N + \rho_A$, and the green curves represent the topological Hall resistivity (ρ_T). See the text for more details.

with Eq. 6.12 is not perfect due to the topological Hall contribution. Thus, by including the topological Hall effect (THE) contribution, the total Hall resistivity can be expressed by $\rho_{xy}(H) = \mu_0 R_0 H + \mu_0 R_s M + \rho^T$ and the topological Hall resistivity (ρ^T) is extracted using the relation $\rho^T = \rho_{xy}(H) - (\mu_0 R_0 H + \mu_0 R_s M)$ [93, 40]. In Fig. 6.5(c), the green-colored curves represent the topological Hall resistivity.

Figure 6.6(a) depicts the charge-carrier density (n) plotted as a function of temperature, estimated from the normal Hall coefficient R_0 following the relation $n = 1/(R_0 q)$. Here q is the hole-carrier charge. The derived carrier concentration n decreases with increasing temperature up to 40 K. However, above 40 K, it increases monotonously with temperature. In Cr_xTe_y systems, the competition between the FM and AFM phases plays a vital role in the magnetotransport properties [42, 39, 40]. Similarly, in Fig. 6.2(f), the in-plane $\Delta M(T)$ changes abruptly around T≈ 40 K, plausibly originating the non-monotonic changes of carrier concentration around 40 K. Next, the anomalous Hall conductivity (AHC), σ_{xy}, obtained using the relation $\sigma_{xy} = \frac{\rho_{xy}}{\rho_{xy}^2 + \rho_{xx}^2}$ is presented in Fig. 6.6(b). σ_{xy} increases with increasing temperature up to 40 K. Beyond 40 K, it monotonically decreases with increasing temperature. A maximum $\sigma_{xy} \approx 52\ \Omega^{-1} cm^{-1}$ is found at around 40 K. In general, the anomalous Hall conductivity can intrinsically arise from the electronic

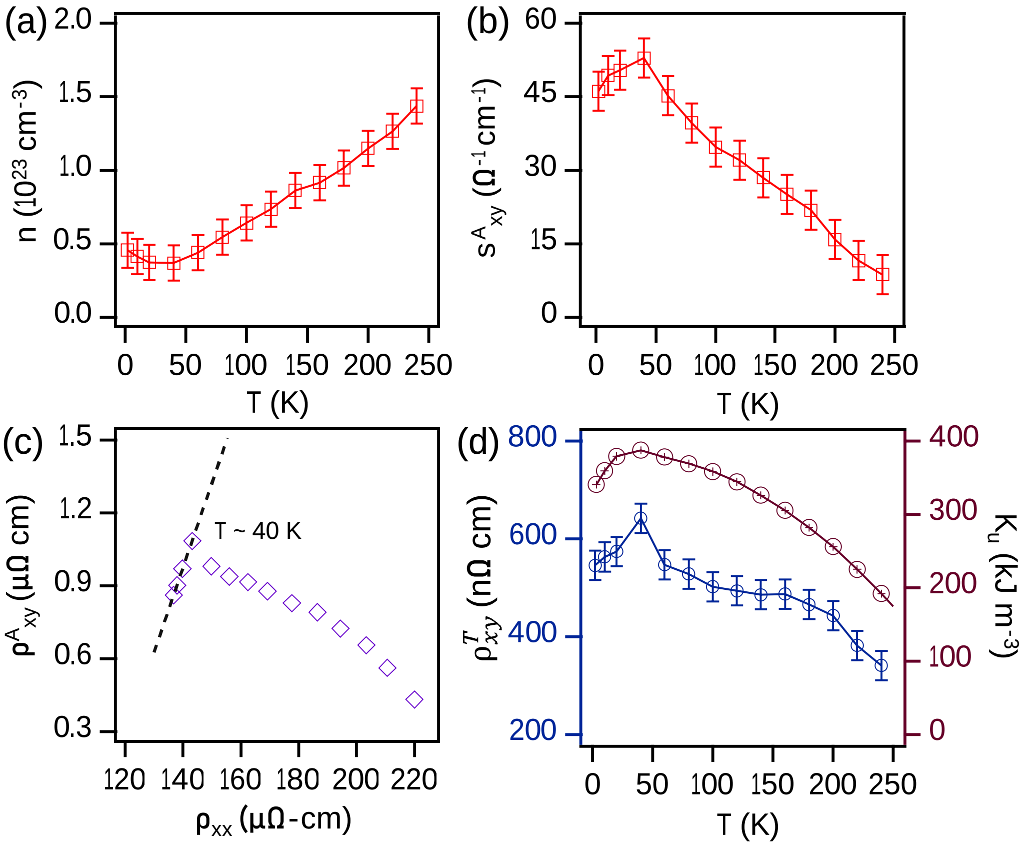

Figure 6.6: Temperature dependence of (a) derived calculated carrier density n. (b) Anomalous Hall conductivity σ^A_{xy}. (c) Plot of ρ^A_{xy} vs. ρ_{xx} with linear fitting up to $40K$. (d) Maximum value of topological Hall resistivity $\rho^{T,max}_{xy}$ (left axis) and magneto-crystalline anisotropy density, K_u (right axis), plotted as a function of temperature.

structure-originated non-zero Berry curvature [92, 94] or extrinsically due to magnetism-originated side-jump/skew-scattering mechanisms [95, 92].

To understand the nature of AHE in $Cr_{0.83}Te$ we plotted ρ_{xy} *vs.* ρ_{xx} in Fig. 6.6(c). The Hall resistivity for an itinerant ferromagnetic metal is generally expressed by the formula $\rho_{xy} = \alpha\rho_{xx} + \beta\rho^2_{xx}$, where α and β represent the skew-scattering and side-jump coefficients, respectively [92, 96]. From Fig. 6.6(c), a linear dependence of ρ_{xy} on ρ_{xx} is evident up to 40 K, beyond which a deviation occurs with increasing temperature. This observation hints at the skew-scattering mechanism that originated anomalous Hall effect in $Cr_{0.83}Te$, consistent with the other Cr_xTe_y systems [40, 90, 97]. Furthermore, Fig. 6.6(d) depicts the maximum amplitude of topological Hall resistivity ($\rho^{T,max}_{xy}$) (left axis) plotted as a function of temperature. $\rho^{T,max}_{xy}$ increases with temperature and reaches a maximum value of approximately 620 nΩ-cm at around 40 K, consistent with $\Delta M(T)$ ($H \parallel xy$) of Fig. 6.2(f). The right axis of Fig. 6.6(d) displays the magnetocrystalline anisotropy energy constant, K_u, calculated using Eq. 6.3. It is worth mentioning here that the critical point of 40 K observed from ρ^A_{xy}, ρ^T_{xy}, and K_u (see Fig. 6.6) originates from a canted antiferromagnetic transition noticed at around 40 K (from $M(T)$ measured with 2 T, not shown), which is consistent with the other $\mathrm{Cr}_x\mathrm{Te}_y$ based systems [62, 65].

Several theories have been proposed to elucidate the origin of the chiral spin texture that can manifest the topological Hall effect. These theories include the Dzyaloshinskii-Moriya interaction (DMI) in noncentrosymmetric systems under a strong spin-orbit coupling [98–101, 93], geometrically frustrated magnetic interactions [102], and noncoplanar spin structure stabilized by the magnetocrystalline anisotropy (MCA) [48, 40]. On the other hand, the intricate magnetism observed in $\mathrm{Cr}_x\mathrm{Te}_y$ type systems results from a complex interplay of magnetic interactions, including direct, super-exchange, and double exchange mechanisms, noncollinear magnetism, and a mixed valence state of the Cr ions [39, 56, 103]. The derived critical exponents, which deviate from any single universality class (as discussed above), strongly suggest the presence of robust magnetocrystalline anisotropy (MCA) in $\mathrm{Cr}_{0.83}\mathrm{Te}$. Consequently, the large MCA can stabilize the requisite chiral spin structure [104, 47]. Thus, in the presence of chiral-spin structure, the itinerant electrons acquire real-space Berry curvature, leading to a non-zero scalar-spin chirality $\chi_{ijk} = S_i(S_j \times S_k) \neq 0$ to produce the topological Hall effect [102, 100]. The analogy of chiral-spin structure stabilized by the large MCA is consistent with our experimental data shown in Fig. 6.6(d) (right-axis), where the temperature-dependent topological Hall resistivity (ρ_{xy}^T) replicates the temperature dependence of MCA energy density K_u, having the maximum ρ_{xy}^T at the maximum $\mathrm{K}_u \approx 390$ kJ/m^3 at 40 K.

6.4 Summary

We investigated the intricate magnetism, electrical, and magnetotransport properties in the hexagonal itinerant ferromagnet $\mathrm{Cr}_{0.83}\mathrm{Te}$. The magnetotransport study reveals a substantial topological Hall effect, originating from the noncoplanar spin structure in the presence of strong magnetic anisotropy and the skew-scattering-induced anomalous Hall effect. We observe a remarkable cooling efficacy of $-\Delta S_m^{max} \approx 2.77$ J $kg^{-1}K^{-1}$ and RCP $\approx$ 88.29 J/kg at an applied field of 5 Tesla. By utilizing the magneto-entropy scaling analysis, we extracted the critical exponents $\beta = 0.4739(4)$, $\gamma = 1.2812(3)$, and $\delta = 3.7037(5)$, which do not follow any single universality class, suggesting a complex magnetic interaction in $\mathrm{Cr}_{0.83}\mathrm{Te}$. Re-scaled $-\Delta S_m(T, H)$ curves fall into a single universal curve, confirming the second-order magnetic transition. The spin-fluctuation parameter, derived from the critical magnetization isotherms based on the SCR theory, confirms the itinerant ferromagnetic nature of $\mathrm{Cr}_{0.83}\mathrm{Te}$.

References

[1] Y. Deng, Y. Yu, Y. Song, J. Zhang, N. Z. Wang, Z. Sun, Y. Yi, Y. Z. Wu, S. Wu, J. Zhu, et al., Gate-tunable room-temperature ferromagnetism in two-dimensional

Fe_3GeTe_2, Nature 563 (2018) 94–99.

[2] B. Wang, Y. Zhang, L. Ma, Q. Wu, Y. Guo, X. Zhang, J. Wang, MnX (X= P, As) monolayers: a new type of two-dimensional intrinsic room temperature ferromagnetic half-metallic material with large magnetic anisotropy, Nanoscale 11 (2019) 4204–4209.

[3] A. K. Geim, I. V. Grigorieva, Van der Waals heterostructures, Nature 499 (2013) 419–425.

[4] J. T. Heron, M. Trassin, K. Ashraf, M. Gajek, Q. He, S. Y. Yang, D. E. Nikonov, Y.-H. Chu, S. Salahuddin, R. Ramesh, Electric-Field-Induced Magnetization Reversal in a Ferromagnet-Multiferroic Heterostructure, Phys. Rev. Lett. 107 (2011) 217202.

[5] Y. Khan, S. M. Obaidulla, M. R. Habib, A. Gayen, T. Liang, X. Wang, M. Xu, Recent breakthroughs in two-dimensional van der Waals magnetic materials and emerging applications, Nano Today 34 (2020) 100902.

[6] M. Hossain, B. Qin, B. Li, X. Duan, Synthesis, characterization, properties and applications of two-dimensional magnetic materials, Nano Today 42 (2022) 101338.

[7] C. Gong, L. Li, Z. Li, H. Ji, A. Stern, Y. Xia, T. Cao, W. Bao, C. Wang, Y. Wang, et al., Discovery of intrinsic ferromagnetism in two-dimensional van der Waals crystals, Nature 546 (2017) 265–269.

[8] K. L. Seyler, D. Zhong, D. R. Klein, S. Gao, X. Zhang, B. Huang, E. Navarro-Moratalla, L. Yang, D. H. Cobden, M. A. McGuire, et al., Ligand-field helical luminescence in a 2D ferromagnetic insulator, Nat. Phys. 14 (2018) 277–281.

[9] Z. Fei, B. Huang, P. Malinowski, W. Wang, T. Song, J. Sanchez, W. Yao, D. Xiao, X. Zhu, A. F. May, et al., Two-dimensional itinerant ferromagnetism in atomically thin Fe_3GeTe_2, Nat. Mater. 17 (2018) 778–782.

[10] M. Gibertini, M. Koperski, A. F. Morpurgo, K. S. Novoselov, Magnetic 2D materials and heterostructures, Nat. Nanotechnol. 14 (2019) 408–419.

[11] H. L. Zhuang, P. R. C. Kent, R. G. Hennig, Strong anisotropy and magnetostriction in the two-dimensional Stoner ferromagnet Fe_3GeTe_2, Phys. Rev. B 93 (2016) 134407.

[12] Mermin, N. D. and Wagner, H., Absence of Ferromagnetism or Antiferromagnetism in One- or Two-Dimensional Isotropic Heisenberg Models, Phys. Rev. Lett. 17 (1966) 1133–1136.

[13] B. Huang, G. Clark, E. Navarro-Moratalla, D. R. Klein, R. Cheng, K. L. Seyler, D. Zhong, E. Schmidgall, M. A. McGuire, D. H. Cobden, W. Yao, D. Xiao, P. Jarillo-Herrero, X. Xu, Layer-dependent ferromagnetism in a van der Waals crystal down to the monolayer limit, Nature 546 (2017) 270–273.

[14] Y. Liu, C. Petrovic, Critical behavior of quasi-two-dimensional semiconducting ferromagnet $Cr_2Ge_2Te_6$, Phys. Rev. B 96 (2017) 054406.

[15] T. J. Williams, A. A. Aczel, M. D. Lumsden, S. E. Nagler, M. B. Stone, J.-Q. Yan, D. Mandrus, Magnetic correlations in the quasi-two-dimensional semiconducting ferromagnet $CrSiTe_3$, Phys. Rev. B 92 (2015) 144404.

[16] Q. Xie, Y. Liu, M. Wu, H. Lu, W. Wang, L. He, X. Wu, Two stage magnetization in van der Waals layered $CrXTe_3$ (X = Si, Ge) single crystals, Mater. Lett. 246 (2019) 60–62.

[17] X. Feng, J. Li, J. Wu, Anisotropy of magnetocaloric effect in Fe_3GeTe_2, Phys. B Condens. Matter 625 (2022) 413478.

[18] X. Sun, S. Zhao, A. Bachmatiuk, M. H. Rümmeli, S. Gorantla, M. Zeng, L. Fu, 2D Intrinsic Ferromagnetic MnP Single Crystals, Small 16 (2020) 2001484.

[19] L. M. Moreno-Ramírez, V. Franco, Reversibility of the Magnetocaloric Effect in the Bean-Rodbell Model, Magnetochemistry 7 (2021) 60.

[20] V. Y. Verchenko, A. A. Tsirlin, A. V. Sobolev, I. A. Presniakov, A. V. Shevelkov, Ferromagnetic Order, Strong Magnetocrystalline Anisotropy, and Magnetocaloric Effect in the Layered Telluride Fe_3GeTe_2, Inorg. Chem. 54 (2015) 8598–8607.

[21] Y. Liu, M. Abeykoon, E. Stavitski, K. Attenkofer, C. Petrovic, Magnetic anisotropy and entropy change in trigonal Cr_5Te_8, Phys. Rev. B 100 (2019) 245114.

[22] Y. Liu, C. Petrovic, Anisotropic magnetic entropy change in $Cr_2X_2Te_6$ (X = Si and Ge), Phys. Rev. Materials 3 (2019) 014001.

[23] Y. Zhu, X. Kong, T. D. Rhone, H. Guo, Systematic search for two-dimensional ferromagnetic materials, Phys. Rev. Materials 2 (2018) 081001.

[24] T. Eto, M. Ishizuka, S. Endo, T. Kanomata, T. Kikegawa, Pressure-induced structural phase transition in a ferromagnet CrTe, J. Alloys Compd. 315 (2001) 16–21.

[25] F. Wang, J. Du, F. Sun, R. F. Sabirianov, N. Al-Aqtash, D. Sengupta, H. Zeng, X. Xu, Ferromagnetic Cr_2Te_3 nanorods with ultrahigh coercivity, Nanoscale 10 (2018) 11028–11033.

[26] B. Hessen, T. Siegrist, T. Palstra, S. Tanzler, M. Steigerwald, Hexakis (triethylphosphine) octatelluridohexachromium and a molecule-based synthesis of chromium telluride, Cr_3Te_4, Inorg. Chem. 32 (1993) 5165–5169.

[27] L.-Z. Zhang, A.-L. Zhang, X.-D. He, X.-W. Ben, Q.-L. Xiao, W.-L. Lu, F. Chen, Z. Feng, S. Cao, J. Zhang, J.-Y. Ge, Critical behavior and magnetocaloric effect of the quasi-two-dimensional room-temperature ferromagnet Cr_4Te_5, Phys. Rev. B 101 (2020) 214413.

[28] H. Liu, J. Fan, H. Zheng, J. Wang, C. Ma, H. Wang, L. Zhang, C. Wang, Y. Zhu, H. Yang, Magnetic properties and critical behavior of quasi-2D layered Cr_4Te_5 thin film, Front. Phys. 18 (2023) 13302.

[29] W. Wang, J. Fan, H. Liu, H. Zheng, C. Ma, L. Zhang, Y. Sun, C. Wang, Y. Zhu, H. Yang, Fabrication and magnetic-electronic properties of van der Waals Cr_4Te_5 ferromagnetic films, CrystEngComm 24 (2022) 674–680.

[30] Y. Wang, J. Yan, J. Li, S. Wang, M. Song, J. Song, Z. Li, K. Chen, Y. Qin, L. Ling, H. Du, L. Cao, X. Luo, Y. Xiong, Y. Sun, Magnetic anisotropy and topological Hall effect in the trigonal chromium tellurides Cr_5Te_8, Phys. Rev. B 100 (2019) 024434.

[31] X.-H. Luo, W.-J. Ren, Z.-D. Zhang, Magnetic properties and magnetocaloric effect of a trigonal Te-rich Cr_5Te_8 single crystal, J. Magn. Magn. Mater. 445 (2018) 37–43.

[32] J. Dijkstra, H. Weitering, C. Van Bruggen, C. Haas, R. De Groot, Band-structure calculations, and magnetic and transport properties of ferromagnetic chromium tellurides (CrTe, Cr_3Te_4, Cr_2Te_3), J. Phys.: Condens. Matter 1 (1989) 9141.

[33] Z.-L. Huang, W. Bensch, D. Benea, H. Ebert, Anion substitution effects on structure and magnetism in the chromium chalcogenide Cr5Te8—Part I: Cluster glass behavior in trigonal Cr(1+x)Q2 with basic cell (Q=Te, Se; Te:Se=7:1), J. Solid State Chem. 177 (2004) 3245–3253.

[34] Z.-L. Huang, W. Bensch, S. Mankovsky, S. Polesya, H. Ebert, R. K. Kremer, Anion substitution effects on structure and magnetism of the chromium chalcogenide Cr_5Te_8 Part II: Cluster-glass and spin-glass behavior in trigonal Cr(1+x) Q2 with basic cells and trigonal Cr(5+x) Q8 with superstructures (Q=Te, Se; Te:Se=6:2), J. Solid State Chem. 179 (2006) 2067–2078.

[35] J. Wontcheu, W. Bensch, S. Mankovsky, S. Polesya, H. Ebert, R. K. Kremer, E. Brücher, Anion substitution effects on the structure and magnetism of the chromium chalcogenide Cr5Te8—Part III: Structures and magnetism of the high-temperature modification Cr(1+x)Q2 and the low-temperature modification Cr(5+x)Q8 (Q=Te, Se; Te:Se=5:3), J. Solid State Chem. 181 (2008) 1492–1505.

[36] H. Ipser, K. L. Komarek, K. O. Klepp, Transition metal-chalcogen systems viii: The CrTe phase diagram, Journal of the Less Common Metals 92 (1983) 265–282.

[37] C. Zhang, C. Liu, J. Zhang, Y. Yuan, Y. Wen, Y. Li, D. Zheng, Q. Zhang, Z. Hou, G. Yin, et al., Room-Temperature Magnetic Skyrmions and Large Topological Hall Effect in Chromium Telluride Engineered by Self-Intercalation, Adv. Mater. 35 (2023) 2205967.

[38] B. Li, X. Deng, W. Shu, X. Cheng, Q. Qian, Z. Wan, B. Zhao, X. Shen, R. Wu, S. Shi, et al., Air-stable ultrathin Cr_3Te_4 nanosheets with thickness-dependent magnetic biskyrmions, Mater. Today 57 (2022) 66–74.

[39] Y. Chen, Y. Zhu, R. Lin, W. Niu, R. Liu, W. Zhuang, X. Zhang, J. Liang, W. Sun, Z. Chen, et al., Observation of colossal topological Hall effect in noncoplanar ferromagnet Cr_5Te_6 thin films, Adv. Funct. Mater. (2023) 2302984.

[40] S. Purwar, A. Low, A. Bose, A. Narayan, S. Thirupathaiah, Investigation of the anomalous and topological Hall effects in layered monoclinic ferromagnet $Cr_{2.76}Te_4$, Phys. Rev. Mater. 7 (2023) 094204.

[41] M. Huang, L. Gao, Y. Zhang, X. Lei, G. Hu, J. Xiang, H. Zeng, X. Fu, Z. Zhang, G. Chai, et al., Possible Topological Hall Effect above Room Temperature in Layered $Cr_{1.2}Te_2$ Ferromagnet, Nano Lett. 21 (2021) 4280–4286.

[42] J. Liu, B. Ding, J. Liang, X. Li, Y. Yao, W. Wang, Magnetic Skyrmionic bubbles at room temperature and sign reversal of the topological Hall effect in a layered ferromagnet $Cr_{0.87}Te$, ACS Nano 16 (2022) 13911–13918.

[43] Y. He, J. Kroder, J. Gayles, C. Fu, Y. Pan, W. Schnelle, C. Felser, G. H. Fecher, Large topological Hall effect in an easy-cone ferromagnet $Cr_{0.9}B_{0.1}Te$, Appl. Phys. Lett. 117 (2020) 052409.

[44] Kaul, SN, Static critical phenomena in ferromagnets with quenched disorder, J. Magn. Magn. Mater. 53 (1985) 5–53.

[45] A. Bedoya-Pinto, J.-R. Ji, A. K. Pandeya, P. Gargiani, M. Valvidares, P. Sessi, J. M. Taylor, F. Radu, K. Chang, S. S. Parkin, Intrinsic 2D-XY ferromagnetism in a van der Waals monolayer, Science 374 (2021) 616–620.

[46] S. Lee, J. Park, Y. Choi, K. Raju, W.-T. Chen, R. Sankar, K.-Y. Choi, Chemical tuning of magnetic anisotropy and correlations in $Ni_{1-x}Fe_xPS_3$, Phys. Rev. B 104 (2021) 174412.

[47] M. Preißinger, K. Karube, D. Ehlers, B. Szigeti, H.-A. Krug von Nidda, J. S. White, V. Ukleev, H. M. Rønnow, Y. Tokunaga, A. Kikkawa, Y. Tokura, Y. Taguchi, I. Kézsmárki, Vital role of magnetocrystalline anisotropy in cubic chiral skyrmion hosts, npj Quantum Materials 6 (2021) 65.

[48] A. Low, S. Ghosh, S. Changdar, S. Routh, S. Purwar, S. Thirupathaiah, Tuning of topological properties in the strongly correlated antiferromagnet Mn_3Sn via Fe doping, Phys. Rev. B 106 (2022) 144429.

[49] Y. Liu, C. Petrovic, Critical behavior of the quasi-two-dimensional weak itinerant ferromagnet trigonal chromium telluride $Cr_{0.62}Te$, Phys. Rev. B 96 (2017) 134410.

[50] H. Liu, H. Zheng, Y. Wang, C. Huang, C. Ma, Y. Zhu, H. Yang, L. Ling, L. Zhang, J. Fan, Long-Range Magnetic Exchange Coupling in Quasi-2D CrTe Ferromagnetic Thin Films, Phys. Status Solidi RRL 17 (2023) 2300209.

[51] H. Zheng, C. Huang, F. Lin, J. Fan, H. Liu, L. Zhang, C. Ma, C. Wang, Y. Zhu, H. Yang, Two-dimensional van der Waals ferromagnetic thin film $CrTe_2$ with high Curie temperature and metallic conductivity, Appl. Phys. Lett. 122 (2023) 023103.

[52] H. Wu, W. Zhang, L. Yang, J. Wang, J. Li, L. Li, Y. Gao, L. Zhang, J. Du, H. Shu, et al., Strong intrinsic room-temperature ferromagnetism in freestanding non-van der Waals ultrathin 2D crystals, Nat. Commun. 12 (2021) 5688.

[53] R. Sbiaa, H. Meng, S. N. Piramanayagam, Materials with perpendicular magnetic anisotropy for magnetic random access memory, Phys. Status Solidi RRL 5 (2011) 413–419.

[54] D. L. Cortie, G. L. Causer, K. C. Rule, H. Fritzsche, W. Kreuzpaintner, F. Klose, Two-Dimensional Magnets: Forgotten History and Recent Progress towards Spintronic Applications, Adv. Funct. Mater. 30 (2020) 1901414.

[55] V. Krizakova, E. Grimaldi, K. Garello, G. Sala, S. Couet, G. S. Kar, P. Gambardella, Interplay of Voltage Control of Magnetic Anisotropy, Spin-Transfer Torque, and Heat in the Spin-Orbit-Torque Switching of Three-Terminal Magnetic Tunnel Junctions, Phys. Rev. Appl. 15 (2021) 054055.

[56] L.-Z. Zhang, Q.-L. Xiao, F. Chen, Z. Feng, S. Cao, J. Zhang, J.-Y. Ge, Multiple magnetic phase transitions and critical behavior in single crystal Cr_5Te_6, J. Magn. Magn. Mater. 546 (2022) 168770.

[57] Oesterreicher, H and Parker, FT., Magnetic cooling near Curie temperatures above 300 K, J. Appl. Phys. 55 (1984) 4334–4338.

[58] J. Y. Law, V. Franco, L. M. Moreno-Ramírez, A. Conde, D. Y. Karpenkov, I. Radulov, K. P. Skokov, O. Gutfleisch, A quantitative criterion for determining the order of magnetic phase transitions using the magnetocaloric effect, Nat. Commun. 9 (2018) 1–9.

[59] T. Hashimoto, K. Hoya, M. Yamaguchi, I. Ichitsubo, Magnetic properties of single crystals $Cr_{2-\delta}Te_3$, J. Phys. Soc. Jpn. 31 (1971) 679–682.

[60] Ido, Hideaki and Shirakawa, Kiwamu and Suzuki, Takanobu and Kaneko, Takejiro, Exchange striction of ferromagnetic compound CrTe, J. Phys. Soc. Jpn. 26 (1969) 663–665.

[61] F. Meng, W. Liu, A. Rahman, J. Zhang, J. Fan, C. Ma, M. Ge, T. Yao, L. Pi, L. Zhang, Y. Zhang, Crossover of critical behavior and nontrivial magnetism in the chiral soliton lattice host $Cr_{1/3}TaS_2$, Phys. Rev. B 107 (2023) 144425.

[62] C. Li, K. Liu, D. Jiang, C. Jin, T. Pei, T. Wen, B. Yue, Y. Wang, Diverse Thermal Expansion Behaviors in Ferromagnetic $Cr_{1-\delta}Te$ with NiAs-Type, Defective Structures, Inorg. Chem. 61 (2022) 14641–14647.

[63] C. Chen, X. Chen, C. Wu, X. Wang, Y. Ping, X. Wei, X. Zhou, J. Lu, L. Zhu, J. Zhou, et al., Air-Stable 2D Cr_5Te_8 Nanosheets with Thickness-Tunable Ferromagnetism, Adv. Mater. 34 (2022) 2107512.

[64] L.-Z. Zhang, X.-D. He, A.-L. Zhang, Q.-L. Xiao, W.-L. Lu, F. Chen, Z. Feng, S. Cao, J. Zhang, J.-Y. Ge, Tunable Curie temperature in layered ferromagnetic $Cr_{5+\delta}Te_8$ single crystals, APL Mater. 8 (2020) 031101.

[65] Z.-L. Huang, W. Kockelmann, M. Telling, W. Bensch, A neutron diffraction study of structural and magnetic properties of monoclinic Cr_5Te_8, Solid State Sci. 10 (2008) 1099–1105.

[66] A. Roy, S. Guchhait, R. Dey, T. Pramanik, C.-C. Hsieh, A. Rai, S. K. Banerjee, Perpendicular magnetic anisotropy and spin glass-like behavior in molecular beam epitaxy grown chromium telluride thin films, ACS Nano 9 (2015) 3772–3779.

[67] Y. Fujisawa, M. Pardo-Almanza, J. Garland, K. Yamagami, X. Zhu, X. Chen, K. Araki, T. Takeda, M. Kobayashi, Y. Takeda, C. H. Hsu, F. C. Chuang, R. Laskowski, K. H. Khoo, A. Soumyanarayanan, Y. Okada, Tailoring magnetism in self-intercalated $Cr_{1+\delta}Te_2$ epitaxial films, Phys. Rev. Mater. 4 (2020) 114001.

[68] K. Shimada, T. Saitoh, H. Namatame, A. Fujimori, S. Ishida, S. Asano, M. Matoba, S. Anzai, Photoemission study of itinerant ferromagnet $Cr_{1-\delta}Te$, Phys. Rev. B 53 (1996) 7673–7683.

[69] Takahashi, Yoshinori, On the origin of the Curie-Weiss law of the magnetic susceptibility in itinerant electron ferromagnetism, J. Phys. Soc. Jpn. 55 (1986) 3553–3573.

[70] M. Imai, C. Michioka, H. Ueda, K. Yoshimura, Static and dynamical magnetic properties of the itinerant ferromagnet $LaCo_2P_2$, Phys. Rev. B 91 (2015) 184414.

[71] S. Mondal, N. Khan, S. M. Mishra, B. Satpati, P. Mandal, Critical behavior in the van der Waals itinerant ferromagnet Fe_4GeTe_2, Phys. Rev. B 104 (2021) 094405.

[72] H. Ohta, C. Michioka, A. Matsuo, K. Kindo, K. Yoshimura, Magnetic study of SmCoAsO showing a ferromagnetic-antiferromagnetic transition, Phys. Rev. B 82 (2010) 054421.

[73] Y. Takahashi, Spin fluctuation theory of itinerant electron magnetism, volume 9, Springer, 2013.

[74] N. Richter, D. Weber, F. Martin, N. Singh, U. Schwingenschlögl, B. V. Lotsch, M. Kläui, Temperature-dependent magnetic anisotropy in the layered magnetic semiconductors CrI_3 and $CrBr_3$, Phys. Rev. Materials 2 (2018) 024004.

[75] J. Seo, D. Y. Kim, E. S. An, K. Kim, G.-Y. Kim, S.-Y. Hwang, D. W. Kim, B. G. Jang, H. Kim, G. Eom, et al., Nearly room temperature ferromagnetism in a magnetic metal-rich van der Waals metal, Sci. Adv. 6 (2020) eaay8912.

[76] N. León-Brito, E. D. Bauer, F. Ronning, J. D. Thompson, R. Movshovich, Magnetic microstructure and magnetic properties of uniaxial itinerant ferromagnet Fe_3GeTe_2, J. Appl. Phys. 120 (2016) 083903.

[77] C. Zener, Classical Theory of the Temperature Dependence of Magnetic Anisotropy Energy, Phys. Rev. 96 (1954) 1335–1337.

[78] Carr Jr, WJ, Temperature dependence of ferromagnetic anisotropy, Phys. Rev. 109 (1958) 1971.

[79] V. K. Pecharsky, K. A. Gschneidner Jr, Magnetocaloric effect and magnetic refrigeration, J. Magn. Magn. Mater. 200 (1999) 44–56.

[80] Arrott, Anthony, Criterion for Ferromagnetism from Observations of Magnetic Isotherms, Phys. Rev. 108 (1957) 1394–1396.

[81] Y. Liu, J. Li, J. Tao, Y. Zhu, C. Petrovic, Anisotropic magnetocaloric effect in $Fe_{3-x}GeTe_2$, Sci. Rep. 9 (2019) 13233.

[82] Y. Liu, C. Petrovic, Anisotropic magnetocaloric effect in single crystals of CrI_3, Phys. Rev. B 97 (2018) 174418.

[83] X. Yu, X. Zhang, Q. Shi, S. Tian, H. Lei, K. Xu, H. Hosono, Large magnetocaloric effect in van der Waals crystal $CrBr_3$, Front. Phys-beijing. 14 (2019) 43501.

[84] K. Gschneidner Jr, V. Pecharsky, A. Pecharsky, C. Zimm, Recent developments in magnetic refrigeration, in: Materials science forum, volume 315, Trans Tech Publ, pp. 69–76.

[85] V. Franco, J. Blázquez, A. Conde, Field dependence of the magnetocaloric effect in materials with a second order phase transition: A master curve for the magnetic entropy change, Appl. Phys. Lett. 89 (2006) 222512.

[86] Widom, B., Degree of the critical isotherm, J. Chem. Phys. 41 (1964) 1633–1634.

[87] V. Franco, C. Conde, J. Blázquez, A. Conde, P. Švec, D. Janičkovič, L. Kiss, A constant magnetocaloric response in FeMoCuB amorphous alloys with different Fe/B ratios, J. Appl. Phys. 101 (2007) 093903.

[88] V. Franco, J. Law, A. Conde, V. Brabander, D. Karpenkov, I. Radulov, K. Skokov, O. Gutfleisch, Predicting the tricritical point composition of a series of LaFeSi magnetocaloric alloys via universal scaling, J. Phys. D: Appl. Phys. 50 (2017) 414004.

[89] V. Franco, R. Caballero-Flores, A. Conde, Q. Dong, H. Zhang, The influence of a minority magnetic phase on the field dependence of the magnetocaloric effect, J. Magn. Magn. Mater. 321 (2009) 1115–1120.

[90] Y. Liu, C. Petrovic, Anomalous Hall effect in the trigonal Cr_5Te_8 single crystal, Phys. Rev. B 98 (2018) 195122.

[91] K. Ueda, T. Moriya, Contribution of spin fluctuations to the electrical and thermal resistivities of weakly and nearly ferromagnetic metals, J. Phys. Soc. Jpn. 39 (1975) 605–615.

[92] N. Nagaosa, J. Sinova, S. Onoda, A. H. MacDonald, N. P. Ong, Anomalous Hall effect, Rev. Mod. Phys. 82 (2010) 1539–1592.

[93] N. Kanazawa, Y. Onose, T. Arima, D. Okuyama, K. Ohoyama, S. Wakimoto, K. Kakurai, S. Ishiwata, Y. Tokura, Large Topological Hall Effect in a Short-Period Helimagnet MnGe, Phys. Rev. Lett. 106 (2011) 156603.

[94] C. Zeng, Y. Yao, Q. Niu, H. H. Weitering, Linear magnetization dependence of the intrinsic anomalous Hall effect, Phys. Rev. Lett. 96 (2006) 037204.

[95] Smit, Jan, The spontaneous Hall effect in ferromagnetics II, Physica 24 (1958) 39–51.

[96] L. Berger, Side-Jump Mechanism for the Hall Effect of Ferromagnets, Phys. Rev. B 2 (1970) 4559–4566.

[97] Z. Z. Jiang, X. Luo, J. Yan, J. J. Gao, W. Wang, G. C. Zhao, Y. Sun, J. G. Si, W. J. Lu, P. Tong, X. B. Zhu, W. H. Song, Y. P. Sun, Magnetic anisotropy and anomalous Hall effect in monoclinic single crystal Cr_5Te_8, Phys. Rev. B 102 (2020) 144433.

[98] S. D. Yi, S. Onoda, N. Nagaosa, J. H. Han, Skyrmions and anomalous Hall effect in a Dzyaloshinskii-Moriya spiral magnet, Phys. Rev. B 80 (2009) 054416.

[99] Y. Li, N. Kanazawa, X. Z. Yu, A. Tsukazaki, M. Kawasaki, M. Ichikawa, X. F. Jin, F. Kagawa, Y. Tokura, Robust Formation of Skyrmions and Topological Hall Effect Anomaly in Epitaxial Thin Films of MnSi, Phys. Rev. Lett. 110 (2013) 117202.

[100] H. Wang, Y. Dai, G.-M. Chow, J. Chen, Topological hall transport: Materials, mechanisms and potential applications, Prog. Mater Sci. 130 (2022) 100971.

[101] Q. Shao, Y. Liu, G. Yu, S. K. Kim, X. Che, C. Tang, Q. L. He, Y. Tserkovnyak, J. Shi, K. L. Wang, Topological Hall effect at above room temperature in heterostructures composed of a magnetic insulator and a heavy metal, Nature Electronics 2 (2019) 182–186.

[102] Y. Machida, S. Nakatsuji, Y. Maeno, T. Tayama, T. Sakakibara, S. Onoda, Unconventional Anomalous Hall Effect Enhanced by a Noncoplanar Spin Texture in the Frustrated Kondo Lattice $Pr_2Ir_2O_7$, Phys. Rev. Lett. 98 (2007) 057203.

[103] X. Zhang, B. Wang, Y. Guo, Y. Zhang, Y. Chen, J. Wang, High Curie temperature and intrinsic ferromagnetic half-metallicity in two-dimensional Cr_3X_4 (X= S, Se, Te) nanosheets, Nanoscale Horiz. 4 (2019) 859–866.

[104] W. Wang, M. W. Daniels, Z. Liao, Y. Zhao, J. Wang, G. Koster, G. Rijnders, C.-Z. Chang, D. Xiao, W. Wu, Spin chirality fluctuation in two-dimensional ferromagnets with perpendicular magnetic anisotropy, Nat. Mater. 18 (2019) 1054–1059.

Chapter 7

$\mathbf{Sn_{0.06}Cr_3Te_4}$: A Skyrmion Superconductor

7.1 Introduction

Superconductivity observed with a topological quantum phase is a much-anticipated phenomenon as it opens a new window of potential technological applications in superconducting electronics, such as topological quantum computations [1]. Thus, designing new materials and their experimental realization is an essential scientific sequence for garnering futuristic quantum technological applications. Several proposals exist for achieving topological superconductivity, such as the hereto-structure of a superconductor and a topological insulator or a doped topological insulator. In topological superconductors, the Cooper pairs are trapped at the vertices of the interface in the form of Majorana fermions due to the proximity effect [2–5] or at the junction of a superconductor and a magnet deposited on the surface of a topological insulator [6]. Nevertheless, several experimental studies were carried out to realize the superconductivity in the presence of quantum topology [7–9].

In addition, superconductivity has been found in many van der Waals (vdW) materials such as $NaSn_2As_2$ (T_c = 1.3 K) [10], $Na_{1-x}Sn_2P_2$ (T_c = 2 K) [11], $NbSe_2$ (T_c = 6 K) [12], and $Re_6Se_8Cl_2$ (T_c = 8 K) [13]. Further, there exists another class of vdW materials in which the superconductivity is induced by the metal-ion intercalation, such as $A_xBi_2Se_3$ (A = Sr, Cu) [14, 15], $Sn_{0.5}TaSe_2$ [16], Sn_xNbSe_2 [17], and Cu_xTiSe_2 [18]. In these systems, the intercalated metal ions act as charge carrier donors, increasing the carrier density near the Fermi level and, thus, the superconductivity. Most importantly, all these intercalated vdW superconductors are nonmagnetic and do not have chiral spin structure in their pristine phase.

On the other hand, the layered Cr_xTe_y based systems are potential candidates to have chiral spin structures originating the topological skyrmion lattice [19–25]. Notably,

---

This chapter is based on the publication: **Shubham Purwar et al., Applied Materials Today, 39, 102328 (2024)** these systems are formed by the alternative stacking of Cr-full ($CrTe_2$-layer) and Cr-vacant (intercalated Cr-layer) layers along the crystal growth axis [26]. Therefore, the intercalated Cr concentration is critical in forming the magnetic and topological properties. As the van der Waals gap separates $CrTe_2$ layers, introducing the alien atoms within the vdW gap is quite feasible. We chose to intercalate Sn within the vdW gap of $CrTe_2$-layers to induce the superconductivity in a topological ferromagnet, Cr_3Te_4 [22]. This way, the intriguing exotic quantum phases, ferromagnetism, and superconductivity can be achieved in a topological skyrmion lattice. It is worth mentioning here that no study is available to date demonstrating the superconducting phase within a skyrmion lattice. Further, such an experimental observation is quite challenging as the ground state properties like ferromagnetism and superconductivity are found to be competing, if not coexisting, unless the ferromagnetism is weak [27–29].

In this study, we successfully intercalated Sn within the van der Waals gap of topological Cr_3Te_4 to induce superconductivity. We could simultaneously identify all three quantum phases, superconductivity, magnetism, and the topological Hall effect in $Sn_{0.06}Cr_3Te_4$. The pristine Cr_3Te_4 shows a topological Hall resistivity (ρ^T_{xy}) of 240 $n\Omega - cm$, but the Sn intercalation significantly reduces it to 16 $n\Omega - cm$. In addition, despite the magnetism and Meissner effects being anisotropic, the superconductivity observed from the in-plane electrical resistivity (ρ_{bc}) is nearly isotropic between $H \parallel bc$ and $H \parallel a$, suggesting separate channels of conduction electrons responsible for the superconductivity and magnetism of this system, which is supported by our spin-resolved DFT calculations. We identify two orders of higher carrier density in superconducting $Sn_{0.06}Cr_3Te_4$ than the parent Cr_3Te_4. A jump in the specific heat is noticed around the T_c with a volume fraction of 33%, confirming the bulk superconductivity in $Sn_{0.06}Cr_3Te_4$. Importantly, for the first time, this study demonstrates superconductivity in a skyrmion lattice, offering a new class of topological quantum materials.

7.2 Methodology

7.2.1 Experimental Details

Single crystals of Sn intercalated Cr_3Te_4 were grown by the Sn-flux method by mixing high purity elements of Cr (5N, Alfa Aesar) and Te (5N, Alfa Aesar) powders as per the stoichiometric ratio in an alumina crucible, added with Sn (99.998%, Alfa Aesar) shots, and sealed the crucible inside a quartz ampoule under argon atmosphere. A schematic diagram of the single crystal growth heat treatment is shown in Fig. 7.4(b). Plate-like single crystals with a typical size of 3×2 mm^2 with a thickness of 0.15 mm were collected after the reaction. Single crystals of Cr_3Te_4 were grown by the chemical vapor transport (CVT) technique with iodine as a transport agent as per the procedure described earlier [30]. Structural and elemental characterizations were performed using an X-ray diffractometer (Rigaku-9kW, Cu K_α of 1.54059 Å wavelength at Room temperature) and energy dispersive spectroscopy (EDS) techniques, respectively. Temperature-dependent electrical transport, Hall effect, and magnetization measurements were performed using the 9 Tesla physical property measurement system (PPMS, Quantum Design, DynaCool). Electrical resistivity and Hall effect measurements were performed in the standard four-probe method. Temperature-dependent heat capacity measurements were taken using the relaxation method using the Quantum Design-PPMS system. The high-resolution transmission electron microscopy (HRTEM) was done in an FEI, TECNAI TF 20, S-TWIN microscope operated at 200 KV. The samples were prepared by drop-casting onto a carbon-coated copper grid of a 3 mm diameter. Raman spectra were captured by using a micro-Raman spectrometer (LabRam HR Evolution HORIBA France SAS) equipped with a 532 nm laser.

7.2.2 DFT Calculations

Spin-polarized DFT calculations have been carried out on Cr_3Te_4 and $Sn_{0.06}Cr_3Te_4$ (one unit cell consists of 1 Sn, 6 Cr, and 8 Te atoms) based on the projector augmented wave (PAW) method [31] as implemented in the Quantum Espresso package [32, 33]. For the exchange-correlation interaction, we considered the Perdew-Burke-Ernzerhof [34] form of the generalized gradient approximation (GGA). To consider the van der Waals forces, semi-empirical Grimme's DFT-D2 correction [35] was considered. To optimize the atomic positions, a cutoff value of 10^{-3} Ry/Bohr was chosen for the Hellmann-Feynmann forces. A plane wave cutoff of 50 Ry was employed. $4 \times 16 \times 8$ and $8 \times 32 \times 16$ k-mesh with Γ-centered were used for the self-consistency and DOS calculations, respectively.

7.3 Results and Discussion

7.3.1 Structural Properties

The exact chemical composition of the Sn intercalated and the parent single crystals was found to be $Sn_{0.06}Cr_{2.74}Te_4$ and $Cr_{2.76}Te_4$, respectively, using the EDS measurements. For convenience, we use the nominal composition formula of Cr_3Te_4. Fig. 7.1(a) shows the XRD pattern of the crushed Cr_3Te_4 single crystals measured at room temperature. All peaks in the XRD pattern can be attributed to the monoclinic crystal structure of the $C2/m$ space group (No.12). This is consistent with the crystal structure of Cr_3Te_4 [36–38]. Rietveld refinement further confirms the monoclinic structure with lattice parameters, a=13.9655(2) Å, b=3.9354(4) Å, c=6.8651(7) Å, $\alpha=\beta=90°$, and $\gamma = 118.326(7)°$ with χ^2=2.95. Similarly, Fig. 7.1(b) shows the XRD pattern of the crushed $Sn_{0.06}Cr_3Te_4$

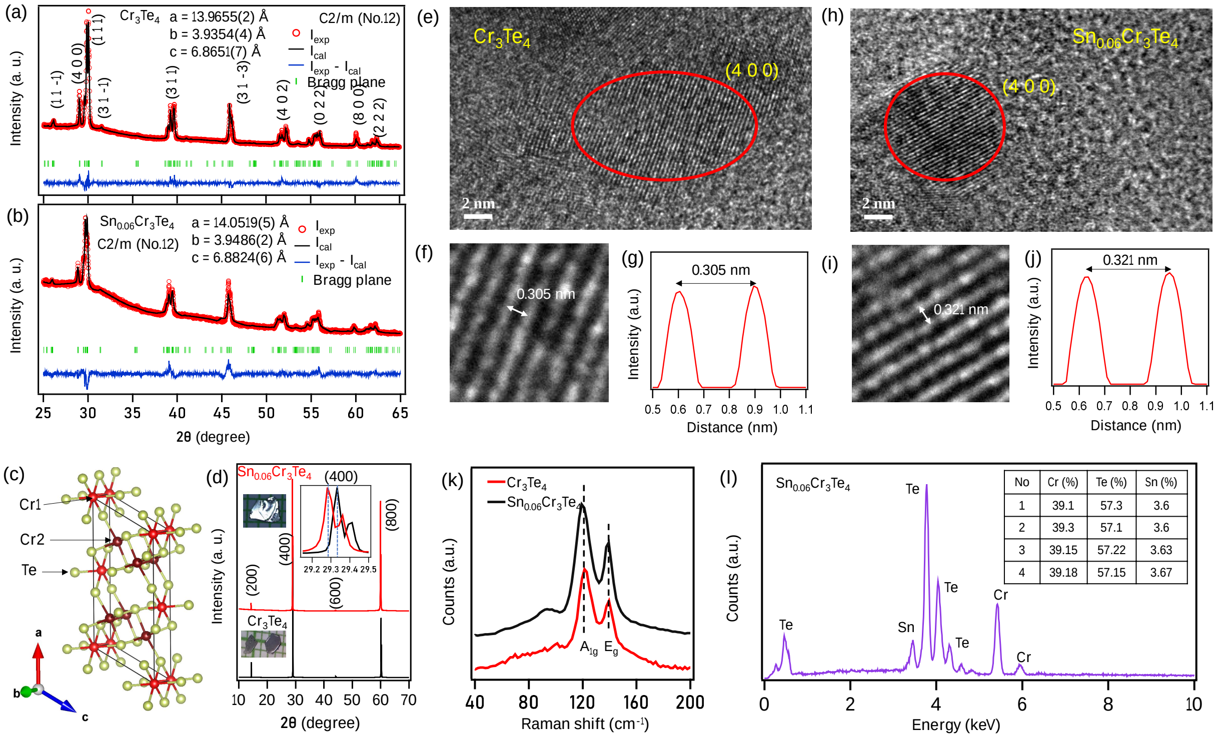

No	Cr (%)	Te (%)	Sn (%)
1	39.1	57.3	3.6
2	39.3	57.1	3.6
3	39.15	57.22	3.63
4	39.18	57.15	3.67

Figure 7.1: (a) and (b) XRD patterns of the crushed single crystals of Cr_3Te_4 and $Sn_{0.06}Cr_3Te_4$, respectively, overlapped with Rietveld refinement. (c) Schematic image of the monoclinic crystal structure of Cr_3Te_4. (d) XRD patterns of Cr_3Te_4 (bottom panel) and $Sn_{0.06}Cr_3Te_4$ (top panel) single crystals. Top-middle inset in (c) shows zoomed-in (4 0 0) Bragg's peak demonstrating the lattice shift between the parent and the Sn intercalated samples. Optical images of typical single crystals are shown in the left-side insets of (d). (e) HRTEM image taken on Cr_3Te_4 crystallite, demonstrating the lattice planes corresponding to the (4 0 0) plane. (f) Zoomed-in HRTEM image from (e), displaying the interplanar distance of 0.305 nm. (g) (4 0 0) lattice plane intensity plot confirming the interplanar distance. (h)-(j) Same as (e)-(g) but from $Sn_{0.06}Cr_3Te_4$ crystallite. (k) Raman spectra measured on Cr_3Te_4 and $Sn_{0.06}Cr_3Te_4$ single crystals. (l) EDS spectra measured on four different $Sn_{0.06}Cr_3Te_4$ crystallites, confirming the uniform chemical composition. Atomic weight percentages of respective elements are tabulated in the inset of (l).

single crystals measured at room temperature. Again, all peaks in the XRD pattern can be attributed to the monoclinic crystal structure of the $C2/m$ space group without any Sn impurity phases. Rietveld refinement further confirms the monoclinic structure with lattice parameters, a=14.0551(4) Å, b=3.9494(3) Å, c=6.8839(5) Å, α=β=90°, and γ = 118.376(7)° with χ^2=3.35. We can see that the Sn intercalation slightly increases the a-axis lattice parameter, while the change in lattice parameters of b and c is negligible. Fig. 7.1(c) depicts the schematic crystal structure of Cr_3Te_4 in which the alternative staking of Cr(1) and Cr(2) layers is demonstrated along the a-axis.

The XRD patterns taken on the single crystal of Cr_3Te_4 and $Sn_{0.06}Cr_3Te_4$ are shown in the bottom and top panels of Fig. 7.1(d), respectively, which are consistent with the monoclinic space group of $C2/m$, suggesting that the crystal growth axis is parallel to the a-axis [37, 38, 22]. Inset in Fig 7.1(d) shows the overlapped (4 0 0) reflections from Cr_3Te_4 and $Sn_{0.06}Cr_3Te_4$ in which the peak position is shifted towards the lower 2θ for $Sn_{0.06}Cr_3Te_4$ compared to Cr_3Te_4. The XRD peak shifting to a lower 2θ value indicates an expansion of the interplanar spacing along the a-axis due to Sn intercalation [16, 17]. Fig. 7.1(e) shows the HRTEM image taken on Cr_3Te_4 crystallite, demonstrating the lattice planes corresponding to the (4 0 0) plane. Fig. 7.1(f) depicts the zoomed-in HRTEM image of Fig. 7.1(e), displaying the interplanar distance of 0.305 nm which is in agreement with the interplanar spacing of 0.307 nm [(4 0 0)] derived from the Rietveld refinement. This is further confirmed from the lattice plane intensity plot as shown in Fig. 7.1(g). Figs. 7.1(h)-(j) depicts information of (4 0 0) plane as similar as shown in Figs. 7.1(e)-(g) but from a $Sn_{0.06}Cr_3Te_4$ crystallite. From Figs. 7.1(i) and 7.1(j), we can clearly notice that Sn intercalation increases the (4 0 0) interplanar spacing of about 0.016 nm compared to the parent system. This is in good agrement with the XRD peak shifting to lower 2θ angle with Sn intercalation [see inset in Fig. 7.1(d)].

Next, from the Raman spectra as shown in Fig. 7.1(k), we mainly observe two prominent phonon peaks, positioned at approximately 123.5 cm^{-1} and 139.79 cm^{-1}. These peaks correspond to the distinct vibrational modes such as the out-of-plane A_{1g} and the in-plane E_g, of a typical Cr_xTe_y system [39, 40]. This observation confirms that the intercalated Sn atoms take the positions in the Cr(2)-intercalated layer [see Fig. 7.1(c)]. Importantly, we do not observe any additional Raman modes corresponding to the Sn impurity which shall be at around 202.5 cm^{-1} [41]. Further, to be more accurate on the chemical composition, particularly, of the Sn intercalated system, we performed EDS measurements on several crystallites of $Sn_{0.06}Cr_3Te_4$ as shown Fig. 7.1(l). From Fig. 7.1(l), it is evident that the chemical composition is uniform across all the measured crystallites within the error-bars ($Sn_{0.063(2)}Cr_{2.74(1)}Te_4$).

7.3.2 Magnetic Properties

Magnetization [$M(T)$], plotted as a function of temperature for $Sn_{0.06}Cr_3Te_4$ both field-cooled (FC) and zero-field-cooled (ZFC) modes, measured with a magnetic field of 50 Oe applied parallel to a-axis ($H \parallel a$) is shown in Fig. 7.2(a) and the field applied parallel to bc-plane ($H \parallel bc$) is shown in Fig. 7.2(b). The Meissner effect is clearly visible from the ZFC data of $H \parallel a$, as shown in the inset of Fig. 7.2(a), at an onset transition temperature of 3.5 K, below which the magnetization becomes negative due to diamagnetism in the superconducting phase. In addition to the Meissner effect at 3.5 K, we also identify a sharp decrease in magnetization from FC and ZFC modes at around 100 K, possibly due to a canted antiferromagnetic (AFM) transition [42]. In contrast to $H \parallel a$, the magnetization measured for $H \parallel bc$ shows a different character as demonstrated in Fig. 7.2(b). Firstly, we do not observe the Meissner effect below 3.5 K from the ZFC data, and secondly, only

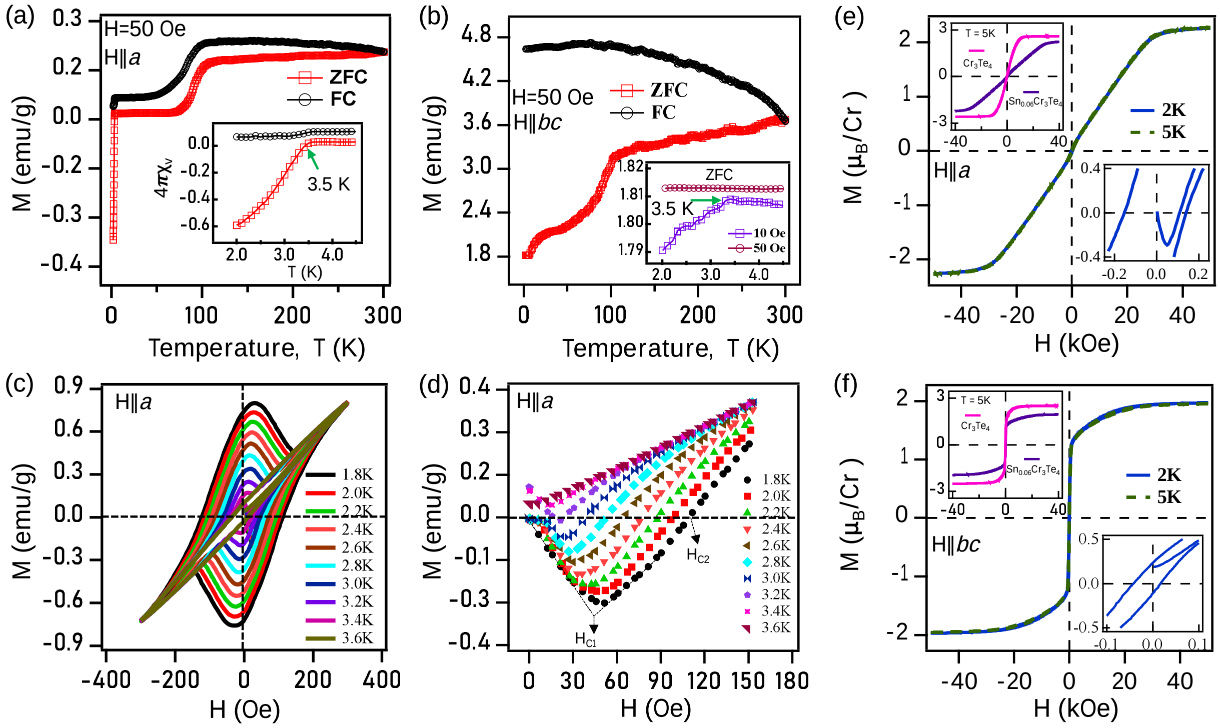

Figure 7.2: Magnetic properties of $Sn_{0.06}Cr_3Te_4$ single crystal. (a) Temperature dependent magnetization $[M(T)]$ measured with H = 50 Oe for $H \parallel a$. Inset of (a) shows the susceptibility near the superconducting region. (b) Same as (a) but measured for H$\parallel$ bc. Inset of (b) shows overlapped $M(T)$ measured with 10 and 50 Oe. (c) and (d) Show low field Isothermal magnetization $[M(H)]$ curves, demonstrating the Meissner effect within the temperature range of 1.8-3.6 K. H_{c1} and H_{c2} in (d) represent lower and upper critical fields, respectively. (e) $M(H)$ curve measured at 2 and 5 K for $H \parallel a$. Top-left inset in (e) shows $M(H)$ curves measured at 5 K from Cr_3Te_4 and $Sn_{0.06}Cr_3Te_4$ single crystals for $H \parallel a$. Bottom-right inset of (e) shows zoomed-in $M(H)$, demonstrating the Meissner effect in presence of significant coercive field. (f) $M(H)$ curve measured at 2 and 5 K for $H \parallel bc$. Top-left inset in (f) shows $M(H)$ curves measured at 5 K from Cr_3Te_4 and $Sn_{0.06}Cr_3Te_4$ single crystals for $H \parallel bc$. Bottom-right inset of (f) shows zoomed-in $M(H)$, demonstrating the absence of Meissner effect for $H \parallel bc$.

the ZFC data shows a AFM transition at around 100 K, but not the FC data. In fact, the saturated magnetization derived from the FC data ($M_S \approx$4.65 emu/g) at 2 K for $H \parallel bc$ is almost 20 times higher than the saturation magnetization ($M_S \approx$0.23 emu/g) of $H \parallel a$, indicating a large magnetic anisotropy present in the system [43]. This, further implies that the bc-plane is the easy magnetization plane with stronger magnetic exchange interactions, suppressing the superconducting state in the bc plane. In support of this, the $M(T)$ data measured with an applied field of 10 Oe for $H \parallel bc$ [see the inset of Fig. 7.2(b)] shows a slight decrease in magnetization precisely at the onset temperature of 3.5 K, suggesting the coexistence of both magnetism and superconductivity in the bc-plane though the stronger ferromagnetic exchange interactions dominate the Meissner effect.

Isothermal magnetization curves $[M(H)]$ across the superconducting transition temperature for $H \parallel a$ are shown in Fig. 7.2(c). Fig. 7.2(d) shows the zoomed-in data of

Fig. 7.2(c) taken for positive applied fields. From Fig. 7.2(d), we notice that at lower fields, the negative magnetization increases linearly with the field up to a lower critical field of H_{c1}. However, beyond a certain field, the negative magnetization starts decreasing with increasing field and approaches zero magnetization at an upper critical field of H_{c2}. This observation is consistent at all measured temperatures up to 3.4 K, indicating $Sn_{0.06}Cr_3Te_4$ to a type-II superconductor [44]. Interestingly, at 3.4 K, despite the magnetization initially decreasing with increasing field like in a typical superconductor, unusually, it is always positive. This could be due to the coexistence of magnetism and superconductivity [45]. Figs. 7.2(e) and 7.2(f) show the magnetization isotherms measured at 2 and 5 K for both $H \parallel a$ and $H \parallel bc$, respectively. These data show that the out-of-plane magnetization (a-axis) linearly increases with the field up to 3 T and then saturates to 2.2 μ_B/Cr. The bottom-right inset of Fig. 7.2(e) measured at 2 K again demonstrates the superconducting state at lower fields together with a significant coercivity of 150 Oe.

The top-left inset of Fig. 7.2(e) shows the magnetization isotherms $[M(H)]$ measured at 5 K from both parent and the superconducting $Sn_{0.06}Cr_3Te_4$ for $H \parallel a$. From this data, we can see that the magnetization of Cr_3Te_4 saturates faster than that of $Sn_{0.06}Cr_3Te_4$. On the other, the in-plane magnetization (bc-plane) of $Sn_{0.06}Cr_3Te_4$ spontaneously saturates to 2 μ_B/Cr under the applied magnetic field as shown in Fig. 7.2(f), indicating that the bc-plane is the easy-plane of magnetization similar to the parent system [46, 47]. The bottom-right inset of Fig. 7.2(f) shows the $M(H)$ data measured at 2 K, demonstrating an absence of a superconducting state in the bc-plane even at very low applied fields. The top-left inset of Fig. 7.2(f) shows magnetization isotherms $[M(H)]$ measured at 5 K from both Cr_3Te_4 and the superconducting $Sn_{0.06}Cr_3Te_4$ for $H \parallel bc$. This data shows that the Sn intercalation has no effect on the in-plane magnetization of Cr_3Te_4 except for a slight reduction in the saturated magnetic moment.

7.3.3 Electrical Properties

In-plane (ρ_{bc}) electrical resistivity of $Sn_{0.06}Cr_3Te_4$ plotted as a function of temperature is shown in Fig. 7.3(a). At around 100 K, we identify a hump in the resistivity curve due to the AFM transition. The high-temperature resistivity between 100 and 300 K is linearly dependent on the temperature, as the black-dashed-line fitting demonstrates. The top-left inset of Fig. 7.3(a) demonstrates a drop in resistivity to zero at an onset superconducting transition temperature of $T_c \approx 3.5$ K. The bottom-right inset of Fig. 7.3(a) suggests Fermi-liquid type electrical resistivity at very low temperatures (< 40 K), as the resistivity quadratically depends on the temperature. In addition, the large residual resistivity ratio (RRR) of $\frac{\rho_{300K}}{\rho_{4K}} \approx 164$ confirms the high quality of the studied samples. Fig. 7.3(b) shows the electrical resistivity measured by varying the field strength. In Fig. 7.3(b), a gradual decrease in the onset T_c is noticed with increasing the field. Interestingly, despite

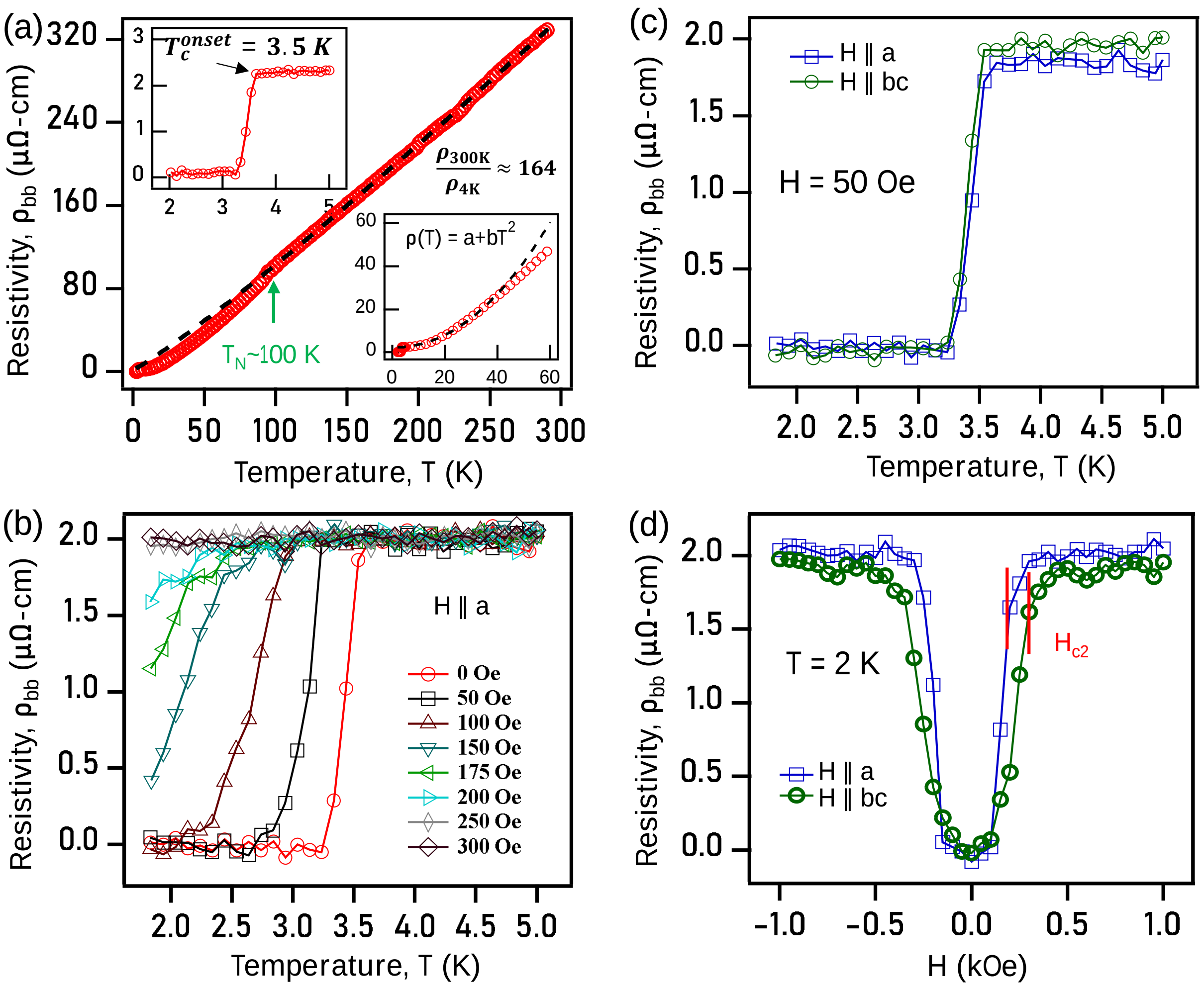

Figure 7.3: Electrical transport properties of $Sn_{0.06}Cr_3Te_4$ single crystal. (a) Temperature dependent in-plane electrical resistivity ($\rho_{bc}(T)$). Top inset of (a) shows onset superconducting transition of $T_c \approx 3.5$ K. Bottom inset of (a) represents Fermi-liquid fitting at low temperature region. (b) $\rho_{bc}(T)$ measured under various magnetic field within temperature range of 1.8-5 K for $H \parallel a$. (c) $\rho_{bc}(T)$ measured within temperature range of 1.8-5 K for $H \parallel a$ and $H \parallel bc$ at an applied field of 50 Oe. (d) $\rho_{bc}(H)$ measured as a function of field for $H \parallel a$ and $H \parallel bc$ at 2 K.

the anisotropic magnetization, the superconducting transition temperature is found to be unchanged between $H \parallel a$ and $H \parallel bc$ as $\rho_{bc}(T)$ shows equal onset T_c of 3.5 K when measured with 50 Oe [see Fig. 7.3(c)]. Fig. 7.3(d) depicts ρ_{bc} plotted as a function magnetic field for $H \parallel a$ and $H \parallel bc$ at 2 K. We observe that the upper critical field of H_{c2}≈300 Oe is higher for $H \parallel bc$ compared to H_{c2}≈200 Oe for $H \parallel a$.

Critical fields (H_{c1} and H_{c2}) and critical temperatures (T_c) estimated from Fig. 7.2(d) are plotted in Fig. 7.4(a). The data of $H_{c1}(T)$ is reasonably fitted using the Ginzburg-Landau equation of quadratic field dependence on the temperature [48], $H_{c1}(T) = H_{c1}(0)[1-(T/T_c)^2]$. From the fitting, we obtained a lower critical field of $H_{c1}(0) = 58 \pm 4$ Oe at zero temperature. On the other hand, the upper critical field of $H_{c2}(T)$ is reasonably fitted using the modified Ginzburg-Landau model which takes the form $H_{c2}(T) =$

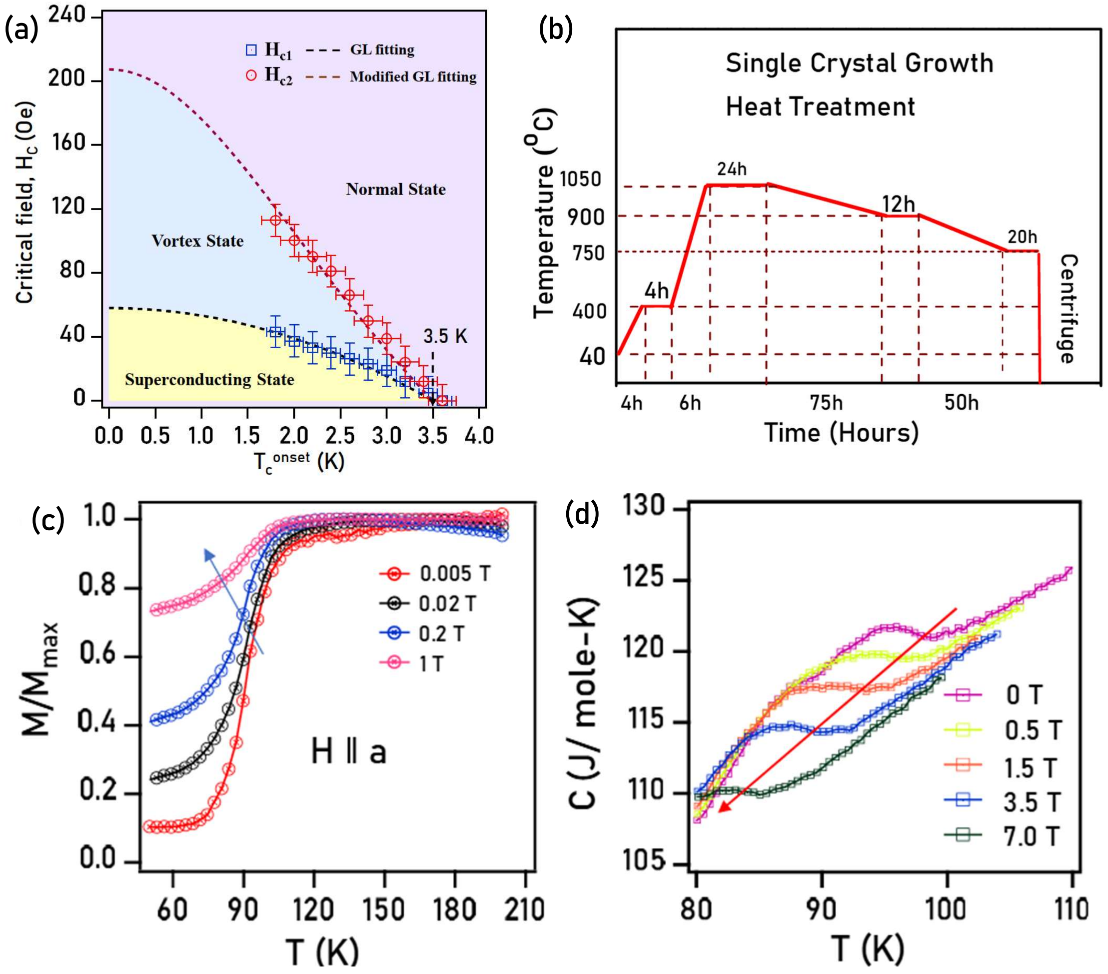

Figure 7.4: (a) Temperature dependence of lower critical field H_{c1} and upper critical field H_{c2} along with schematic diagram of shaded superconducting, vortex, and normal state regions, (b) Heat treatment diagram for the growth of $\mathrm{Sn_{0.06}Cr_3Te_4}$ single crystals, (c) Magnetization and (d) Specific heat as a function of temperature, measured under various magnetic fields with $H \parallel a$ for $\mathrm{Sn_{0.06}Cr_3Te_4}$. Both magnetization and specific heat data indicate that the magnetic transition at 98 K is of the canted antiferromagnetic (AFM) type, as the magnetic transition temperature decreases with increasing field.

$H_{\mathrm{c2}}(0)[(1-t^2)/(1+t^2)]$, where $t = T/T_{\mathrm{c}}$. From this fitting, we obtained an upper critical field of $H_{\mathrm{c2}}(0) = 205 \pm 10$ Oe at zero temperature. The Ginzburg-Landau coherence length, $\xi(0) = 1264.8 \pm 90$ Å, is estimated using the relation $H_{\mathrm{c2}}(0) = \phi_0/2\pi\xi(0)^2$, where ϕ_0 is the flux quanta. The mean critical field H_c is quantified to 109 ± 9 Oe using the relation, $\mathrm{H_c} = \sqrt{\mathrm{H_{c1}H_{c2}}}$. Now, by knowing the upper critical field $H_{\mathrm{c2}}(0)$ and mean critical field $\mathrm{H_c}$ one can estimate the GL parameter (κ) using the relation, $\mathrm{H_{c2}}(0) = \sqrt{2}\kappa\mathrm{H_c}$. Thus, the obtained $\kappa = 1.33$ in this study is well above the threshold value of $\frac{1}{\sqrt{2}}$, again confirming the type-II superconductivity of this system. With the help of GL coherence length ($\xi(0)$) and GL parameter (κ), we further estimated the London penetration depth (λ_L) equal to 1682.1 ± 120 Å at zero temperature, using the relation $\lambda_L(0) = \kappa\xi(0)$. This value is much larger than any other ferromagnetic superconductor. The mean-free path (l) of the charge

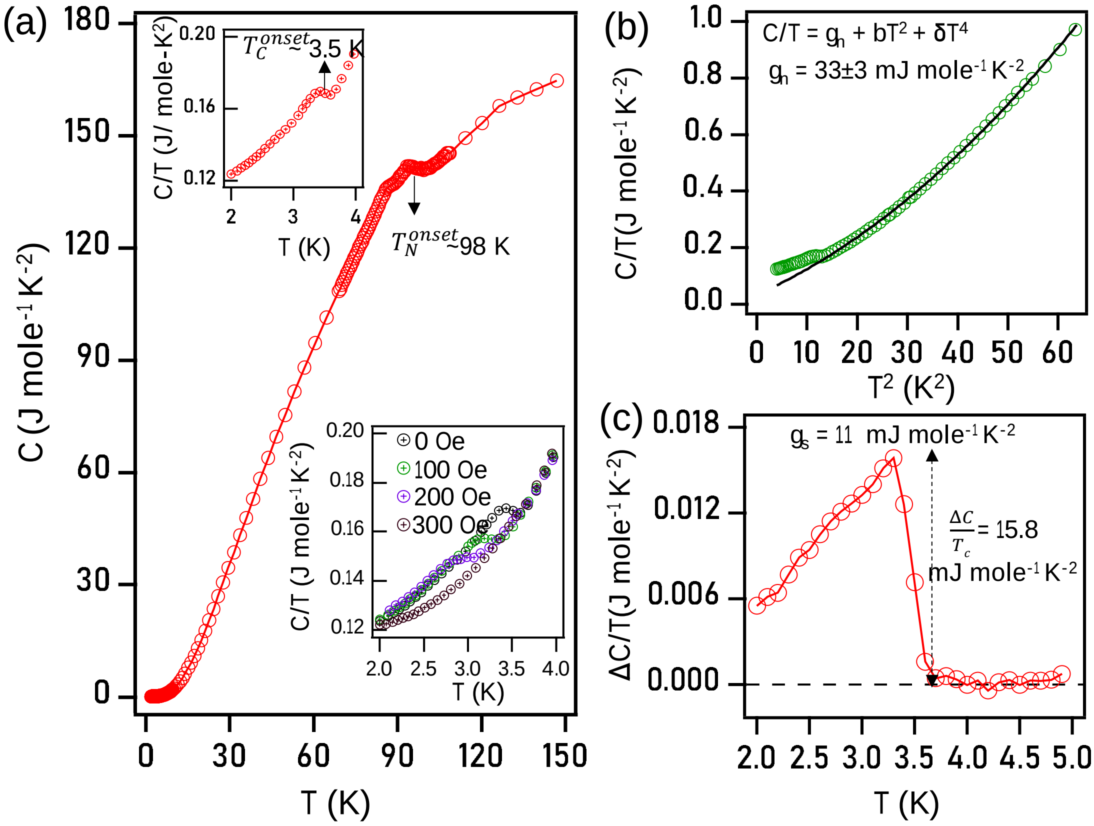

Figure 7.5: Specific heat $C(T)$ measurements on $\mathrm{Sn_{0.06}Cr_3Te_4}$ single crystal. (a) Temperature dependent $C(T)$. Top-right inset of (a) shows zoomed-in $C(T)$ taken around the T_c. Bottom-left inset of (a) shows $C(T)$ measured under magnetic applied fields. (b) $C(T)$ data fitting using the relation $C(T)/T = \gamma_n + \beta T^2 + \delta T^4$ to extract the Sommerfeld coefficient in the normal state. (c) Depicts $\Delta C/T$ plotted as a function of temperature.

carriers is estimated using the relation $l = hk_F/2\pi\rho_0 ne^2$, where k_F is approximated to $(3\pi^2 n)^{1/3}$ by considering a spherical Fermi surface. Inserting the values, $\rho_0 = 1.78\times10^{-8}\,\Omega$-m and $n = 1.09 \times 10^{29}\ m^{-3}$, we obtained $l = 313.4$ Å. Thus, as $l << \xi(0)$, $\mathrm{Sn_{0.06}Cr_3Te_4}$ falls in to the dirty-limit of superconductivity [49].

7.3.4 Specific Heat Capacity

To confirm the bulk superconductivity of $\mathrm{Sn_{0.06}Cr_3Te_4}$, we performed specific heat $[C(T)]$ measurements within the temperature range of 2-150 K as shown in Fig. 7.5(a). A specific heat jump at an onset transition temperature $T_c \approx 3.5$ K is noticed from the top-left inset of Fig. 7.5(a), which is in agreement with the magnetic and transport data shown in Fig. 7.2(a) and Fig. 7.3, respectively. The bottom-right inset of Fig. 7.5(a) depicts the specific heat data measured under various magnetic fields for $H \parallel a$. The T_c and the height of the specific heat jump decrease with increasing the field, and the superconductivity is completely suppressed at an applied field of 300 Oe. In addition, we also observe a specific heat jump around the magnetic transition of 98 K. In Fig. 7.4(b), we provided field-dependent $C(T, H)$ data from which the magnetic transition at 98 K is concluded to be an AFM-type. From Fig. 7.5(a), we observe the Debye-type increase in heat capacity with temperature up to 150 K, and beyond 150 K it reaches the Dulong-Petit limit. In agreement to this observation, the calculated heat capacity $C = 176.1$ J mole^{-1} K^{-1}, following the Dulong-Petit law [$C = 3nR$], is close to the experimental heat capacity value at 150 K ($C = 165$ J mole^{-1} K^{-1}). Here $n = 7.06$ is the number of atoms per formula unit ($Sn_{0.06}Cr_3Te_4$) and $R = 8.3144598$ J mole^{-1} K^{-1} is the universal gas constant.

Further, we could reasonably fit the normal state heat capacity data, taken at zero fields, following the relation $C(T) = \gamma_n T + \beta T^3 + \delta T^5$ [see Fig. 7.5(b)]. Here, the first term ($\gamma_n T$) represents the electronic contribution, and the second and third terms ($\beta T^3 + \delta T^5$) represent the phonon contribution to the total heat capacity. From the fitting, we derived a Sommerfeld coefficient (γ_n) of the electronic specific heat in the normal state $\gamma_n = 33\pm3$ mJ mole^{-1} K^{-2} and the coefficients related to the phonon contribution (Debye constants) $\beta = 8\pm0.2$ mJ mole^{-1} K^{-4} and $\delta = 0.1\pm0.04$ mJ mole^{-1} K^{-6}. We also estimated the Sommerfeld coefficient in the superconducting state $\gamma_s = 11$ mJ mole^{-1} K^{-2} [see Fig. 7.5(c)] using the BCS equation of the weak-coupling limit, $\Delta C/T_c = [C(H = 0\ Oe) - C(H = 300\ Oe)]/T_c = 1.43 * \gamma_s$. Finally, the superconducting volume fraction is estimated using the relation $\frac{\gamma_s}{\gamma_n} \times 100 \approx 33 \pm 4\%$ [50], which is much larger than the Sn concentration (8%) present in $Sn_{0.06}Cr_3Te_4$. Thus, the large SC volume fraction rules out the Sn impurity phase superconductivity.

7.3.5 Topological Hall Effect

The parent Cr_3Te_4 is known to show significant topological Hall effect (THE) originated by the skyrmion lattice [51, 52, 22]. In order to uncover the presence of THE in the superconducting $Sn_{0.06}Cr_3Te_4$, we performed Hall measurements on both Cr_3Te_4 and $Sn_{0.06}Cr_3Te_4$ as shown in Fig. 7.6. Figs. 7.6(a) and 7.6(b) show the field dependent total Hall resistivity $\rho_{yz}(H)$ of Cr_3Te_4 measured at 1.8 K and 5 K, respectively. Similarly, Figs. 7.6(c) and 7.6(d) show $\rho_{yz}(H)$ of $Sn_{0.06}Cr_3Te_4$ measured at 1.8 K and 5 K, respectively. ρ_{yz} is measured with current along the y-axis and magnetic field applied along the x-axis to get the Hall voltage along the z-axis. The total Hall resistivity (ρ_{yz}) may have contributions from the normal Hall effect (ρ^N) and the anomalous Hall effect (ρ^A). Thus, the total Hall resistivity can be expressed by the empirical formula, $\rho_{yz}(H) = \rho^N(H) + \rho^A(H) = \mu_0 R_0 H + \mu_0 R_S M$, where R_0 and R_S are the normal and anomalous Hall coefficients, respectively. The fitting (black curves) should be nearly perfect if there is no topological Hall contribution. However, from Figs. 7.6 (a)-(d), we can notice that the fitting is not perfect. Therefore, the topological Hall resistivity also contributes to the total Hall resistivity, which is expressed by $\rho_{yz}(H) = \rho^N(H) + \rho^A(H) + \rho^T(H)$. Thus, the topological Hall contribution is extracted using the relation, $\rho^T(H) = \rho_{yz}(H) - [\rho^N(H) + \rho^A(H)]$ [53–55] which are shown in the

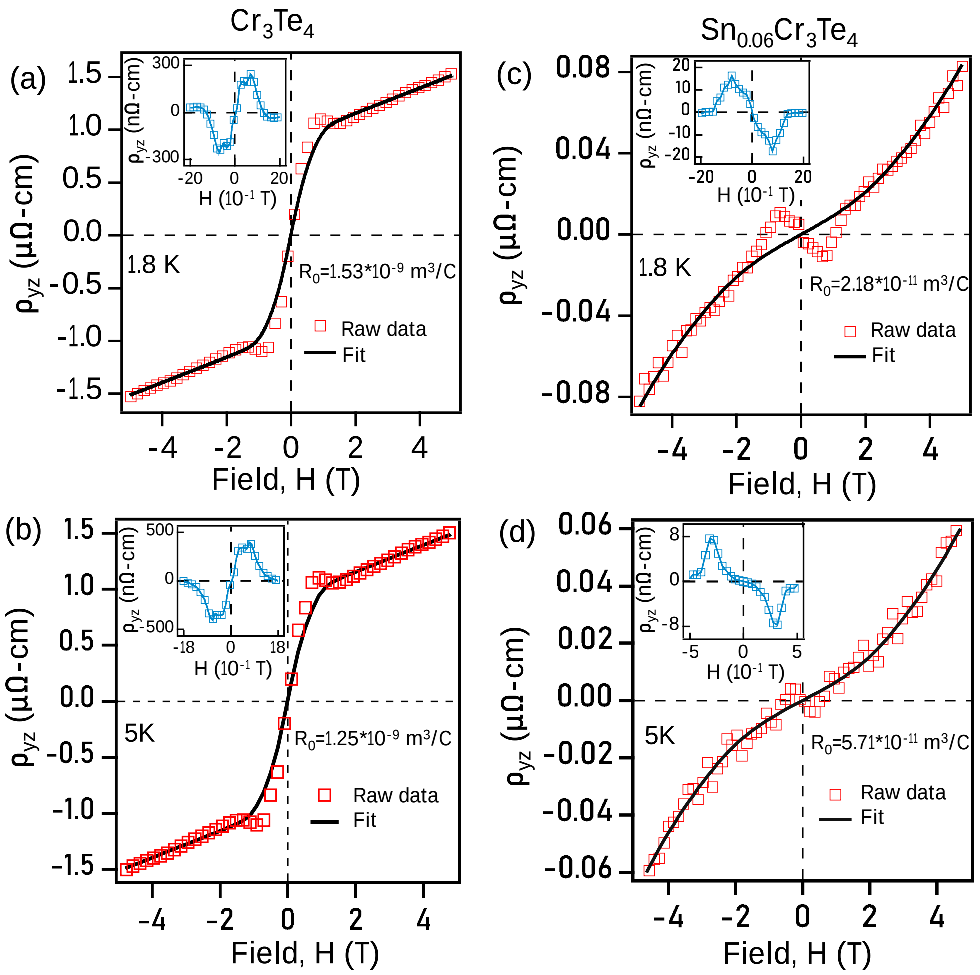

Figure 7.6: (a) and (b) Hall resistivity (ρ_{yz}) plotted as a function of field for Cr_3Te_4 measured at 1.8 and 5 K, respectively. (c) and (d) are same as (a) and (b) but measured on $Sn_{0.06}Cr_3Te_4$ (b). The black-curves are fits to the data. Insets in (a)-(d) show the topological Hall resistivity platted as a function of field (see the text for more details).

insets of Figs. 7.6 (a)-(d).

Further, as can be seen from the insets of Figs. 7.6 (a) and (b), at 2 K, a maximum topological Hall resistivity of $\rho^T_{yz} \approx 240\ n\Omega - cm$ is found in Cr_3Te_4 at a critical field of 0.7 T, while $\rho^T_{yz} \approx 16\ n\Omega - cm$ is observed from $Sn_{0.06}Cr_3Te_4$ around at the same critical field of 0.8 T. On the other hand, at 5 K, the maximum topological Hall resistivity of $8\ n\Omega - cm$ is observed in $Sn_{0.06}Cr_3Te_4$ at a critical field of 0.3 T whereas in Cr_3Te_4 we observe a slight increase in ρ^T_{yz} to $345\ n\Omega - cm$. An inverted topological Hall signal between Cr_3Te_4 and $Sn_{0.06}Cr_3Te_4$ [see the insets of Figs. 7.6(a) and 7.6(c)] hints at the helicity switching of the skyrmion lattice [56, 57]. These observations demonstrates a tuning of topological properties in Cr_3Te_4 by the Sn intercalation. Importantly, we successfully demonstrate the topological Hall effect in the presence of superconducting state, implying the coexistence of exotic quantum phases skyrmion lattice and superconductivity. Next, the carrier concentration (n) of Cr_3Te_4 and $Sn_{0.06}Cr_3Te_4$ is calculated by using the formula $n = 1/(R_0|q|)$, where q is the carrier charge. We obtained the carrier concentration (n) of

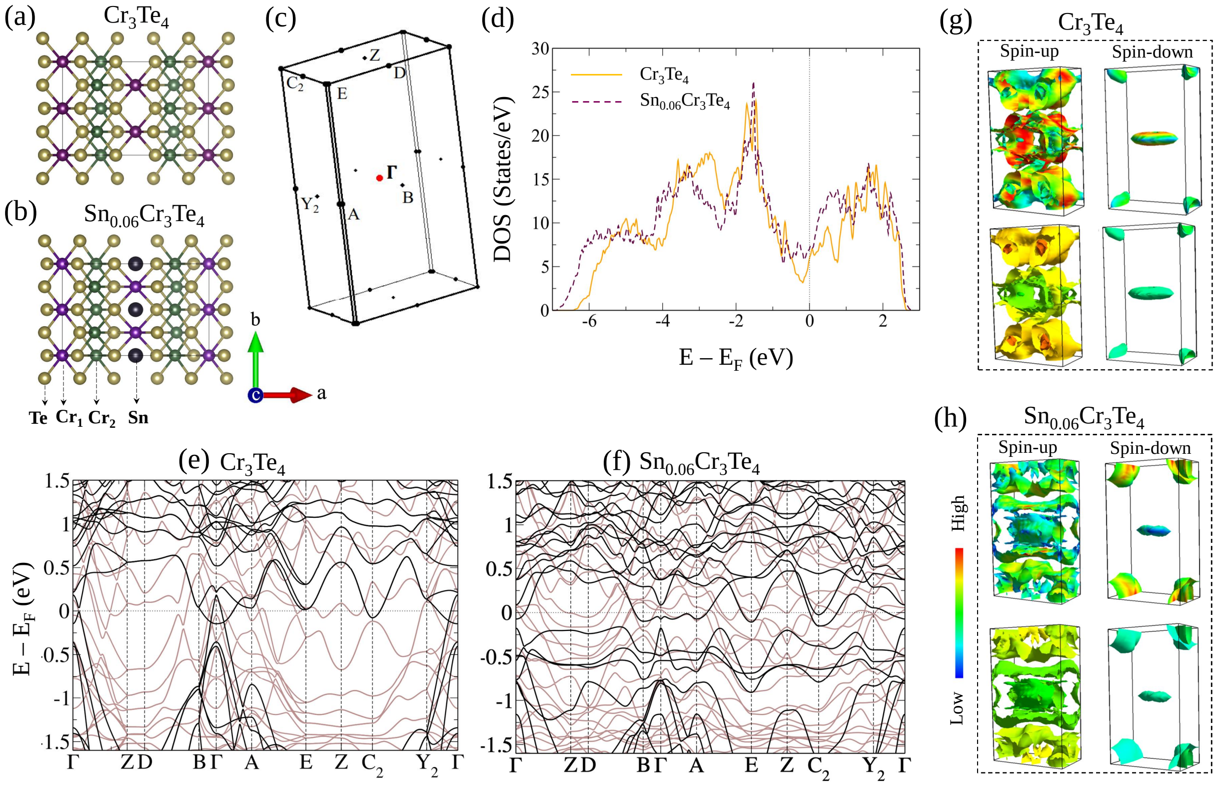

Figure 7.7: Crystal structure of parent Cr_3Te_4 (a) and $Sn_{0.06}Cr_3Te_4$ (b) projected onto the *ab*-plane. Magenta, green, yellow and black spheres represent Cr1, Cr2, Te, and Sn atoms, respectively. (c) High symmetry points defined on the monoclinic Brillouin zone. (d) Yellow solid and maroon dashed lines denote the density of states (DOS) for the parent Cr_3Te_4 and $Sn_{0.06}Cr_3Te_4$ systems, respectively. Spin polarised band structures for the parent Cr_3Te_4 (e) and Sn intercalated Cr_3Te_4 (f). Brown and black colours in (e) and (f) denote the bands for the up and down spins, respectively. (g) Fermi surfaces of Cr_3Te_4 plotted for the spin-up and spin-down channels. (h) Fermi surfaces of Sn intercalated Cr_3Te_4 plotted for the spin-up and spin-down channels. The color scale in (g) and (h) represent the Fermi velocity.

4.07×10^{21} cm^{-3} and 2.86×10^{23} cm^{-3} from Cr_3Te_4 and $Sn_{0.06}Cr_3Te_4$ at 2 K, respectively. On the other hand, at 5 K, these values are given by 5.01×10^{21} cm^{-3} and 1.10×10^{23} cm^{-3} from Cr_3Te_4 and $Sn_{0.06}Cr_3Te_4$, respectively. This clearly indicates that the Sn intercalation enhances the carrier density in Cr_3Te_4 by an order of two. The hole carrier density of Cr_3Te_4 estimated in this study is consistent with previous reports [58, 59].

Several mechanisms are proposed to understand the topological Hall effect in quantum materials. Such as the Dzyaloshinskii–Moriya (DM) interaction in the noncentrosymmetric systems [60–62] or the uniaxial magnetocrystalline anisotropy (MCA) in the centrosymmetric systems [63–66]. In our present case of the centrosymmetric Cr_3Te_4, the chiral-spin structure is stabilized by the strong MCA as already reported earlier by the same authors [22]. The chiral-spin structure is crucial to obtain the THE as the itinerant electrons acquire a real-space Berry curvature associated with finite scalar-spin chirality $\chi_{ijk} = S_i.(S_j \times S_k)$ which serves as fictitious magnetic field to generate the topological

Hall signal [67–69]. An array of chiral-spin structures can form a lattice structure called the skyrmion lattice. Our findings of topological Hall effect in Cr_3Te_4 and $Sn_{0.06}Cr_3Te_4$ are consistent with earlier studies on Cr_xTe_y-type systems demonstrating the presence of skyrmion lattice [20, 19, 70, 25].

7.3.6 Electronic Band Structure

Our experimental results of increased charge carrier density with Sn intercalation are qualitatively supported by the density functional theory (DFT) calculations. For the DFT calculations, we considered the conventional unit cell of Cr_3Te_4, consisting of 6 Cr atoms (2 Cr1-type and 4 Cr2-type) and 8 Te atoms per unit cell as shown in Fig. 7.7(a). For the Sn intercalated Cr_3Te_4, we considered one Sn atom per primitive unit cell [see Fig. 7.7(b)]. From the DFT calculations, we find that Cr_3Te_4 is a ferromagnetic metal with an average magnetic moment of 3.32 μ_B/Cr. With the intercalation of Sn, the metallicity and ferromagnetic nature persist, but the average magnetic moment slightly reduces to 3.29μ_B/Cr. These values are slightly higher than the experimental values of 2.56 μ_B/Cr for Cr_3Te_4 [36, 71] and 2.10 μ_B/Cr for $Sn_{0.06}Cr_3Te_4$ when measured at 2 K. Fig. 7.7(d) shows the total density of states (DOS) plotted for Cr_3Te_4 and 8% Sn intercalated Cr_3Te_4. We observe that the density of states (DOS) of $Sn_{0.06}Cr_3Te_4$, near the Fermi level, are significantly increased compared to the DOS of Cr_3Te_4. This behaviour is consistent with the experimental observation of enhanced charge carrier density with Sn intercalation. Moreover, the calculated Fermi energy of $E_F = 9.4650$ eV for Cr_3Te_4 increases to 10.9425 eV by the Sn intercalation. That means, the Fermi energy is shifted by about 1.5 eV towards the higher kinetic energy due to a significant change in the low-energy electronic structure of Cr_3Te_4 with the Sn intercalation. We also performed DFT+U calculations [72] for different values of U ranging up to $U = 3$ eV [see Fig. 7.8 (a-h)]. Interestingly, for all the values of U up to 1 eV, the calculations show enhanced DOS near the Fermi energy in $Sn_{0.06}Cr_3Te_4$ compared to Cr_3Te_4 [see Fig. 7.8 (i)]. However, for $U = 2$ eV and higher we do not find a significant difference in the DOS near E_F between $Sn_{0.06}Cr_3Te_4$ and Cr_3Te_4.

From the spin-resolved PDOS (see Fig. 7.8 (j-m)), we identify that the Cr 3d orbitals dominate the spin-up DOS near the Fermi level, while they have a negligible contribution to the spin-down DOS. Specifically, we notice that the spin-up DOS is dominated by d_{xy}, $d_{x^2-y^2}$, and d_{zx} orbitals in the vicinity of Fermi level. However, by the Sn intercalation, we notice a decrease in the spin-up DOS and drastic increase (about two times) in the spin-down DOS of $d_{x^2-y^2}$ and d_{zx}. On the other hand, the change in d_{xy} DOS is almost negligible by the Sn intercalation. This clearly indicates that the orbitals, $d_{x^2-y^2}$ and d_{zx} are critical for the superconductivity in $Sn_{0.06}Cr_3Te_4$. Having understood the orbital contribution near the Fermi level, we then went on to examine the band dispersions [see Figs. 7.7(e) and 7.7(f)] and Fermi surfaces [see Figs. 7.7(g) and 7.7(h)]. It is evident from the

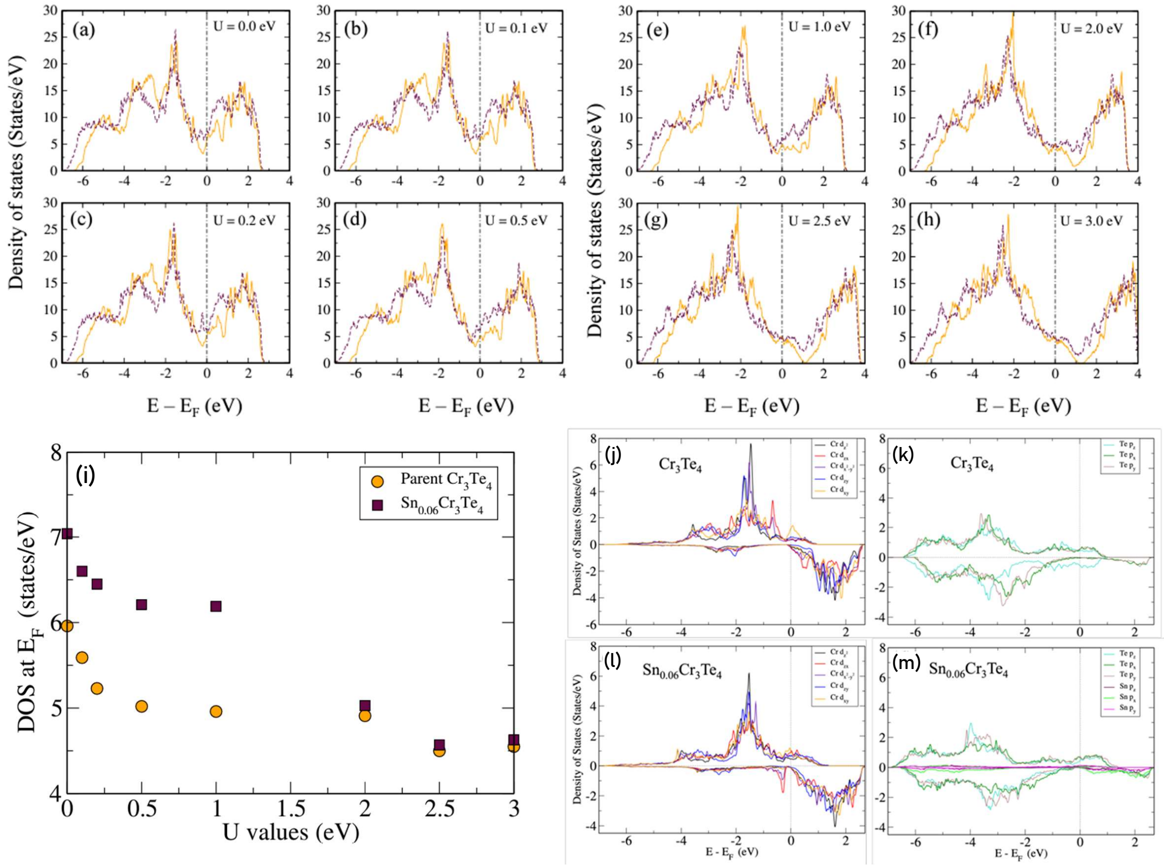

Figure 7.8: (a-h) Density of states of parent Cr_3Te_4 (yellow solid line) and 6% Sn-intercalated Cr_3Te_4 (maroon dashed line) calculated at different values of the Hubbard (U) parameter, (i) DOS at E_F as a function of U. Yellow circles and maroon squares represent the parent Cr_3Te_4 and $Sn_{0.06}Cr_3Te_4$ systems, respectively, (j-m) Projected density of states (PDOS) from the parent Cr_3Te_4 for Cr-d orbitals (a) and Te-p orbitals (b). PDOS of the Sn intercalated system for Cr-d orbitals (c), and for p orbitals of Te and Sn atoms (d). The negative values indicate down-spin states, while the positive values show the up-spin states.

band dispersions that the Sn intercalation not only shifts the Fermi level to higher kinetic energies but significantly alters the band structure near the Fermi level. Particularly, from a closer look at the spin-down Fermi surface of Cr_3Te_4, we notice an almost equal size of the hole ($k_F = 0.12\ au$) and electron($k_F = 0.16\ au$) pockets at the Brillouin zone center and zone corner, respectively [see Fig. 7.7(g)]. This observation hints at a possibility of Fermi surface nesting as observed from the unconventional superconductors such as in the Fe-based [73–75] and Cu-based [76, 77] systems in their magnetic state. Moreover, by the Sn intercalation, the size of the electron pocket increases at the zone corner, while the hole pockets are barely visible at the zone center [see Fig. 7.7(h)]. Thus, the reduced Fermi surface nesting is demonstrated in the superconducting state of $Sn_{0.06}Cr_3Te_4$, again consistent with $BaFe_{2-x}Co_xAs_2$ superconductor in which the highest T_c was obtained when the size of the hole pockets at the zone center is significantly reduced [78].

7.4 Conclusions

In conclusion, we successfully induced superconductivity in the topological vdWs ferromagnetic Cr_3Te_4 by Sn intercalation at an onset transition temperature of $T_c \approx 3.5$ K. We conclude that $Sn_{0.06}Cr_3Te_4$ is a type-II superconductor with a lower critical field of $H_{c1} = 58 \pm 4$ Oe and an upper critical field of $H_{c2} = 209 \pm 10$ Oe. A jump in the specific heat noticed around the T_c with a volume fraction of 33% confirms the bulk superconductivity in $Sn_{0.06}Cr_3Te_4$. Spin-polarized DFT calculations on Cr_3Te_4 and $Sn_{0.06}Cr_3Te_4$ provide a better understanding on the orbital contributions near the Fermi level. Tuning of topological Hall effect originating from the skyrmion lattice is noticed with Sn intercalation in Cr_3Te_4. Most importantly, for the first time, this study demonstrates superconductivity in a skyrmion lattice, offering a new class of topological quantum materials.

References

[1] C. Nayak, S. H. Simon, A. Stern, M. Freedman, S. Das Sarma, Non-Abelian anyons and topological quantum computation, Rev. Mod. Phys. 80 (2008) 1083–1159.

[2] L. Fu, C. L. Kane, Superconducting Proximity Effect and Majorana Fermions at the Surface of a Topological Insulator, Phys. Rev. Lett. 100 (2008) 096407.

[3] J. Nilsson, A. R. Akhmerov, C. W. J. Beenakker, Splitting of a Cooper Pair by a Pair of Majorana Bound States, Phys. Rev. Lett. 101 (2008) 120403.

[4] M. Veldhorst, M. Snelder, M. Hoek, T. Gang, V. K. Guduru, X. L. Wang, U. Zeitler, W. G. van der Wiel, A. A. Golubov, H. Hilgenkamp, A. Brinkman, Josephson supercurrent through a topological insulator surface state, Nat. Mater. 11 (2012) 417–421.

[5] H. D. Scammell, J. Ingham, M. Geier, T. Li, Intrinsic first- and higher-order topological superconductivity in a doped topological insulator, Phys. Rev. B 105 (2022) 195149.

[6] L. Fu, C. L. Kane, Probing Neutral Majorana Fermion Edge Modes with Charge Transport, Phys. Rev. Lett. 102 (2009) 216403.

[7] A. R. Akhmerov, J. Nilsson, C. W. J. Beenakker, Electrically Detected Interferometry of Majorana Fermions in a Topological Insulator, Phys. Rev. Lett. 102 (2009) 216404.

[8] L. A. Wray, S.-Y. Xu, Y. Xia, Y. S. Hor, D. Qian, A. V. Fedorov, H. Lin, A. Bansil, R. J. Cava, M. Z. Hasan, Observation of topological order in a superconducting doped topological insulator, Nat. Phys. 6 (2010) 855–859.

[9] A. Banerjee, A. Sundaresh, R. Ganesan, P. S. A. Kumar, Signatures of Topological Superconductivity in Bulk-Insulating Topological Insulator $\mathrm{BiSbTe_{1.25}Se_{1.75}}$ in Proximity with Superconducting $\mathrm{NbSe_2}$, ACS Nano 12 (2018) 12665–12672.

[10] Y. Goto, A. Yamada, T. D. Matsuda, Y. Aoki, Y. Mizuguchi, SnAs-based layered superconductor $NaSn_2As_2$, J. Phys. Soc. Japan 86 (2017) 123701.

[11] Y. Goto, A. Miura, C. Moriyoshi, Y. Kuroiwa, T. D. Matsuda, Y. Aoki, Y. Mizuguchi, $Na_{1-x}Sn_2P_2$ as a new member of van der Waals-type layered tin pnictide superconductors, Sci. Rep. 8 (2018) 1–8.

[12] X. Xiaoxiang, et al., Strongly enhanced cdws in monolayer nbse2, Nature nanotechnology 10 (2015) 765–769.

[13] E. J. Telford, J. C. Russell, J. R. Swann, B. Fowler, X. Wang, K. Lee, A. Zangiabadi, K. Watanabe, T. Taniguchi, C. Nuckolls, et al., Doping-induced superconductivity in the van der Waals superatomic crystal $Re_6Se_8Cl_2$, Nano Lett. 20 (2020) 1718–1724.

[14] Shruti, V. K. Maurya, P. Neha, P. Srivastava, S. Patnaik, Superconductivity by Sr intercalation in the layered topological insulator $\mathrm{Bi_2Se_3}$, Phys. Rev. B 92 (2015) 020506.

[15] Y. S. Hor, A. J. Williams, J. G. Checkelsky, P. Roushan, J. Seo, Q. Xu, H. W. Zandbergen, A. Yazdani, N. P. Ong, R. J. Cava, Superconductivity in $\mathrm{Cu}_x\mathrm{Bi_2Se_3}$ and its Implications for Pairing in the Undoped Topological Insulator, Phys. Rev. Lett. 104 (2010) 057001.

[16] M. L. Adam, Z. Liu, O. A. Moses, X. Wu, L. Song, Superconducting properties and topological nodal lines features in centrosymmetric $Sn_{0.5}TaSe_2$, Nano Res. 14 (2021) 2613–2619.

[17] S. Naik, G. K. Pradhan, S. G. Bhat, B. C. Behera, P. A. Kumar, S. L. Samal, D. Samal, The effect of Sn intercalation on the superconducting properties of $2H-NbSe_2$, Phys. C Supercond. Its Appl. 561 (2019) 18–23.

[18] E. Morosan, H. W. Zandbergen, B. S. Dennis, J. W. G. Bos, Y. Onose, T. Klimczuk, A. P. Ramirez, N. P. Ong, R. J. Cava, Superconductivity in $\mathrm{Cu}_x\mathrm{TiSe_2}$, Nature Physics 2 (2006) 544–550.

[19] J. Liu, B. Ding, J. Liang, X. Li, Y. Yao, W. Wang, Magnetic Skyrmionic Bubbles at Room Temperature and Sign Reversal of the Topological Hall Effect in a Layered Ferromagnet $\mathrm{Cr_{0.87}Te}$, ACS Nano 16 (2022) 13911.

[20] R. Saha, H. L. Meyerheim, B. Göbel, B. K. Hazra, H. Deniz, K. Mohseni, V. Antonov, A. Ernst, D. Knyazev, A. Bedoya-Pinto, I. Mertig, S. S. P. Parkin, Observation of Neel-type skyrmions in acentric self-intercalated $Cr_{1+x}Te_2$, Nat. Commun. 13 (2022).

[21] B. Li, X. Deng, W. Shu, X. Cheng, Q. Qian, Z. Wan, B. Zhao, X. Shen, R. Wu, S. Shi, H. Zhang, Z. Zhang, X. Yang, J. Zhang, M. Zhong, Q. Xia, J. Li, Y. Liu, L. Liao, Y. Ye, L. Dai, Y. Peng, B. Li, X. Duan, Air-stable ultrathin Cr_3Te_4 nanosheets with thickness-dependent magnetic biskyrmions, Materials Today 57 (2022) 66–74.

[22] S. Purwar, A. Low, A. Bose, A. Narayan, S. Thirupathaiah, Investigation of the anomalous and topological Hall effects in layered monoclinic ferromagnet $Cr_{2.76}Te_4$, Phys. Rev. Mater. 7 (2023) 094204.

[23] Y. Fujisawa, M. Pardo-Almanza, C.-H. Hsu, A. Mohamed, K. Yamagami, A. Krishnadas, G. Chang, F.-C. Chuang, K. H. Khoo, J. Zang, A. Soumyanarayanan, Y. Okada, Widely Tunable Berry Curvature in the Magnetic Semimetal $Cr_{1+\delta}Te_2$, Adv. Mater. 35 (2023) 2207121.

[24] H. Chi, Y. Ou, T. B. Eldred, W. Gao, S. Kwon, J. Murray, M. Dreyer, R. E. Butera, A. C. Foucher, H. Ambaye, J. Keum, A. T. Greenberg, Y. Liu, M. R. Neupane, G. J. de Coster, O. A. Vail, P. J. Taylor, P. A. Folkes, C. Rong, G. Yin, R. K. Lake, F. M. Ross, V. Lauter, D. Heiman, J. S. Moodera, Strain-tunable Berry curvature in quasi-two-dimensional chromium telluride, Nat. Commun. 14 (2023).

[25] C. Zhang, C. Liu, J. Zhang, Y. Yuan, Y. Wen, Y. Li, D. Zheng, Q. Zhang, Z. Hou, G. Yin, K. Liu, Y. Peng, X.-X. Zhang, Room-Temperature Magnetic Skyrmions and Large Topological Hall Effect in Chromium Telluride Engineered by Self-Intercalation, Adv. Mater. 35 (2023) 2205967.

[26] J. Dijkstra, H. H. Weitering, C. F. van Bruggen, C. Haas, R. A. de Groot, Band-structure calculations, and magnetic and transport properties of ferromagnetic chromium tellurides ($CrTe, Cr_3Te_4, Cr_2Te_3$), J. Phys.: Condens. Matter 1 (1989) 9141–9161.

[27] C. Pfleiderer, M. Uhlarz, S. M. Hayden, R. Vollmer, H. v. Löhneysen, N. R. Bernhoeft, G. G. Lonzarich, Coexistence of superconductivity and ferromagnetism in the d-band metal $ZrZn_2$, Nature 412 (2001) 58–61.

[28] C. Y. Yang, B. C. Chang, H. C. Ku, Y. Y. Hsu, Critical fields and the spontaneous vortex state in the weakly ferromagnetic superconductor $RuSr_2GdCu_2O_8$, Phys. Rev. B 72 (2005) 174508.

[29] N. T. Huy, A. Gasparini, D. E. de Nijs, Y. Huang, J. C. P. Klaasse, T. Gortenmulder, A. de Visser, A. Hamann, T. Görlach, H. v. Löhneysen, Superconductivity on the

Border of Weak Itinerant Ferromagnetism in UCoGe, Phys. Rev. Lett. 99 (2007) 067006.

[30] T. Hashimoto, K. Hoya, M. Yamaguchi, I. Ichitsubo, Magnetic Properties of Single Crystals $\mathrm{Cr_2Te_3}$, J. Phys. Soc. Japan 31 (1971) 679–682.

[31] P. E. Blöchl, Projector augmented-wave method, Phys. Rev. B 50 (1994) 17953–17979.

[32] P. Giannozzi, S. Baroni, N. Bonini, M. Calandra, R. Car, C. Cavazzoni, D. Ceresoli, G. L. Chiarotti, M. Cococcioni, I. Dabo, et al., QUANTUM ESPRESSO: a modular and open-source software project for quantum simulations of materials, J. Phys. Condens. Matter 21 (2009) 395502.

[33] P. Giannozzi, O. Andreussi, T. Brumme, O. Bunau, M. B. Nardelli, M. Calandra, R. Car, C. Cavazzoni, D. Ceresoli, M. Cococcioni, et al., Advanced capabilities for materials modelling with Quantum ESPRESSO, J. Phys. Condens. Matter 29 (2017) 465901.

[34] J. P. Perdew, K. Burke, M. Ernzerhof, Generalized gradient approximation made simple, Phys. Rev. Lett. 77 (1996) 3865–3868.

[35] S. Grimme, Semiempirical GGA-type density functional constructed with a long-range dispersion correction, J. Comput. Chem. 27 (2006) 1787–1799.

[36] M. Yamaguchi, T. Hashimoto, Magnetic Properties of Cr_3Te_4 in Ferromagnetic Region, J. Phys. Soc. Jpn. 32 (1972) 635–638.

[37] S. Ohta, Magnetic Properties of $(Cr_{1-u}V_u)_3Te_4$, J. Phys. Soc. Jpn. 54 (1985) 1076–1086.

[38] D. Babot, M. Wintenberger, B. Lambert-Andron, M. Chevreton, Propriétés magnétiques et conductibilité electrique des composés ternaires $Cr_3Se_{4-x}Te_x$, J. Solid State Chem. 8 (1973) 175–181.

[39] C. Chen, X. Chen, C. Wu, X. Wang, Y. Ping, X. Wei, X. Zhou, J. Lu, L. Zhu, J. Zhou, et al., Air-Stable 2D $\mathrm{Cr_5Te_8}$ Nanosheets with Thickness-Tunable Ferromagnetism, Adv. Mater. 34 (2022) 2107512.

[40] C. Li, K. Liu, D. Jiang, C. Jin, T. Pei, T. Wen, B. Yue, Y. Wang, Diverse Thermal Expansion Behaviors in Ferromagnetic $\mathrm{Cr_{1-\delta}Te}$ with NiAs-Type, Defective Structures, Inorg. Chem. 61 (2022) 14641.

[41] D. T. Wang, A. Göbel, J. Zegenhagen, M. Cardona, Raman scattering on α-Sn: Dependence on isotopic composition, Phys. Rev. B 56 (1997) 13167–13171.

[42] A. F. ANDRESEN, E. Zeppezauer, T. Boive, B. Nordström, C. Brändén, Magnetic structure of cr 2 te 3, cr 3 te 4, and cr 5 te 6, Acta Chem. Scand. 24 (1970) 3495–3509.

[43] W.-H. Jiao, Q. Tao, J.-K. Bao, Y.-L. Sun, C.-M. Feng, Z.-A. Xu, I. Nowik, I. Felner, G.-H. Cao, Anisotropic superconductivity in $Eu(Fe_{0.75}Ru_{0.25})_2As_2$ ferromagnetic superconductor, EPL (Europhysics Letters) 95 (2011) 67007.

[44] M. Tinkham, Introduction to Superconductivity, Medtech, 2017.

[45] S. Ishida, D. Kagerbauer, S. Holleis, K. Iida, K. Munakata, A. Nakao, A. Iyo, H. Ogino, K. Kawashima, M. Eisterer, H. Eisaki, Superconductivity-driven ferromagnetism and spin manipulation using vortices in the magnetic superconductor $EuRbFe_4As_4$, Proc. Natl. Acad. Sci. 118 (2021) e2101101118.

[46] T. Hamasaki, T. Hashimoto, Y. Yamaguchi, H. Watanabe, Neutron diffraction study of Cr_2Te_3 single crystal, Solid State Commun. 16 (1975) 895–897.

[47] J. Dijkstra, C. F. van Bruggen, C. Haas, R. A. de Groot, Electronic band-structure calculations of some magnetic chromium compounds, Journal of Physics: Condensed Matter 1 (1989) 9163–9174.

[48] V. Ginzburg, Antagonie von magnetismus und supraleitung, Journal of Experimental and Theoretical Physics 4 (1957) 153.

[49] R. D. Parks, Superconductivity, Routledge, 2018.

[50] J. S. Kim, R. K. Kremer, L. Boeri, F. S. Razavi, Specific Heat of the Ca-Intercalated Graphite Superconductor $\mathrm{CaC_6}$, Phys. Rev. Lett. 96 (2006) 217002.

[51] Y. Liu, C. Petrovic, Critical behavior of the quasi-two-dimensional weak itinerant ferromagnet trigonal chromium telluride $\mathrm{Cr_{0.62}Te}$, Phys. Rev. B 96 (2017) 134410.

[52] Y. Zhu, X. Kong, T. D. Rhone, H. Guo, Systematic search for two-dimensional ferromagnetic materials, Phys. Rev. Materials 2 (2018) 081001.

[53] S. Nakatsuji, N. Kiyohara, T. Higo, Large anomalous Hall effect in a non-collinear antiferromagnet at room temperature, Nature 527 (2015) 212–215.

[54] K. Kuroda, T. Tomita, M.-T. Suzuki, C. Bareille, A. Nugroho, P. Goswami, M. Ochi, M. Ikhlas, M. Nakayama, S. Akebi, R. Noguchi, R. Ishii, N. Inami, K. Ono, H. Kumigashira, A. Varykhalov, T. Muro, T. Koretsune, R. Arita, S. Shin, T. Kondo, S. Nakatsuji, Evidence for magnetic Weyl fermions in a correlated metal, Nat. Mater. 16 (2017) 1090–1095.

[55] N. Kanazawa, Y. Onose, T. Arima, D. Okuyama, K. Ohoyama, S. Wakimoto, K. Kakurai, S. Ishiwata, Y. Tokura, Large Topological Hall Effect in a Short-Period Helimagnet MnGe, Phys. Rev. Lett. 106 (2011) 156603.

[56] K. Shibata, X. Z. Yu, T. Hara, D. Morikawa, N. Kanazawa, K. Kimoto, S. Ishiwata, Y. Matsui, Y. Tokura, Towards control of the size and helicity of skyrmions in helimagnetic alloys by spin–orbit coupling, Nat. Nanotechnol. 8 (2013) 723.

[57] X. Yao, J. Chen, S. Dong, Controlling the helicity of magnetic skyrmions by electrical field in frustrated magnets, New J. Phys. 22 (2020) 083032.

[58] L. Zhou, J. Chen, X. Chen, B. Xi, Y. Qiu, J. Zhang, L. Wang, R. Zhang, B. Ye, P. Chen, X. Zhang, G. Guo, D. Yu, J.-W. Mei, F. Ye, G. Wang, H. He, Topological Hall Effect in Traditional Ferromagnet Embedded with Black-Phosphorus-Like Bismuth Nanosheets, ACS Appl. Mater. Interfaces 12 (2020) 25135–25142. PMID: 32338493.

[59] H. Li, L. Wang, J. Chen, T. Yu, L. Zhou, Y. Qiu, H. He, F. Ye, I. K. Sou, G. Wang, Molecular Beam Epitaxy Grown Cr_2Te_3 Thin Films with Tunable Curie Temperatures for Spintronic Devices, ACS Appl. Nano Mater. 2 (2019) 6809–6817.

[60] X. Yu, Y. Onose, N. Kanazawa, J. H. Park, J. Han, Y. Matsui, N. Nagaosa, Y. Tokura, Real-space observation of a two-dimensional skyrmion crystal, Nature 465 (2010) 901–904.

[61] W. Jiang, G. Chen, K. Liu, J. Zang, S. G. Te Velthuis, A. Hoffmann, Skyrmions in magnetic multilayers, Physics Reports 704 (2017) 1–49.

[62] O. Meshcheriakova, S. Chadov, A. K. Nayak, U. K. Rößler, J. Kübler, G. André, A. A. Tsirlin, J. Kiss, S. Hausdorf, A. Kalache, W. Schnelle, M. Nicklas, C. Felser, Large Noncollinearity and Spin Reorientation in the Novel $\mathrm{Mn_2RhSn}$ Heusler Magnet, Phys. Rev. Lett. 113 (2014) 087203.

[63] P. K. Rout, P. V. P. Madduri, S. K. Manna, A. K. Nayak, Field-induced topological Hall effect in the noncoplanar triangular antiferromagnetic geometry of $\mathrm{Mn_3Sn}$, Phys. Rev. B 99 (2019) 094430.

[64] B. Ding, Z. Li, G. Xu, H. Li, Z. Hou, E. Liu, X. Xi, F. Xu, Y. Yao, W. Wang, Observation of magnetic skyrmion bubbles in a van der Waals ferromagnet $\mathrm{Fe_3GeTe_2}$, Nano Letters 20 (2019) 868–873.

[65] D. A. Gilbert, B. B. Maranville, A. L. Balk, B. J. Kirby, P. Fischer, D. T. Pierce, J. Unguris, J. A. Borchers, K. Liu, Realization of ground-state artificial skyrmion lattices at room temperature, Nat. Commun. 6 (2015) 1–7.

[66] M. Nakamura, D. Morikawa, X. Yu, F. Kagawa, T.-h. Arima, Y. Tokura, M. Kawasaki, Emergence of Topological Hall Effect in Half-Metallic Manganite Thin Films by Tuning Perpendicular Magnetic Anisotropy, J. Phys. Soc. Jpn. 87 (2018) 074704.

[67] Y. Machida, S. Nakatsuji, Y. Maeno, T. Tayama, T. Sakakibara, S. Onoda, Unconventional anomalous hall effect enhanced by a noncoplanar spin texture in the frustrated kondo lattice $\mathrm{Pr_2Ir_2O_7}$, Phys. Rev. Lett. 98 (2007) 057203.

[68] Y. Taguchi, Y. Oohara, H. Yoshizawa, N. Nagaosa, Y. Tokura, Spin chirality, berry phase, and anomalous hall effect in a frustrated ferromagnet, Science 291 (2001) 2573–2576.

[69] H. Wang, Y. Dai, G. M. Chow, J. Chen, Topological Hall transport: materials, mechanisms and potential applications, Prog. Mater Sci. (2022) 100971.

[70] D. Feng, Z. Shen, Y. Xue, Z. Guan, R. Xiao, C. Song, Strain-induced magnetic phase transition, magnetic anisotropy switching and bilayer antiferromagnetic skyrmions in van der Waals magnet CrTe2, Nanoscale 15 (2023) 1561.

[71] Y. Wang, S. Kajihara, H. Matsuoka, B. K. Saika, K. Yamagami, Y. Takeda, H. Wadati, K. Ishizaka, Y. Iwasa, M. Nakano, Layer-Number-Independent Two-Dimensional Ferromagnetism in Cr_3Te_4, Nano Lett. 22 (2022) 9964–9971.

[72] A. I. Liechtenstein, V. I. Anisimov, J. Zaanen, Density-functional theory and strong interactions: Orbital ordering in Mott-Hubbard insulators, Phys. Rev. B 52 (1995) R5467–R5470.

[73] A. V. Chubukov, D. V. Efremov, I. Eremin, Magnetism, superconductivity, and pairing symmetry in iron-based superconductors, Phys. Rev. B 78 (2008) 134512.

[74] I. I. Mazin, D. J. Singh, M. D. Johannes, M. H. Du, Unconventional Superconductivity with a Sign Reversal in the Order Parameter of $\mathrm{LaFeAsO}_{1-x}\mathrm{F}_x$, Phys. Rev. Lett. 101 (2008) 057003.

[75] K. Terashima, Y. Sekiba, J. H. Bowen, K. Nakayama, T. Kawahara, T. Sato, P. Richard, Y.-M. Xu, L. J. Li, G. H. Cao, Z.-A. Xu, H. Ding, T. Takahashi, Fermi surface nesting induced strong pairing in iron-based superconductors, Proc. Natl. Acad. Sci. 106 (2009) 7330–7333.

[76] J. Ruvalds, C. T. Rieck, S. Tewari, J. Thoma, A. Virosztek, Nesting mechanism for d-symmetry superconductors, Phys. Rev. B 51 (1995) 3797–3805.

[77] T. Valla, A. V. Fedorov, J. Lee, J. C. Davis, G. D. Gu, The Ground State of the Pseudogap in Cuprate Superconductors, Science 314 (2006) 1914–1916.

[78] S. Thirupathaiah, S. de Jong, R. Ovsyannikov, H. A. Dürr, A. Varykhalov, R. Follath, Y. Huang, R. Huisman, M. S. Golden, Y.-Z. Zhang, H. O. Jeschke, R. Valentí, A. Erb, A. Gloskovskii, J. Fink, Orbital character variation of the Fermi surface and doping dependent changes of the dimensionality in $BaFe_{2-x}Co_xAs_2$ from angle-resolved photoemission spectroscopy, Phys. Rev. B 81 (2010) 104512.

Chapter 8

Summary of works

Chapter:1

This thesis comprehensively explores the magnetic, transport, and structural properties of layered chromium telluride systems. It begins with fundamental concepts of magnetism, emphasizing exchange interactions, spin-orbit coupling, magnetic anisotropy, and critical phenomena near phase transitions. The magnetocaloric effect's relevance to magnetic and spintronic applications is highlighted. The introduction also lays the groundwork for understanding the anomalous Hall effect (AHE) and topological Hall effect (THE) in terms of Berry curvature and nontrivial spin textures, themes examined in detail later.

Chapter:2

High-quality single crystals of Cr_xTe_y compounds were synthesized via chemical vapor transport (CVT) and self-flux methods. Structural and compositional integrity were verified through X-ray diffraction (XRD) and energy dispersive X-ray spectroscopy (EDXS). Magnetic and transport properties were systematically studied using a vibrating sample magnetometer (VSM) and a Physical Property Measurement System (PPMS).

Chapter:3

In this study, our investigation on the critical behavior of Cr_2Te_3 across the ferromagnetic to paramagnetic (FM-PM) transition temperature of 170 K reveals crucial insights into the magnetic exchange interactions. Specifically, the Kouvel-Fisher (KF) method derives the critical exponents, $\beta = 0.353(4)$ and $\gamma = 1.213(5)$, suggesting complex magnetic interactions falling in between the 3D-Ising and 3D-Heisenberg models. Furthermore, the renormalization group theory analysis indicates a 3D-Ising-type magnetic interaction decaying with distance as $J(r) = r^{-4.89}$. Importantly, the uniaxial magnetocrystalline anisotropy

(MAE) of $K_u = 2065$ kJ/m^3 is the highest ever known experimental value in Cr_xTe_y systems. We suggest that the 3D-Ising-type magnetic interactions in Cr_2Te_3 are stabilized by the extremely large uniaxial MAE. Further, density functional theory (DFT) calculations predict a large MAE of $K_u = 8230$ kJ/m^3, leading to a ground-state noncollinear ferromagnetic structure with dominant out-of-plane ferromagnetic and dominant in-plane antiferromagnetic Cr-spin arrangements. The self-consistent renormalization (SCR) theory suggests Cr_2Te_3 to be an out-of-plane itinerant ferromagnet. Investigating the magnetic entropy change, $-\Delta S_M^{\max}$, as a function of temperature provided insights into the magnetocaloric effect in this system. These findings collectively lay a robust groundwork for advancing magnetocaloric and spintronic technologies.

Chapter:4

Building on this, We have grown high-quality single crystals of layered ferromagnetic $Cr_{2.76}Te_4$ in the monoclinic phase to study the electrical transport, Hall effect, and magnetic properties. Our studies suggest $Cr_{2.76}Te_4$ to be a soft ferromagnet with negligible coercivity. The easy axis of magnetization is found to be parallel to the *bc* plane, leading to strong magnetocrystalline anisotropy. Below 50 K, an antiferromagnetic-like (AFM-like) transition is observed. Interestingly, in going from 50 K to 150 K, the strength of the magnetic moment switches between out-of-plane and in-plane configurations, suggesting fluctuating Cr spins. From the electrical resistivity measurements, the system is found to be metallic throughout the measured temperature range, with a noticeable kink around 50 K due to AFM ordering. Magnetotransport measurements demonstrate large anomalous Hall effect (AHE) and topological Hall effect (THE) in this system. First-principles calculations indicate an intrinsic AHE arising from nonzero Berry curvature near the Fermi level, while experimental results suggest the AHE is extrinsic, driven by skew scattering. The topological Hall effect is attributed to the noncoplanar spin structure stabilized by strong magnetocrystalline anisotropy.

Chapter:5

The study then transitions to $Cr_{1.38}Te_2$, We studied the magnetocrystalline anisotropy, critical behavior, and magnetocaloric effect in the layered room-temperature monoclinic ferromagnet $Cr_{1.38}Te_2$. Our systematic investigation of the structural properties of $Cr_{1.38}Te_2$ as a function of temperature establishes a relationship between the magnetic transitions and the crystal lattice. The derived critical exponents $\beta = 0.429(5)$ ($T_C \approx 315.84(2)$ K), $\gamma = 1.123(4)$ ($T_C \approx 315.87(5)$ K) using the Kouvel-Fisher (KF) method, and $\delta = 3.662(6)$ using the critical isothermal (CI) analysis at $T_C = 316$ K are self-consistent and obey the rescaling analysis. The renormalization group (RG) theory suggests that the derived critical exponents of $Cr_{1.38}Te_2$ exhibit three-dimensional (3D) Ising-like long-range exchange interactions $[J(r)]$, decaying as $J(r) = r^{-(d+\sigma)} = r^{-4.73}$. The RG theory suggests 3D-Ising-type magnetic interactions in this system, which are further confirmed by Monte Carlo simulations. Further, the magnetocrystalline anisotropy energy density (K_u) is found to be temperature-dependent and reaches a maximum of 180 kJ/m^3 at 110 K. The maximum entropy change, $-\Delta S_M^{\max} \approx 2.51$ J/kg-K, is observed near T_C for $H \parallel bc$. Density functional theory (DFT) predicts the *b*-axis as the magnetic easy axis by analyzing the magnetocrystalline anisotropy energy values for different spin configurations.

Chapter:6

The magnetotransport properties of $Cr_{0.83}Te$ were then studied, We investigated the intricate magnetism, electrical, and magnetotransport properties in the hexagonal itinerant ferromagnet $Cr_{0.83}Te$. The magnetotransport study reveals a substantial topological Hall effect (THE), originating from the noncoplanar spin structure in the presence of strong magnetic anisotropy and the skew-scattering-induced anomalous Hall effect (AHE). We observe a remarkable cooling efficacy of $-\Delta S_M^{\max} \approx 2.77$ J kg^{-1} K^{-1} and RCP ≈ 88.29 J/kg at an applied field of 5 T. By utilizing the magneto-entropy scaling analysis, we extracted the critical exponents $\beta = 0.4739(4)$, $\gamma = 1.2812(3)$, and $\delta = 3.7037(5)$, which do not follow any single universality class, suggesting a complex magnetic interaction in $Cr_{0.83}Te$. Re-scaled $-\Delta S_M(T, H)$ curves fall into a single universal curve, confirming the second-order magnetic transition. The spin-fluctuation parameter, derived from the critical magnetization isotherms based on the self-consistent renormalization (SCR) theory, confirms the itinerant ferromagnetic nature of $Cr_{0.83}Te$.

Chapter:7

The thesis concludes with an exploration of superconductivity induced in Cr_3Te_4 through Sn intercalation. This led to the discovery of a superconducting transition at 3.5 K, with specific heat measurements confirming bulk superconductivity. Interestingly, this system also demonstrated coexistence of superconductivity and skyrmion-like spin textures, potentially enabling novel quantum phases. The interplay between magnetism and superconductivity in these materials represents a culmination of the themes explored throughout this thesis.

Future Plan

This thesis paves the way for several promising research avenues aimed at deepening our understanding of 2D magnetic materials and their magneto-transport properties. Key aspects of future work include:

Neutron differaction studies in $Cr_{1+\delta}Te_2$

$Cr_{1+\delta}Te_2$ exhibits complex magnetism due to Cr intercalation between $CrTe_2$ layers. By varying δ, we have demonstrated tunable Curie temperatures exceeding room temperature, structural transitions across trigonal, monoclinic, and hexagonal phases, and a rotation of magnetic anisotropy from out-of-plane to in-plane orientations. Additionally, a spin dimensionality shift from Ising to Heisenberg behavior was identified through critical behavior analysis. Magnetotransport studies have revealed intriguing anomalous and topological Hall effects, linked to spin-orbit coupling and magnetic anisotropy. The canting angle of Cr spins changes with intercalation, significantly influencing transport properties. To uncover the precise magnetic structure and interlayer interactions, neutron scattering measurements will be performed.

Fe_xSe_y Polycrystalline System

Polycrystalline Fe_xSe_y was synthesized, revealing metal-to-insulator transitions accompanied by structural distortions. These findings indicate the material's potential as a 2D ferrimagnet with rich electronic and magnetic phases. A manuscript detailing these studies is currently under preparation.

Exploration of Other 2D Magnetic Materials

Growth of additional 2D magnetic materials, including $CrSiTe_3$, $NbFeTe_2$, and $Fe_{0.25}ZrS_2$, opens new opportunities to investigate their magnetic and magnetotransport properties. Preliminary work on these systems will focus on detailed structural, magnetic, and electronic characterization to elucidate their unique magnetic phenomena and potential for spintronic applications.